# APOFERRITIN CRYSTALLIZATION IN RELATION TO EYE CATARACT

A Dissertation
Presented to
The Academic Faculty

By

Karsten Bartling

In Partial Fulfillment
Of the Requirements for the Degree
Doctor of Philosophy in Bioengineering
School of Chemical & Biomolecular Engineering

Georgia Institute of Technology

December, 2006

**APOFERRITIN CRYSTALLIZATION IN RELATION TO EYE CATARACT**

Approved by:

Dr. Ronald W. Rousseau, Advisor
School of Chemical & Biomolecular
Engineering
*Georgia Institute of Technology*

Dr. Joe Le Doux
School of Biomedical Engineering
*Georgia Institute of Technology*

Dr. Athanassios Sambanis, Co-advisor
School of Chemical & Biomolecular
Engineering
*Georgia Institute of Technology*

Dr. Timothy M. Wick
Department of Biomedical Engineering
*The University of Alabama at
Birmingham*

Dr. Victor Breedveld
School of Chemical & Biomolecular
Engineering
*Georgia Institute of Technology*

Date Approved: August 11, 2006

To my wife and family

# ACKNOWLEDGEMENTS

# TABLE OF CONTENTS

# LIST OF TABLES

# LIST OF FIGURES

# NOMENCLATURE

| | |
|---|---|
| $A$ | dimensionless second virial coefficient; peak area, area, $m^2$ |
| $B$ | Jones-Dole viscosity $B$ coefficient ; second virial coefficient, $mol \cdot mL/g^2$ |
| $B, C, ...$ | virial coefficients |
| $c$ | solute concentration, g/mL |
| $D$ | thickness, mm |
| $\Delta E_a$ | activation energy, kJ/mol |
| $h$ | convection heat transfer coefficient, $W/m^2 \cdot K$ |
| $I$ | Light intensity, $W/m^2$ |
| $k$ | thermal conductivity, $W/m \cdot K$ |
| $kD$ | kilo Dalton |
| $K$ | Optical constant, $cm^2 \cdot mol/g^2$ |
| $K_{sp}$ | solubility product |
| $L$ | characteristic length, mm |
| $M_W$ | molecular weight, g/mol |
| $m$ | mass, g |
| $pKa$ | acid dissociation constant |
| $q$ | heat transfer rate, W |
| $R$ | universal gas constant |
| $R^2$ | correlation coefficient |
| $t$ | time, s |
| $T$ | temperature, ºC or K |
| $x, y, z$ | rectangular coordinates, mm |
| $W$ | characteristic width, mm |
| $W (r)$ | potential of mean force |

**Greek Letters**

$\alpha$          polarizability

$\infty$          free stream conditions

$\theta$          geometric angle; temperature difference, K

$\lambda$          wavelength, nm

$\Pi$          Osmotic pressure, atm

**Subscripts**

*0, S*          incident and scattered, respectively

*1, 2*          species in binary mixture

*a*          activation

*c*          cross-sectional area

*conv.*          convection

*cryst.*          crystallization

*L, 0*          based on characteristic length

# ABBREVIATIONS

| | |
|---|---|
| AAS | Atomic absorption spectrometry |
| AMD | Age-related macular degeneration |
| ATP | Adenosine triphosphate |
| BMCD | Biological acromolecule Crystallization Database |
| BSA | Bovine serum albumin |
| CD | Circular dichroism |
| EDTA | Ethylenediaminetetraacetic acid |
| EMBP | Eosinophil Major Basic Protein |
| HHCS | Hereditary Hyperferritinemia Cataract Syndrome |
| HPLC | High-Performance Liquid Chromatography |
| LEC | Lens epithelial cells |
| NDSB | Non-detergent sulfobetaine |
| NMR | Nuclear magnetic resonance |
| NGO | Non-governmental organization |
| ICP-OES | Inductively Coupled Plasma - Optical Emission Spectroscopy |
| IRE | Iron Responsive Element |
| IRP | Iron Regulatory Protein |
| MR | Mandelate racemase |
| ONCHO | Onchocerciasis |
| PDB | Protein Data Bank |
| SEC | Size exclusion chromatography |
| SOD | Superoxide dismutase |
| WHO | World Health Organization |

# SUMMARY

Protein crystallization is significant in both biotechnology and biomedical applications. In biotechnology, crystallization is essential for determining the structure of both native and synthesized therapeutically important proteins. It can also be used as a final purification step and as a stable form for protein storage. With regard to biomedical systems, protein crystallization appears to be involved in the development and manifestation of certain human diseases. In particular, there exists evidence that L-rich ferritin crystals are involved in Hereditary Hyperferritinemia Cataract Syndrome (HHCS).

In the current research a microbatch crystallization apparatus has been introduced that enables (1) multiple batch crystallization experiments at various temperatures and solution conditions in parallel and (2) quantitative monitoring of crystal growth without disturbing the progress of an experiment for observation. The primary application of the apparatus is, but not limited to, screening of protein crystallization conditions, although the system can also be used for other macromolecular and small-molecule crystallization experiments.

Multiwell microbatch experiments demonstrated the dependence of apoferritin crystal growth kinetics and final crystal size on temperature and cadmium concentration. Although the solubility of apoferritin might be independent of temperature, the results of this study show that the crystal growth kinetics *are* affected by temperature, profoundly under some conditions.

For apoferritin under near physiological conditions the solution thermodynamics in the form of the second virial coefficient have proofed to be a valuable predictor for the crystallization outcome. Furthermore, the significance of the elevated level of some divalent cations in cataractous lenses has been studied both in dilute solutions and under crystallization conditions and cadmium seems to be sole menace in apoferritin condensation.

# CHAPTER 1

## INTRODUCTION AND MOTIVATION

The research conducted constitutes an important step towards a better understanding of the role of protein-protein interactions in cataract formation. The common treatment for cataracts is the surgical removal of the lens. In the case of Hereditary Hyperferritinemia Cataract Syndrome (HHCS), hereditary disposition causes the propagation to follow a certain pattern involving L-ferritin crystallization or precipitation in the lens, thus facilitating potential treatment options to prevent the onset of cataracts. HHCS is the first case reported where protein condensation leads to the formation of crystalline deposits. Being able to predict that protein crystallization or precipitation is about to occur, and to implement specific steps to inhibit this event, would help to understand the pathophysiology of HHCS and, importantly, propose specific pharmacological approaches for preventing the development of the disease. The research set the stage towards meeting these long-term objectives by investigating the underlying scientific hypothesis in well-defined *in vitro* systems.

The World Health Organization (WHO) and non-governmental organizations (NGOs) implemented a common plan for global action "VISION 2020 – The Right to Sight' in 2000 to reverse the trend of ever increasing avoidable blindness. The justification of this initiative is the total number of 40-45 million blind people worldwide, with a predicted number to reach 100 million in the year 2020. Approximately 50% of the blind people suffer from cataract (Congdon et al. 2004; Pizzarello et al. 2004). In the

US alone about 17% of the general population over 40 years in age suffer from cataracts, and their treatment accounts for about 60% of vision-related Medicare costs (Congdon et al. 2004). The proposed research plan shares the objective of the WHO initiative by targeting cataract prevention and control. The research focuses on the Hereditary Hyperferritinemia Cataract Syndrome (HHCS), a newly discovered and hence rare congenital genetic disorder characterized by elevated serum ferritin and early onset cataract formation (Allerson et al. 1999). Although an elevated serum ferritin level is associated with this disease, the occurrence of cataract through the crystallization of ferritin molecules is the only clinical feature of HHCS (Mumford et al. 2000).

The causes of senile cataract are poorly understood and there is no current treatment other than surgery. Kupfer (Kupfer 1985) has stated that if a factor could be found that would delay cataract onset by 10 years, a decrease in cataract surgery of about 45% could be achieved. Although studies have been trying to link nutritional differences to cataract formation, such a link has not been established. Analysis of different blood constituents in cataract patients, such as total protein, calcium, glucose, urea and bilirubin, indicated that all these parameters fell within normal physiological levels (Mirsamadi and Nourmohammadi 2003). In HHCS the ferritin level in the body is elevated but the protein only crystallizes in the lens. This leads to the hypothesis that in HHCS the physicochemical environment of the lens promotes ferritin crystallization.

The abnormal divalent ion levels in cataractous lenses may contribute to the crystallization of ferritin (Avunduk et al. 1999; 1999). The question is if the elevated level of cadmium ions in affected lenses leads to cataract formation, since divalent ions are used *in vitro* as protein crystallization agents. The other possibility would be that the

divalent ion concentration is elevated because those ions are present in the solid protein phase, therefore increasing their overall ocular concentration.

Protein solubility is a strong function of temperature. For instance, lysozyme solubility essentially doubles when the temperature is increased from 30 °C to 37 °C (Cacioppo and Pusey 1991). The lower eye temperature relative to body temperature (Rosenbluth and Fatt 1977), and the decrease in eye temperature with age (Alio and Padron 1982), may thus be factors promoting the formation of ferritin crystals.

The research investigated fundamental aspects of apoferritin crystallization from solution, and evaluated the effect of temperature and divalent cation and solubilizers on protein-protein interaction in solution and the resulting crystallization outcome. Furthermore, it investigated whether a single thermodynamic parameter, the second virial coefficient, can predict the fate of a protein in solution, irrespective of the means used to establish the driving force for crystallization or precipitation. This, in itself, was significant, but it also set the stage for developing predictive assays on the tendency of proteins to crystallize out of biological fluids and for evaluating the efficacy of solubilizers at preventing the occurrence of crystallization. Assessing the risk of individuals for developing HHCS and administering treatments based on protein solubilizers could potentially be of significant clinical value.

## SPECIFIC AIMS

Many proteins have been successfully crystallized; however, identifying conditions appropriate for crystallization remains a mostly empirical task. A thorough, quantitative and mechanistic understanding of protein crystallization processes and of the

conditions affecting them is currently lacking. My *long-range* goal was to explain how the thermodynamics of biological solutions determine the crystallization or amorphous precipitation of proteins out of such solutions, and how additives can predictably affect the crystallization or precipitation outcome. The *objective of this research* was to evaluate the correlation between solution thermodynamics and crystallization outcome of apoferritin, and to characterize the effect of temperature, divalent cations and solubilizers on the protein-protein interactions, nucleation and growth of apoferritin crystals. The *central hypotheses* of this research were that temperature, cadmium concentration and the addition of solubilizers influence the crystallization behavior of apoferritin and that a single thermodynamic parameter, namely, the second virial coefficient of apoferritin solutions, is predictive of whether the protein remains in solution or crystallizes or precipitates out of it. Crystallization can be effected by different variables, including temperature, divalent cations and protein solubilizers; however, the second virial coefficient retains its predictive capacity irrespective of the means to generate the driving force for the protein to come out of solution. The *rationale* for the conducted research was that the understanding to be developed would help evaluate the propensity of specific proteins to crystallize or precipitate out of physiologic fluids, thereby elucidating means to encourage proteins to remain in solution. Thus, this research may suggest innovative pharmacological approaches to prevent cataract disease.

The two *specific aims* of this research were as follows:


- **Specific Aim 1:** Determine the role of temperature and of cadmium ions on the protein−protein interactions and on the crystallization characteristics of apoferritin with different H−chain to L−chain ratios.

The protein–protein interactions were evaluated by measuring the second virial coefficient of the protein in solution by static light scattering. The effect of the ions on apoferritin crystallization was evaluated by measuring the number and size of crystals that appear after the system had reached equilibrium.

- **Specific Aim 2:** Determine the effect of additives on the protein–protein interactions and crystallization characteristics of apoferritin with different H–chain to L–chain ratios.

Solubility–increasing substrates, such as non–detergent sulfobetaines (NDSB), were used to prevent the crystallization of apoferritin *in vitro* under conditions favoring crystallization, as identified in Aim 1. The protein–protein interactions again were evaluated via static light scattering.

The proposed work is *innovative* because it focused on an unstudied crystallization process of a medically relevant protein under medically relevant conditions. Additionally, it investigated for the first time the correlation between protein solution thermodynamics and the crystallization or precipitation result. With respect to *expected outcomes*, the combination of work proposed in Aims 1 and 2 is collectively expected to identify solution conditions that result in apoferritin crystallization, as well as to characterize the effect of agents that can inhibit crystallization from occurring. These experiments set the stage for future *in vivo* studies on apoferritin crystallization in animal models of cataracts, which were not a subject of the conducted research but can be incorporated in future research work.

# CHAPTER 2

# BACKGROUND

## 2.1 Biological Examples of Protein Crystallization

The primary interest of protein crystallization is to obtain structural information of the protein of interest through X-ray diffraction, to transform the proteins into a more stable crystalline form or as a purification tool in many downstream processes. Although *in vivo* protein crystallization might be perceived as an atypical behavior, since protein aggregation and crystallization is normally expected to compromise the viability of the cells, it nevertheless occurs spontaneously in living cells and tissue. However, the majority of proteins synthesized within cells do not condense readily into a solid state *in vivo* or even in the laboratory. It was therefore postulated that the difficulty of crystallizing proteins *in vitro* may reflect the 'negative selection' that has evolved *in vivo* over the easily crystallizable protein variants (Doye et al. 2004).

Historically, reserve or storage proteins were second only to hemoglobin to be investigated in terms of their crystallization characteristics. These proteins, belonging to the class of globulins, naturally form crystals in the seeds of certain plants. The plant kingdom furthermore provided the first crystallization of intact viruses, like the tobacco mosaic virus, and even ribosomes and ribosomal subunits (McPherson 1999). In general, protein crystals provide a form of protein storage, serve as a temporary reservoir, or are means of disposal for inactive molecules or molecules produced in excess in living cells and tissue. A possible advantage of a macromolecular condensate over proteins free in solution is that the solid form provides an efficient storage mode which uses a minimum

of space and water while still retaining the necessary biological function. The retention of the biological function might be the significant driving force for the preference of the crystalline over the amorphous state since for example crystallized enzymes retain their catalytic activity in the solid state (Margolin 1996). Examples of crystalline state enzyme clusters are peroxisomes, which are cell organelles that contain an enzyme crystal core for certain oxidative reactions (Sulter et al. 1990).

The protein crystals in plant seeds mentioned above are an example of protein storage within plants. The, at times, very high concentration of certain seed proteins result in the formation of protein crystals in membrane bound protein storage vesicles. Another example of *in vivo* storage of macromolecular molecules are virus crystals in infected cells. Virus particles are structurally very complex, indicated by their high degree of symmetry. Nevertheless, they condense into perfect crystals upon reaching supersaturation in obviously normal-physiological environments in the absence of precipitants or other crystal growth inducers (McPherson 1999). Other examples of proteins stored in tissues in crystal form is insulin in the secretory vesicles of pancreatic cells (Abel 1926; Bergeron et al. 2003; Arvan 2004), the eosinophil major basic protein (EMBP) in the secretory granules of granulocytes involved in the immune response (Guo et al. 2000) and bacterial proteins that act as insecticidal toxins which are highly concentrated and stable in the crystal form (McPherson 1999; Doye and Poon 2006).

Beside storage, protein crystals *in vivo* also serve to encapsulate in particular virus particles, as some viruses assume a quiescent state in insect cells by becoming embedded in a matrix of crystalline protein. The viruses induce the expression of large quantities of proteins, such as polyhedron, granulin and spheroidin, in the infected cells and also serve

as heterogeneous nucleants to promote crystal growth around them. The so embedded virus particles, then called virions, provide a protective environment for the viruses until new insect larva are infected, as the crystalline shield provides higher mechanical stability compared to other protein crystals (McPherson 1999; Doye and Poon 2006).

Furthermore, protein crystalline inclusion bodies are associated with many pathological conditions, especially in various types of neurodegenerative diseases, such as Alzheimer's and Creutzfeld-Jacob disease. Besides neurodegenerative diseases protein inclusion bodies are involved in other pathologies, the most prominent one being sickle cell anemia. Here, hemoglobin inside the red blood cell forms a crystalline structure elongating the cells and therefore inducing the characteristic cell shape that can resemble sickles. Other diseases where protein crystal formation is involved are certain cataracts, for example mutations on $\gamma$-crystallin within the ocular lens leads to congenital cataract formation (Kmoch et al. 2000).

## 2.2 Ocular Lens Physiology

### 2.2.1 Ocular Lens

The lens is located directly behind the iris. Anteriorly, it is bathed in aqueous humor; posteriorly, it lies against the vitreous humor (Figure 2-1). The lens has no innervation or blood supply after fetal development. The transparency of the crystalline lens has been attributed to the complex, ordered arrangement of its components at both microscopic and molecular levels. At the microscopic level, the regular array of flattened, hexagonal cross-sections of fiber cells characterizes lens tissue (Taylor et al.

1996). The human lens grows throughout the human lifespan through epithelial cell division and the formation of generations of differentiated fiber cells forming layers of fiber cells (Bron et al. 2000). The most inner cells within the lens are hence the oldest cells and due to the almost non-existence of metabolic activity also contain the body's oldest proteins. The growth of the lens through adding layers of new cells on top of the already existing cells in the absence of cell shedding can be compared to the growth of a tree: the age of the lens is represented spatially across its profile with those cells at the center being as old as the individual in whom they reside.
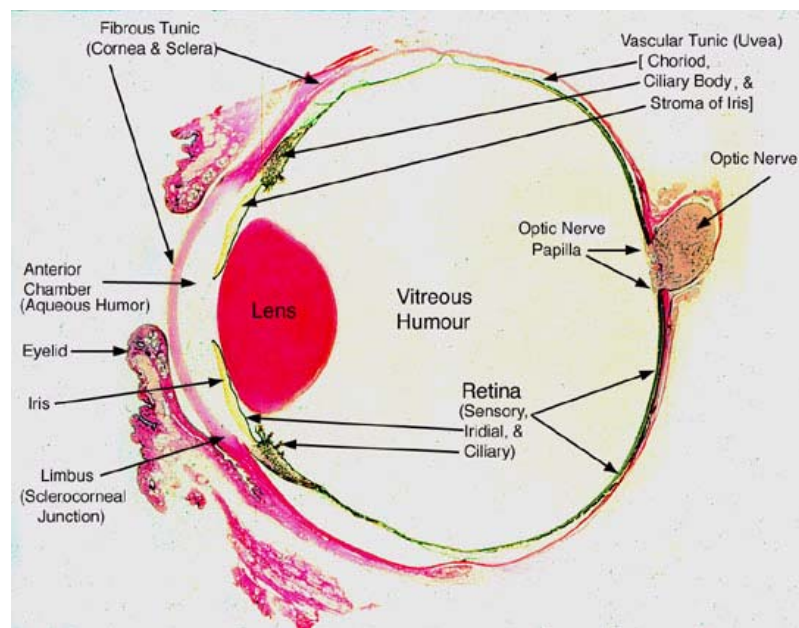


Figure 2-1. Anatomy of the ocular lens (Source:
http://faculty.une.edu/com/abell/histo/histolab3b.htm)

The metabolism of the lens and the removal of its waste products are performed by the surrounding aqueous and vitreous humor. The composition of the aqueous humor

is similar, although not identical, to that of blood plasma (Lens 1999). Cataract, or opacification of the ocular lens, is the most common cause of visual impairment worldwide. It is only treatable at present by surgical removal.

Mature lens fibers do not divide, and there is minimal turnover of their protein constituents resulting in age–dependent protein concentration (Figure 2-2 and Figure 2-3).
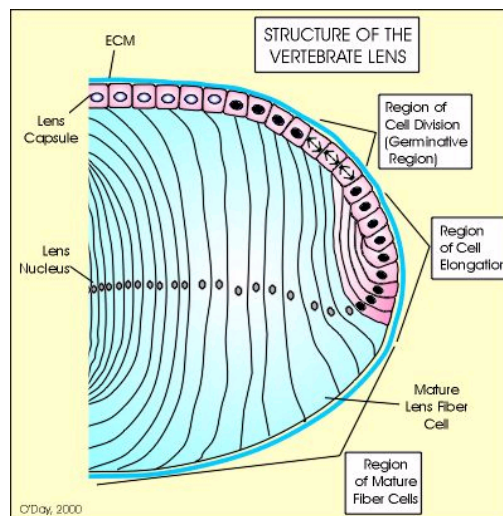


Figure 2-2. Structure of the vertebrate lens (Source: http://www.uia.ua.ac.be/u/clauwaer/html/figure2.html from April 12th 2006)

Transparency of the lens results from the highly ordered arrangement of the macro-molecular components of constituent cells and the regular arrangement of lens fibers. Protein accounts for a third of the wet weight of the lens, nearly double that found in other tissues (Francis et al. 1999). The high level of proteins maximizes the transparency of the lens (Nugent and Whelan 1984).
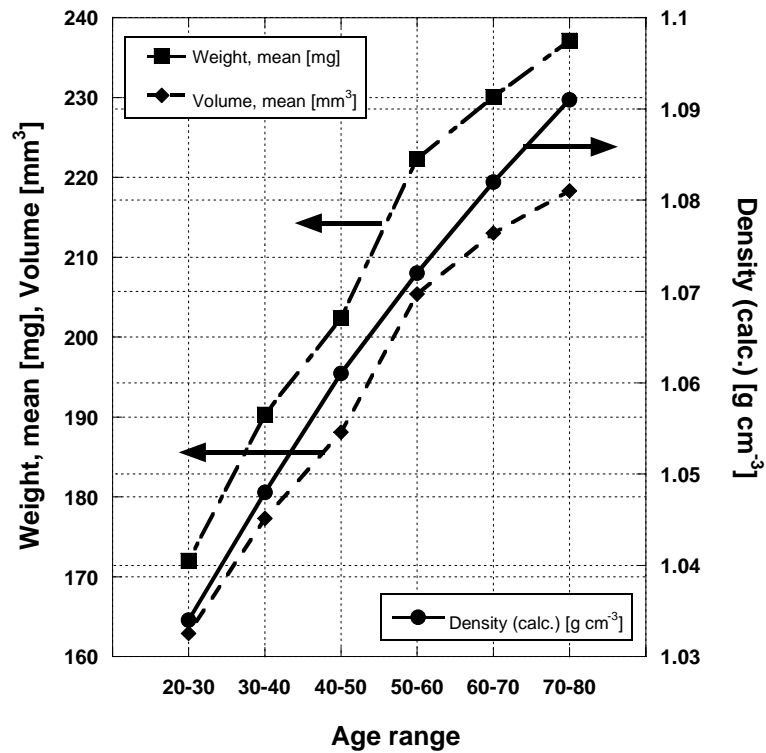
Figure 2-3. Lens physiology as a function of age

The dimension of the lens changes with age. At early fetal life the lens is almost perfectly spherical and becomes ellipsoidal after birth. At birth the lens diameter is about 6.5 mm and its thickness is about 3 mm. The dimensions increase to about 9-10 mm in equatorial diameter and 5-6 mm in thickness by the ninth decade (Bron et al. 2000).

### 2.2.2 Ocular Temperature

The ocular temperature differs from the main body temperature. Ocular temperature measurements in rabbits revealed that there is a nonlinear temperature gradient of ~35.7 °C to ~38.3 °C from the anterior to the posterior lens along the

papillary axis, at a body temperature of about 39 °C (Rosenbluth and Fatt 1977). In another study on rabbits, the midlens temperature was measured at ~35.6 °C at an environmental temperature of about 22 °C (Schwartz 1965). Again with rabbits, the ocular temperature was found to be dependent on environmental temperature: the midlens temperature decreased from about 35 °C at 23 °C ambient temperature to about 31 °C at −14 °C ambient temperature (Freeman and Fatt 1973). Additionally, the ocular temperature was found to be influenced by exposure to sunlight (both ultraviolet and infrared) (Alghadyan and Cotlier 1986). This strong dependence of ocular temperature on environmental conditions is due to the cornea being both metabolically stagnant and avascular, making the environment its main source of heat (Mapstone 1968).

To my knowledge, there are no values of human interior ocular temperature measurements reported in the literature, but the same qualitative temperature distribution is expected for the human eye as that found in animal studies. Furthermore, an age influence on the ocular temperature has been identified. The temperature of the anterior segment of the eye decreases linearly with increasing age (15 weeks to 80 years of age), and the temperature of the center of the cornea decreases from about 34 °C to about 32.5 °C over the same age range (see Figure 2-4) (Alio and Padron 1982). The significance of this temperature decrease becomes clear if one considers that the solubility of lysozyme decreases by 15.3% in a Na−acetate / NaCl solution over the same temperature range (Forsythe and Pusey 1996). Most cataract formations are age−dependent, thus a correlation with the decreasing ocular temperature may indeed exist.
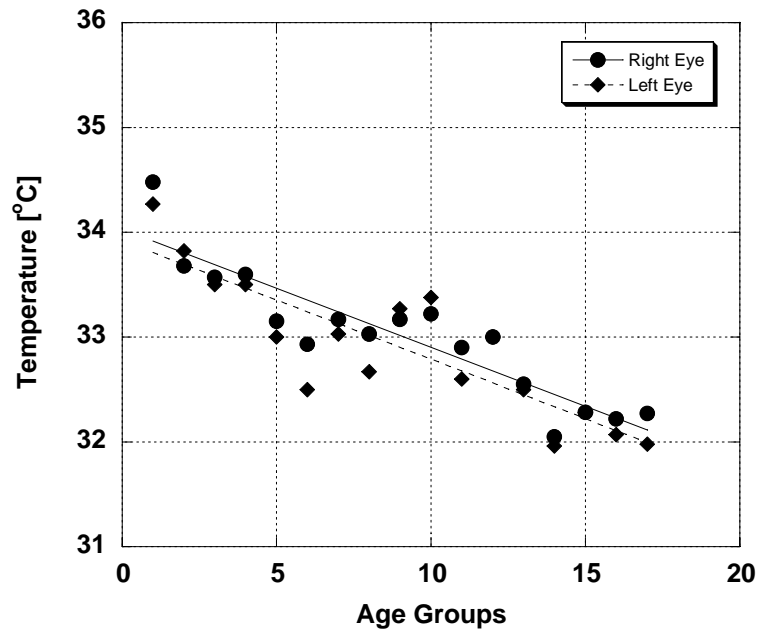
Figure 2-4. Ocular temperature gradient as a function of age (each age group refers to 5 year period of age) (data adopted from (Alio and Padron 1982))

## 2.3 Cataract

### 2.3.1 General Information

Cataract is clouding of the lens of the eye and in general describes any opacity which affects the cortex or nucleus of the lens. Cataracts are broadly divided into two major groups. First, developmental or congenital cataract in which the normal development of the lens is affected by genetic, nutritional or inflammatory changes and second, degenerative cataract, which includes senile cataract and cataract associated with radiation or systemic disease (Armstrong 2000).

According to the World Health Organization, in 2002 more than 161 million people were visually impaired. Except for the most developed countries, cataract remains the leading cause of blindness world wide (see Figure 2-5).
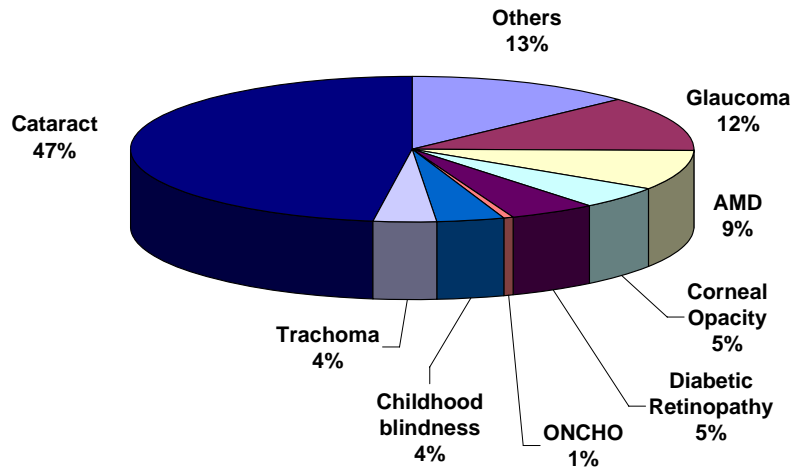
Figure 2-5. Global causes of blindness (World Health Organization 2004) (AMD - Age-related macular degeneration, ONCHO – Onchocerciasis)

Approximately one quarter to one-third of congenital cataracts are hereditary. Congenital cataracts have been reported with all three types of Mendelian inheritance, i.e., autosomal dominant, autosomal recessive, and X chromosome-linked. Autosomal dominant congenital cataracts appear to be the most common and typically are symmetrical in affected individuals (He and Li 2000).

**2.3.2 Hereditary Hyperferritinemia Cataract Syndrome (HHCS)**

HHCS is an autosomal dominant disorder (see Figure 2-6 for the gene location of HHCS) characterized by bilateral cataracts and increased serum and tissue L−ferritin, in the absence of iron overload (Girelli et al. 1997; Cicilano et al. 1999; Roetto et al. 2002). At the molecular level, HHCS has been identified as a disease that arises from mutations within the protein−binding site of an RNA regulatory element (Allerson et al. 1999; Roetto et al. 2002).
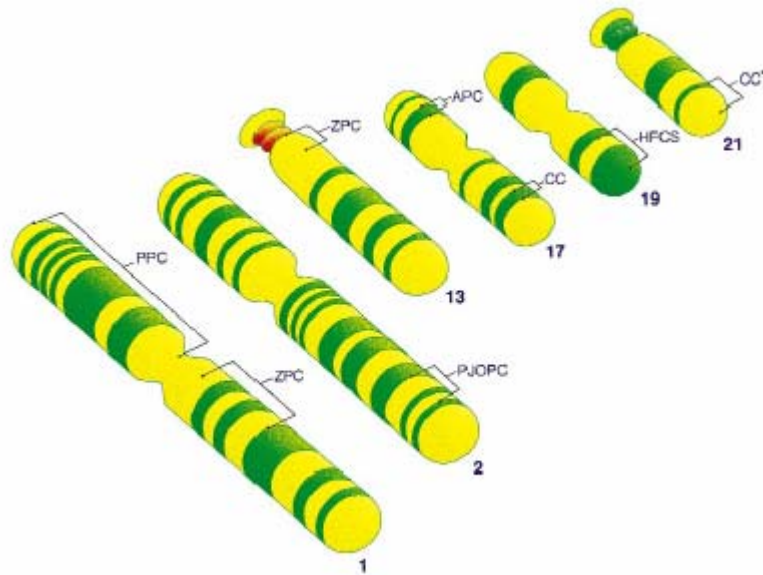


Figure 2-6: Location of some of the major genes associated with cataract. HFCS = Hyperferritinemia cataract syndrome ≜ HHCS (Roetto et al. 2002)

In normal individuals with low iron content, the transcription of ferritin is blocked, making iron available by limiting the iron storage capacity. In the case of iron overload, the docking of the iron regulatory protein (IRP) onto the iron responsive element (IRE) is blocked by iron in the form of iron sulfate (FeS), enabling the synthesis of ferritin. In patients with HHCS the IRE has several point mutations severely lowering

the affinity of IRP to IRE of the L−ferritin mRNA. As a result, L−ferritin production occurs irrespective of the iron level (Figure 2-7).
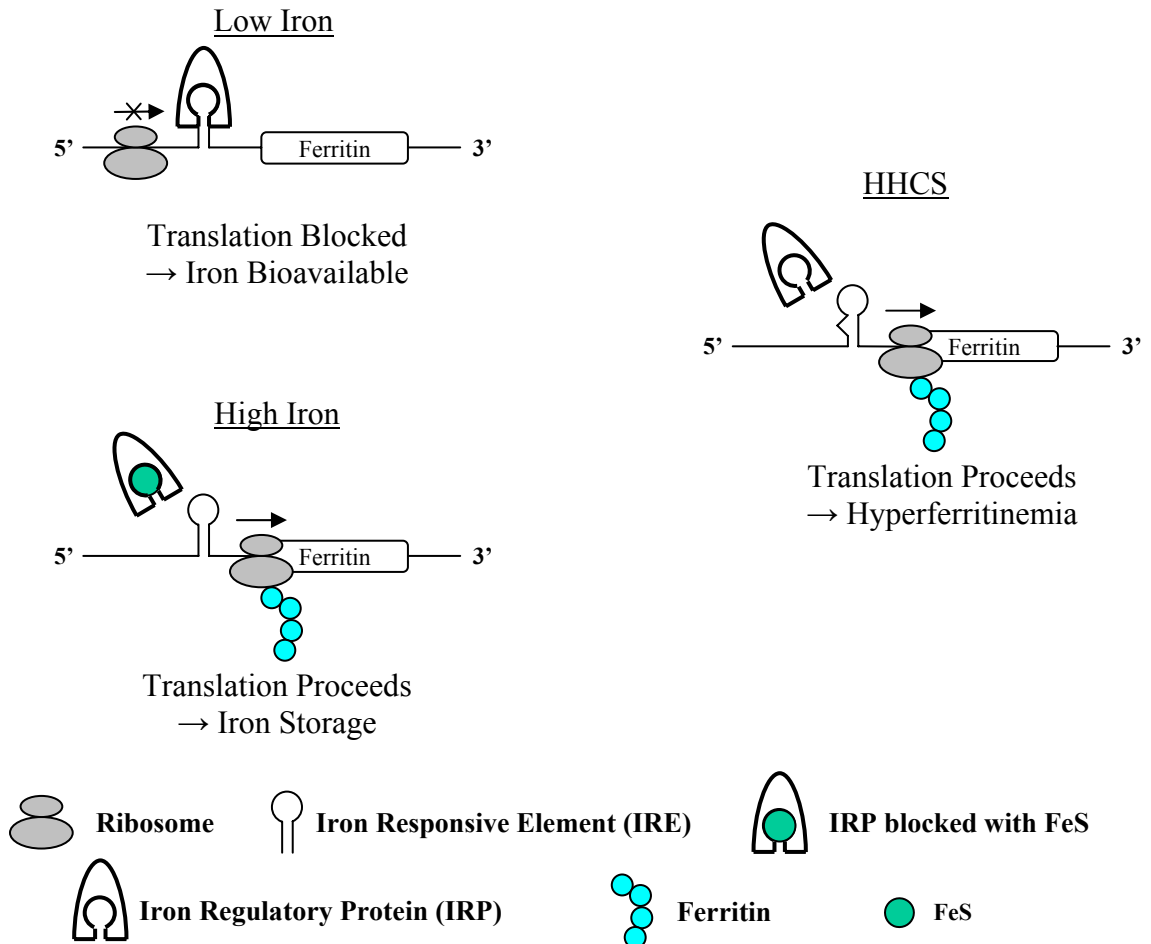


Figure 2-7. Schematic of ferritin metabolism (Crichton et al. 2002)

Different point mutations of the IRE cause a variable clinical severity of HHCS, with serum ferritin levels ranging anywhere from 2− to 10− fold higher than normal. The overproduction of L−ferritin monomers causes the formation of homopolymers or heteropolymers with low H−ferritin content. Since it is the H−ferritin chains that have

the ferroxidase activity necessary to incorporate iron into the multimeric protein, L–ferritin–rich proteins are not able to take up iron efficiently (Mumford et al. 2000; Craig et al. 2003).

Thus, L–rich ferritin in HHCS forms complexes with only few iron molecules, if any, hence closely resembling apoferritin. Although oxidative damage of certain proteins in the lens may be involved in some cataract formations, oxidative damage of ferritin or ferritin subunits does not appear to be a causative factor of HHCS (Mumford et al. 2000).

The crystalline lens opacities in HHCS patients are scattered predominantly in the lens cortex but can also be found in the lens nucleus (Craig et al. 2003). The lens deposits were initially described as white vacuolar deposits of dust–like spots (pulverent cataract) (Bonneau et al. 1995) and by others as breadcrumb–like deposits (see Figure 2-8) (Chang-Godinich et al. 2001).
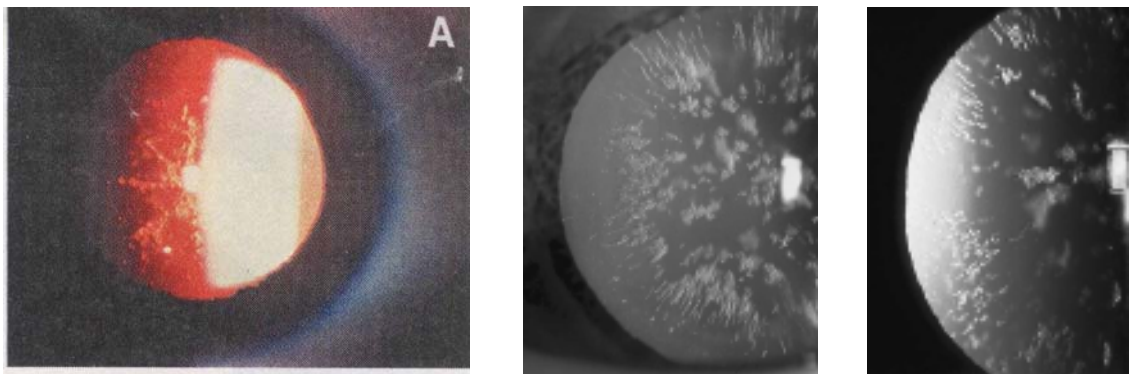


Figure 2-8: Retroillumated slit-lamp photographs of HHCS lenses (Chang-Godinich et al. 2001; Brooks et al. 2002)

To determine the kind of precipitate the ferritin molecules actually form in the lens of HHCS patients, Brooks et al have analyzed the deposits by transmission electron

microscopy with fast Fourier transformation (Brooks et al. 2002). The deposits revealed a macromolecular crystalline structure (see Figure 2-9 and Figure 2-10).
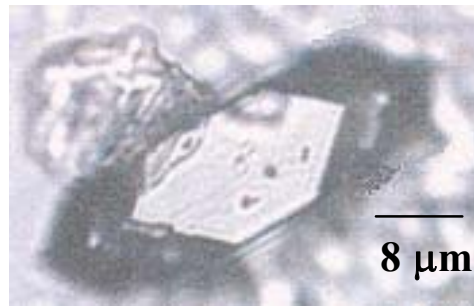


Figure 2-9. Apparent crystalline deposit in HHCS lens aspirate with a typical polygonal appearance (adopted from Brooks et al 2002)
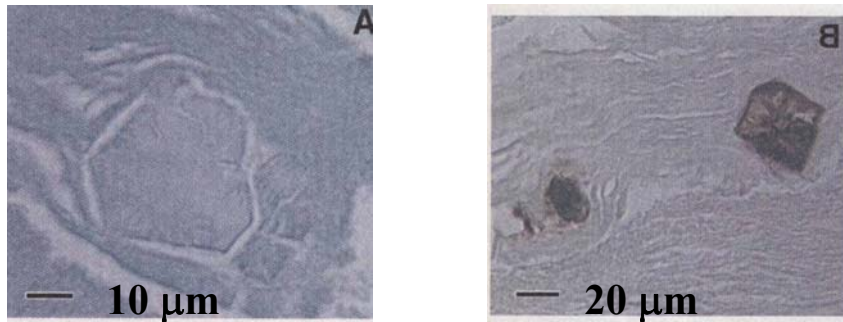


Figure 2-10: Anti-ferritin immunostaining of HHCS lens aspirate. The deposits disrupt the close, parallel packing of the lens fibers (Brooks et al. 2002)

The composition of the crystals was identified as L–ferritin rich by immuno-histochemistry. In another study, inclusion bodies having square–shaped crystal morphology were identified in the lens of a patient who underwent extracapsular cataract extraction (Mumford et al. 2000). The same investigators further observed that cataract is the only clinical feature of HHCS. The lens opacities can be severe enough to require surgical intervention or mild enough to have no detectable effect on visual acuity (Allerson et al. 1999).

### 2.3.3 Ferritin and Apoferritin

Ferritin plays a key role in iron metabolism. Uptake of iron by ferritin serves two physiologic functions: one is detoxification by removing free iron from biological fluids; the second, is that the ferritin–iron complex serves as an iron storage pool (Figure 2-12). The three–dimensional structure of ferritin is highly conserved among living species (Harrison and Arosio 1996). Assembly of L (light chain) and H (heavy chain) ferritin subunits into a 24–subunit complex yields apoferritin (see Figure 2-11) (Brooks et al. 2002).
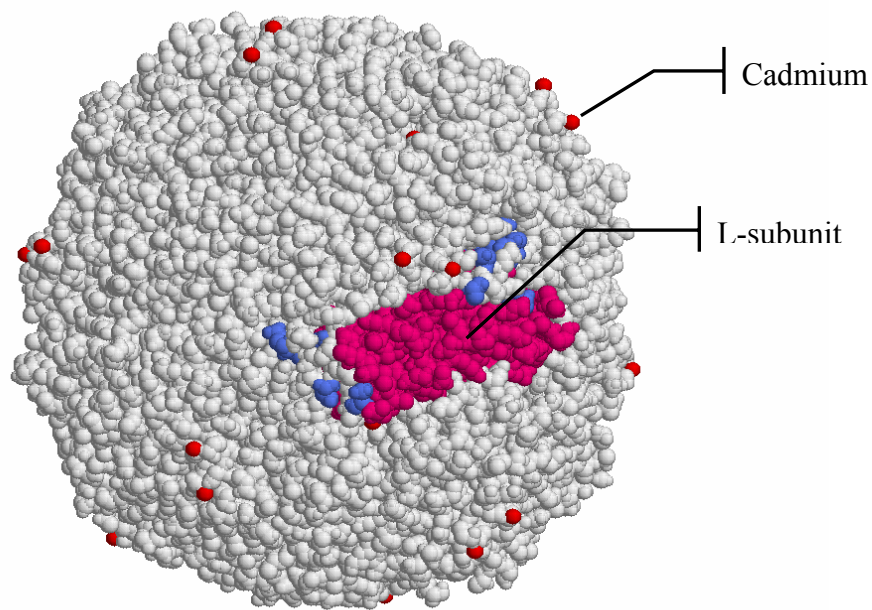


Figure 2-11. L-ferritin homopolymer molecule (assembled with Swiss-PdbViewer software (Guex and Peitsch 1997) obtained from http://www.expasy.org/spdbv/ and with ferritin structural data from the Protein Data Bank – 1IER (Granier et al. 1997))

Apoferritin, the iron–free counterpart of ferritin, has a cage–like structure that is capable of including up to 4,000 atoms of mostly iron. The ability of ferritin to also sequester other metal ions such as zinc, cobalt and manganese (Price and Joshi 1983;

Pead et al. 1995) offers an opportunity for a wide variety of potential uses of ferritin molecules such as bioreactors for environmental pollution analysis (Huang et al. 2000) or as magnetoferritins in biomedical image analysis (Wong et al. 1998).

$Fe^{2+}$      $Fe^{2+}$

**Serum**

Uptake

Serum

$Fe^{3+}$  $Fe^{3+}$

**Cell**

$Fe^{2+}$

$Fe^{3+}$  $Fe^{3+}$

$Fe^{3+}$  $Fe^{3+}$

Dietary Fe:
12-18 mg/day

Solubility:
$Fe^{3+}$ $10^{-17}$ M

Absorbance:
1-2 mg/day

$Fe^{2+}$

Transferrin      Transferrin Receptor

Proteins      $Fe^{3+}$
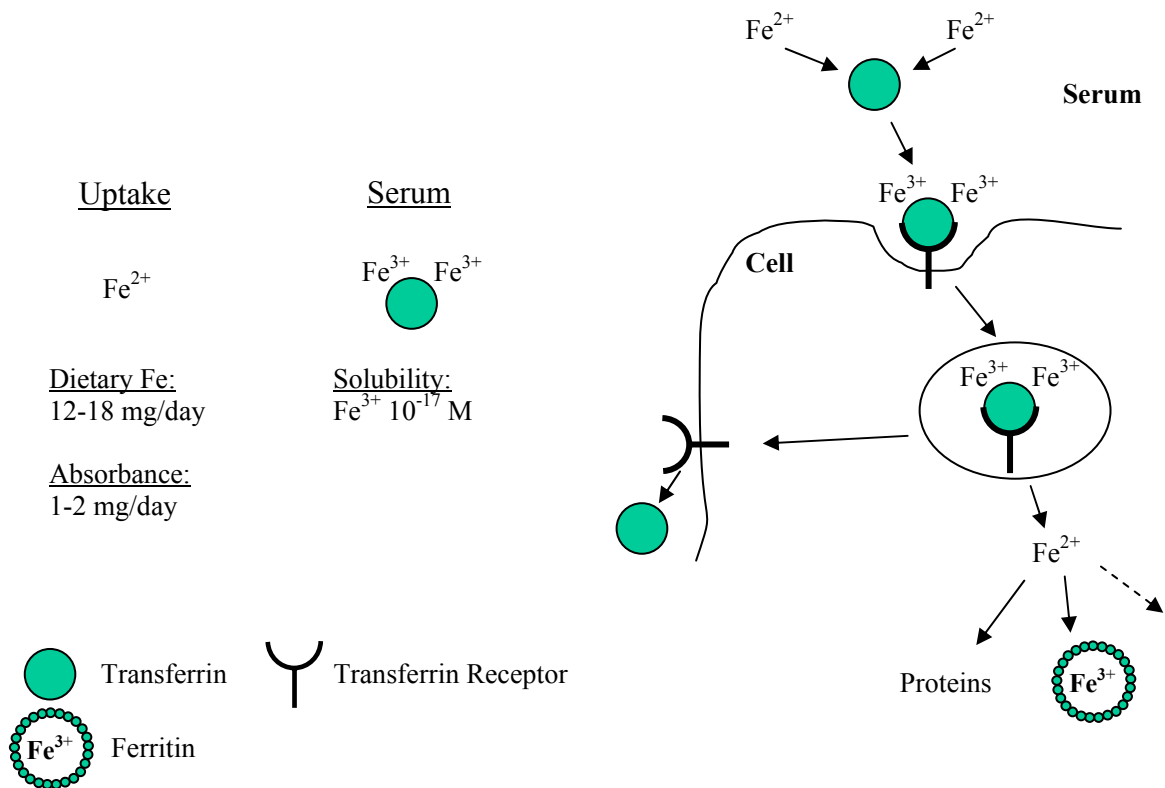
$Fe^{3+}$  Ferritin

Figure 2-12.  Schematic diagram of the iron uptake into cells (adopted from (Aisen et al. 2001))

H−ferritin translocates and oxidizes ferrous iron inside the ferritin cage. L−ferritin, which doesn't bind iron directly, facilitates mineralization of ferric iron inside the cage to form ferritin.  The coordinated action of L− and H−ferritin subunits detoxifies ferric iron inside the ferritin cage, thereby limiting redox cycling of iron and generation of reactive oxygen species (Brooks et al. 2002).  Ferritin can be found in multiple forms,

isoferritins, in human tissue with variable proportions of the H– and L–subunits (see Figure 2-13) (Harrison and Arosio 1996; Cazzola and Skoda 2000).
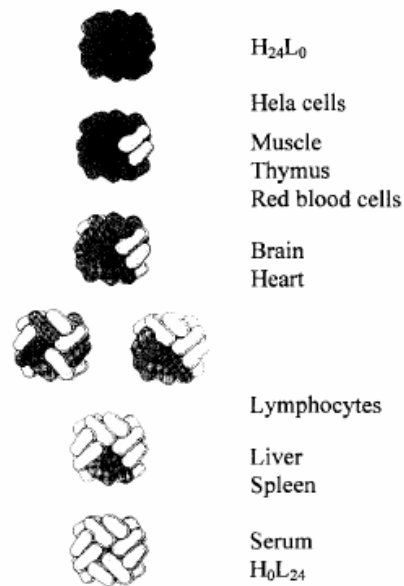


Figure 2-13: Schematic drawings of human 'isoferritins' of different subunit composition (Harrison and Arosio 1996)

Ferritin is mostly an intracellular protein, with the extracellular ferritin found in serum and body fluids accounting for a minor proportion of the total ferritin (Harrison and Arosio 1996). The ferritin multimer has a spherical shape (diameter 120–130 Å), with an inner cavity of about 80 Å diameter (Harrison and Arosio 1996).

At physiological oxygen concentrations the stable state of iron in most of its biological complexes is $Fe^{3+}$. Reduction reactions therefore have a critical role in iron metabolism, since transmembrane transport of iron, deposition of iron in the storage protein ferritin, and synthesis of heme all make use of ferrous iron, $Fe^{2+}$.

The apoferritin shell is notable for its stability to heat (treatment for 5-10 min at 70 °C is routinely used as a preparative step) and to urea or guanidinium chloride. The large numbers of intra- and inter-subunit salt bridges and hydrogen bonds contribute to this stability (Harrison and Arosio 1996).

Ferritins are among the most ancient proteins of iron metabolism, found substantially conserved in species from bacteria to plants to man. Form and function are closely matched in ferritins. Mammalian ferritins are all heteropolymers of 24 subunits of two types, designated H for heavy ($M_r \approx 21,000$) or heart, the tissue in which it abounds, and L for light $M_r \approx 19,500$) or liver. The mature protein shell therefore has a molecular weight near 450,000, with subunits are arranged to form a nearly spherical diameter capable of accommodating up to 4,000 oxygen- and hydroxyl-bridged iron atoms, essentially as ferrihydrate (Crichton et al. 2002). As isolated, however, ferritins of most tissues bear 2,000-2,500 iron atoms. When intracellular iron exceeds cellular requirements, the excess is kept from noxious chemistry yet is still bioavailable via sequestering in ferritin. Expression of ferritin is regulated at the post-translational level.

Iron levels within the cell regulate the levels of other iron-related proteins, most notably ferritin, via iron regulatory proteins (IRPs). Under low intracellular iron conditions, IRPs bind to the mRNA stem-loop structures known as the IREs (iron responsive elements), located in the untranslated regions (UTRs) of ferritin mRNA and prevent translation (left hand side of Figure 2-14) (Harrison and Arosio 1996).
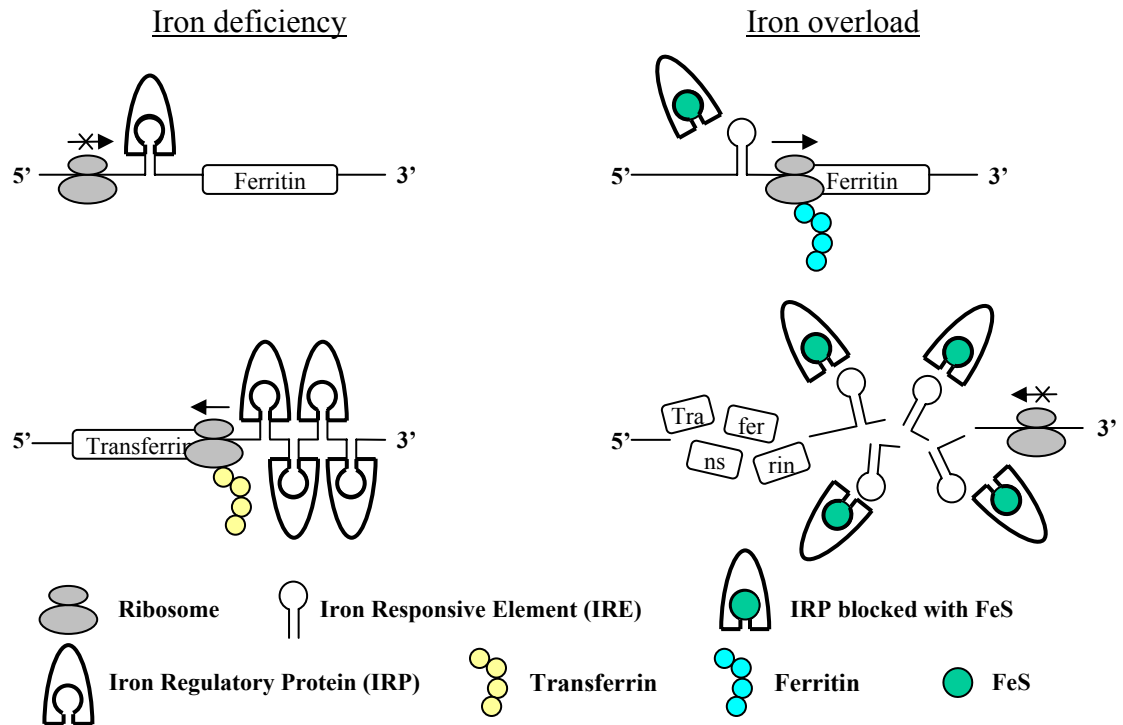
Figure 2-14: Production of transferrin and ferritin is regulated at the level of mRNA by the iron regulatory proteins (Crichton et al. 2002).

Under high intracellular iron concentrations, when it is desirable to synthesize ferritin in order to sequester iron and prevent iron-catalyzed oxidative damage to the cell, IRPs no longer bind to IREs (right hand side of Figure 2-14). As a result, ferritin synthesis increases and iron is sequestered within the cell (Aisen et al. 2001).

In a study on the overexpression of ferritin subunits by transiently transfected lens epithelial cells (LEC) it was found that the LECs regulated the concentration of the ferritin subunits in the cytosol differently. The expression of H-chain subunits was determined to be more strictly controlled compared to the expression of the L-chain subunits. If the cells were manipulated to overexpress the L-chain subunits a higher percentage of L-chain homopolymers and an overall higher concentration of the

intracellular ferritin molecules could be detected compared to the control cells. On the contrary, the overexpression of the H-chain subunits did not lead to a change in the H-/L-chain subunit ratio when compared to the control cells and the overall ferritin concentration was 10-times lower compared to the L-transfected cells. While the accumulation of L-chain homopolymers did not seem to have any negative effects on the cells, it was postulated that H-rich ferritin in the cytosol could deregulate the highly controlled iron homeostasis and therefore affect cell proliferation. The only known negative effect of increased L-chain homopolymer synthesis and the resulting protein accumulation is the opacification of lenses in humans with hereditary hyperferritinemia cataract syndrome (Goralska et al. 2003).

### 2.3.4 Divalent Cations

It has been shown that levels of divalent cations (such as cadmium) are elevated in cataractous lenses compared to normal control lenses (see Table 2-2). One possible source of the increased cadmium levels is cigarette smoke (Avunduk et al. 1999; Avunduk et al. 1999). Furthermore, results indicate there is a 3-fold increase of cadmium concentration in the blood of tobacco chewers as compared to non-chewers (Sulochana et al. 1998).

Cadmium is taken up from the lung and the gastrointestinal tract and transported via the blood to liver and kidney. It has been shown that initially, after exposure, cadmium in the blood is bound to albumin and other proteins. Once inside the body, cadmium induces the synthesis of metallothionein, a low molecular weight protein

24

(6.5 kD) involved in cadmium, zinc and copper metabolism. Metallothionein plays an important role in the intracellular metabolism of cadmium by chelating the metal ions in the tissue, therefore protecting sensitive metabolic functions in the cells (Post et al. 1984). Metallothionein binds cadmium in a stable biocomplex which is filtered out of the bloodstream by the kidneys causing an accumulation of cadmium in these organs of individuals which are chronically exposed to cadmium (Nordberg 1984; Post et al. 1984). Beside kidneys, metallothionein-bound cadmium is furthermore accumulated in the liver. In both cases about 90% of the bound cadmium is found in the cytosol (Waku 1984). The toxic effect of cadmium arises from the fact that it can compete with other divalent elements like copper, zinc and selenium and replace them in enzymes like superoxide dismutase (SOD) and glutathione peroxidase. Therefore, the activity of these enzymes may be lost or diminished (Sulochana et al. 1998). For example, the catalytic activity of SOD was decreased by 33% in the tobacco chewers compared to non-chewers.

As the concentration of cadmium increases in the blood, it binds to hemoglobin which might lose its oxygen-transporting capacity and delivery of oxygen to tissues. Cadmium can replace copper in cytochrome oxidase. This would lead to decreased biological oxidation and ATP production and availability of energy. Like other heavy metals such as mercury and lead, cadmium could intercalate with blood, tissue and lens proteins and denature or precipitate them. Cadmium can inactivate SOD by replacing manganese, copper and zinc. This could weaken the antioxidant defense. The oxidants could oxidize the membrane lipids and proteins. Accumulation of cadmium in blood and decrease of SOD might affect the lens and be responsible for early onset of cataractogenesis in tobacco chewers (Sulochana et al. 1998).

The crystallization of apoferritin and ferritin *in vitro* is enhanced by the presence of divalent cations such as cadmium. With cadmium in particular, its use to promote crystallization of ferritin dates back to even before the advent of protein crystallography (Trakhanov et al. 1998). Historically, ferritin was distinguished from other proteins by the fact that it crystallizes out of solution by addition of cadmium sulfate (Michaelis 1947). Changes in divalent cation concentration can also change the overall crystal habit in a crystallization experiment (Trakhanov and Quiocho 1995). Trakahnov and Quiocho further indicated that cadmium ions surpass the crystallization enhancing properties of a variety of other divalent cations. Molecular simulations revealed that monovalent ions present in low concentration protein solutions cause the potential of mean force, $W$ (r), between the macromolecules to be repulsive. In contrast, divalent ions cause the electrostatic forces between two proteins to become attractive at a certain intermolecular distance (Wu et al. 1998).

Table 2-1. Cataractous and normal lens concentrations of Cadmium, Copper, Lead and Calcium in groups with different smoking habits (ppm) (Cekic 1998; Cekic 1998)

| Lenses | Concentration (µg/g dry tissue weight = ppm) | | | |
|---|---|---|---|---|
| Cataractous | $Cd^{2+}$ | $Cu^{2+}$ | $Pb^{2+}$ | $Ca^{2+}$ |
| Overall | 0.99 | 2.11 | 5.17 | 82.31 |
| Males | 1.05 | 2.13 | 5.00 | 80.36 |
| Females | 0.88 | 2.04 | 5.53 | 86.83 |
| 1–10 cigarettes/day | 1.01 | | | |
| > 20 cigarettes/day | 1.19 | | | |
| Non–smokers | 0.79 | | | |
| Normal | | | | |
| Overall | 0.045 | 0.69 | 0.00 | 15.11 |
| Males | 0.055 | 0.66 | 0.00 | 15.18 |
| Females | 0.032 | 0.72 | 0.00 | 15.01 |
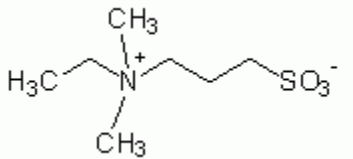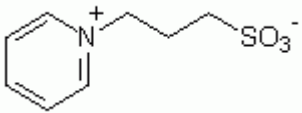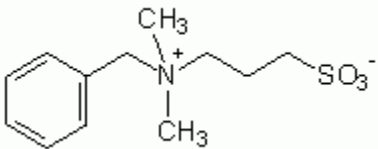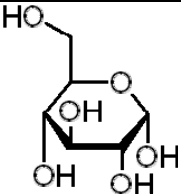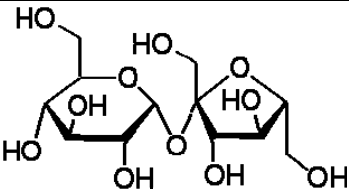
## 2.3.5 Protein Solubilizers

The issue of protein solubility is of importance in both lab– and production–scale crystallization and purification operations (Vuillard et al. 1995; Vuillard et al. 1995; Lilie et al. 1998; Expert-Bezancon et al. 2003). Recently, non–detergent sulphobetaines (NDSB, see Table 2-2) have been used as protein solubilizers. These molecules are zwitterionic ammonium propane sulphonic derivatives. A zwitterionic compound is any monomer containing a zwitterionic functional group. A zwitterionic functional group refers to a pendant group, bound to the backbone of the monomer, having at least one positive and one negative group. Generally, zwitterionic functionality can be formed from a group containing both an acidic and a basic functionality such that when placed in conditions of appropriate pH, preferably a neutralized buffer saline solution, each of these functionalities exists in ionized form.

It appears that NDSBs show a negative value of the binding parameters, indicating that there is an excess of water around the protein molecule, i.e., that the macromolecule is preferentially hydrated. It was further stated the increased solubility occurs at high concentrations of the co-solvents, typically above 1 M concentration (Conti et al. 1997).

Furthermore, activity assays performed on several enzymes showed that protein solubilization by NDSB was not accomplished at the expense of denaturation (Vuillard et al. 1996). With NDSBs it is possible to reduce protein aggregation and, at the same time, stabilize proteins in solution. Sulfobetaines are used in contact lens solutions (Heiler and Groemminger 1998), thus the possibility that such compounds form the basis for the pharmacological prevention and treatment of cataracts appears reasonable.

Table 2-2. Chemical additives used throughout the experimental research

| Name | Chemical name | $M_W$ [g/mol] | Chemical structure |
|------|---------------|---------------|--------------------|
| NDSB 195 | Dimethylethylammonium propane sulfonate | 195.3 |  |
| NDSB 201 | 3-(1-Pyridino)-1-propane Sulfonate | 201.2 |  |
| NDSB 256 | Dimethyl-(2-Hydroxyethyl)-(3-Sulfopropyl)-ammonium, Inner Salt | 257.4 |  |
| Glucose | 6-(hydroxymethyl)oxane-2,3,4,5-tetrol | 180.16 |  |
| Sucrose | β-D-fructofuranosyl α-D-glucopyranoside | 342.34 |  |

The NDSBs used in the study (see Table 2-2) were chosen since they were commercially available and, according to reports in the literature, there were indications of increased protein solubility in the presence of these NDSBs. It was reported that NDSB 195 tripled the solubility of lysozyme in solution under certain conditions. Lysozyme crystals grown in the presence of NDSB 195 displayed the same unit cell dimensions compared to the controls in the absence of NDSB 195 (Vuillard et al. 1996). Furthermore, NDSB 195 increased the yield in protein separation while simultaneously

increasing the enzymatic activity and thermal stability compared to controls (Vuillard et al. 1995; Vuillard et al. 1995). NDSB 201 increased the protein yield in a protein separation step and decreased the tendency of certain proteins to precipitate and furthermore increased the enzymatic activity similar to NDSB 195 (Vuillard et al. 1995; Vuillard et al. 1995). NDSB 256 was used successfully in renaturation experiments with bovine serum albumin (BSA) by decreasing the aggregation of BSA molecules after refolding (Expert-Bezancon et al. 2003). The same NDSB also increased the protein solubility under otherwise aggregation-favorable conditions. Sucrose also showed the ability to maintain proteins in solution under otherwise unfavorable conditions (Conti et al. 1997).

## 2.4 Protein Crystallization

### 2.4.1 Introduction

The structure determination of biological macromolecules is accomplished by either x-ray crystallography or by nuclear magnetic resonance (NMR). The latter technique is limited to molecules of up to 50 kD and is therefore not often used. Crystallographic structure determination begins with the growth of a suitable crystal. The equipment involved in x-ray crystallography is becoming more and more sophisticated; therefore crystallization is now considered the rate-limiting step in the process.

The initial step in the growth of macroscopic protein crystals is, as a result of statistical fluctuations, the association of protein aggregates. Eventually these pre-nuclear aggregates reach the size of the critical nucleus where the intermolecular contacts

resemble those found in the final crystal.  Once the stable nucleus has formed the crystal grows through the addition of molecules to the crystalline lattice (Figure 2-15).  The formation of a solid state by coalescence of molecules free in solution is a classical example of phase transition.

Both nucleation and crystal growth occur in supersaturated solution where the protein concentration exceeds its equilibrium solubility value.  The region of solution parameter space suitable for crystallization is generally represented on the phase diagram by the solubility curve (Figure 2-16).
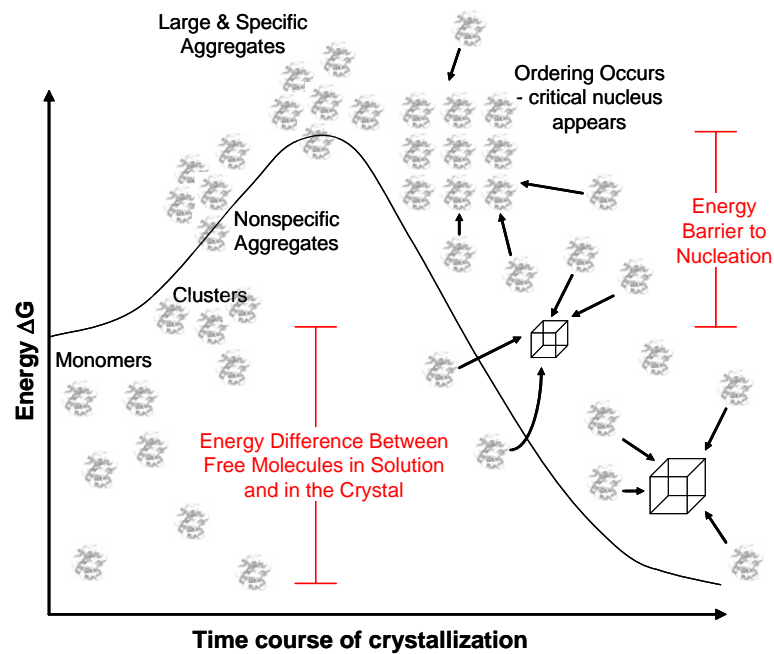


Figure 2-15.  Energy diagram of protein crystallization (adapted from (McPherson 1999))

A solution that is supersaturated with respect to a particular macromolecule must, according to thermodynamics, return to equilibrium by segregating a solid phase until equilibrium is achieved.  However, it is shown experimentally that a threshold value of

supersaturation must be exceeded for precipitation to occur spontaneously (Malkin and McPherson 1993; Malkin and McPherson 1994).
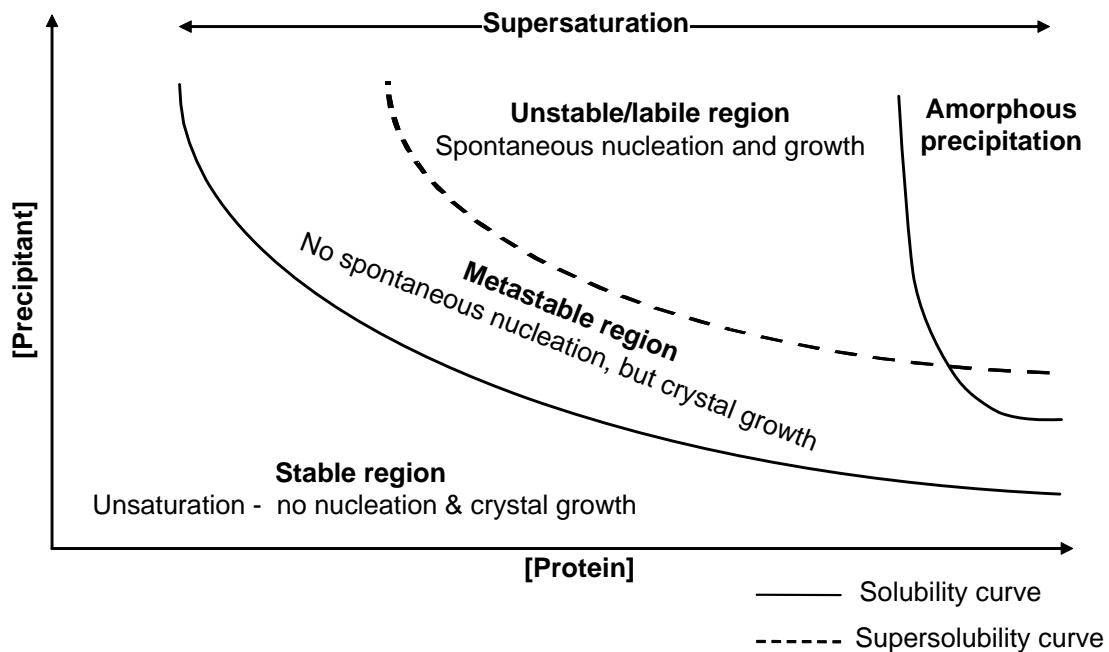


Figure 2-16. Protein crystallization phase diagram (adapted from (Garcia-Ruiz 2003))

The supersaturation threshold is depicted in Figure 2-15 in terms of an energy barrier that has to be overcome to form a stable nucleus. The energy barrier is due to two energy contributions (Figure 2-17). The first, a surface contribution, reflects protein-solvent interactions that keep the proteins in solution. The second, a volume contribution, is due to protein-protein interactions. The maximum of the energy barrier coincides with the critical nuclear radius, $r^*$, both depending on the relative strength of surface to volume contributions.
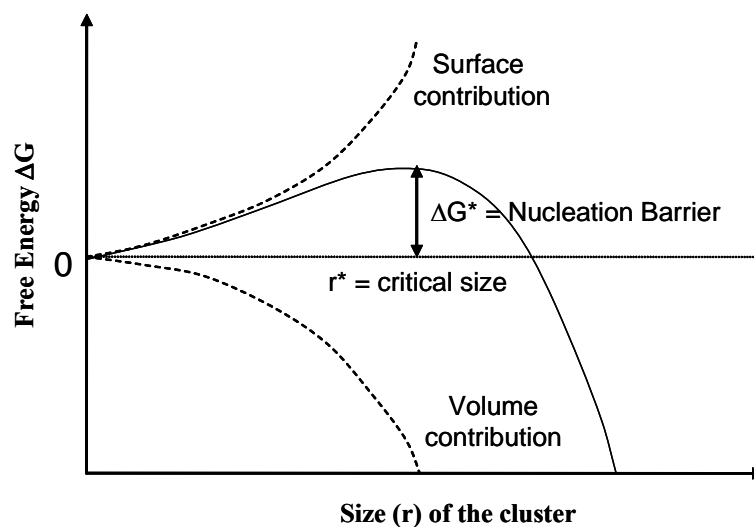
Figure 2-17: Energy contributions to protein crystallization

## 2.4.2 Supersaturation

Supersaturation depends on the concentration of the protein and factors that affect its solubility. It is achieved at high protein concentrations, and at increasing precipitant concentrations. Precipitants in general are solution parameters that decrease protein solubility. A list of the most frequently used precipitants is shown in Figure 2-18. While these agents are commonly known as precipitating agents, they are actually solubility-influencing agents with precipitation being just one special case of protein condensation. Besides chemical additives the solubility of proteins can be altered by changes in temperature and pH. Figure 2-19 depicts the unimodal frequency distribution for the crystallization pH of proteins with mean = 6.6, median = 6.8 and mode = 7.0. Finally, the directional changes in solution parameters that result in decreased macromolecular solubility enhance protein crystallization (see Figure 2-16)

The supersaturation requirements for crystal nucleation and growth are different. This is depicted in Figure 2-16 where the supersaturated region of the phase diagram is further divided into a metastable region and an unstable or labile region. In the region of higher supersaturation (labile region) both nucleation and growth occurs while in the lower supersaturated region (metastable region) only crystal growth is supported. The labile region is thermodynamically unstable, but kinetically stable, whereas the opposite is true for the metastable region. Common for all homogeneous crystallization techniques is that the protein solution has to be transferred into the unstable region for crystal growth to occur.
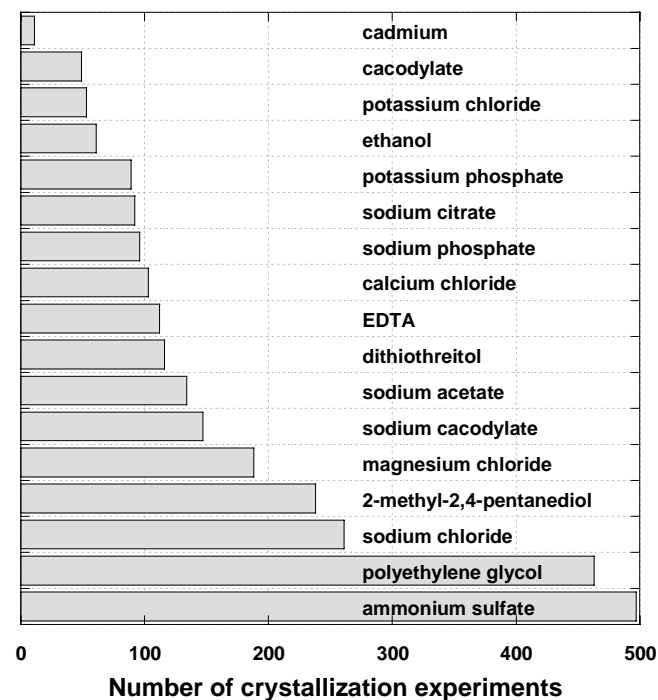


Figure 2-18. Chemical additives used to decrease macromolecular solubility (adopted from (Gilliland et al. 1994))

The further the system is from equilibrium, hence at greater supersaturation, the greater the driving force is to regain thermodynamic equilibrium.
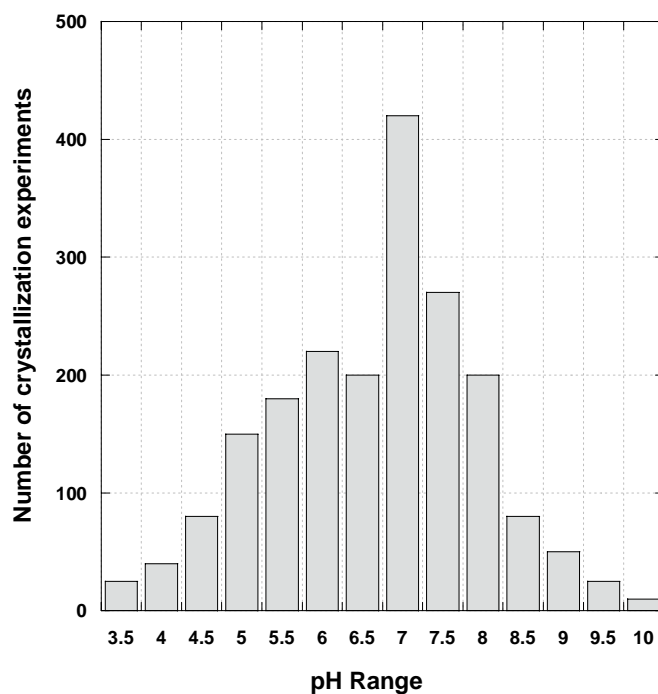


Figure 2-19. Histogram of pH values at which proteins were crystallized (data obtained from the BMCD database (Gilliland et al. 1994))

At the far right hand site of the unstable region of supersaturation (Figure 2-16) amorphous precipitate forms rather than crystal nuclei. Even if no amorphous precipitate occurs at very high supersaturation, in that region of the protein phase diagram it is likely to obtain a shower of microcrystals rather than few, large single crystals. Furthermore crystals grown from initially very high supersaturated solutions are more likely to include lattice defects and less orderly growth, making them less desirable for x-ray crystallography (McPherson 1999).

### 2.4.3 Crystallization Methods

In general, the crystallization of biological macromolecules is not significantly different from the crystallization of conventional small molecules. The primary difference of macromolecular crystallization compared to that of small molecules is that proteins and nucleic acids are inherently more labile and sensitive and hence the requirement of maintaining them at or near physiological pH and temperature. Thus the usual methods of evaporation, dramatic temperature variation, or the addition of strong organic solvents are excluded and must be replaced with more gentle and restricted techniques (McPherson 1985).

Many physical, chemical and biochemical factors can influence the crystallization of macromolecules (Table 2-3). Some of the factors are more significant than others and the assignment of importance depends on the properties of the macromolecule. Each factor may differ considerably in importance for an individual protein. The uniqueness of proteins does not always allow predicting in advance the specific values of a variable or sets of conditions that might be most profitably explored. Furthermore, the various variables in protein crystallization are not independent and the effect on each other is often difficult to determine. Nevertheless, the knowledge of which factor is essential in terms of the protein crystallization characteristics is vital to implement an appropriate crystallization method (McPherson 1999).

To generate the required thermodynamic driving force for crystallization, vapor diffusion is most often used followed by batch crystallization and dialysis (Figure 2-21) according to the Biological Macromolecule Crystallization Database and the NASA Archive for Protein Crystal Growth Data (Gilliland et al. 1994; Chayen 1998; Gilliland et

al. 2002). A good and extensive description of other crystallization methods can be found in the literature (Weber 1997).

Table 2-3. Factors affecting crystallization (McPherson 1999)

| Physical | Chemical | Biochemical |
|---|---|---|
| Temperature/temperature variations | pH | Purity of the macromolecule/impurities |
| Surfaces | Precipitant type | Ligands, inhibitors, effectors |
| Methodology/approach to equilibrium | Precipitant concentration | Aggregation state of the macromolecule |
| Gravity | Ionic strength | Posttranslational modifications |
| Pressure | Specific ions | Source of macromolecule |
| Time | Degree of supersaturation | Proteolysis/hydrolysis |
| Vibrations/sound/ mechanical perturbations | Reductive/oxidative environment | Chemical modifications |
| Electrostatic/magnetic fields | Concentration of the macromolecule | Genetic modifications |
| Dielectric properties of the medium | Metal ions | Inherent symmetry of the macromolecule |
| Viscosity of the medium | Cross-linker/polyions | Stability of the macromolecule |
| Rate of equilibration | Detergents/surfactants/ amphophiles | Isoelectric point |
| Homogeneous or heterogeneous nucleants | Non-macromolecular impurities | History of the samples |

The vapor-diffusion method results in a dynamic crystallization system in which the protein of interest proceeds through a range of conditions as both the protein and precipitant concentrations increase with solvent (generally, water) evaporation. The initially undersaturated protein droplet equilibrates with the mother liquor (Figure 2-20) which is initially at a higher precipitant concentration. In the course of the crystallization

experiment the protein of interest proceeds through a range of conditions as both the protein and precipitant concentrations increase (Figure 2-23).
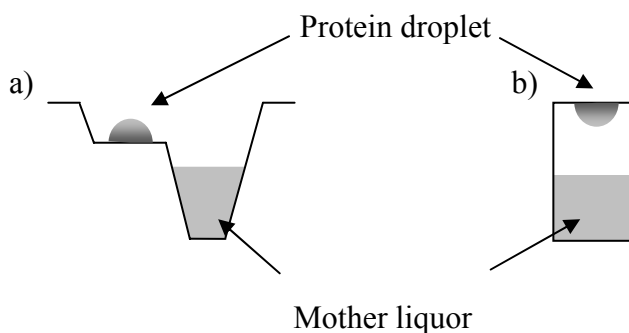


Figure 2-20. Schematic of vapor diffusion. a) sitting drop, b) hanging drop

Nucleation conditions that may occur during this process are difficult to determine precisely due to the dynamic nature of the experiment (Bartling et al. 2005). Additionally, vapor diffusion is a multifactorial technique, with many of the system parameters being set at specific values. Such parameters include the volume of the droplet of protein solution, the contact angle between the droplet and the coverslip, and the distance from the droplet to the well containing the reservoir into which water is transported (Fowlis et al. 1988). Although this high number of degrees of freedom provides for flexibility, it may also increase to unmanageable levels the number of experiments that need to be performed to identify nucleation and crystal growth conditions.
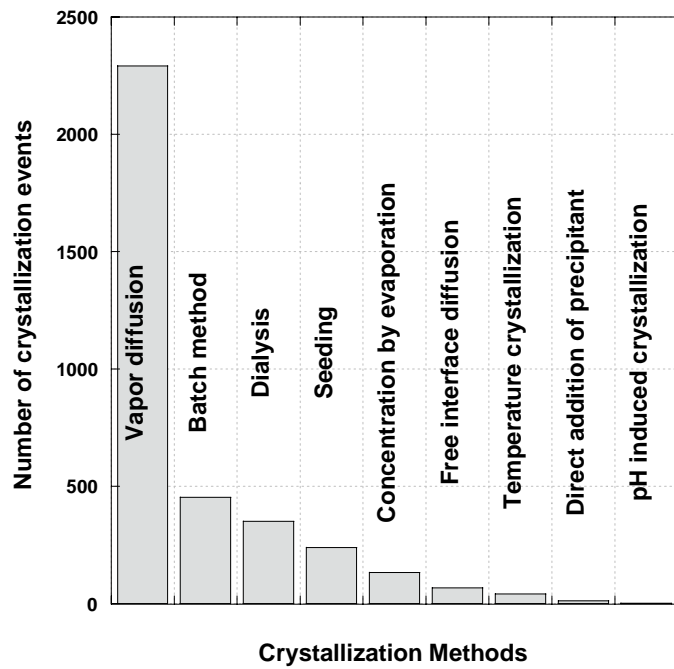
Figure 2-21.  Methods used for crystallizing proteins (data from (Gilliland et al. 1994)

Batch crystallization on the other hand is a static system in which the precipitant and protein concentrations are predefined. In a batch crystallization experiment, supersaturation is achieved upon mixing of the protein solution and the precipitate solution (Figure 2-22).
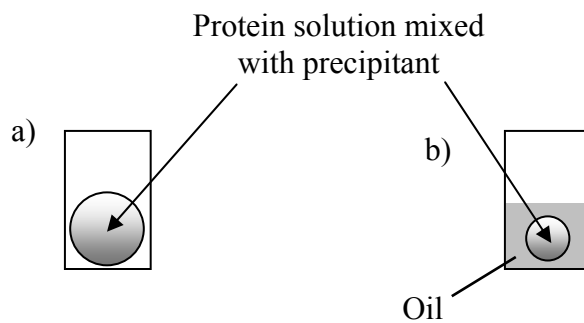


Figure 2-22.  Schematic of batch crystallization setup. a) batch crystallization, b) microbatch crystallization under oil
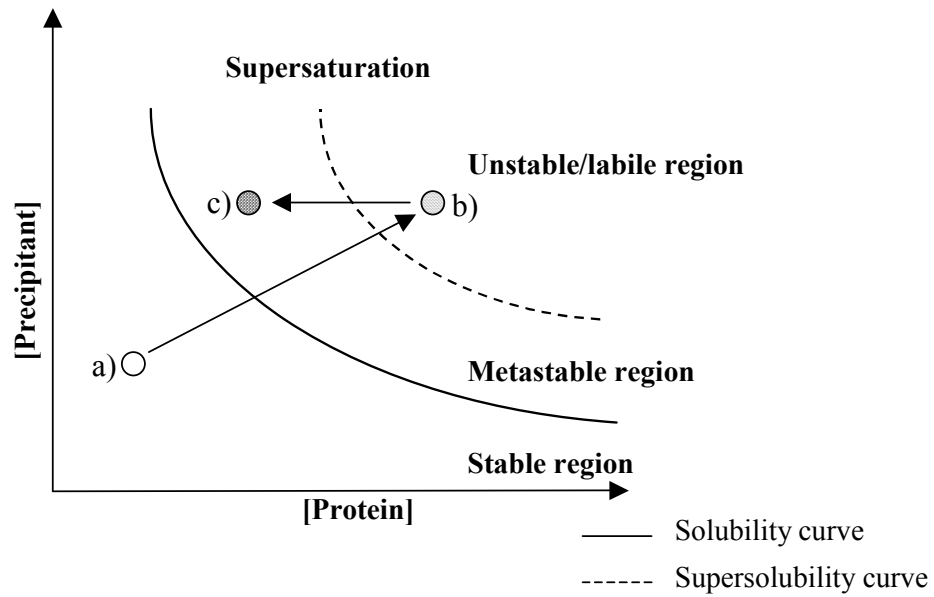
Figure 2-23.  Schematic of vapor diffusion crystallization ( a. undersaturated solution, b. formation of nuclei, c. growth of nuclei into stable crystals)
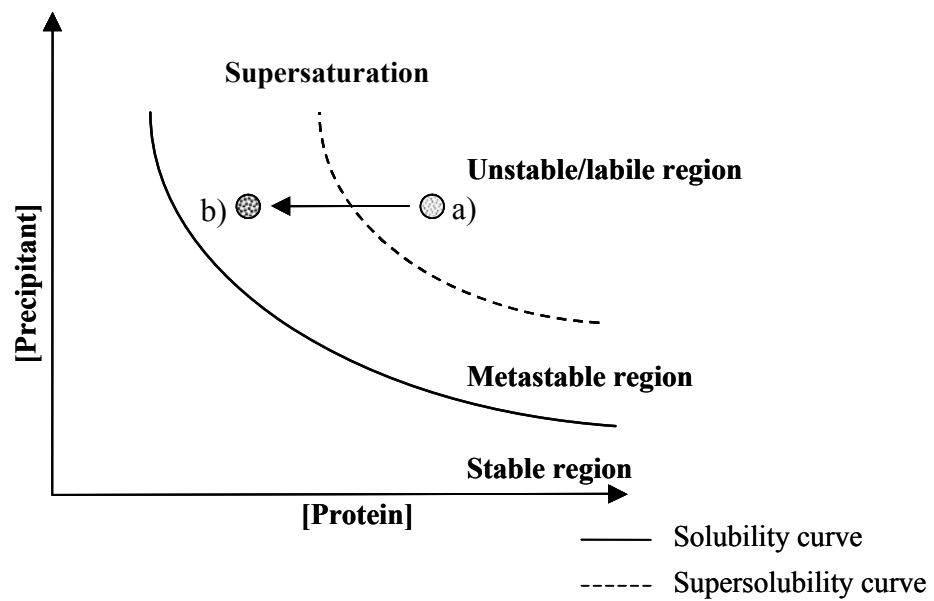


Figure 2-24.  Schematic of batch crystallization ( a) initially supersaturated protein solution forms nuclei, b) growth of nuclei into stable crystals)

There is less exploration of the phase diagram, since the concentration of the initial crystallization ingredients essentially do not change until after nucleation has occurred (Figure 2-24). A modification of the batch crystallization technique was achieved with the introduction of protein microbatch crystallization under oil (Chayen et al. 1992; Chayen 1997; Chayen 1999)

### 2.4.4 Protein-protein Interactions

As described in Chapter 2.2.4, the potential of mean force $W$ (r) between proteins in solution is dependent on the type of cations present. Since the second virial coefficient, $B$, is related to the potential of mean force through equilibrium solution theory and can be measured readily, its evaluation can give a qualitative measure of two–body (protein–protein) interactions in a dilute solution (George and Wilson 1994). Positive $B$ values generally indicate larger protein–solvent interactions compared to protein–protein interactions, i.e. the net protein intermolecular forces are repulsive. Negative values for $B$ imply overall attractive forces between the protein molecules in solution. Therefore $B$ has a predictive character regarding protein crystallization and/or precipitation from a solution. In fact, it appears that there exists a region of $B$ values where crystallization is favored for about 20 different protein solvent pairs. The values for $B$ in this region are $(-1$ to $-8) \times 10^{-4}$ mL· mol·g$^{-2}$. Values outside this region do not appear to favor crystallization ($B>0$) or lead to amorphous protein precipitation ($B<<0$) (George and Wilson 1994). Since apoferritin was not included in this study, it remains unknown whether the second virial coefficient correlates with the crystallization outcome for this protein, especially if crystallization is induced by various means.

Solubility is another important solution property affecting protein crystallization. Indeed, the solubility of proteins may be dependent on the second virial coefficient (Gripon et al. 1997; Guo B 1999; Haas C et al. 1999; Haas et al. 1999; Curtis et al. 2001). The solubility and the second virial coefficient both are determined by the protein–protein interactions. However, the solubility depends on the short–range protein–protein interactions in the crystal with restricted orientations of the proteins, while the second virial coefficient provides a measure of the dilute protein–protein interactions that are Boltzmann–averaged over all distances and orientations in the liquid phase (Haas et al. 1999; Curtis et al. 2001). Curtis et al. further suggest that the second virial coefficient can likely be extrapolated to describe interactions in the crystal.

The thermodynamics of liquid solutions is determined by the manner in which the chemical potentials of the components depend on composition. It is customary to define an ideal solution as one in which for each component (Smith et al. 1995)

$$\mu_i = \mu_i^0 + RT \ln X_i \tag{2.1}$$

where $X_i$ is the mole fraction of the $i$th component and $\mu_i^0$ is the standard chemical potential. In dilute solutions only the solvent is customarily expressed in terms of its mole fraction. For a two component system with $X_1 \gg X_2$, $\ln X_1 = \ln (1-X_2) = -X_2 - 0.5X_2^2$ ..., with subsequent terms falling off rapidly (Tanford 1961). Thus (with $F_1^0$ replacing $\mu_1^0$)

$$\mu_1 - F_1^0 = -RT \left( X_2 + \frac{1}{2} X_2^2 + \cdots \right) \tag{2.2}$$

Alternatively, the weight concentration of solute, $c$, can be used in place of $X_2$

$$\mu_1 - F_1^0 = -RTV_1^0\left[\left(1/M_W\right)c + \left(V_1^0/2M_W^2\right)c^2 + \cdots\right] \qquad (2.3)$$

A general expression in which the non-ideal behavior of the solution is expressed in terms of the empirical parameter activity, $a$, is as follows

$$\mu_i = \mu_i^0 + RT\ln a_i \qquad (2.4)$$

To obtain numerical values for $a_i$ it is customary to replace it by the product of the corresponding concentration unit and an activity coefficient, e.g. $a_i = y_i c_i$.

An alternative procedure, most useful for the solvent in dilute solutions, is to express the chemical potential as a power series in the concentration. This procedure is analogous to that used in the theory of non-ideal gases. The $PV$ product per mole of gas is expressed in terms of the virial equation (Smith et al. 1995),

$$PV = RT\left(1 + BP + CP^2 + \cdots\right) \qquad (2.5)$$

The coefficients $B$, $C$, etc. are known as the second, third, etc. virial coefficients. The equation reduces at zero pressure to the ideal gas equation. The corresponding equation for the solvent can, for instance, be written, after the form of Equation (2.3), as

$$\mu_1 - F_1^0 = RTV_1^0 c\left(1/M_W + Bc + Cc^2 + \cdots\right) \qquad (2.6)$$

The first term being the same as that of Equation (2.3) so that ideal behavior is attained as $c$ becomes very small.

A number of experimental measurements provide essentially a measure of the chemical potential of the solvent in a solution, relative to that of pure solvent, i.e. a measure of $\mu_1 - F_1^0$. It is clear from Equation (2.6) that these properties always permit the determination of the molecular weight, $M_W$, of the solute. The experimental

quantities which can be used in this way are known as the colligative properties of a solution, such as vapor pressure and osmotic pressure. The latter is used commonly for large solute molecules.

The osmotic pressure, $\Pi$, can be expressed as (Tanford 1961)

$$\Pi = -\frac{\mu_1 - F_1^0}{V_1} \tag{2.7}$$

Where $V_1$ being the partial molal volume of the solvent. Using Equation (2.7) it is customary to plot $\Pi / c$ versus $c$, so a plot in dilute solutions would be according to Equation (2.6) (Zimm 1948)

$$\Pi/c = RT\left(1/M_W + Bc + Cc^2 + \cdots\right) \tag{2.8}$$

The limiting slope of such a plot would give a value for the second virial coefficient, $B$.

# CHAPTER 3

# METHODOLOGY

## 3.1 Experimental Methodology

### 3.1.1 Size Exclusion Chromatography (SEC)

Biological macromolecules have special functions which are controlled *in vivo* by small changes in the environment. Changes in pH, concentrations of metal ions, cofactors etc. may have a profound effect on the molecules being studied and it is clearly necessary to have available mild separation techniques which operate independently of these factors. Gel filtration or size exclusion chromatography is such a technique.

In size exclusion chromatography molecules in solution are separated according to differences in their sizes as they pass through a column packed with a chromatographic medium which is a gel in bead form. The pores in the gel matrix which are filled with the mobile phase are comparable in size to the molecules that have to be separated. Relatively small molecules can diffuse almost freely into the pores of the gel matrix from the surrounding solution, whereas relatively large molecules will be prevented by their size from diffusing into the pores. Hence, the first molecules that elute from the column are the largest molecules in the mixture, while the smallest molecules are retained within the gel matrix the longest and therefore elute from the column last.

3.1.1.1 Preparative size exclusion chromatography for protein purification

The initial purification of as-received apoferritin solution to remove impurities such as apoferritin oligomers, apoferritin subunits and possibly other proteins present, was achieved by preparative size exclusion chromatography (Petsev et al. 2001; Vekilov 2002). The mobile phase was pumped over the SEC-column (HiPrep 16/60 Sephacryl S300 High Resolution, Amersham Biosciences) with a HPLC system consisting of a multiple solvent delivery system (CM 4000, LDC Analytical) equipped with a UV detector (SPD-10AV UV-VIS Detector, Shimadzu Corporation). A detailed protocol including the settings and buffers used for the preparative SEC-HPLC can be found in Appendix B.2.

3.1.1.2 Analytical size exclusion chromatography assay

The purified apoferritin samples were analyzed for their monomer purities through analytical size exclusion chromatography. The mobile phase was pumped over the analytical SEC-column (Bio-Sil SEC-400-5, Bio-Rad Laboratories) with a HPLC system (Shimadzu Corporation) consisting of a multiple solvent delivery system (LC-10AT VP), a system controller (SCL-10A VP), degasser (DGU-14A), UV detector (SPD-10AV VP), and an auto injector (SIL-10A). The chromatogram was recorded and analyzed through Class-VP software (version 7.2.1, Shimadzu Corporation).

**3.1.2 Apoferritin Concentration Measurement**

The apoferritin protein concentration was measured with a dye-binding spectro-photometric total protein assay (Coomassie Protein Assay Kit, #23200, Pierce Biotechnology, Inc.) which is based on the differential color change of a dye in response to various concentrations of protein. Furthermore, the apoferritin concentration was determined via UV absorption at 280 nm using the apoferritin absorption coefficient at 280 nm, $E_{280\,nm}^{1cm,1mg/mL}$.

For the total protein assay, a 2 mg/mL stock solution of bovine serum albumin (BSA, A-7888, Sigma Chemicals) was prepared in ultra-pure water (Water Pro PS, Labconco) including 10 mM sodium azide (S-2002, Sigma Chemicals) as preservative and 150 mM sodium chloride (3624-01, J. T. Baker). The stock solution was filtered through a 0.02 µm filter to remove particulates and stored as 1.5 mL aliquots in microcentrifuge tubes at 4 °C. BSA standards were then prepared for each assay according to Table 3-1 and vortexed.

Table 3-1. Preparation of BSA dilution standards in microcentrifuge tubes

| Vial | Volume of Diluent [µL] | Volume and Source of BSA [µL] | Final BSA concentration [µg/mL] |
|------|------------------------|-------------------------------|---------------------------------|
| A | 0 | 300 of stock | 2,000 |
| B | 125 | 375 of stock | 1,500 |
| C | 325 | 325 of stock | 1,000 |
| D | 175 | 175 of vial B dilution | 750 |
| E | 325 | 325 of vial C dilution | 500 |
| F | 325 | 325 of vial E dilution | 250 |
| G | 325 | 325 of vial F dilution | 125 |
| H | 400 | 100 of vial G dilution | 25 |
| I | 400 | 0 | 0 (blank) |

The total protein assay was performed in standard clear 96-well plates. Therefore, 5 µL of the each protein sample and each BSA standard was combined with 250 µL Coomassie Protein Assay Reagent (part of the Coomassie Protein Assay Kit, #23200, Pierce Biotechnology, Inc.), that has been gently mixed by inverting the bottle a few times and brought to room temperature in advance. Each sample and standard and unknown sample were added in replicates to the multiwell plate. Since the color response with the Coomassie Protein Reagent is non-linear with increasing protein concentration, the BSA standard had to be run alongside the unknown samples and a standard curve had to be generated with each assay. After the protein samples have been combined with the Coomassie Protein Reagent the multiwell plate was gently shaken for 30 seconds to mix the solutions. The absorbance was then measured at 595 nm with a plate reader (Spectramax Plus 384, Molecular Devices). The averaged 595 nm measurements for the blank were subtracted from the 595 nm measurements of all other individual standard and unknown sample replicates. Finally a standard curve was prepared by plotting the average blank-corrected 595 nm measurements of each BSA standard versus its concentration in µg/mL. The standard curve was used to determine the concentration of the unknown protein samples. Due to the non-linear nature of the standard curve a quadratic best-fit was used. The BSA standards that were prepared according to Table 3-1 could be used for several assays at the same day or even few days later (stored at room temperature) without loosing any of the assays accuracy or precision. A necessary requirement for the total protein assay was that the unknown samples had to be within the concentration working range of the assay (0-2,000 µg/mL). Since most of the times the protein concentration could be at best roughly estimated, a

dilution series was prepared of each unknown, hoping that one of the dilutions would fall within the working range of the assay. A typical BSA standard curve obtained through the total protein assay is displayed in Figure B-14 in Appendix B.

On some occasions the apoferritin protein concentration was determined through UV absorption measurements at 280 nm. A necessary requirement here was that the absorption coefficient for apoferritin had to be determined. Therefore, standards of as-received apoferritin (A-3641, Sigma Chemicals) according to the BSA standards in Table 3-1 were prepared as before in 150 mM sodium chloride and 10 mM sodium azide. The apoferritin standards were measured by the total protein assay as described above and by measuring the absorption at 280 nm in glass cuvettes (100 μL sample volume, 1 cm path length, #14-385-928D, Fisher Scientific) that were blanket against the same solution that was used as the blank in the total protein assay in the same apparatus as the multiwell plates (Spectramax Plus 384, Molecular Devices).

The results of both the total protein assay and the UV absorption measurements were plotted in the same graph to compare both methods (Figure 3-1). The absorption coefficient of apoferritin, i.e. the fitting factor of the UV absorption calibration curve to the ideal line in Figure 3-1, was basically the slope of the UV calibration curve itself. The UV absorption coefficient was determined to be $E_{280nm}^{1cm,1mg/mL} = 0.876$, which was reasonably close to an absorption coefficient for apoferritin reported in the literature, $E_{280nm}^{1cm,1mg/mL} = 0.90$ (Bryce and Crichton 1973). From the plot in Figure 3-1 it was obvious that both methods could be employed to determine the apoferritin concentration, but the total protein assay was used more often due to the lower volume requirement for protein concentration determination.
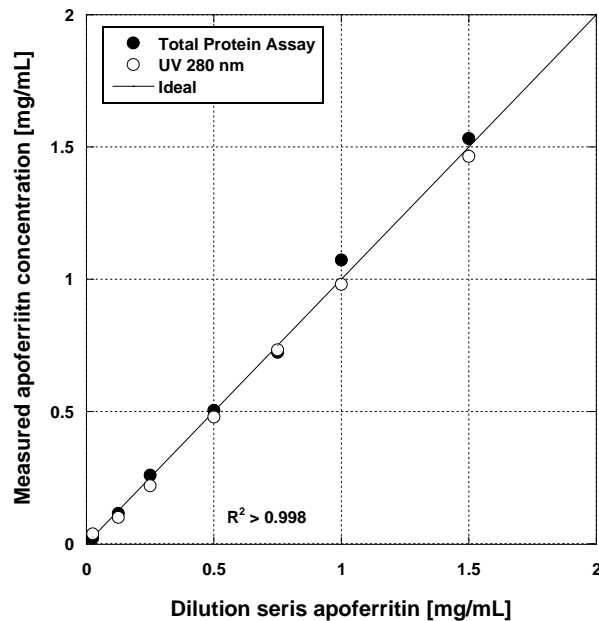
Figure 3-1. Comparison of apoferritin concentration determination via UV-Vis$_{280\,nm}$ vs. total protein assay

### 3.1.3 Ferritin De-Ironization

The de-ironization of ferritin from different sources was performed according to a method described earlier (Wong et al. 1998). The ferritins used were obtained from Cortex Biochem and Sigma Chemicals:

- Equine Spleen Ferritin (F-4503, 77 mg/mL, Sigma Chemicals)
- Human Spleen Ferritin, Pure (CP1003, 3.5 mg/mL, Cortex Biochem)
- Human Liver Ferritin, Pure (CP1004, 4.1 mg/mL, Cortex Biochem)

Thioglycolic acid (Sigma Chemicals) was used to reduce the ferric iron, which makes up the mineral core of ferritin proteins, to its soluble ferrous state (see Figure 3-2).
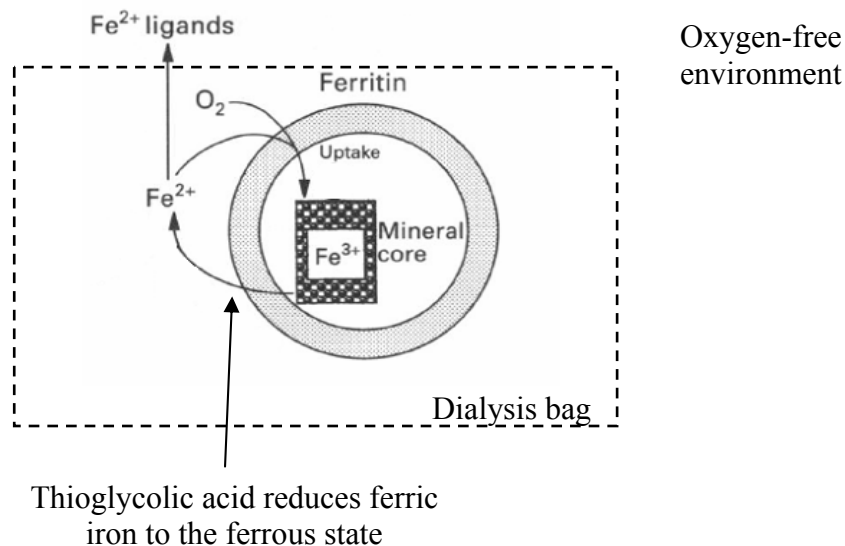
Figure 3-2. Schematic of iron removal from the ferritin mineral core

Ferritin from Sigma Chemicals was diluted to 5 mg/mL with 150 mM NaCl, 10 mM $NaN_3$ solution prior to the treatment to have similar protein concentrations throughout the de-ironization experiment. Preceding the de-ironization experiment the ferritins were analyzed by analytical SEC-HPLC for differences in retention time, relative peak areas and impurities present in the solutions. The SEC-HPLC settings were:

- Shimadzu HPLC (incl. SCL-10A VP system controller, LC-10AT VP HPLC pump, FCV-10AL VP, DGU-14A degasser, SPD-10AV VP UV-VIS detector, SIL-10A auto injector)
- Column: BioRad Bio-Sil SEC-400-5 column
- Buffer: 50 mM Tris-HCl, 150 mM NaCl, 10 mM $NaN_3$, pH 7.4
- Flow rate: 1 mL/min
- Detector settings: $UV_{280\,nm}$

The chromatograms of the ferritins pre-de-ironization together with the chromatogram of apoferritin (A-4603, Sigma Chemicals) can be found in Appendix B.1. The retention times for the monomer peaks of all three ferritin samples were similar and compared well to the retention time of the monomer peak of the apoferritin sample. This was expected since the iron uptake by ferritin does not alter the overall shape and size of the protein itself. Although the overall mass per protein molecule changes depending on its iron load this could not be picked up by size exclusion chromatography which separates solely by size. The equine spleen ferritin sample had a major peak with a retention time around 8.1 minutes representing ferritin dimers. The human ferritin samples (Figure B-3 and Figure B-4, Appendix B) had oligomer contents similar to the apoferritin sample (Figure B-1, Appendix B) with the human liver ferritin lacking a major peak at a retention time around 12.1 minutes representing ferritin subunits.

About 0.5 mL of the ferritin samples were loaded into dialyze frames (Slide-A-Lyzer, 10 kD $M_W$ cut off, Pierce Biotechnology, Inc.) with a syringe and floated in sodium acetate buffer (50 mM, 600 mL, pH 4.5) (Figure 3-3).
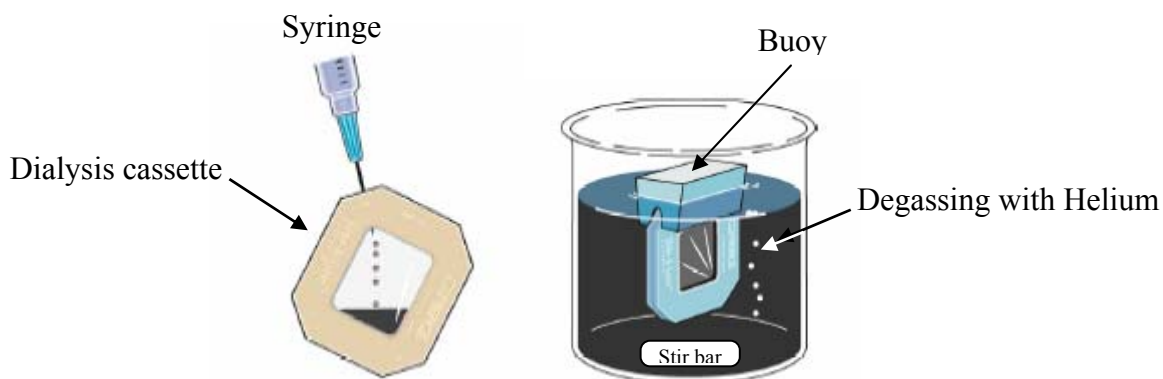


Figure 3-3. a) Slide-A-Lyzer loading, b) dialyzation (images adopted from Pierce Biotechnology, Inc.)

All three ferritin samples had a reddish color due to their iron load. At almost equivalent protein concentration, by visual inspection, the equine spleen ferritin (Figure 3-4 a)) seemed to have the highest iron content, followed by human spleen ferritin (Figure 3-4 b)) and human liver ferritin (Figure 3-4 c)), respectively.
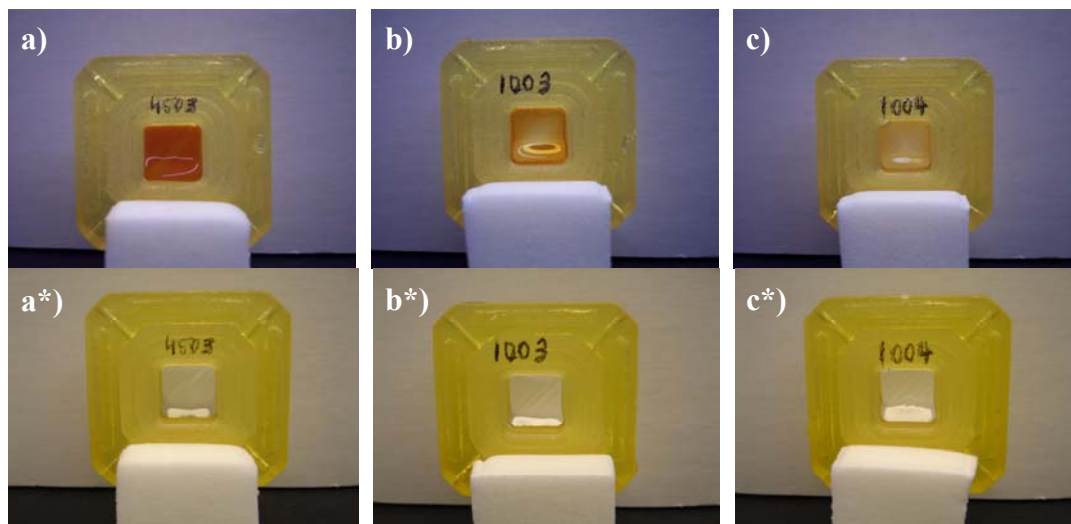


Figure 3-4. Visual check on the de-ironization performance of ferritins from different sources. a) equine spleen ferritin (F-4603, Sigma Chemicals), b) human spleen ferritin (CP1003, Cortex Biochem), c) human liver ferritin (CP1004, Cortex Biochem); * de-ironized samples (apoferritin)

The de-ironization step was done at pH 4.5 because it has been reported that at decreasing pH the relative iron removal increased (Funk et al. 1985) and hence the time the proteins were subjected to thioglycolic acid was kept at a minimum (see Figure 3-5).

The buffer solution was constantly stirred and degassed with helium to remove oxygen that would otherwise re-oxidize ferrous iron. After 1.5 hours thioglycolic acid was added to the buffer (12 mL, 20 mM). After 2.5 hours more thioglycolic acid was added (6 mL, 10 mM) and the buffer was exchanged with fresh sodium acetate solution

(50 mM, 500 mL, pH 4.5) after another 3.5 hours and continuously degassed with helium.  20 minutes after the buffer exchange thioglycolic acid was added to the buffer (10 mL, 20 mM) and the dialysis continued for another 2 hours when more thioglycolic acid was added (5 mL, 10 mM).
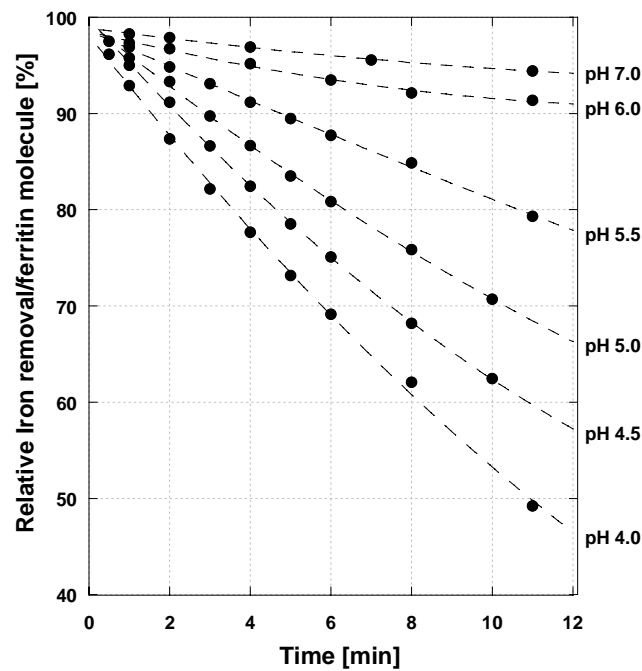


Figure 3-5.  Iron removal from ferritin at different pH values (adopted from (Funk et al. 1985)

At that point the protein solutions appeared clear indicating the successful removal of the mineral core.  After another hour of thioglycolic acid treatment the buffer was changed to 500 mL isotonic sodium chloride solution to remove the thioglycolic acid and the ferrous iron.  At this point the degassing with helium was stopped.  The dialysis cassettes were transferred to tris-buffer (running buffer; 50 mM Tris-HCl, 150 mM NaCl,

10 mM NaN$_3$, pH 7.4 at 35 °C) after one hour and dialysis continued overnight at 4 °C. The next morning the protein solutions were transferred from the dialysis cassettes to sterile microcentrifuge tubes and stored at 4 °C. Protein concentrations were determined by total protein assay (see Chapter 2.4.1). The entire process of the ferritin de-ironization is depicted as a flow diagram in Figure 3-6.

The de-ironized ferritin samples (from now on called apoferritin) were removed from the dialysis chambers, subjected to analytical SEC-HPLC (see Figure B-5 through Figure B-7, Appendix B.1.2) and stored at 4 °C. From the chromatograms it was obvious that de-ironization of equine spleen ferritin (Figure B-2) to obtain equine spleen apoferritin (Figure B-5) resembled very closely the as-received equine spleen apoferritin (Figure B-1) and hence the de-ironization step was regarded successful. Interestingly, the as-received equine spleen ferritin displayed a dominant peak at around 5.6 minutes of elution time indicative of a very large amount of ferritin oligomers present (see Figure B-2). The thioglycolate treatment in the de-ironization step removed almost all of the oligomers that were initially present (see Figure B-5).
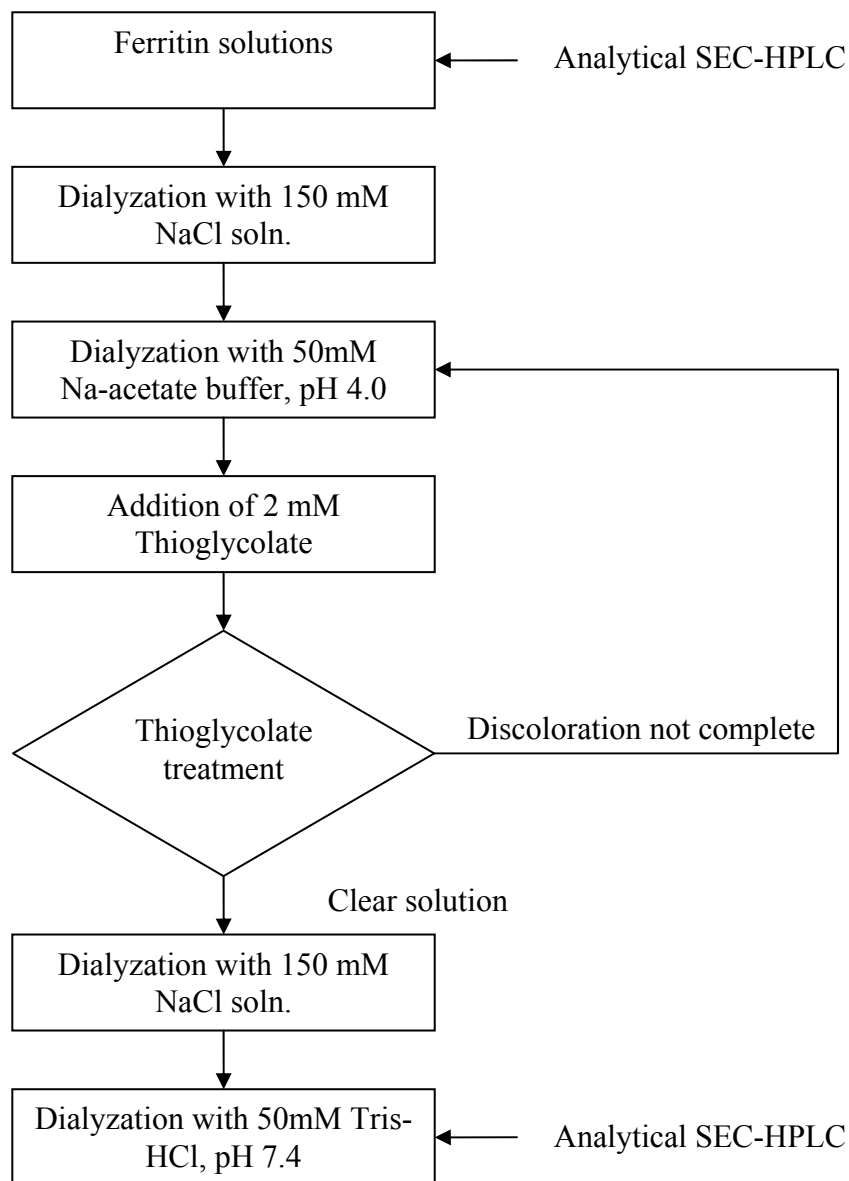
Figure 3-6.  Flow diagram of ferritin de-ironization

### 3.1.4 Circular Dichroism

Circular Dichroism (CD) is an absorptive phenomenon that can be observed when optically active matter absorbs left– and right–hand circular polarized light differently (Figure 3-7).  A shift in absorption can occur when a protein in solution suffers a change in its structural conformation.  The far ultraviolet (UV) region of the CD spectrum (185–250 nm) gives information about the following secondary structural elements of a protein:  $\alpha$–helix, $\beta$–sheet, various turns, and random structures.  The near ultraviolet region of the CD spectrum (250–350 nm) of a protein solution is considered a "fingerprint" of the overall folding of a protein.  Although there is little interpretable structural information in the near–UV spectrum, its utility is often in determining differences between the folded and unfolded states of a protein (Havel 1995).
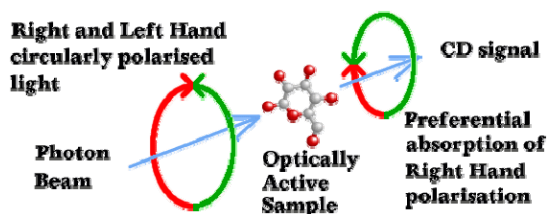


Figure 3-7.  Schematic of circular dichroism principle

### 3.1.5 Static Light Scattering

Detailed description of the apparatus for making light scattering measurements are given by Zimm (Zimm 1948).  Figure 3-8 shows a simplified schematic of a typical light scattering apparatus.  The polarized laser light beam is scattered by a molecule in

solution and the deflected light beam is detected by either a single photomultiplier that can be moved radially in a plane around the scattering volume.  In another setup multiple detectors are arranged radially in a plane around the scattering volume enabling simultaneous measurements at multiple angles.
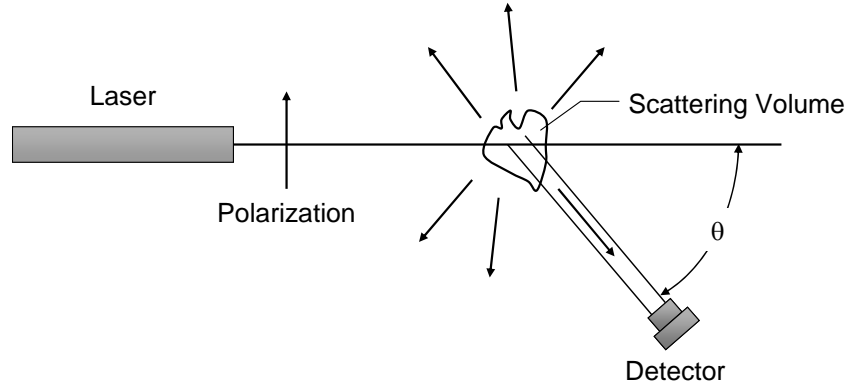


Figure 3-8.  Schematic diagram of the apparatus for light scattering measurements.  The detector can rotated about an axis around the scattering volume that is contained in a glass cuvette.

Lord Rayleigh has derived an equation that relates the incident light intensity, $I_0$, to the scattered light intensity, $I_S$ (Tanford 1961)

$$\frac{I_S}{I_0} = \frac{16\pi^4\alpha^2 \sin^2\theta}{\lambda^4 r^2} \tag{3.1}$$

where $\lambda$ is the wavelength of the laser beam (in vacuum), $\theta$ is the scattering angle and $\alpha$ is the polarizability of the scatterer, which in turn is related to the macroscopic dielectric constant of the medium of interest.   The strong dependence of scattering on the wavelength of the incident light beam (Equation (3.1)) accounts for a few natural phenomena, e.g. the fact that sunlight scattered by the earth's atmosphere is greatly

enriched in the blue wavelengths. The further away from the sun the richer the blue color of the sky is since mostly the blue photons are scattered. The red sky at sunrise and sunset is due to the fact that the sunrays have to travel longer distance through the atmosphere and hence the blue wavelengths are scattered more and do not reach the observers eye.

Combing Equation (3.1) with the following relationship for the polarizability, $\alpha$

$$\alpha = \frac{M_W \left( dn/dc \right)}{2\pi N_A} \tag{3.2}$$

where $N_A$ is the Avogadro's number, $dn/dc$ is the refractive index increment of the solution containing the scattering molecules and $M_W$ is the molecular weight of the scatterer, yields the following general relation for the scattered and incident light intensity

$$\frac{I_S}{I_0} = \frac{4\pi^2 \sin^2 \theta \left( dn/dc \right)^2 M_W c}{N_A \lambda^4 r^2} \tag{3.3}$$

The quantity that is determined through light scattering is the Rayleigh Ratio

$$R_\theta \equiv \frac{r^2 I_S}{I_0 \sin^2 \theta} \tag{3.4}$$

which is given by

$$R_\theta = \frac{Kc}{1/M_W + 2Bc + 3Cc^2 + \cdots} \tag{3.5}$$

Here $K$ is an optical constant of the system

$$K = \frac{2\pi^2 n_0^2 \left( dn/dc \right)^2}{N\lambda^4} \tag{3.6}$$

In the above equation $n_0$ is the refractive index of the pure solvent not including the scattering molecules. Equation (3.5) shows the dependence of the chemical potential of the solvent on the concentration of the solute which is expressed in terms of Equation (2.7).

If the scattering molecules are small compared to the wavelength of the incident laser light beam than the light scattering has no angular dependence and measurements are done at a single angle, usually with the detector placed at $\theta = 90°$ to the incident light beam. To determine molecular parameters Equation (3.5) can be rewritten as

$$\frac{Kc}{R_\theta} = \frac{1}{M_W} + 2Bc + 3Cc^2 + \cdots \qquad (3.7)$$

and plotted as $Kc/R_\theta$ versus $c$. The information to be obtained is essentially the same as that obtained from osmotic pressure measurements on a two-component systems (see Equation (2.9)), the intercept giving the molecular weight and the limiting slope being a measure of the second virial coefficient. The limiting slope or the truncation of Equation (3.7) at the coefficient of the first power gives the more familiar form used in analyzing light scattering data (Zimm 1948)

$$\frac{Kc}{R_\theta} = \frac{1}{M_W} + 2Bc \qquad (3.8)$$

In Equation (3.8) the second virial coefficient, $B$, is in its dimensional form, but commonly it is represented in a dimensionless way, $A$,

$$\frac{KcM_W}{R_\theta} = 1 + 2A\phi \qquad (3.9)$$

where $\phi$ is the volume fraction of the scattering molecule in solution,

$$\phi = \frac{N_A \pi \cdot c \cdot d_h^3}{6 M_W} \tag{3.10}$$

with $d_h$ being the hydrodynamic diameter of the protein.

By comparing Equation (3.8) and Equation (3.9) an expression can be derived relating the dimensional second virial coefficient, $B$, to the dimensionless second virial coefficient, $A$

$$A = \frac{B \cdot c \cdot M_W}{\phi} \tag{3.11}$$

Or with Equation (3.10)

$$A = \frac{6 B \cdot M_W^2}{N_A \pi d_h^3} \tag{3.12}$$

## 3.2 Development of certain aspects of the Experimental Methodology

### 3.2.1 Thermal Gradient Plate

The initial thermal gradient plate was designed after a thermal gradient plate reported in the literature (Luft et al. 1999) (see Chapter 4 and Appendix A for more detail). Since the thermal gradient plate did not provide a linear and unidirectional thermal gradient a new plate design was developed. The following design considerations were applied to the newly designed thermal gradient plate:

- Support of multiwell plates with general 96-well plate footage
- Low weight to accommodate the weight limitations of the automated stage
- Design insulation plate to the automated stage of the microscope

The new design was simplified in that the thermal gradient plate was sized to fit the flat bottom of the multiwell plates. This eliminated the need to machine a groove into the top surface of the thermal gradient plate as in the case of the first generation design to accommodate the outer rim of the multiwell plates (see Figure A-2 and Figure A-5 in Appendix A).

The thermal gradient plate was modeled as a thin slab with thickness, $D$, width, $W$, and length, $L$ (see Figure 3-9). It was assumed that the width and the length of the plate were much greater compared to its thickness ($W$, $L \gg D$). The plate is insulted on its bottom and sides and thermally joined to heat sources at its ends, $T_0$ and $T_H$, respectively. The goal was to find a relationship that determines the temperature distribution within the plate.
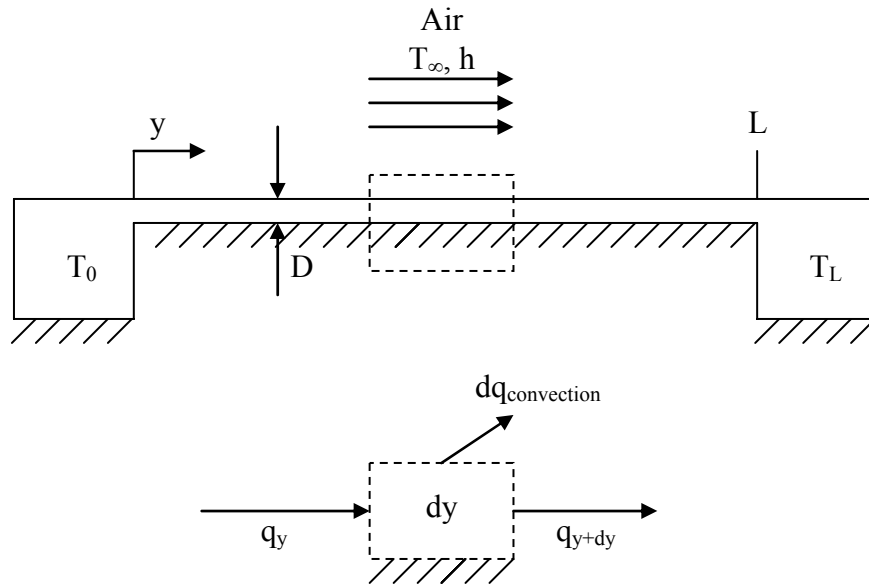
Figure 3-9. Schematic of the thermal gradient plate for modeling purposes

For the modeling of the thermal gradient the following assumptions were made:

- steady state conditions
- one-dimensional conduction along the y-axis ($W, L \gg D$)
- constant properties
- adiabatic bottom and sides
- negligible contact resistance
- uniform surface heat flux and convection coefficient

Applying the conservation of energy to the differential control volume in Figure 3-9

$$q_y = q_{y+dy} + dq_{conv.} \tag{3.13}$$

where

$$q_{y+dy} = q_y + \left(\frac{dq_y}{dy}\right)dy \tag{3.14}$$

and

$$dq_{conv.} = h(T - T_\infty)(W \cdot dy) \tag{3.15}$$

Hence, the one dimensional heat transfer rate was obtained

$$q_y = q_y + \left(\frac{dq_y}{dy}\right)dy + h(T - T_\infty)(W \cdot dy) \tag{3.16}$$

After canceling terms

$$\left(\frac{dq_y}{dy}\right) + h(T - T_\infty)W = 0 \tag{3.17}$$

Using Fourier's law

$$q_y = -k(D \cdot W)\frac{dT}{dy}$$ (3.18)

the following equation was obtained

$$-kD \cdot W \frac{d^2T}{dy^2} + h \cdot W(T - T_\infty) = 0$$ (3.19)

By canceling terms

$$\frac{d^2T}{dy^2} - \frac{h}{kD}(T - T_\infty) = 0$$ (3.20)

Now $\theta = T - T_\infty$ was introduced to obtain a 2$^{nd}$ order differential equation (ODE)

$$\frac{d^2\theta}{dx^2} - \frac{h}{kt}\theta = 0$$ (3.21)

with

$$\lambda^2 = \frac{h}{kD}$$ (3.22)

The general solution of the ODE was

$$\theta = C_1 e^{\lambda y} + C_2 e^{-\lambda y}$$ (3.23)

The appropriate boundary conditions for the problem were

$$\theta(0) = T_0 - T_\infty$$ (3.24)

and

$$\theta(L) = T_L - T_\infty$$ (3.25)

Substituting (3.24) and (3.25) into the general solution, equation (3.23)

$$\theta_0 = C_1 e^0 + C_2 e^0 \tag{3.26}$$

$$\theta_L = C_1 e^{\lambda L} + C_2 e^{-\lambda L} \tag{3.27}$$

To solve for $C_2$, (3.26) was multiplied by $-e^{\lambda L}$ and the result was added to (3.27)

$$-\theta_0 e^{\lambda L} + \theta_L = C_2\left(-e^{\lambda L} + e^{-\lambda L}\right) \tag{3.28}$$

Therefore $C_2$ is

$$C_2 = \frac{-\theta_0 e^{\lambda L} + \theta_L}{-e^{\lambda L} + e^{-\lambda L}} \tag{3.29}$$

Substituting (3.29) into (3.26)

$$\theta_0 = C_1 + \frac{-\theta_0 e^{\lambda L} + \theta_L}{-e^{\lambda L} + e^{-\lambda L}} \tag{3.30}$$

$$C_1 = \theta_0 - \frac{-\theta_0 e^{\lambda L} + \theta_L}{-e^{\lambda L} + e^{-\lambda L}} \tag{3.31}$$

Using (3.29) and (3.26) in (3.23), the temperature distribution could be expressed as

$$\theta(y) = \left[\theta_0 - \frac{-\theta_0 e^{\lambda L} + \theta_L}{-e^{\lambda L} + e^{-\lambda L}}\right]e^{\lambda y} + \left[\frac{-\theta_0 e^{\lambda L} + \theta_L}{-e^{\lambda L} + e^{-\lambda L}}\right]e^{-\lambda y} \tag{3.32}$$

or

$$\theta(y) = \theta_0 e^{\lambda y} - \left[\frac{-\theta_0 e^{\lambda L} + \theta_L}{-e^{\lambda L} + e^{-\lambda L}}\right]e^{\lambda y} + \frac{-\theta_0 e^{\lambda L} e^{-\lambda y}}{-e^{\lambda L} + e^{-\lambda L}} + \frac{\theta_L e^{-\lambda y}}{-e^{\lambda L} + e^{-\lambda L}} \tag{3.33}$$

or

$$\theta(y) = \theta_0 e^{\lambda y} + \frac{\theta_0 e^{\lambda L} e^{\lambda y}}{-e^{\lambda L} + e^{-\lambda L}} - \frac{\theta_L e^{\lambda y}}{-e^{\lambda L} + e^{-\lambda L}} - \frac{\theta_0 e^{\lambda L} e^{-\lambda y}}{-e^{\lambda L} + e^{-\lambda L}} + \frac{\theta_L e^{-\lambda y}}{-e^{\lambda L} + e^{-\lambda L}} \tag{3.34}$$

Combining terms for $\theta_0$ and $\theta_L$

$$\theta(y) = \theta_0 \left[ e^{\lambda y} + \frac{e^{\lambda L} e^{\lambda y}}{-e^{\lambda L} + e^{-\lambda L}} - \frac{e^{\lambda L} e^{-\lambda y}}{-e^{\lambda L} + e^{-\lambda L}} \right] + \theta_L \left[ \frac{e^{-\lambda y}}{-e^{\lambda L} + e^{-\lambda L}} - \frac{e^{\lambda y}}{-e^{\lambda L} + e^{-\lambda L}} \right] \qquad (3.35)$$

or

$$\theta(y) = \theta_0 \left[ e^{\lambda y} + e^{\lambda L} \left( \frac{e^{\lambda y} - e^{-\lambda y}}{-e^{\lambda L} + e^{-\lambda L}} \right) \right] + \theta_L \frac{e^{-\lambda y} - e^{\lambda y}}{-e^{\lambda L} + e^{-\lambda L}} \qquad (3.36)$$

With $sinh(y) = \dfrac{e^y - e^{-y}}{2}$

$$\theta(y) = \theta_0 \left[ e^{\lambda y} + e^{\lambda L} \frac{sinh(\lambda y)}{sinh(\lambda L)} \right] + \theta_L \frac{sinh(\lambda y)}{sinh(\lambda L)} \qquad (3.37)$$

Substituting back for $\theta = T_y - T_\infty$ and using equation (3.37)

$$T_y = \theta(y) + T_\infty \qquad (3.38)$$

The dimensions for the plate were

- $L$ (mm): 109.982
- $W$ (mm): 77.978
- $D$ (mm): 5.08
- The cross-sectional area of the plate, $A_c$, for $0 < y < L$ was 0.0003961 m$^2$.

Three different materials were considered for the thermal gradient plate, brass, stainless steel and aluminum as these materials are widely used for similar applications. The following physical properties for the material and the overall system were used to model the thermal gradient plate:

- Thermal conductivity, $k$ (W/m*K):
- Aluminum:          230.0
- Brass:             112.0

- Stainless Steel:       14.9

- Convection coefficient $h$ (W/m$^2$*K): 100 (assumed)

($h$ = 2-25 W/m$^2$*K for free convection, $h$ = 25-250 W/m$^2$*K for forced convection

(Incropera and Dewitt 2000))

Now, the heat transfer rate from the plate is $q_p = -q_y(0) + q_y(L)$ and using Fourier's

law, the conducting heat rates, with $A_c = W \cdot D$ are

$$q_y(0) = -kA_c \left. \frac{d\theta}{dx} \right|_{y=0} = -kA_c \left[ \left( \lambda e^0 - \frac{e^{\lambda L}}{\sinh(\lambda L)} \lambda \right) \theta_0 + \frac{\lambda}{\sinh(\lambda L)} \theta_L \right] \qquad (3.39)$$

$$q_x(L) = -kA_c \left. \frac{d\theta}{dx} \right|_{y=L} = -kA_c \left[ \left( \lambda e^L - \frac{e^{\lambda L}}{\sinh(\lambda L)} \lambda \cdot \cosh(\lambda L) \right) \theta_0 + \frac{\lambda \cdot \cosh(\lambda L)}{\sinh(\lambda L)} \theta_L \right] \qquad (3.40)$$

The above calculations were used to determine what materials to consider, the influence of the ambient temperature and the impact of the convective air movement on the thermal gradient. In Figure 3-10 the influence of the different thermal conductivities of the metals on the thermal gradient is shown. Aluminum having the highest thermal conductivity provided a linear temperature gradient along the y-axis of the plate, while especially the theoretical results for stainless steel were highly non-linear. The influence of the ambient temperature on the linearity of the thermal gradient is depicted in Figure 3-11. Compared to an ambient temperature that is the average of the minimum and maximum temperature of the thermal gradient, a shift away from that temperature results in greater non-linearities of the thermal gradient, even for aluminum.
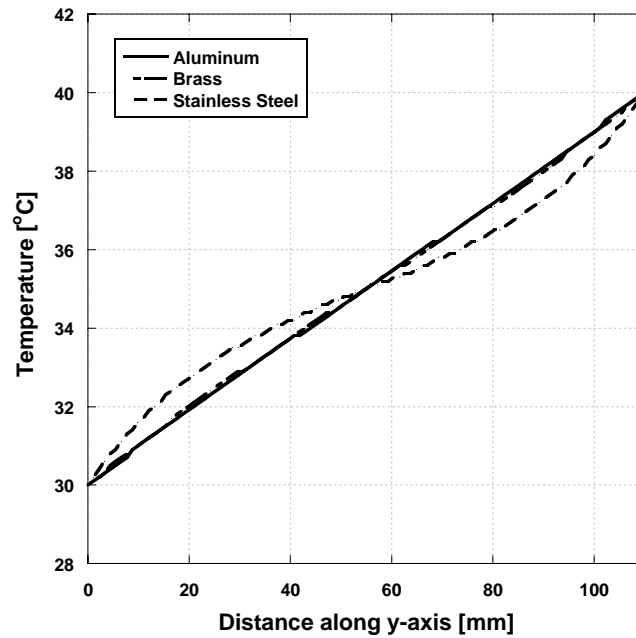
Figure 3-10.  Thermal gradients (theoretically) obtained with different materials of the thermal gradient plate (35 ºC ambient temperature)
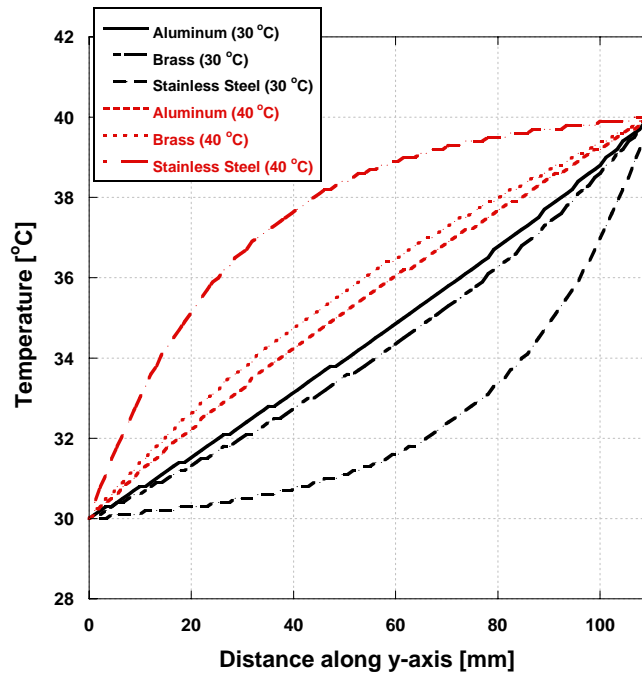


Figure 3-11:  Influence of ambient temperature on (theoretical) thermal gradient (30 ºC and 40 ºC ambient temperature, respectively)
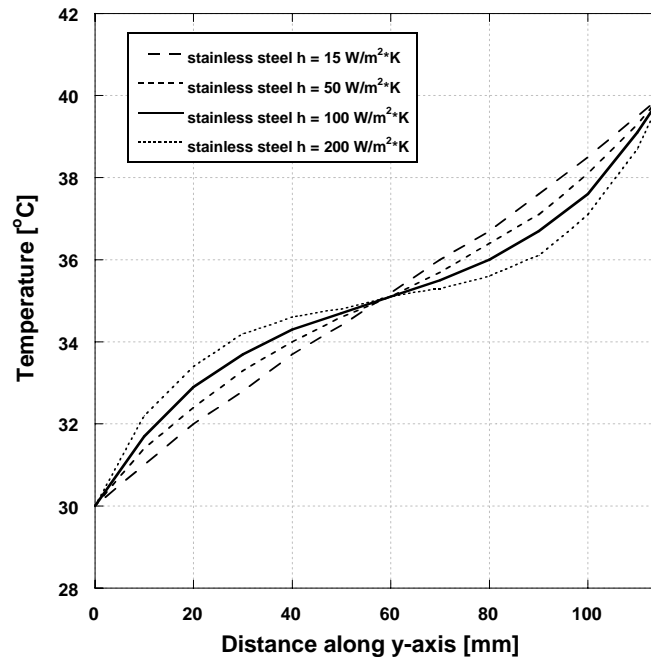
Figure 3-12: Temperature distribution as a function of air movement across the plate (at 35 °C ambient temperature)

The importance of a controlled ambient temperature led to the construction of a temperature controlled enclosure for the automated stage of the light microscope. The performance of the actual thermal gradient plate at 35 °C ambient temperature is depicted in Figure 3-13. Here, the temperature in water droplets of 4 μL volume submerged in 8 μL paraffin oil (HR-411, Hampton Research) was monitored with hypodermic needle probes (Omega) in three different wells of a 384-well plate over an extended period of time. Furthermore the temperature in the enclosed chamber as well as the actual laboratory temperature were measured with temperature probes and recorded with a temperature acquisition system (Omega). Although the laboratory temperature fluctuated substantially over several hours, the chamber temperature and even more importantly, the

temperature within the water droplets remained constant, with standard deviations of less than 0.03 °C per droplet.
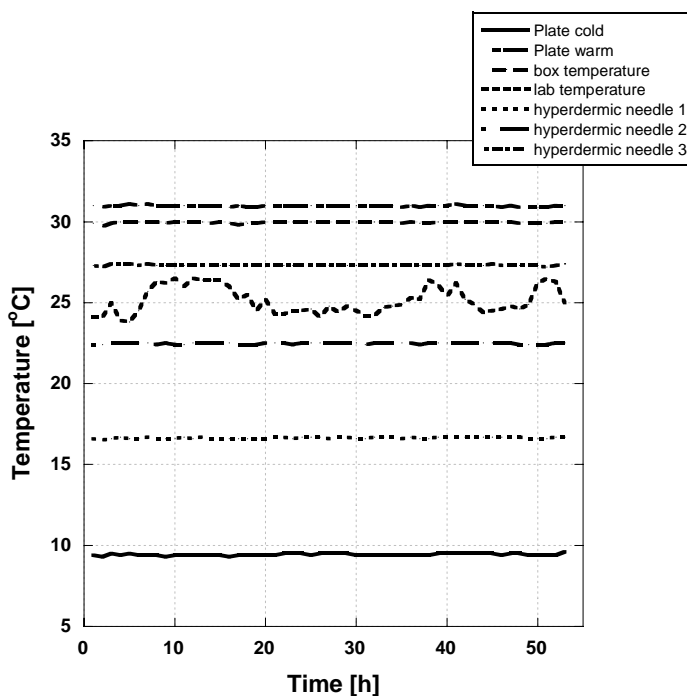


Figure 3-13. Thermal stability within water droplets in oil-filled wells with respect to the surrounding temperature

More details on the actual performance together with images and pictures of the thermal gradient plate can be found in Chapter 4. The actual dimensions of the thermal gradient plate are depicted in Figure A-7 in Appendix A.

### 3.2.2 Buffer Systems

The initial step in preparing for the proposed crystallization experiments of apoferritin was the identification of an appropriate buffer system, since pH is the single most important variable that must be maintained throughout protein handling (McPherson

1999).  The main two requirements for the buffer are buffering capacity at the appropriate pH value and pH stability with respect to temperature. Furthermore undesired interaction of the buffer with the biopolymer, redox stability and metal ion complexing properties are of great concern when choosing the appropriate buffer system.

The temperature gradient that is introduced in the crystallization experiments is from 30 °C to 40 °C, therefore covering the human body temperature as well as the lower ocular temperature.  The criteria used to find an appropriate buffer system was its pKa value (defined as $\log_{10} K_A$, with $K_A$ being the dissociation constant) at the proposed temperature range.  The pH in the ocular lens is about 7.40 and so the pKa of the buffer system has to be about the same value within proposed temperature range to be effective.

The buffer testing apparatus consisted of a 1 liter jacketed glass beaker that was connected to a waterbath (VWR 1157) for temperature control (Figure 3-14).

The liquid was mixed through a magnetic stirrer and the pH as well as the temperature of the buffer was determined by a temperature compensated pH meter (WTW pH 340).  The buffers were prepared mainly according to the recipes by McPherson (McPherson 1999).  The buffers used together with their chemical structure are listed in Table 3-3 and all buffers contained 150 mM NaCl.

The buffers were subjected to increasing temperatures starting at 30 °C with 2 °C increments up to 40 °C.  About 300-400 mL of each buffer was added to the testing system and the pH was adjusted to pH 7.40 at 30 °C.  After the temperature of the waterbath was increased, the liquid was given appropriate time to equilibrate to the temperature step-change (~30 minutes).
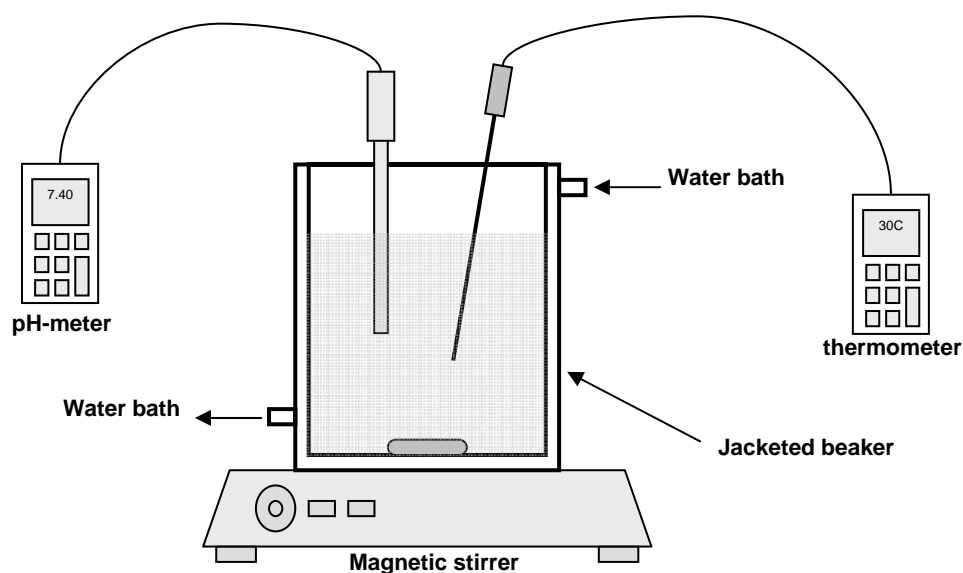
Figure 3-14. Schematic of pH-stability measurement system

The first buffer tested was inorganic phosphate buffer that is known for its good pH stability with respect to temperature. The buffer was adjusted to the desired pH by mixing two equimolar solutions of phosphate mono- and dibasic. The phosphate buffer showed a negative linear temperature dependency of -0.008 pH/1 °C (see Figure 3-15).

The buffer was then "challenged" by the addition of 5% (w/v) cadmium chloride. The cadmium level is elevated in the cataract diseased lens and, together with its common use in apoferritin crystallization *in vitro*, led to its selection as the precipitant agent in the batch crystallization experiments. Upon the addition of the divalent cation, the buffer turned cloudy immediately. Next, cadmium sulfate and cadmium nitrate were added to pure phosphate buffer but the result was the same in all cases: a cloudy precipitation formed instantly. The same outcome was observed for 2% (w/v) of the cadmium salts. The anion was therefore ruled out as the main component of the precipitate formed. A literature search revealed that phosphate precipitates most

polyvalent cations (Good et al. 1966) and is therefore not an appropriate buffer system for the type of research conducted. The literature search furthermore indicated that almost all inorganic buffers are incompatible with polyvalent cations.
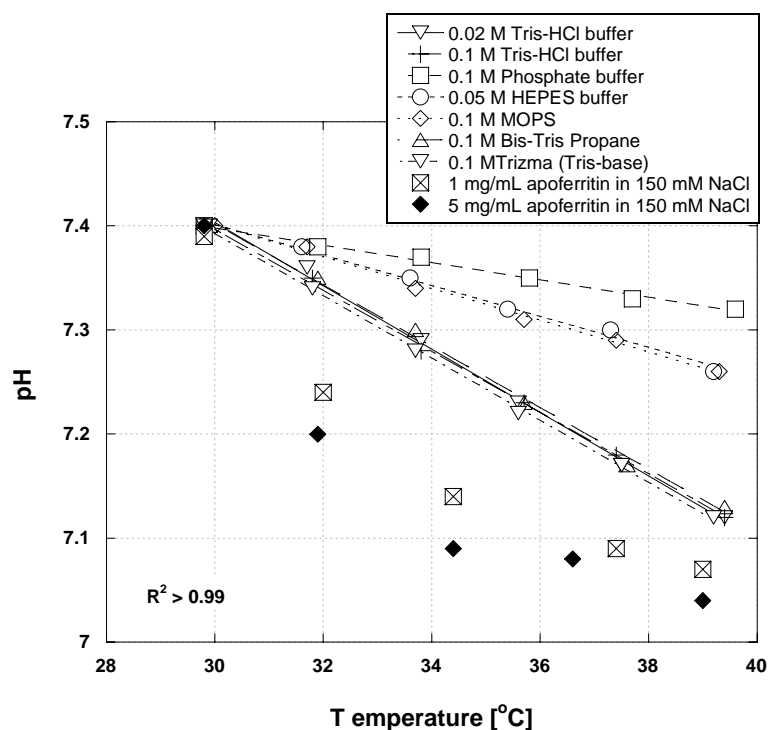


Figure 3-15.  pH stability of several buffer systems with respect to temperature (note: The pH of 0.1 M Trizma (tris-base) was adjusted to pH 7.40 at 30 °C with equimolar HCl)

The other major class of buffers with a pKa around 7.40 and good compatibility with divalent cations are organic amine buffers (Good et al. 1966). As HEPES buffer was readily available in the laboratory its temperature stability and cadmium compatibility was tested next. The buffer was adjusted to pH 7.40 at 30 °C with sodium hydroxide and showed a negative linear pH dependency with increasing temperature as well. The pH dropped about 0.14 over the 10 °C range. Upon the addition of 5% (w/v)

cadmium chloride the salt dissolved almost completely, but the solution turned cloudy after a few minutes. The next buffer tested was tris-HCl since it is compatible with cadmium ions (Hanlon et al. 1966). Two buffer solutions with two different concentrations, 0.1 M and 0.02 M, have been tested for their pH stability with respect to temperature. Both buffer solutions were equally, but less stable compared to HEPES and phosphate buffer. The pH dropped about 0.03 pH/1 °C. The addition of cadmium chloride resulted in a clear solution, but a drop in pH to 6.0 was observed. Upon the addition of 0.1 M sodium hydroxide the solution turned cloudy at a pH around 7.0. It was therefore suspected that NaOH might have an impact on the formation of the precipitate. Therefore in a next test tris base (not containing HCl) was used. Tris base adjusted to pH 7.40 with equimolar HCl solution had the same temperature stability compared to tris-HCl, where the pH was adjusted with NaOH. The idea was to dissolve cadmium chloride into the tris base solution before the pH was adjusted to pH 7.40 with equimolar HCl solution. The reasoning was that starting at a pH well above pH 7.40 would not require the addition of NaOH for pH adjustment but rather the addition of HCl. Upon addition of cadmium chloride the solution turned cloudy immediately, but upon addition of equimolar HCl the buffer turned clear and remained clear. This triggered the idea that a base other than NaOH might work for HEPES buffer including cadmium chloride. The temperature stability of HEPES adjusted to pH 7.40 with 1 M tris base was comparable to the other HEPES buffer (data not shown). The pH readjustment after the addition of 5% (w/v) cadmium chloride to pH 7.40 with Tris base resulted in the HEPES buffer turning cloudy again.

Bis-tris propane was comparable to the tris buffer in terms of the temperature coefficient but did also displayed incompatibility with cadmium comparable to HEPES. Another buffer, MOPS, that is structurally related to HEPES has been tested for temperature stability and cadmium compatibility. MOPS performed comparable to HEPES with respect to temperature stability but was also not chemically stable upon the addition of cadmium.

Finally, the temperature coefficient for pure apoferritin (in the presence of 150 mM NaCl) was determined. From Figure 3-15and Figure 3-16 it can be seen that the pH does not drop linearly with increasing temperature for solutions containing 1 mg/mL and 5 mg/mL apoferritin as it was the case for the other buffer systems tested.
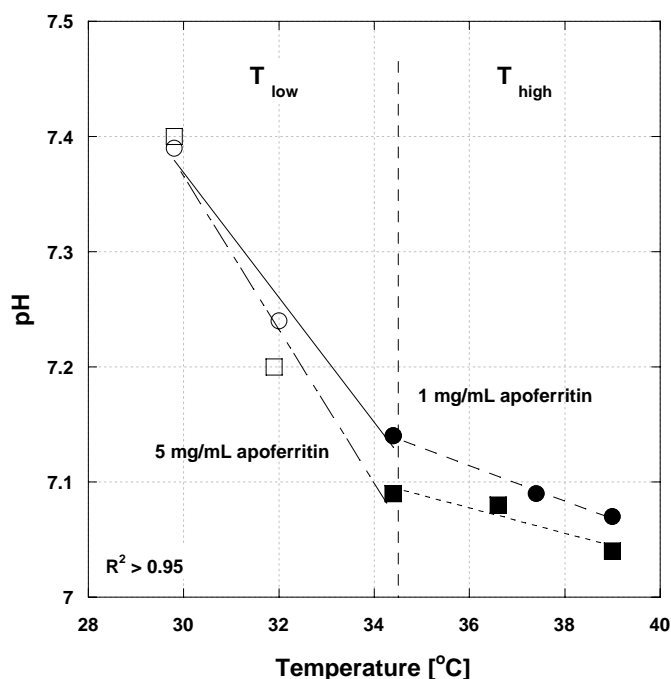


Figure 3-16. pH stability of apoferritin (in 150 mM NaCl) with no buffer present

Figure 3-16 reiterate the result from Figure 3-15 but with the graph being divided into two temperature regions. At the lower temperature regime, $T_{low}$, both apoferritin solutions had a more negative temperature coefficient compared to the higher temperature regime, $T_{high}$. The results for all tested buffer systems and the comparison to published data on temperature coefficients are shown in Table 3-2.

Due to the relatively low temperature coefficient and the good cadmium compatibility tris-HCl was chosen as the buffer system for all protein crystallization experiments and protein-protein interaction measurements.

Table 3-2. Temperature stability of various buffer systems ([‡](Anon 2006), [#](Good et al. 1966), [$](Sankar and Bates 1978))

| Buffer | pH range | Temperature coefficient (pH unit/°C) measured | Temperature coefficient (pH unit/°C) literature |
|---|---|---|---|
| 0.02 M Tris-HCl | 7.0-9.0 | -0.03 | -0.031[#] |
| 0.1 M Tris-HCl | 7.0-9.0 | -0.029 | |
| 0.1 M Phosphate buffer | 5.8-8.0 | -0.008 | |
| 0.05 M HEPES | 6.8-8.2 | -0.015 | -0.014[#] |
| MOPS | 6.5-7.9 | -0.015 | -0.012[$] |
| Bis-Tris Propane | 5.8-7.2 | -0.029 | -0.016 |
| Trizma | 7.0-9.0 | -0.03 | |
| Apoferritin 1 mg/mL $T_{low}$ | N/A | -0.054 | Not available |
| 1 mg/mL $T_{high}$ | N/A | -0.015 | Not available |
| 5 mg/mL $T_{low}$ | N/A | -0.067 | Not available |
| 5 mg/mL $T_{high}$ | N/A | -0.011 | Not available |

Table 3-3.  List of possible buffers for crystallization experiments ([‡] (McPherson 1999))

| Name | Useful pH range | pKa (37 °C)[‡] | Chemical structure |
|---|---|---|---|
| Trizma ($C_4H_{11}NO_3$) | 7.0-9.0 | 7.72 | CH$_2$OH, H$_2$COH—C—CH$_2$OH, NH$_2$ |
| Trizma HCl ($C_{11}H_{26}N_2O_6$) | 7.0-9.0 | 7.72 | CH$_2$OH, H$_2$COH—C—CH$_2$OH  HCl, NH$_2$ |
| Bis-Tris Propane ($C_{11}H_{26}N_2O_6$) | 5.8-7.2 | 6.80 | CH$_2$OH, HOH$_2$C—C—NHCH$_2$CH$_2$CH$_2$NH—C—CH$_2$OH, CH$_2$OH, CH$_2$OH |
| HEPES ($C_8H_{18}N_2O_4S$) | 6.8-8.2 | 7.55 | H$_2$CH$_2$CHO—N(piperazine ring)N—CH$_2$CH$_2$—S(=O)(=O)—OH |
| MOPS ($C_7H_{15}NO_4S$) | 6.5-7.9 | 7.20 | (morpholine ring)N—CH$_2$CH$_2$CH$_2$—S(=O)(=O)—OH |
| Phosphate buffer | 5.8-8.0 | 7.21 | N/A |

# CHAPTER 4

# A MULTIWELL MICROBATCH CRYSTALLIZATION ON A THERMAL GRADIENT

## 4.1 Abstract

A versatile and inexpensive microbatch crystallization apparatus with an integrated thermal gradient is introduced. The device is designed to fit onto automated microscope stages for timed image acquisition. The thermal gradient is established through an aluminum plate machined to house commercially available microplates with a standard 96-well footprint. The novelty of the design includes online monitoring of crystal growth without interfering with the established thermal gradient. The temperature stability and unidirectional temperature gradient were demonstrated. Hen egg white lysozyme (HEWL) was used as a model macromolecule to observe the effect of temperature variations on crystal habit and the number and size of crystals produced.

## 4.2 Introduction

Protein crystallization has gained an essential role in the post-genomic era. Along with cloning, protein expression and purification, and X-ray diffraction, crystallization of proteins is an essential step towards the discovery of protein structures in what is called the structural genomics production line (Abbott 2000). Here, the crystallization step is regarded as the rate-determining step by which new protein structures are evaluated (Stevens 2000; Kuhn et al. 2002).

77

Attempts to obtain crystals that can be used to determine protein structures have not been generally successful; in fact, only about 10% of such efforts have resulted in the production of crystals of sufficient quality. It is important, then, that attention be given to screening techniques to identify conditions that result in protein crystals of sufficient quality for structural determinations, rather than microcrystals or precipitates (Chayen 2002).

To generate the required thermodynamic driving force for crystallization, vapor diffusion is most often used followed by batch crystallization and dialysis (Gilliland et al. 1994; Chayen 1998). The vapor-diffusion method results in a dynamic crystallization system in which the protein of interest proceeds through a range of conditions as both the protein and precipitant concentrations increase with solvent (generally, water) evaporation. Nucleation conditions that may occur during this process are difficult to determine precisely due to the dynamic nature of the experiment. Additionally, vapor diffusion is a multifactorial technique, with many of the system parameters being set at specific values. Such parameters include the volume of the droplet of protein solution, the contact angle between the droplet and the coverslip, and the distance from the droplet to the well containing the reservoir into which water is transported (Fowlis et al. 1988). Although this high number of degrees of freedom provides for flexibility, it may also increase to unmanageable levels the number of experiments that need to be performed to identify nucleation and crystal growth conditions.

Batch crystallization on the other hand is a static system in which the precipitant and protein concentrations are predefined. In a batch crystallization experiment, supersaturation is achieved upon mixing of the protein solution and the precipitate

solution. There is less exploration of the phase diagram, since the concentration of the initial crystallization ingredients essentially do not change until after nucleation has occurred (Chayen 1998). A modification of the batch crystallization technique was achieved with the introduction of protein microbatch crystallization under oil (Chayen et al. 1992; Chayen 1997; Chayen 1999).

Temperature can have a significant effect on both the thermodynamics of protein solutions and the kinetics by which crystals are nucleated and grown from such solutions. Attention is often given to the effect of temperature on protein solubility and the influence of this variable on crystallization behavior. Even for macromolecular systems whose solubility has a low sensitivity to temperature, the temperature responsiveness of the solubility can be increased by changing the buffer to low salt concentrations (Jones et al. 2001).

In cases where temperature may not seem pertinent in determining whether or not crystals can be obtained, it nevertheless can have a major impact on the rate at which such crystals are formed and on the final quality of the crystals, as determined by crystal habit, size or purity (McPherson 1999). An investigation of crystallization temperature using data from the Biological Macromolecule Crystallization Database (BMCD), a compilation of crystallization conditions of macromolecules with more than 3500 entries for which diffraction-quality crystals have been obtained, revealed that about 90% of all experiments were conducted at only two narrow temperature ranges, as is shown in Figure 4-1 (Gilliland et al. 1994; Gilliland et al. 2002). Thus, variations in the temperature of macromolecular crystallization have not been thoroughly investigated. This is unfortunate, since temperature is a physical variable that can be controlled to

relatively high levels of precision and there are many mechanisms for both regulating and monitoring temperature. Furthermore temperature variation gives the ability to change the relative supersaturation of a solution by changing the protein saturation concentration, compared to a change of solution concentration at constant temperature (Jones et al. 2001).
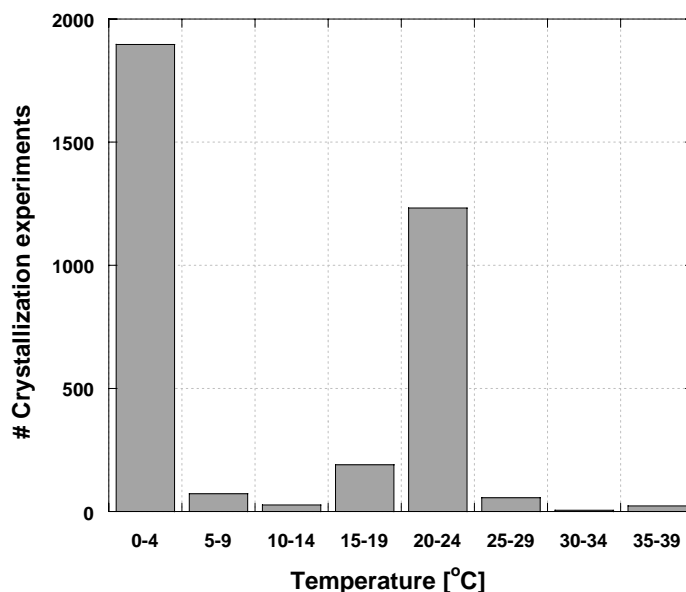


Figure 4-1. Histogram of protein crystallization temperatures used in previously reported experiments (source: wwwbmcd.nist.gov:8080/bmcd/bmcd.html)

The common temperature ranges in Figure 4-1, 0 to 4 °C and 20 to 24 °C, are convenient since they can be easily controlled by placing the crystallization experiments in a refrigerator or by leaving them out on the laboratory bench, respectively. The low-temperature cases without integrated image acquisition systems are especially problematic when the experimental progress is to be assessed through microscopic observation of outcomes at room temperature. Indeed, the temperature of small protein

volumes can increase rapidly as plates are taken out of a refrigerator, and this may have a strong influence on the outcome of crystallization experiments.

An apparatus that integrates a thermal gradient with a high-throughput system to test additional crystallization parameters and an online image acquisition system would be a valuable tool in macromolecular crystallization experiments. Although apparatuses with integrated thermal gradients for protein crystallization have been reported previously (DeMattei and Feigelson 1992; DeMattei and Feigelson 1993; Luft et al. 1999; Juarez-Martinez et al. 2002), none of them provide the type of integration mentioned above. This paper reports on the design and validation of a relatively inexpensive apparatus that addresses these experimental requirements.

## 4.3 Materials and Methods

### 4.3.1 Apparatus

The entire crystallization apparatus is shown schematically in Figure 4-2. The centerpiece of the apparatus is a light microscope (Leica DMLM) with a digital camera (CoolSNAP-Pro cf, Roper Scientific) and an automated stage (Prior H128).

The stage accommodates a multi-well plate (Figure 4-3A) along the *y*-direction of which a temperature gradient is established. Solutions are placed in the wells of the plate and observed by the microscope. To establish the temperature gradient, the multi-well plate is placed onto a thermal-gradient plate (Figure 4-3B) made out of aluminum and mounted onto a thermal-insulator plate (Figure 4-3C) made out of polycarbonate. Good heat transfer between well plate and thermal gradient plate is ensured through the use of a thin film of a thermally conductive paste (Omega-Therm 201) that is applied to the

contact area between the two plates. The temperature gradient is created by two water channels, one along each edge of the *x*-axis of the plate, that are connected to separate water baths (VWR 1157) for temperature adjustment. The plastic tubing to and from the water baths is well-insulated to prevent heat transfer with the surroundings.
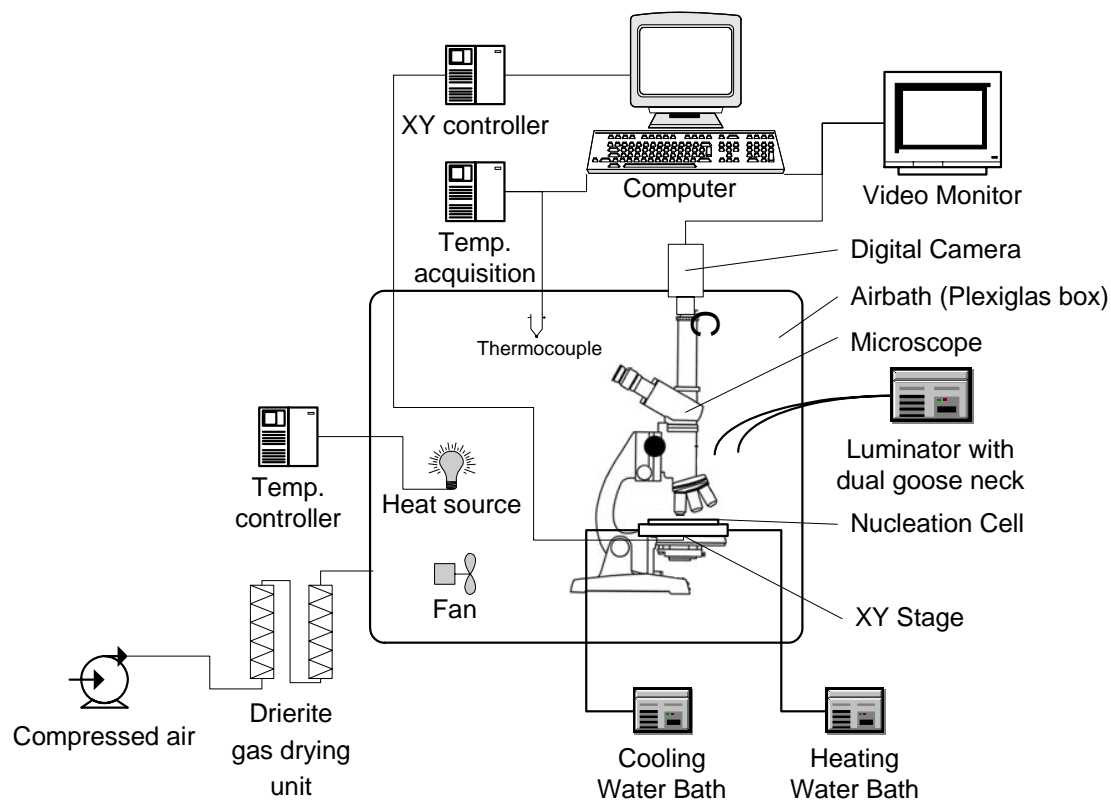


Figure 4-2. Schematic of crystallization apparatus

The material of the plate was chosen after modeling the temperature gradient for the given plate geometry. Other heat-conducting metals such as stainless steel and brass demonstrated non-linear temperature gradients due to their lower thermal conductivity (data not shown). The insulation plate is machined to fit onto the automated stage of the light microscope as shown in Figure 4-3 and Figure 4-4. The use of the insulation plate

makes the system even more versatile since only the bottom part of the insulation plate has to be altered to accommodate various automated stage configurations, while the temperature-gradient plate itself remains unchanged. The number of wells per microplate can range from standard 96 wells up to 1536 wells for the Nunc-Immuno™ plate for example. The only requirement is a flat bottom for good physical contact to the thermal gradient plate.
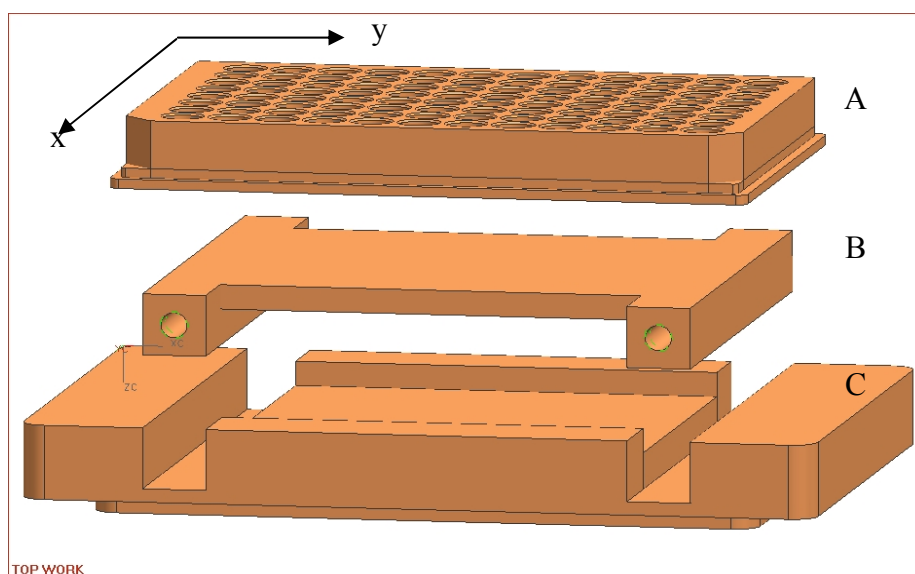


Figure 4-3. Schematic of thermal gradient apparatus assembly (A: well plate; B: thermal gradient plate; C: insulation plate)

The microscope, together with the automated stage, is contained in a Plexiglas® box to provide a temperature-controlled environment. It has been shown that temporary temperature changes or an accidental exposure to some unintended thermal environment can have a dramatic effect on the crystallization outcome (McPherson 1999). The box is continuously purged with dry air to prevent water condensation on the cold part of the

temperature-gradient plate. A fan provides steady forced-air convection inside the box. The temperature inside the box is held constant via a temperature controller (Omega N6402) and is, together with the plate temperatures, independently monitored via a temperature acquisition system (Omega OMB-DAQ-56).

Imaging is regarded as a major design consideration for high-throughput crystallization experiments (Stevens 2000), and therefore the setup uses image analysis software to acquire images at preset time intervals. The crystallization wells are illuminated with a dual gooseneck fiberoptic light (Schott-Fostec ACE-I). Image-Pro and Scope-Pro software (Media Cybernetics) is used for the image acquisition and stage control, respectively. A macro was programmed to implement timed image acquisition from a predetermined array of wells on the crystallization plate. The software further allows image assessment and crystal size determination.
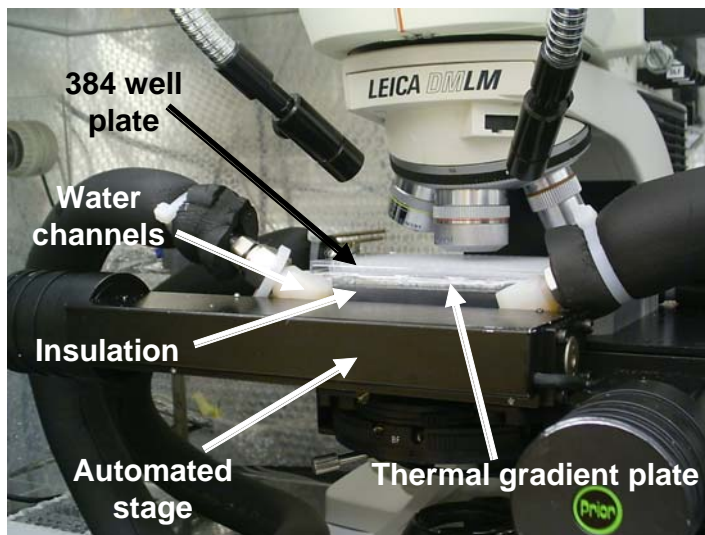


Figure 4-4. Close-up picture of experimental setup

## 4.3.2 Temperature Measurements

The temperature stability and the linearity of the thermal gradient were assessed in an initial experiment by submerging an 8-µL water droplet under an 8-µL droplet of paraffin oil in each well of a low-profile 384 ShallowWell Plate (Nunc, cat# 264340) (16x24 wells). These wells are conical, flat-bottomed with an optimized plate height for excellent optical observation. The apparatus was assembled as shown in Figure 4-3. The temperature within each water droplet was measured with a hypodermic needle probe (Omega, HYP1-30-1/2-T-G-60-SMP-M) in conjunction with a digital thermometer (Barnant Dual J-T-E-K$^{TM}$). The box temperature was set to 24 °C and the water baths were set to 14 °C and 30 °C, respectively.

The long-term temperature stability within the water droplets was determined by fixing the same hypodermic needle probes to random wells and monitoring the droplet temperature as well as the laboratory and box temperature continuously via a temperature acquisition system (Omega OMB-DAQ-56).

## 4.3.3 Protein Crystallization

Lysozyme (Sigma L-6876) was used as received. HPLC grade water (W5, Fisher Scientific) was used for all buffer preparation. Standard 100 mM sodium acetate buffers were prepared at pH values ranging from 4.0 to 5.2. The precipitate buffer was prepared by adding NaCl to a portion of the standard buffers to obtain 20% (w/v) NaCl solutions (equivalent to 3.42 mol/L NaCl). Lysozyme was weighed and dissolved into each standard buffer to obtain protein stock solutions of 240 mg/mL lysozyme. All buffers were readjusted for their pH with 1M NaOH and 1M HCl. The protein stock solutions

were passed through centrifugal filters (0.22 μm, Corning Spin-X), aliquoted into centrifuge tubes, and stored at – 20 °C until used.

The crystallization experiments were carried out in a small-scale batch mode on the same low-profile 384-well plates as the temperature measurements. The well plates were cleaned from potential dust particles with ultra-pure compressed air (Air'It, Fisherbrand) before usage. First, 8 μL of paraffin oil was pipetted into each well with an Eppendorf micropipette. The protein stock solutions were mixed with the standard buffer and the precipitate buffer to obtain solutions containing 48 mg/mL lysozyme and 1% (w/v), 2% (w/v) and 3% (w/v) NaCl for each pH used. A total of 12 solutions with pH values of 4.0, 4.4, 4.8 and 5.2, were obtained and used immediately. The mixing procedure followed a recipe in which the protein stock solution was transferred to a centrifuge tube, and the tube was vortexed while adding the standard buffer followed by the precipitant buffer. This was done to reduce local peaks of precipitant concentration that could have led to instantaneous protein precipitation (Rayment 2002). A small droplet (4 μL) of the freshly prepared protein solution was pipetted directly underneath the paraffin oil surface in each well, minimizing the contact time to the surrounding air. Each row of wells along the $y$-axis was used for each of the 12 solution conditions. The plates were assembled according to Figure 4-3. The water baths were set to achieve a thermal gradient from 20 °C to 30 °C along the $y$-axis. The number and location of the wells used for each experiment were specified in the Scope-Pro software and the image acquisition was started by initiating the program macro. For a second experiment, the same procedure was followed but the final protein solutions contained 3% (w/v), 4% (w/v) and 5% (w/v) NaCl.

## 4.4 Results and Discussion

### 4.4.1 Temperature Measurements

Long-term monitoring of the lab air temperature revealed fluctuations of up to ±10% throughout the day. The crystallization apparatus achieved constant temperatures in the wells over a period of days (data not shown) irrespective of these lab temperature fluctuations, with standard deviations of less than 0.03 °C per well.

The temperature gradient measurements of each water droplet submerged in paraffin oil in the 384-well plate demonstrated edge effects along the *y*-axis as well as the *x*-axis. Two rows and two columns along each edge of the 384-well plate showed nonlinear temperature behavior compared to the remaining 240 core wells. In Figure 4-5 the temperature gradient of the remaining 240 core wells is depicted.
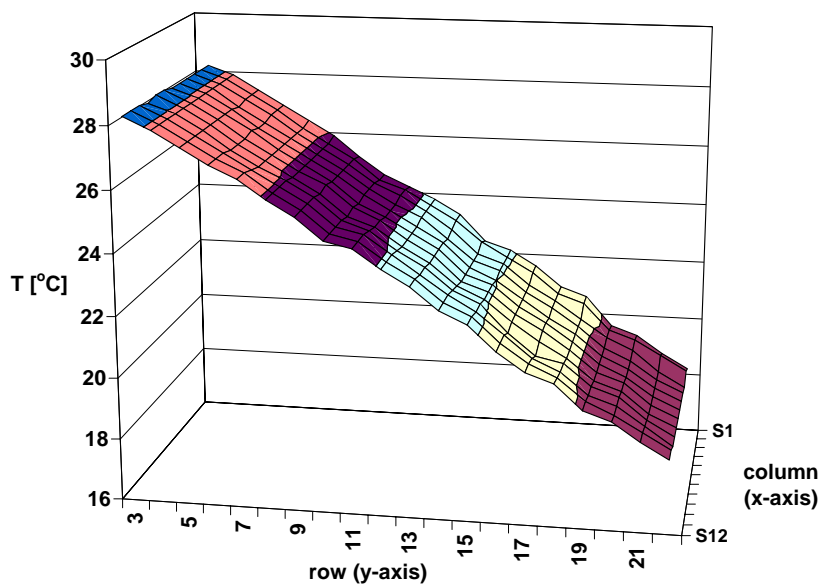


Figure 4-5. Temperature gradient profile measured within 240 wells of the 384-well plate

In Figure 4-6 the average temperature together with the standard deviation of each column of wells (along the *x*-axis) is plotted as a function of well position (*y*-axis). The plot indicates a linear temperature distribution along the *y*-axis, confirming expectations from the calculations of temperature that preceded the design of the thermal-gradient plate.
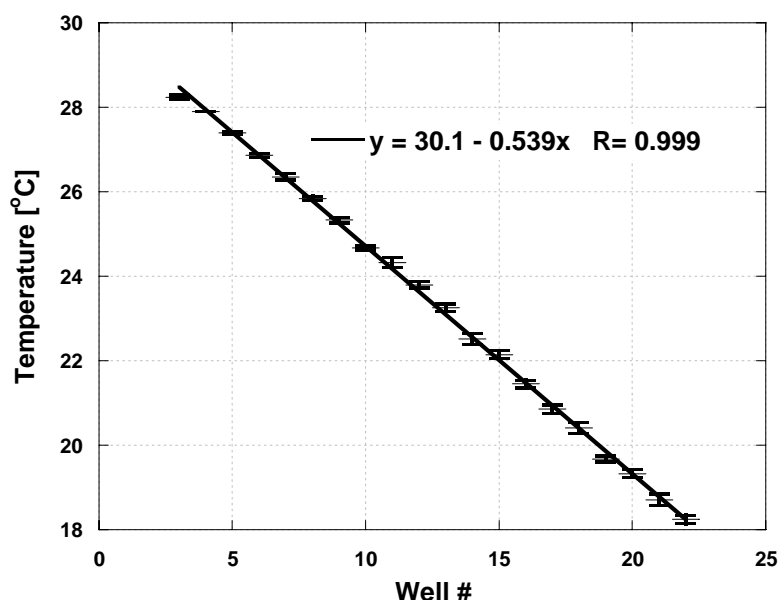


Figure 4-6. Linear temperature distribution of the 240 core wells of the 384-well plate and the standard deviation for each column (along *x*-axis, Figure 4-3)

### 4.4.2 Crystallization

The protein droplets submerged in paraffin oil (HR-311, Hampton Research) were consistently spherical, minimizing the surface-to-volume ratio. The paraffin oil furthermore greatly reduced the occurrence of heterogeneous crystallization (Galkin and Vekilov 2001) and assured that no significant water loss occurred from the drop that would change the solute concentration. In some rare instances, the protein droplet was

non-spherical, extending to the air interface of the well.  In such circumstances, that well was not accounted for since water evaporation was likely to take place, changing the crystallization outcome.

As mentioned above, an innovation of the device developed in the present work is the integrated image acquisition system.  In Figure 4-7, the timed image acquisition of lysozyme crystals within the same well over an extended period of time is shown.  One can clearly observe the crystal growth with the evolution of time that can lead to the determination of crystal growth kinetic data.  The implemented image software from Image-Pro allows for easy image size determination.
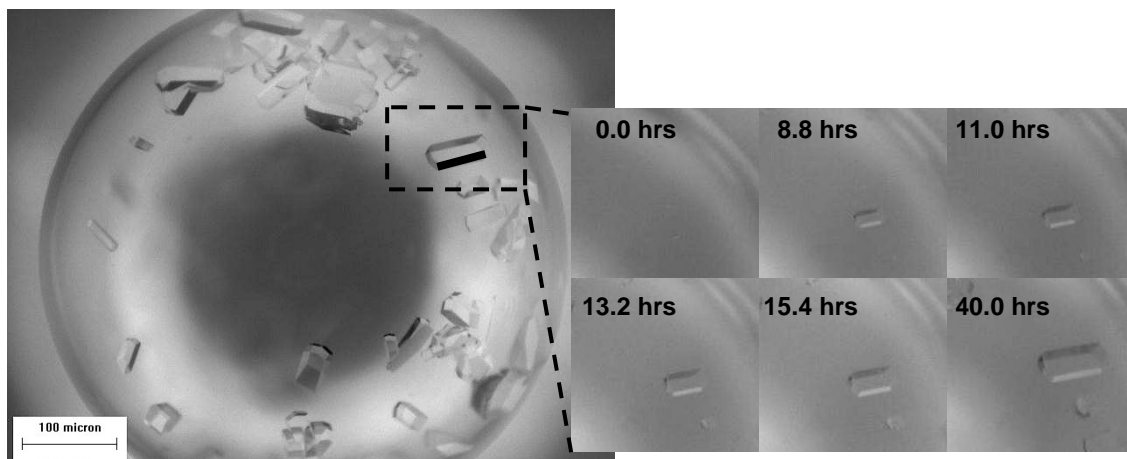


Figure 4-7.  Timed lysozyme crystallization in high-throughput apparatus (Conditions: 20 °C; pH 4.4; 48 mg/mL; 100 mM Na-acetate buffer; 3% NaCl); The framed crystal is tracked for crystal growth kinetics depicted in Figure 4-8.

In Figure 4-8 the growth of a particular crystal, assessed by the length of one of its edges (black bar next to the boxed-in crystal at the bottom, right hand image in Figure 4-7) is shown as an example.  The crystal edge measured showed an almost linear growth

rate initially and flattened out as the system approached equilibrium and the driving force

for crystallization decreased.
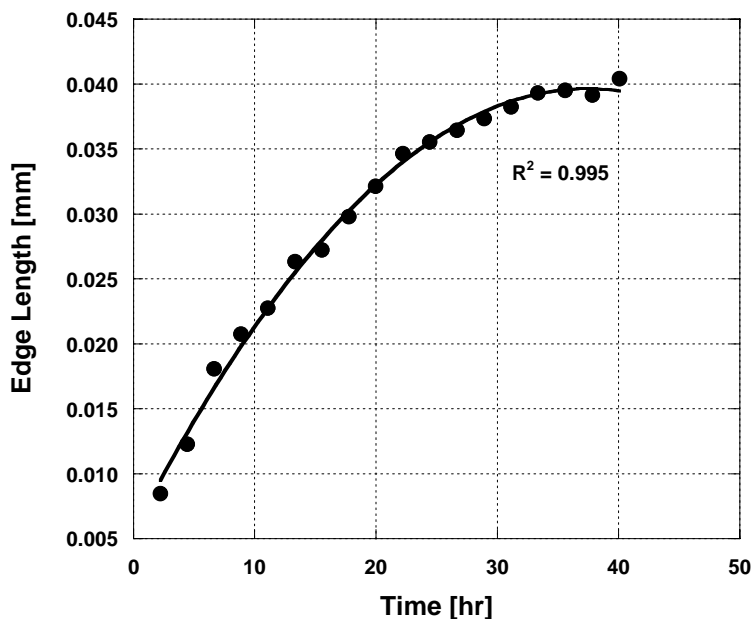


Figure 4-8. Crystal growth kinetics. The black line is a polynomial fit of the data. Here, edge length refers to the bottom edge of the crystal in Figure 4-7

A significant experimental observation was the continuity with which lysozyme

crystallized from the lowest temperature up to a certain temperature for each pH and

NaCl concentration examined. This is an important outcome since it indicates that the

crystallization is strongly affected by temperature in a non-random fashion. Lysozyme

has a positive temperature-solubility correlation; that is, the solubility increases with

increasing temperature, so that the lower temperatures should favor crystallization over

higher temperatures. After 96 hours in the initial run involving NaCl concentrations of

1% (w/v), 2% (w/v) and 3% (w/v), lysozyme crystallization only occurred in the 3% (w/v) NaCl solutions at each pH value (Table 4-1).

Table 4-1. Lysozyme crystal occurrence after 96 h as indicated by the grey bars. The temperatures indicated represent the actual well temperatures.

| | pH = 4 | | | pH = 4.4 | | | pH = 4.8 | | | pH = 5.2 | | |
|---|---|---|---|---|---|---|---|---|---|---|---|---|
| T [°C] | 3% NaCl | 2% NaCl | 1% NaCl | 3% NaCl | 2% NaCl | 1% NaCl | 3% NaCl | 2% NaCl | 1% NaCl | 3% NaCl | 2% NaCl | 1% NaCl |
| 30.0 | | | | | | | | | | | | |
| 29.5 | | | | | | | | | | | | |
| 28.9 | | | | | | | | | | | | |
| 28.4 | | | | | | | | | | | | |
| 27.9 | | | | | | | | | | | | |
| 27.4 | | | | | | | | | | | | |
| 26.8 | | | | | | | | | | | | |
| 26.3 | | | | | | | | | | | | |
| 25.8 | | | | | | | | | | ▓ | | |
| 25.3 | | | | ▓ | | | | | | ▓ | | |
| 24.7 | | | | ▓ | | | | | | ▓ | | |
| 24.2 | ▓ | | | ▓ | | | ▓ | | | ▓ | | |
| 23.7 | ▓ | | | ▓ | | | ▓ | | | ▓ | | |
| 23.2 | ▓ | | | ▓ | | | ▓ | | | ▓ | | |
| 22.6 | ▓ | | | ▓ | | | ▓ | | | ▓ | | |
| 22.1 | ▓ | | | ▓ | | | ▓ | | | ▓ | | |
| 21.6 | ▓ | | | ▓ | | | ▓ | | | ▓ | | |
| 21.1 | ▓ | | | ▓ | | | ▓ | | | ▓ | | |
| 20.5 | ▓ | | | ▓ | | | ▓ | | | ▓ | | |
| 20.0 | ▓ | | | ▓ | | | ▓ | | | ▓ | | |
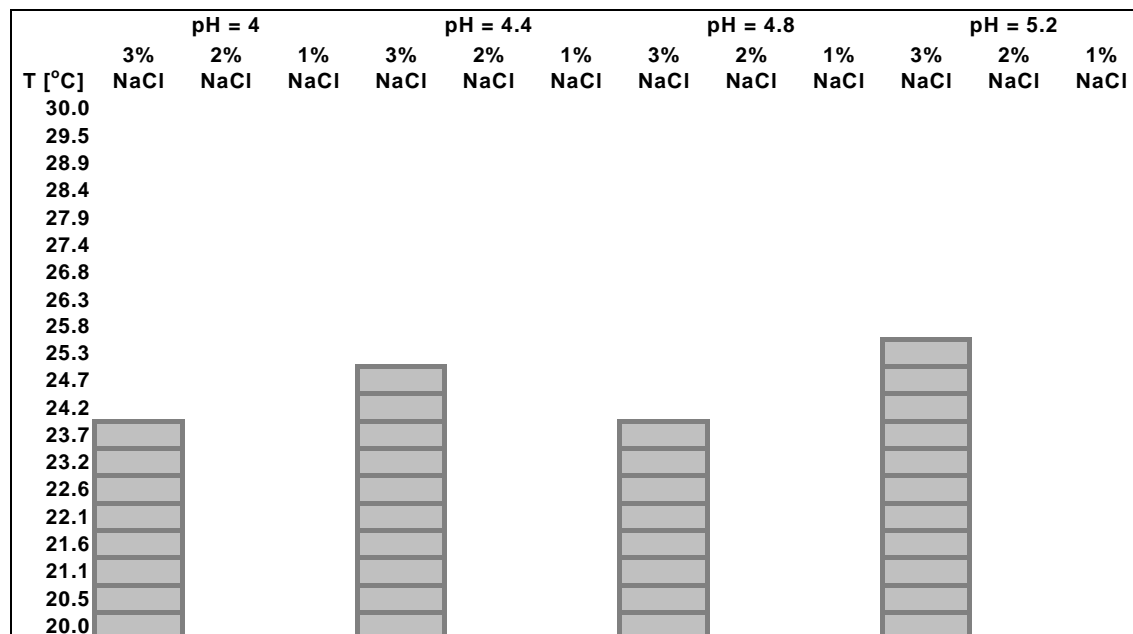
The crystals that appeared after 96 hours had different habits depending on the well temperature. In Figure 4-9, differences in the crystal habits can be observed as the temperature and solution conditions varied. Typical tetragonal crystals appeared at lower temperatures (Figure 4-9B), but these seemed to transform into rod-like crystals at higher temperatures (Figure 4-9A). At a higher pH value the tetragonal single crystals and composite crystals (Figure 4-9H) (Jones et al. 2001) transformed into rod-like crystals as well (Figure 4-9C) with a similar change in temperature.
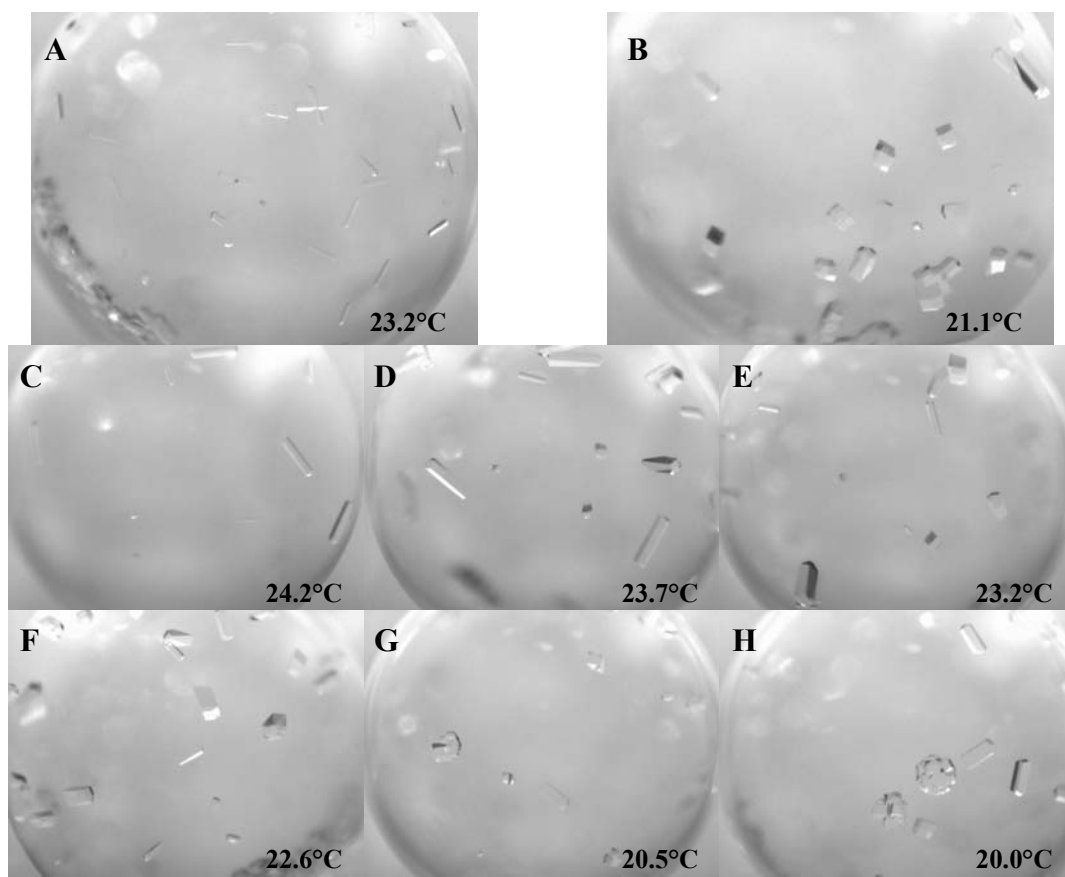
Figure 4-9.  Lysozyme crystals at 3% NaCl after 96 hours: A, B: pH 4.0; C–H: pH 4.4

The change in the crystal habit from the lower temperature to the higher temperature (Figure 4-9C through Figure 4-9H) can be explained by the increasing temperature approaching the transition temperature for lysozyme, where lysozyme crystals change from tetragonal to orthorhombic (Jolles and Berthou 1972).

## 4.5 Conclusions

A microbatch crystallization apparatus has been introduced that enables (1) multiple batch crystallization experiments at various temperatures and solution conditions in parallel and (2) quantitative monitoring of crystal growth without disturbing the progress of an experiment for observation. The primary application of the apparatus is, but not limited to, screening of protein crystallization conditions, although the system can also be used for other macromolecular and small-molecule crystallization experiments. The general design integrates microplates with a standard 96-well footprint that can be extended to vapor-diffusion crystallization experiments by using high-throughput crystallization plates such as CrystalClear Strips, 384-well Corning® CrystalEX™ microplates, or CrystalQuick 96-well Low Profile Plates (source: Hampton Research, www.hamptonresearch.com).

The behavior and performance of the system was demonstrated by simple temperature measurements to determine the stability and linearity of the temperature gradient. Furthermore, an initial set of crystallization experiments with a model protein (lysozyme) was used to demonstrate the effect of temperature on crystallization and to show the ability of the system to track crystal growth over a long run time. More experiments will be required in order to validate the general application of this apparatus.

The high-throughput crystallization apparatus presented in this paper has been constructed from readily available equipment. Microscopes are standard components of a crystallization lab, and many of them are equipped with digital imaging capabilities. The box enclosing the automated stage of the microscope is self-made using Plexiglas, but are also commercially readily available (e.g. Solent Scientific, Portsmouth, UK). Both the

thermal-gradient and the insulation plates can be machined easily due to their simple geometry. The use of readily available well plates makes complicated and time-consuming cleaning procedures obsolete. The new plate can be prepared (that is, filled with paraffin oil) ahead of time so that switching to a new experiment is rapid and it does not jeopardize the experimental outcome by possible protein contaminants from previous tests.

## 4.6 Acknowledgements

# CHAPTER 5

# DEPENDENCE OF APOFERRITIN CRYSTAL GROWTH ON TEMPERATURE AND CADMIUM CONCENTRATION

## 5.1 Abstract

Static light scattering and multiwell microbatch crystallization experiments have been used to determine how apoferritin crystal growth kinetics and final crystal size depend on temperature, pH, and cadmium concentration. The experiments were conducted on a thermal gradient covering a range from 30 °C to 40 °C. Crystal growth was monitored in situ under a microscope without disturbing the thermal environment. A dependence of apoferritin crystal formation and growth on pH was observed, which relates to the varying metal-binding capacities of apoferritin at different pH values. At pH 7.4, the range of cadmium concentrations that resulted in apoferritin crystal growth was evaluated and found to be consistent with the second virial coefficients determined via static light scattering. For the domain of conditions where apoferritin crystal formation occurred, the initial molar growth rate of apoferritin crystals increased linearly with temperature. It was observed that increasing cadmium concentration decreased the dependence of the final crystal size on temperature. The measured dependence of growth kinetics on temperature allowed the estimation of activation energy for crystal growth. By comparing the value of this activation energy with that for nucleation (obtained from the literature), it became possible to explain the observation of larger, but fewer,

apoferritin crystals at higher temperatures, which has also been reported in the literature for other proteins.

## 5.2 Introduction

Protein crystallography currently is the most important and often-used method for protein structure determination. Other methods, such as NMR spectroscopy, are limited to proteins with a molecular mass of up to 30 kDa, and therefore only a small number of protein structures have been obtained by this method (Berman et al. 2000; Vekilov and Chernov 2002). A requirement of protein crystallography is the availability of crystals of adequate size and quality. Growing such crystals can be a difficult task, at least for some proteins. Protein crystallization is furthermore significant in biomedical applications, where it appears to be involved in the development and manifestation of certain human diseases.

Crystal quality is determined primarily by the kinetics of nucleation and growth, and protein crystals are no exception. Both of these kinetic phenomena can be manipulated chemically and physically. The addition of precipitants in the form of salts is the most often used chemical manipulation to foster protein crystallization (Gilliland et al. 1994; McPherson 1999; Gilliland et al. 2002). Initially, at zero ionic strength, the addition of small amounts of salt is required to increase the solubility of proteins in aqueous solutions, which is called salting in. This effect seems to occur because ions of a dissolved salt bind directly to protein molecules and thereby increase their net charge. Since proteins only crystallize as net neutral species the addition of salt increases the

amount of protein molecules with a net charge present in solution and therefore the overall solubility of the protein (Collins 2004).

An increase in salt concentration eventually leads to a decline in protein solubility, which is referred to as salting out. Here the effect is indirect: primarily, anions disrupt the hydration layer on both polar and nonpolar surfaces of the protein molecule. This encourages the protein to minimize its solvent-accessible surface area by forming clusters and aggregates, which are precursors for protein crystals (McPherson 1999).

Crystallization of ferritin and apoferritin in the presence of cadmium is of special interest due to the biochemical significance and physiologic relevance of this system. Ferritin, an iron-storage protein omnipresent among living species, is an important molecule in iron homeostasis (Lawson et al. 1991; Harrison and Arosio 1996). Apoferritin is the iron-free counterpart of ferritin; both are 24mers, which means that the protein is assembled of 24 subunits that together make the functional protein. There are two types of subunits, the L (light chain) and H (heavy chain) subunits, which are the building blocks of apoferritin (Brooks et al. 2002). Cadmium ion is a common precipitant in ferritin and apoferritin crystallization (Michaelis 1947), as its large coordination numbers enable the development of cadmium bridges for intermolecular contacts (Trakhanov and Quiocho 1995; Trakhanov et al. 1998). Notably, cadmium levels are elevated in protein condensation diseases possibly interfering with protein solubility (Racz and Erdohelyi 1988; Harding 1995; Cekic 1998; Cekic 1998).

Divalent cadmium has been used as a precipitate in protein crystallization in only 7 out of the 5018 cases reported in the Biological Macromolecule Crystallization

Database and the NASA Archive for Protein Crystal Growth Data. Three of the 7 uses of divalent cadmium involved the crystallization of ferritin/apoferritin, while the other cases involved retinol binding protein, ribosome, and β-lactoglobulin. The most often used precipitates for protein crystallization are ammonium sulfate, with about 10% of all cases reported, and sodium chloride, with about 5% (see Figure 2-18) (Gilliland et al. 1994; Gilliland et al. 2002).

Cadmium ions that are added to the protein solution interact with specific side groups on the ferritin and apoferritin surface. Cadmium resides at the interface between protein molecules in the crystal and bridges pairs of otherwise repulsive carboxyl groups of opposing aspartate and glutamine side chains (Lawson et al. 1991). The highly ordered placement of the cadmium ions makes them visible on electron density maps in protein crystallography.

Temperature is an example of a physical parameter that influences protein crystallization. It can have significant effects on both the thermodynamics of protein solutions and the kinetics by which crystals are nucleated and grown from solution. In general, the solubility of proteins is a strong function of temperature; the temperature-dependence of the solubility of many proteins may change by about 10% per degree Kelvin (Berg et al. 2002). However, in some cases solubility is less dependent on temperature. For example, the effect of temperature on lysozyme solubility has been reported to decrease significantly in the presence of high precipitant concentrations (Howard et al. 1988; Rosenberger and Meehan 1988).

In cases where temperature may not seem pertinent in determining whether or not crystals can be obtained (i.e., the influence of temperature on solubility is weak), it

nevertheless can have a major impact on the rate at which such crystals are formed and on the final quality of the crystals as determined by crystal habit, size and purity (Judge et al. 1999; McPherson 1999). Necessarily then, good control of temperature is a prerequisite for reproducible crystallization experiments. While temperature can be controlled to relatively high levels of precision and there are many mechanisms for both regulating and monitoring temperature, it is not often used as a variable in protein crystallization (Gilliland et al. 2002; Bartling et al. 2005). Commonly used temperature ranges of $0 - 4$ °C and $20 - 24$ °C for protein crystallization are convenient since they can be easily controlled by placing the crystallization experiments in a refrigerator or by leaving them at ambient laboratory conditions, respectively (Bartling et al. 2005). In these places, however, temperature often fluctuates in an uncontrolled fashion because they are usually not dedicated solely to crystallization experiments (Lorber and Giege 1992).

The above-mentioned physical and chemical determinants influence protein solubility, which depends on short-range protein-protein interactions in the crystalline state where there are restricted orientations of the molecules. Another parameter that is determined by the protein-protein interactions in solution is the mean-force potential, which provides a measure of the dilute protein–protein interactions that are Boltzmann–averaged over all distances and orientations in the liquid phase (Haas et al. 1999; Curtis et al. 2001). Since the readily measured second virial coefficient, $B$, is related to the mean-force potential through equilibrium solution theory, its evaluation can give a qualitative measure of the protein–protein interactions in a dilute solution (George and Wilson 1994). Positive $B$ values generally indicate larger protein–solvent

interactions compared to protein–protein interactions, i.e., the net protein intermolecular forces are repulsive; on the other hand, negative values of $B$ imply overall attractive forces between the protein molecules in solution. Therefore, $B$ has a predictive character regarding protein crystallization and/or precipitation from solution. In fact, it appears that there is a region of $B$ values, called the crystallization window, where crystallization is favored. Values outside this region do not appear to favor crystallization ($B > 0$) or lead to precipitation of amorphous protein ($B << 0$) (George and Wilson 1994). Static light scattering (SLS) has been used to obtain information leading to estimation of the second virial coefficient of lysozyme and chymotrypsinogen, and for mapping the space where intermolecular interactions indicate feasible crystallization regions (Velev et al. 1998).

The present study investigated the influence of cadmium concentration (a chemical parameter) and temperature (a physical parameter) on the crystallization of apoferritin. The influence of these variables on apoferritin crystallization kinetics and final crystal size were evaluated simultaneously. A multiwell microbatch crystallization device controlled the crystallization temperature and provided a thermal gradient with small temperature increments along the gradient (Bartling et al. 2005). The setup allowed testing of a 2-dimensional matrix of crystallization conditions involving temperature and cadmium concentration; apoferritin crystal growth was monitored inline at defined time intervals. The second virial coefficient was measured for certain protein solutions and correlated to the crystallization outcomes.

## 5.3 Materials

Horse spleen apoferritin in 150 mM NaCl solution was purchased from Sigma Chemical Co. (St. Louis, MO).    All buffer solutions used in the experiments were prepared with ultra-pure water (Water Pro PS, Labconco) that was passed through a 0.22-μm filter and degassed prior to usage.

## 5.4 Methods

### 5.4.1 Size Exclusion Chromatography (SEC)

Prior to crystallization experiments the protein solution was purified by preparative size exclusion chromatography (HiPrep 16/60 Sephacryl S-300 High Resolution, Amersham Biosciences) to remove apoferritin oligomers and other impurities that can interfere with crystal nucleation and growth (Judge et al. 1998; Thomas et al. 1998; Judge et al. 1999).  Post purification, the protein solution was concentrated and further diafiltered with centrifugation filtration devices (Centricon YM30, Millipore). The purity of the final apoferritin solution was assessed by analytical size exclusion chromatography (Bio-Sil SEC-400-5 column, BioRad) on a Shimadzu HPLC system, which allowed the apoferritin oligomer and monomer peaks to be well separated and the peak areas to be quantified accurately.  The preparative SEC-HPLC protocol can be found in Appendix B.2 together with the protocol for concentrating protein solutions.

The long-term stability of the apoferritin solution with respect to apoferritin oligomer formation was measured by analytical SEC-HPLC.  Protein solutions were incubated at 4 °C and 37 °C over several days.  Samples were withdrawn periodically and

analyzed for oligomer content by analytical SEC-HPLC. Apoferritin concentrations were determined by a Coomassie protein assay kit (Pierce Biotechnology, Inc.). This method was preferred due to the 20-fold higher sensitivity relative to the absorptive measurement at 280 nm.

### 5.4.2 Static Light Scattering (SLS)

Static light scattering experiments were conducted on a DAWN QELS system (Wyatt Technology Corporation). Protein solutions were diluted with standard buffer and mixed with the crystallization buffer right before data acquisition. To minimize the sample volume a quasi-batch set up was used for the SLS experiments; the final mixture was injected into the flow cell of the SLS equipment via a syringe pump. When the light scattering had reached a steady value the flow was stopped and data acquisition was started.

The second virial coefficients for the protein solutions were measured at room temperature. While these measurements may not precisely reflect the virial coefficients at the higher crystallization temperatures used in this study, they nevertheless provide guidance regarding crystallization feasibility (Petsev et al. 2001).

### 5.4.3 Multiwell Microbatch Crystallization on a Thermal Gradient

Two sets of crystallization experiments were conducted. In the first (Experiment A at low pH), apoferritin was crystallized from solutions having an initial concentration of 1.0 mg/mL and at pH 5.0. These conditions are similar to those previously reported in the literature (Petsev et al. 2001). Thus, the goal of the first experiment was to extend the

established crystallization protocols for apoferritin to conditions of varying temperatures by using the temperature gradient plate. In the second experiment (Experiment B at high pH), the initial apoferritin concentration was 8.0 mg/mL and the pH was increased to 7.4 to examine apoferritin crystallization under physiologically relevant pH conditions. The buffer systems used for both crystallization experiments are listed in Table 5-1.

Table 5-1. Crystallization conditions

| Crystallization Experiments | A | B |
|---|---|---|
| Apoferritin [mg/mL] | 1.0 | 8.0 |
| Standard Buffer | 50 mM Na-acetate<br>150 mM NaCl<br>10 mM $NaN_3$ (preservative) | 50 mM Tris-HCl<br>150 mM NaCl<br>10 mM $NaN_3$ (preservative) |
| Crystallization Buffer | Standard Buffer +<br>70 mM $CdCl_2$ | Standard Buffer +<br>70 mM $CdCl_2$ |
| pH | 5.0 | 7.4 |

Two different buffer systems, Na-acetate and Tris-HCl, were used to establish the low- and high-pH values in Experiments A and B, respectively. Besides mimicking a physiological environment with respect to the blood plasma levels, the addition of 150 mM NaCl increased attractive forces between apoferritin molecules in solution in the absence of cadmium (Petsev and Vekilov 2000). Although unproven, the addition of this quantity of NaCl may have masked the effect that the different buffer ions could have on apoferritin crystallization.

The crystallization conditions were chosen to ensure that there was sufficient cadmium for apoferritin crystallization to occur. Since 72 mol of cadmium are bound to 1 mol of apoferritin in the crystal structure (Granier et al. 1997), 1.26 mM cadmium is the theoretical minimum concentration needed to load fully the 8 mg/mL (0.0175 mM)

apoferritin. In Experiment A the cadmium concentration was varied from 0 to 55 mM, while in Experiment B it was varied from 0 to 25 mM.

Crystallizations in both experiments were carried out under oil in small-scale batch mode on low-profile 384 microwell plates (Nunc, cat# 264340). A microbatch crystallization apparatus, the details of which were given earlier (Bartling et al. 2005), enabled (1) parallel batch crystallization experiments at various temperatures and solution conditions and (2) quantitative monitoring of crystal growth without disturbing the progress of an experiment for observation. The microwell plates consisted of 24 columns (y-axis) and 16 rows (x-axis). Temperature was varied along the y-axis by placing the 384−well plate onto a thermal-gradient plate. The outer two rows and columns were not used so as to eliminate edge effects with respect to temperature. This left 20 wells along the temperature gradient and 12 wells perpendicular to the temperature gradient, a total of 240 wells per plate for experiments. The crystallization screen for both sets of experiments is shown in Table 5-2.

Before the microwell plates were used, they were cleaned with ultra-pure compressed air (Fisher Scientific) to remove dust particles. The microwells were charged by first adding 8 µL of paraffin oil (HR3-411, Hampton Research) into each well with an Eppendorf micropipette. Stock protein solutions were mixed with the standard and crystallization buffers to obtain solutions containing apoferritin and cadmium concentrations given in Table 1. The mixing was performed by transferring the protein stock solution to a centrifuge tube, with the tube being mildly vortexed while adding the standard and/or the crystallization buffers (Rayment 2002). This was done to reduce local cadmium concentration peaks that could have led to instantaneous protein

precipitation.  Then, a small droplet (4 µL) of the freshly prepared protein solution was pipetted directly beneath the paraffin oil surface in each well so as to minimize the contact time with the surrounding air.  Each row of wells along the y-axis was used for one of the solution conditions.  The water baths were set to achieve a thermal gradient of 30 °C to 40 °C along the y-axis.  The number and location of the wells used for each experiment were specified in the Scope-Pro software (MediaCybernetics) and the image acquisition was started by initiating a program macro.  Pictures of each well were taken in 2-hour intervals.

Table 5-2.  2D-crystallization screen.  A, Conditions: 1 mg/mL apoferritin, 50 mM Na-acetate, pH 5.0, 150 mM NaCl, 10 mM NaN3.  B, Conditions: 8 mg/mL apoferritin, 50 mM Tris-HCl, pH 7.4, 150 mM NaCl, 10 mM NaN3.  The temperature increments are equal in size: the unequal representation is due to rounding. The A and B experiments were each run with the plate at the conditions shown.

| Cadmium A [mM] | B [mM] | 30.0 | 30.5 | 31.1 | 31.6 | 32.1 | 32.6 | 33.2 | 33.7 | 34.2 | 34.7 | 35.3 | 35.8 | 36.3 | 36.8 | 37.4 | 37.9 | 38.4 | 38.9 | 39.5 | 40.0 |
|---|---|---|---|---|---|---|---|---|---|---|---|---|---|---|---|---|---|---|---|---|---|
| 0 | 0 | O | O | O | O | O | O | O | O | O | O | O | O | O | O | O | O | O | O | O | O |
| 11 | 5 | O | O | O | O | O | O | O | O | O | O | O | O | O | O | O | O | O | O | O | O |
| 22 | 10 | O | O | O | O | O | O | O | O | O | O | O | O | O | O | O | O | O | O | O | O |
| 33 | 15 | O | O | O | O | O | O | O | O | O | O | O | O | O | O | O | O | O | O | O | O |
| 44 | 20 | O | O | O | O | O | O | O | O | O | O | O | O | O | O | O | O | O | O | O | O |
| 55 | 25 | O | O | O | O | O | O | O | O | O | O | O | O | O | O | O | O | O | O | O | O |

### 5.4.4 Apoferritin Crystal Measurement

All apoferritin crystals exhibited the octahedral shape shown schematically in Figure 5-1.  Crystal growth kinetics were obtained by measuring changes in the maximum lengths of the crystals; the alternative of following the development of a

specific edge length was not chosen because of the uncertainty of repetitively identifying the same edge.
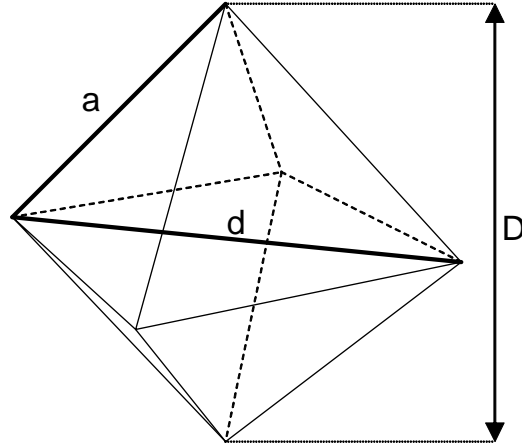


Figure 5-1.  Schematic of a cubic octahedral apoferritin crystal ($d$: square base diagonal, $D$: diagonal)

The maximum length of a cubic octahedron is the diagonal $D$ as shown in Figure 5-1. If the edge length is $a$, then the volume $V$ is twice the volume of a square-base pyramid; i.e.,

$$V = 2\left(\frac{1}{3}a^2 R\right)$$   (5.1)

where $R$ is the circumradius or ½$D$. It can then be shown that

$$V = \frac{1}{6}D^3$$   (5.2)

Equation (5.2) shows that the volume of a cubic octahedral crystal scales with the cube of its maximum length.

## 5.5 Results

Purification of the as-received apoferritin solution successfully removed apoferritin oligomers and subunits. Preparative size-exclusion chromatography increased the apoferritin monomer purity from 67.5% of the sum of all peaks produced to 95.7%, and the oligomer content was reduced in the same step from 7.9% to 4.3%. The analytical size exclusion chromatograms of the as-received apoferritin solution (Figure B-15), the oligomer (Figure B-16), monomer (Figure B-17) and subunit fractions (Figure B-18) of the preparative SEC-HPLC can be found in Appendix B.2.4. Incubation of the purified apoferritin solutions in the standard buffer at either 4 ºC and 37 ºC resulted in no increase in the oligomer content over an extended period of time (>3 days) (see Figure B-19, Figure B-20 and Figure B-21 in Appendix B.3). Furthermore, there were no apoferritin subunits detectable for both incubation temperatures over the same time period. The composition of the apoferritin solution was therefore declared stable in terms of oligomer and subunit composition for the time period of the crystallization experiments (70 hours). Hence, the crystallization results reported below were not influenced by a change in solution composition with time.

In the low-pH experiments (Experiment A), apoferritin crystals were obtained only when the $CdCl_2$ concentration was 33 mM or greater; no crystals appeared in the presence of lower cadmium concentrations or in the absence of cadmium. At the productive concentrations of $CdCl_2$, apoferritin crystals emerged over the entire range of temperatures covered by the thermal gradient, which is important because it indicates non-random crystallization events. Due to resolution limitations of the light microscope that was used for crystal growth measurements, the size of the apoferritin crystals

produced at the initial concentration of 1 mg/mL (experiment A) was inadequate for determination of crystal growth kinetics.

In Experiment B, the apoferritin concentration was elevated to 8 mg/mL so as to produce crystals of sufficient size for growth-rate analysis. The pH was set to 7.4 to evaluate the influence of the pH on the metal ion-binding capacity of apoferritin and therefore on its crystallization behavior. Apoferritin and ferritin are metal-storage proteins and, besides binding iron, both molecules can also take up and store other divalent metal ions (Price and Joshi 1983; Huang et al. 2000; Ueno et al. 2004). The storage capacity for metal ions in apoferritin molecules has been found to be pH-dependent; at a neutral pH the storage capacity is much higher compared to a more acidic solution. In the case of cadmium, the storage capacity had been reported to decrease from 54 moles $Cd^{2+}$/mol apoferritin at pH 7.5 to 3 moles $Cd^{2+}$/mol apoferritin at pH 5.5 (Pead et al. 1995).

In the high-pH experiments the solutions containing 0 mM, 5 mM and 10 mM $CdCl_2$ did not result in apoferritin crystallization and the solutions remained clear and translucent. Solutions containing 15 mM, 20 mM and 25 mM $CdCl_2$ resulted in apoferritin crystallization over the entire range of temperatures tested. Furthermore, the fact that there was no transition from non-crystallization to crystallization outcomes at any cadmium concentration along the thermal gradient indicated that temperature had little or no impact on the occurrence of apoferritin crystallization.

In an initial evaluation of the capacity of the second virial coefficient to predict the crystallization or precipitation outcome, this coefficient was measured by static light scattering in solutions that did not form crystals or exhibited a strong tendency for the

protein to precipitate out of solution. Specifically, solutions of pH 7.4 containing 0 mM

and 10 mM $CdCl_2$, which did not form crystals, had a positive second virial coefficient,

indicating that the protein-protein interactions were not favorable for crystallization. On

the other hand, a solution containing 40 mM $CdCl_2$, higher than the range of $CdCl_2$

concentrations used to form crystals, indicated a strongly negative second virial

coefficient: after the solution was added to the flow cell of the SLS equipment, no steady

reading could be obtained, suggesting immediate protein precipitation or micro-

crystallization. Combined, the SLS and crystallization experiments at pH 7.4 indicate

that apoferritin exhibits a crystallization window, as do other proteins (George and

Wilson 1994), and that values of $B$ can be used as a predictor for apoferritin

crystallization.

Although no effect of temperature on the formation of crystals was found in the

experiments of this study, temperature did have a significant effect on the kinetics of

crystal growth and the resulting crystal size for solutions containing 8 mg/mL apoferritin

and at pH 7.4. The diagonals of crystals measured in these experiments are plotted as a

function of time in Figure 5-2 through Figure 5-4. Although it is not possible to observe

the transition in size over time for the higher two cadmium concentrations, the data from

solutions whose cadmium concentration was 15 mM (Figure 5-2) show the transition

clearly. Moreover, the initial changes in size with time provide estimates of crystal

growth rates at each of the temperatures explored. At each of the temperatures, the linear

increases in crystal size reflect near-constant growth rates that eventually diminished as

the systems approached equilibrium and the driving force for crystallization decreased.
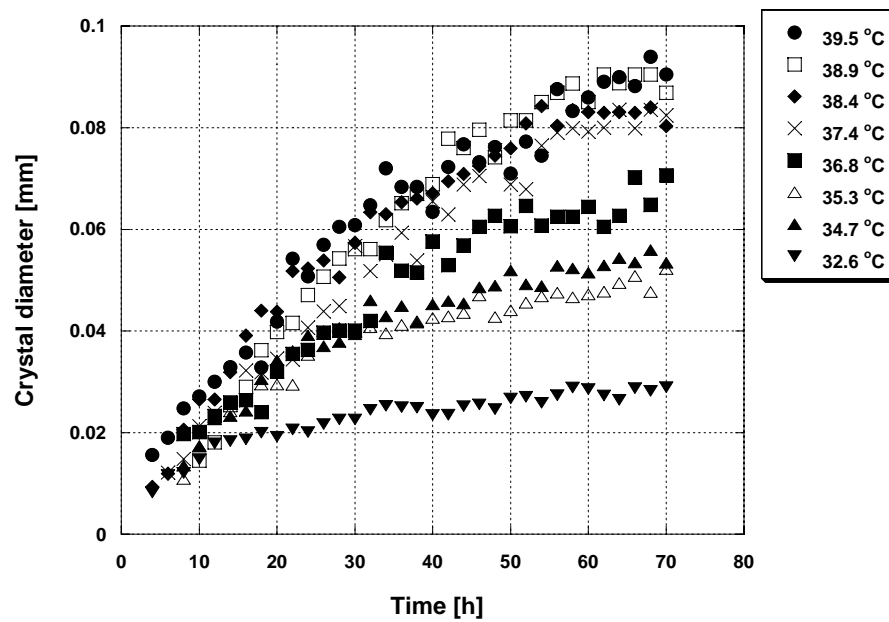
Figure 5-2.  Apoferritin crystal growth in the presence of 15 mM cadmium chloride
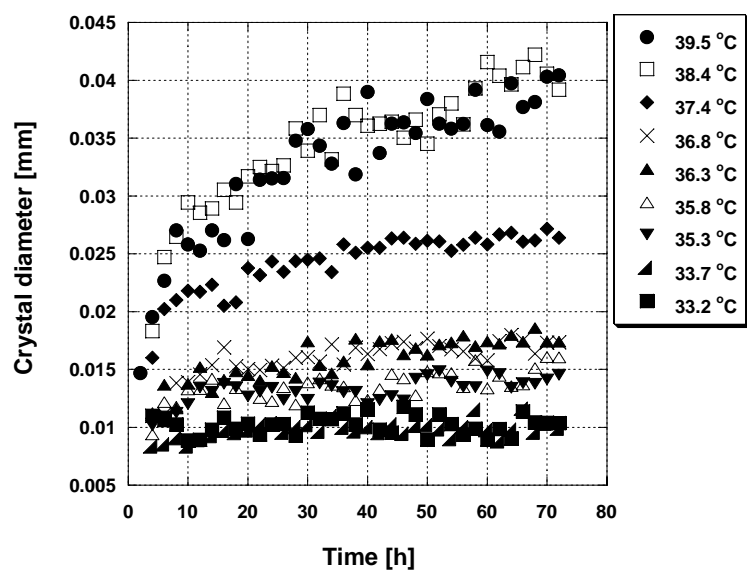


Figure 5-3. Apoferritin crystal growth in the presence of 20 mM cadmium chloride
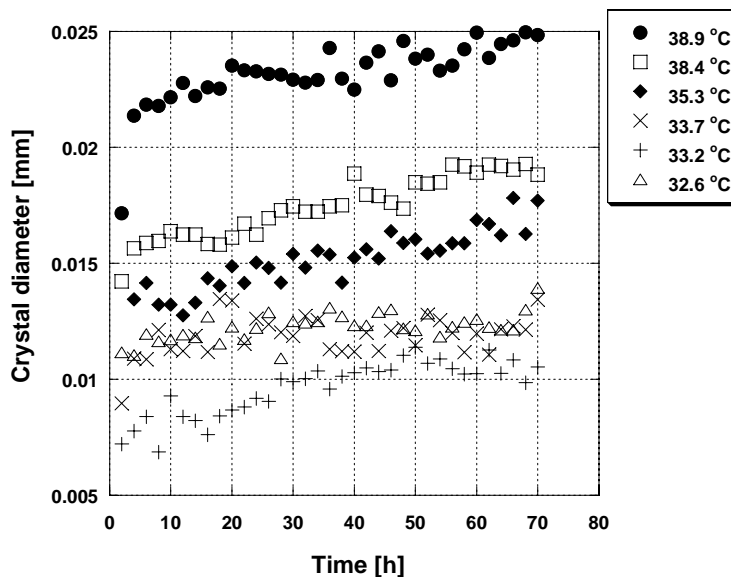
Figure 5-4. Apoferritin crystal growth in the presence of 25 mM cadmium chloride

It was impossible to estimate growth rates in the 20 mM and 25 mM cadmium chloride solutions because the initial growth period was completed prior to acquisition of the first images of the crystals (Figure 5-3 and Figure 5-4). It may be assumed that crystal growth rate is a direct function of cadmium concentration, but no distinction could be made between the 20 and 25 mM cadmium cases.

By averaging the final 3 crystal sizes for each of the data sets in Figure 5-2 through Figure 5-4 and plotting the resulting values as a function of temperature in Figure 5-5, it is apparent that the final apoferritin crystal size increased linearly with increasing temperature for all 3 cadmium concentrations used. The error bars in Figure 5-5 correspond to the spread among the 3 final crystal sizes. At the elevated temperatures of the 15 mM case, no error bars were drawn because only single crystals were found in the wells. Plotting the slopes of the fitted lines ($\Delta D/\Delta T$) in Figure 5-5 as a function of

cadmium concentration resulted in a perfectly linear relationship between these two variables (Figure 5-6).
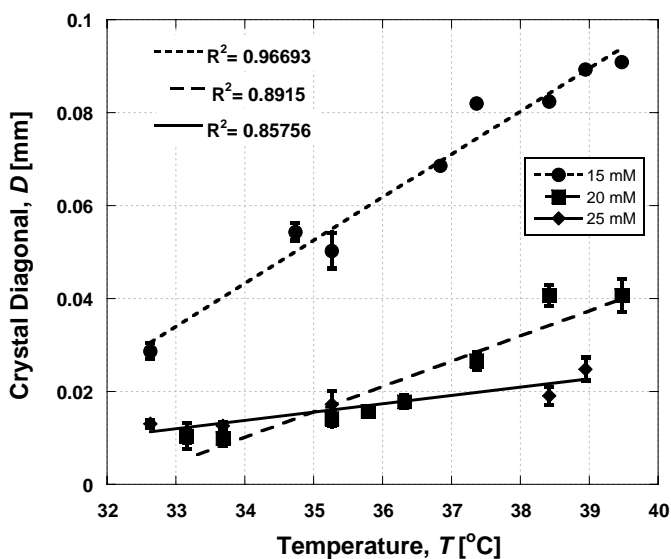


Figure 5-5. Final apoferritin crystal size as a function of temperature and cadmium chloride concentration

The results illustrated in Figure 5-5 show how the effects of temperature and cadmium concentration on crystal size are interrelated; as the cadmium concentration increased, the temperature dependency of the final crystal size ($\Delta D/\Delta T$) was less important, but at low cadmium concentrations the effects of temperature were quite pronounced. This outcome suggests that at sufficiently high cadmium concentrations the effect of temperature on the final crystal size totally vanishes. However, this observation needs to be balanced by the recognition that at still higher cadmium concentration precipitation occurs and the resulting solid is non-crystalline. Likewise, the cadmium concentration must of course be above that required to overcome the barrier to nucleation

associated with the metastable zone of the apoferritin phase diagram where no nucleation and hence no crystallization occur.
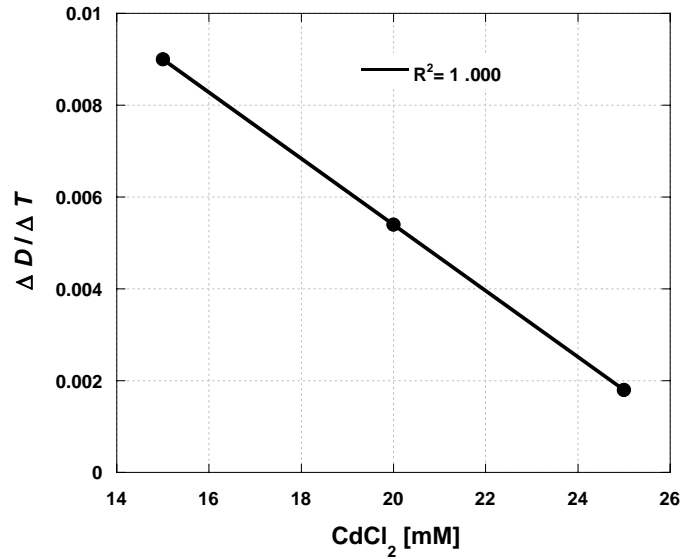


Figure 5-6. Slopes (ΔD/ΔT) of showing the dependence of final crystal size on temperature (from Figure 5-5)

To explore the effect of temperature on apoferritin crystal growth kinetics, assume that the crystal growth rate can be expressed as

$$r_G = k_G \sigma^i \tag{5.3}$$

where $k_G$ is a growth-rate constant and $\sigma$ is relative supersaturation. Accepting the assertion that apoferritin solubility is independent of $T$ (Petsev et al. 2001), then values of $\sigma$ are constant early in the growth process and growth rates vary only with temperature.

Now assuming that growth kinetics follow an Arrhenius dependence on temperature

$$k_{\mathrm{G}} = k_0 \exp\left(-\frac{\Delta E_{\mathrm{G}}}{RT}\right) \tag{5.4}$$

Alternatively, the expression can be written as

$$\frac{d\ln k}{dT} = \frac{\Delta E}{RT^2} \tag{5.5}$$

where $\Delta E_{\mathrm{G}}$ is the activation energy for crystal growth.

Equation (5.2) was used to convert from the size measurements in Figure 5-2 to corresponding crystal volumes. From the density of cubic apoferritin crystals (1.27 g/cm³) [(Gilliland et al. 2002)] and the apoferritin molecular weight (456 kD), the linear growth rates obtained from the initial slopes of the curves in Figure 5-2 were converted to molar growth rates [mol/hr] and plotted in Figure 5-7.
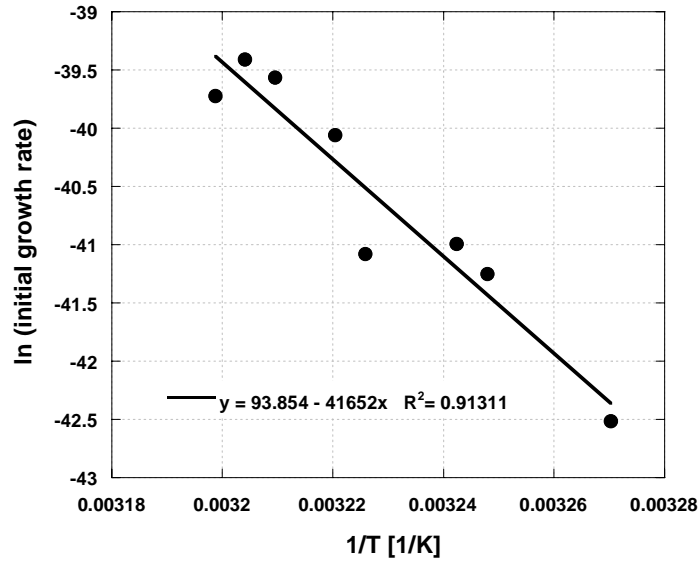


Figure 5-7. Arrhenius plot of the initial apoferritin crystal growth rate [mol/hr] (crystal growth within first 8 hours) in the presence of 15 mM cadmium chloride

The slope of the line in Figure 5-7 corresponds to an activation energy for apoferritin crystal growth of $\Delta E_G = 346$ kJ/mol. In a previous study the activation energy for apoferritin nucleation, $\Delta E_N$, was reported to be 33.5 kJ/mol (Malkin and McPherson 1993). Thus, the experimental data indicate a more than 10-fold difference in the two activation energies. This can be used to explain the formation of fewer and larger crystals at higher temperatures, as observed throughout the crystallization experiments of this study It may also explain similar phenomena that have been reported for lysozyme and thaumatin (Georgalis and Saenger 1993; Juarez-Martinez et al. 2001).

In order to eliminate the pre-exponential factors from the Arrhenius equations, the ratio of growth ($r_G$) -to-nucleation ($r_N$) rate was examined at the lowest ($T_L$, 32.5 °C) and highest ($T_H$, 39.5 °C) temperatures of this study. In particular, if the ratio

$$\frac{\left(\dfrac{r_G}{r_N}\right)_{39.5^{o}C}}{\left(\dfrac{r_G}{r_N}\right)_{32.5^{o}C}} \tag{5.6}$$

has a value greater than one, there is a larger increase of the rate of crystallization than the rate of nucleation with temperature, corresponding to fewer, larger crystals at the higher temperature. Using the above activation energies, this ratio is calculated to have a value of 15.7 for apoferritin, which is consistent with the experimental observation of increasing protein crystal size with temperature.

## 5.6 Conclusions

Multiwell microbatch experiments demonstrated the dependence of apoferritin crystal growth kinetics and final crystal size on temperature and cadmium concentration. Although the solubility of apoferritin might be independent of temperature, the results of this study show that the crystal growth kinetics *are* affected by temperature, profoundly under some conditions. Clearly, temperature control should be a prerequisite for study of apoferritin crystallization, which is in contrast to published studies where that has not been the case (Yau et al. 2000; Tsekova et al. 2002; Vekilov 2002; Vekilov and Chernov 2002; Vekilov et al. 2002).

In the present study the final crystal size increased with increasing temperature, although the relationship became weaker with increasing cadmium concentration. An analogous effect has been reported for the solubility of lysozyme: at increased precipitant concentrations the solubility became almost independent of temperature, but the solubility was a strong function of temperature at lower precipitant concentrations (Cacioppo and Pusey 1991; Bergeron et al. 2003). This suggests that there might indeed be solution conditions at which the apoferritin solubility becomes temperature sensitive.

The dependence of lysozyme solubility on pH has been reported earlier (Cacioppo and Pusey 1991), and the two pH values explored in the present study led to different crystallization results for apoferritin as well. While in the case of lysozyme there are non-specific interactions between protein and precipitant, the cadmium ions used for the apoferritin crystallization experiments are actually incorporated into the apoferritin crystal, making them detectable by x-ray diffraction. Apoferritin has a higher binding

116

capacity for cadmium at pH 7.5 than at pH 5.5 (Pead et al. 1995). This undoubtedly contributed to the observed difference in crystallization outcomes.

Crystallization experiments, coupled with static light-scattering measurements, provided further support for the use of the second virial coefficient as a predictor for favorable crystallization conditions. Indeed, the outcome of the present experiments supports earlier work on other proteins, not including apoferritin, where that relationship had been followed (George and Wilson 1994).

Experiments in which the growth of apoferritin crystals was monitored demonstrated a dependence of growth kinetics on temperature that would not have been observed had the sole focus been on crystal formation (nucleation). Analysis of the results found activation energies for growth and nucleation that differed by an order of magnitude: i.e., $\Delta E_G > 10\ \Delta E_N$. That can be used to explain the observation of an inverse relationship between crystal number and temperature. Clearly, the positive effects of temperature on nucleation are overshadowed by those on growth.

For inorganic materials, activation energies for crystal growth similar to the one reported here for apoferritin appear to be common (Kempen et al. 2002; Islam et al. 2003; Liu et al. 2004). Unfortunately, there exist only few papers that report the activation energies for both nucleation and crystal growth for the same system. In some cases, the activation energies for both processes were of the same magnitude (Kempen et al. 2002; Liu et al. 2004), whereas in another case the activation energies for nucleation and crystal growth differed by the same factor but inversely compared to the values for apoferritin crystallization[44]. Hence, the large difference in activation energies for apoferritin

nucleation and crystal growth indicated by the data of this study is plausible, but merits further exploration.

## 5.7 Acknowledgements

# CHAPTER 6

# APOFERRITIN SOLUTION THERMODYNAMICS

## 6.1 Abstract

Protein precipitation, liquid-liquid phase separation and protein crystallization are important in biotechnological applications such protein structure determination and protein purification. Furthermore, in biomedical applications protein aggregation and protein crystallization are involved in protein condensation diseases. Pathological phenomena such as sickle cell anemia, systemic and organ-specific amyloidosis and cataracts are representatives of protein condensation diseases. Cataracts are usually considered as a protein condensation disease associated with protein precipitation, not necessarily with protein crystallization. There are clues in lens physiology and biochemistry in normal as well as cataractous lenses that prompted us to investigate cataracts from the standpoint of protein crystallization.

We have focused on Hereditary Hyperferritinemia Cataract Syndrome (HHCS) as a model system. HHCS, which was first described fairly recently, is characterized by early onset of cataract formation. We have investigated the influence of temperature and divalent cations on crystal formation and hence can make predictions on cataract formation. Furthermore, possible treatment options with NDSBs (see Chapter 2.3.5) were investigated by measuring the apoferritin intermolecular interactions in the presence of these solubilizers.

## 6.2 Introduction

Protein crystallization is significant in both biotechnology and biomedical applications. In biotechnology, crystallization is essential for determining the structure of both native and synthesized therapeutically important proteins. It can also be used as a final purification step and as a stable form for protein storage. With regard to biomedical systems, protein crystallization appears to be involved in the development and manifestation of certain human diseases. An example of a molecular condensation disease in which proteins are involved is sickle cell anemia where mutated hemoglobin undergoes a phase transition causing a change in shape and rigidity of the red blood cells (Feeling-Taylor et al. 2004; Galkin and Vekilov 2004). There is also amyloidosis, which constitutes a large group of diseases where extracellular protein aggregation is a cause in Alzheimer disease, scrapie and bovine spongiform encephalopathy (Benedek 1997; Merlini and Bellotti 2003). Furthermore cataract formation is associated with protein condensation and in particular there exists evidence that L-rich ferritin crystals are involved in Hereditary Hyperferritinemia Cataract Syndrome (HHCS) (Brooks et al. 2002).

Many proteins have been successfully crystallized; however, identifying conditions appropriate for crystallization remains a mostly empirical task. This is also the case for biological solutions, where the potential of protein crystallization or precipitation to occur might offer insight into the potential for development of a disease and indicate whether pharmacological intervention would be useful. Previous work (George and Wilson 1994; George et al. 1997) has indicated that a single thermodynamic parameter of the solution, the second virial coefficient, may offer a quantitative measure

120

of a protein to come out of solution, irrespective of the path towards precipitation or crystallization, which may involve one or more of temperature, divalent cations and protein solubilizers.

L−ferritin crystallization or precipitation in the lens is involved in Hereditary Hyperferritinemia Cataract Syndrome (HHCS). In HHCS the ferritin level in the body is elevated but the protein only crystallizes in the lens. Being able to predict that protein crystallization or precipitation is about to occur, and to implement specific steps to inhibit this event, would help to understand the pathophysiology of HHCS and, importantly, propose specific pharmacological approaches for preventing the development of the disease. In this study, the second virial coefficient of apoferritin in the presence of various divalent cations and different temperatures was evaluated by static light scattering and these measurements were correlated with the crystallization or precipitation outcome obtained by batch crystallization under oil on a thermal gradient plate (Bartling et al. 2005).

The crystallization of apoferritin and ferritin *in vitro* is enhanced by the presence of divalent cations such as cadmium. With cadmium in particular, its use to promote crystallization of ferritin dates back to even before the advent of protein crystallography (Trakhanov et al. 1998). Historically, ferritin was distinguished from other proteins by the fact that it crystallizes out of solution by addition of cadmium sulfate (Michaelis 1947). However, other divalent cations were reported to be elevated in cataractous lenses (Lauring and Wergelan 1970; Vallee and Ulmer 1972; Post et al. 1984; Racz and Erdohelyi 1988; Erie et al. 2005) and therefore the crystallization and static light scattering experiments were also conducted in the presence of metal ions other than

cadmium to deduct their possible influence on protein-protein interactions in dilute or concentrated apoferritin solutions.

## 6.3 Materials

Horse spleen ferritin and apoferritin in 150 mM NaCl solution was purchased from Sigma Chemicals.  Human Spleen Ferritin and Human Liver Ferritin were purchased from Cortex Biochem (San Leandro, CA).  Slide-A-Lyzer Dialysis Cassettes (0.1-0.5 mL) were obtained from Pierce Biotechnology, Inc. (Rockford, IL).  NDSB 195 was purchased from Soltec Ventures, NDSB 201 and 256 were purchased from Calbiochem.  All buffer solutions used in the experiments were prepared with ultra-pure water (Water Pro PS, Labconco) that was passed through a 0.22-µm filter and degassed prior to usage.  The solutions used throughout the crystallization and static light scattering experiments were prepared in 150 mM NaCl to approximate physiological electrolyte concentrations.

## 6.4 Methods

### 6.4.1 Size Exclusion Chromatography (SEC)

Prior to crystallization experiments the protein solution was purified by preparative size exclusion chromatography (HiPrep 16/60 Sephacryl S-300 High Resolution, Amersham Biosciences) to remove apoferritin oligomers and other impurities that can interfere with crystal nucleation and growth (Judge et al. 1998; Thomas et al. 1998; Judge et al. 1999).  Post purification, the protein solution was concentrated and

further diafiltered with centrifugation filtration devices (Centricon YM30, Millipore). The purity of the final apoferritin solution was assessed by analytical size exclusion chromatography (Bio-Sil SEC-400-5 column, BioRad) on a Shimadzu HPLC system, which allowed the apoferritin oligomer and monomer peaks to be well separated and the peak areas to be quantified accurately. The preparative SEC-HPLC protocol can be found in Appendix B.2 together with the protocol for concentrating protein solutions.

The long-term stability of the apoferritin solution with respect to apoferritin oligomer formation was measured by analytical SEC-HPLC. Protein solutions were incubated at 4 °C and 37 °C over several days. Samples were withdrawn periodically and analyzed for oligomer content by analytical SEC-HPLC. Apoferritin concentrations were determined by a Coomassie protein assay kit (Pierce Biotechnology, Inc.). This method was preferred due to the 20-fold higher sensitivity relative to the UV absorption measurement at 280 nm (see Chapter 3.1.2).

### 6.4.2 De-Ironization of Ferritin

The human ferritin samples were transformed into their apoferritin analogs by removing the mineral core according to an established method (Wong et al. 1998). Thioglycolic acid (Sigma Chemicals) was used to reduce the ferric iron, which makes up the mineral core of ferritin proteins, to its soluble ferrous state. The human as-received protein solutions from liver and spleen (3.5 mg/mL and 4.1 mg/mL, respectively) were injected into the dialysis cassettes (molecular weight cut-off 10,000) and floated in sodium acetate buffer (50 mM, 600 mL, pH 4.5). Besides the human ferritin samples horse spleen ferritin was also used in the de-ironization experiment. According to Sigma,

horse spleen ferritin (cat# F-4503) is the starting material for their horse spleen apoferritin (cat# A-3641) which is used for all of the crystallization experiments.  The as-received horse spleen ferritin solution was diluted to 5 mg/mL with isotonic sodium chloride solution prior to the dialyzation step, to resemble a concentration that was similar to the human ferritin samples.  The de-ironization step is explained in more detail in Chapter 3.1.3.

The protein samples were dialyzed against 50 mM tris-buffer (pH 7.40) and transferred to sterile microcentrifuge tubes and stored at 4 °C.  Protein concentrations were determined by total protein assay (see Chapter 3.1.2).

### 6.4.3 Static Light Scattering (SLS)

Detailed description of the apparatus for making light scattering measurements are given by Zimm (Zimm 1948).  A polarized laser light beam is scattered by a molecule in solution and the deflected light beam is detected by either a single photomultiplier that can be moved radially in a plane around the scattering volume.  In another setup multiple detectors are arranged radially in a plane around the scattering volume enabling simultaneous measurements at multiple angles.

The quantity that is determined through light scattering is the Rayleigh Ratio, $R_\theta$,

$$R_\theta \equiv \frac{r^2 I_S}{I_0 \sin^2 \theta} \tag{6.1}$$

which, for dilute solutions, can be written as (Tanford 1961)

$$R_\theta = \frac{Kc}{1/M_W + 2Bc + 3Cc^2 + \cdots} \tag{6.2}$$

Here $K$ is an optical constant of the system

$$K = \frac{2\pi^2 n_0^2 \left( dn/dc \right)^2}{N\lambda^4}$$ (6.3)

In the above equation $n_0$ is the refractive index of the pure solvent not including the scattering molecules.

If the scattering molecules are small compared to the wavelength of the incident laser light beam than the light scattering has no angular dependence and measurements are done at a single angle, usually with the detector placed at $\theta = 90°$ to the incident light beam. To determine molecular parameters Equation 6.2 can be rewritten and truncated at the coefficient of the first power

$$\frac{Kc}{R_\theta} = \frac{1}{M_W} + 2Bc$$ (6.4)

and plotted as $Kc/R_\theta$ versus $c$. The information to be obtained is the molecular weight from the intercept and the second virial coefficient which is related to the limiting slope.

In Equation (6.4) the second virial coefficient, $B$, is in its dimensional form, but commonly it is represented in a dimensionless way, $A$,

$$\frac{KcM_W}{R_\theta} = 1 + 2A\phi$$ (6.5)

where $\phi$ is the volume fraction of the scattering molecule in solution,

$$\phi = \frac{N_A \pi \cdot c \cdot d_h^3}{6M_W}$$ (6.6)

with $d_h$ being the hydrodynamic diameter of the protein.

Static light scattering experiments were conducted on a DAWN QELS system (Wyatt Technology Corporation). Protein solutions were diluted with standard buffer and mixed with the crystallization buffer right before data acquisition. The microbatch cuvette (Wyatt Technology Corporation) was used for light scattering experiments to minimize the sample volume (20 μL). Since the scattering protein molecules were small compared to the wavelength of the incident laser light beam ($\lambda$ = 690 nm) the light scattering had no angular dependence (Tanford 1961) and measurements were done at a single angle, with the detector placed at $\theta$ = 90° to the incident light beam. Temperature control during the light scattering data acquisition was achieved by a heating element within the light scattering apparatus. For the system used in the experiments, the refractive index of the solvent water is $n_0$ = 1.3320 and the refractive index increment in the presence of apoferritin is $dn/dc$ = 0.195 mL/g (Bjork 1973). Dilution series for apoferritin were set up to have (0.1, 0.2, 0.3, 0.4, 0.5) mg/mL protein in solution. In case of the human samples dilution series were also created at (0.05, 0.1, 0.15, 0.2, 0.25) mg/mL to preserve valuable material.

### 6.4.4 Multiwell Microbatch Crystallization on a Thermal Gradient

Crystallizations were carried out under oil in small-scale batch mode on low-profile 384 microwell plates (Nunc, cat# 264340). A microbatch crystallization apparatus, the details of which were given earlier (Bartling et al. 2005), enabled parallel batch crystallization experiments at various temperatures and solution conditions. The microwell plates consisted of 24 columns (y-axis) and 16 rows (x-axis). Temperature was varied along the y-axis by placing the 384−well plate onto a thermal-gradient plate.

126

The outer two rows and columns were not used so as to eliminate edge effects with respect to temperature. This left 20 wells along the temperature gradient and 12 wells perpendicular to the temperature gradient, a total of 240 wells per plate for experiments.

Before the microwell plates were used, they were cleaned with ultra-pure compressed air (Fisher Scientific) to remove dust particles. The microwells were charged by first adding 8 µL of paraffin oil (HR3-411, Hampton Research) into each well with an Eppendorf micropipette. Stock protein solutions were mixed with the standard and crystallization buffers to obtain the desired solution conditions. The standard buffer consisted of 50 mM tris-HCl, 150 mM NaCl and 10 mM NaN$_3$ (preservative) while the crystallization buffer was based on the standard buffer but additionally contained cadmium ions at various concentrations. The mixing was performed by transferring the protein stock solution to a centrifuge tube, with the tube being mildly vortexed while adding the standard and/or the crystallization buffers (Rayment 2002). This was done to reduce local cadmium concentration peaks that could have led to instantaneous protein precipitation. Then, a small droplet (4 µL) of the freshly prepared protein solution was pipetted directly beneath the paraffin oil surface in each well so as to minimize the contact time with the surrounding air. Each row of wells along the y-axis was used for one of the solution conditions. The water baths were set to achieve a thermal gradient of 30 °C to 40 °C along the y-axis. The number and location of the wells used for each experiment were specified in the Scope-Pro software (MediaCybernetics) and the image acquisition was started by initiating a program macro. Pictures of each well were taken in 2-hour intervals.

**6.4.5 Protein Stability in the Presence of NDSBs**

The use of chemical solubilizers in protein crystallization to decrease or even prevent the condensation of macromolecular biological molecules (see Chapter 2.3.5) had to first be evaluated with respect to the structural integrity of the proteins in the presence of the solubilizers. Therefore two different methods were employed; circular dichroism (see Chapter 3.1.4) and analytical size exclusion chromatography (see Chapter 3.1.1.2).

<div align="center">

**6.5 Results**

</div>

**6.5.1 Stability Testing via Circular Dichroism**

The intended use of circular dichroism was to confirm that the addition of solubilizers did not cause structural changes of the apoferritin molecule. Therefore pure buffer solutions, solutions containing apoferritin and solutions containing NDSB 201 were measured in a circular dichroism spectrophotometer (Jasco J-810). The settings of the apparatus were:

- Scanning speed:       50 nm/min
- Response:             4 seconds
- Band width:           5 nm
- Data pitch:           1 nm
- Data accumulation:    4 (average of 4 runs per sample)
- Sensitivity:          Standard (100 mdeg)
- Photon pathlength:    1 cm
- Temperature:          30 °C

The results for the circular dichroism measurements in the far UV region for all three tested solutions are depicted in Figure 6-1.  The pure buffer solution (50 mM Tris-HCl) had increased absorption in the far UV spectrum below 215 nm, overlapping the CD spectrum for apoferritin.  The solution containing 1 M NDSB 201 showed strong background absorption over the whole far UV circular dichroism spectrum.
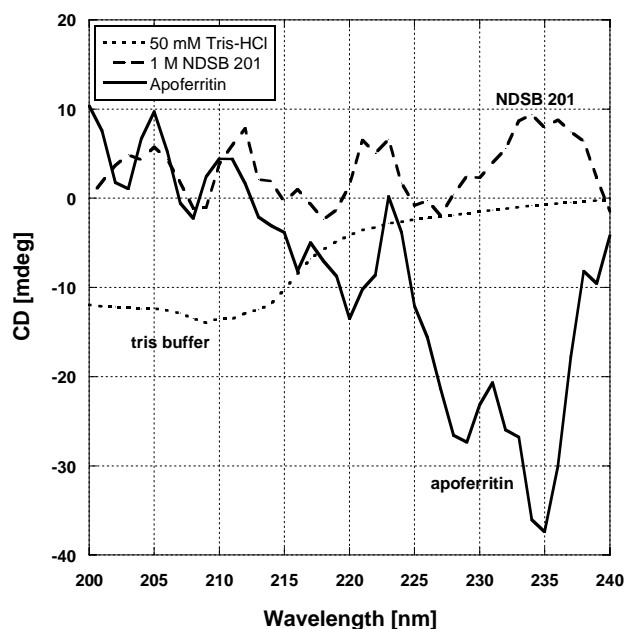


Figure 6-1.  Results for the far UV circular dichroism spectrum

In the near UV circular dichroism spectrum there was almost no background absorption detectable for the pure buffer solution, but the solution containing 1 M NDSB absorbed very strong again over the whole near UV circular dichroism spectrum (Figure 6-2).  The results for the pure apoferritin solutions in Figure 6-1 and Figure 6-2 compared well to far and near UV circular dichroism spectra reported earlier (Figure 6-3).  The slight discrepancies between the far and near UV circular dichroism spectra reported here

and in the literature were most likely due to the use of different buffers, different pH and different temperatures.

Nevertheless, from the results shown in Figure 6-1 and Figure 6-2 it was obvious that circular dichroism could not be used to determine the overall structural integrity of the apoferritin molecules in solution, since NDSB 201 had strong absorption in both spectra resulting on high-level background noise. The strong absorption of NDSB at a concentration of 1 M was also visible on the analytical SEC-HPLC chromatogram (see Figure B-54). Although NDSB 195 was reported to not significantly absorb in the near UV spectrum (Vuillard et al. 1995), NDSB 256 was expected to have similar absorption characteristics to the tested NDSB 201 since it also features a conjugated ring system in its chemical structure (see Table 2-2).
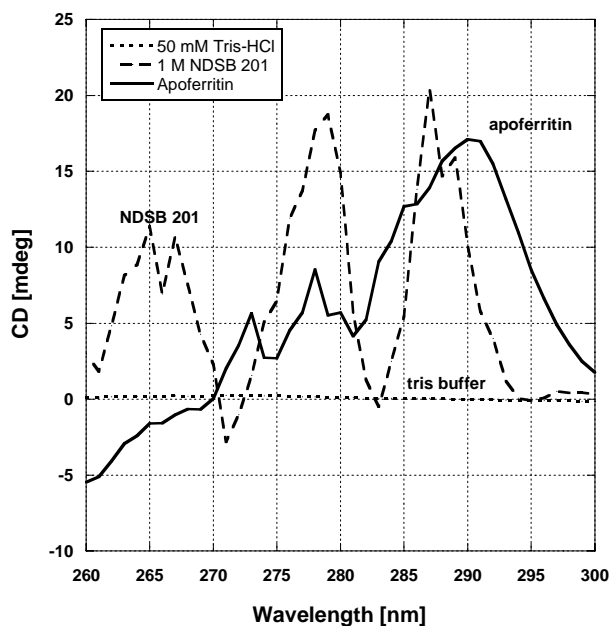


Figure 6-2. Results for the near UV circular dichroism spectrum

The strong presence or lack of absorbance in the near UV region was obvious when examining the chromatograms of NDSB 256 (Figure B-55) and of NDSB 195 (Figure B-53), respectively.
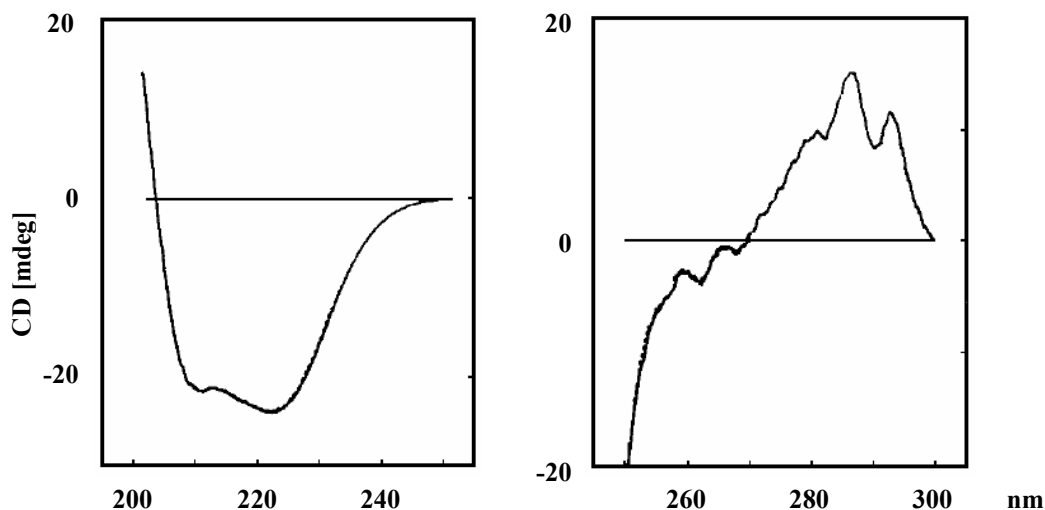


Figure 6-3.  Far UV (left diagram) and near UV (right diagram) circular dichroism spectrum of apoferritin (Stefanini et al. 1996)

## 6.5.2 Stability Testing via Analytical SEC-HPLC

The stability testing of apoferritin in the presence of NDSBs could not be done with circular dichroism due to the large background noise introduced by the NDSBs.  The inherent separation characteristics of the analytical SEC-HPLC provided the opportunity for the smaller free NDSB molecules to be separated from the protein molecules and therefore the protein molecules could be analyzed separately.

A change in structural integrity of the apoferritin molecules in solution would be accompanied by a change in shape and size, which in turn could be picked up by

analytical SEC-HPLC, especially if the proteins denture in the presence of the solubilizers.

First, two sets of as-received apoferritin solutions were mixed with the different solubilizers listed in Table 2-2 to obtain 8 mg/mL apoferritin in 50 mM tris-HCl with 150 mM NaCl, 10 mM NaN$_3$ and 1 M of a particular solubilizer. One set of controls was subjected to analytical SEC-HPLC immediately, while another set of controls was incubated with the remaining solutions in microcentrifuge tubes at 30 °C for 24 hours and then subjected to analytical SEC-HPLC. The chromatograms can be found in Appendix B.4, Figure B-22 through Figure B-39. In Figure 6-4 the retention times of the apoferritin oligomers and monomers present in solution all of the above samples were plotted. The standard deviation for the retention times of the oligomers was ±0.0038 minutes while the standard deviation for the monomer retention times was ±0.0033 minutes.
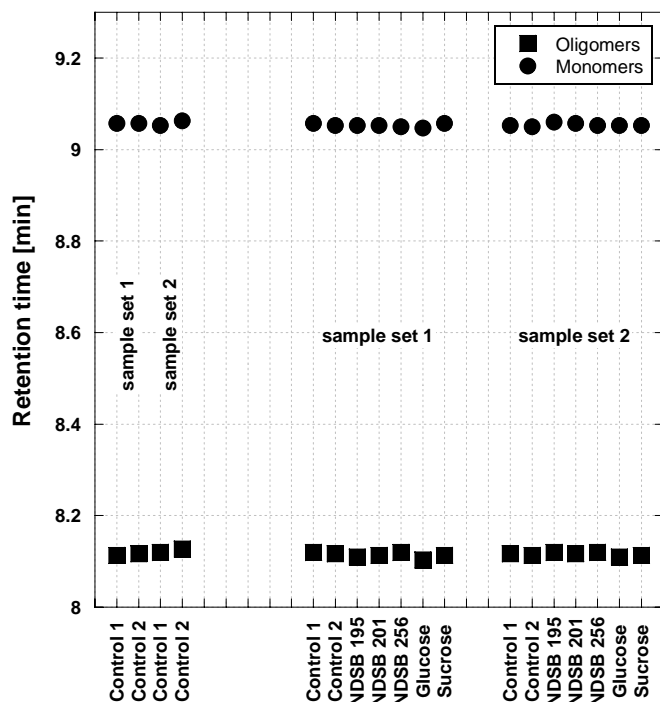


Figure 6-4. Retention times for apoferritin oligomers and monomers in the presence of stabilizers

This was an indication for the retention times to not have changed throughout the incubation time for the protein samples treated neither with the solubilizers nor for the controls. If the solubilizers indeed would have enlarged the hydration layer around the protein molecules a shift towards shorter retention times would have been detected. On the contrary a partial or total denaturation would have been picked up as well through a shift in retention times.

Next, the impact of the NDSBs on the stability of other large multimeric proteins beside apoferritin was tested. Mandelate Racemase (MR) as an octamer and Catalase as a tetramer were used to study possible impacts on the overall structural integrity upon the incubation with 1 M NDSBs. The protein solutions (8 mg/mL protein concentration) were incubated with and without NDSBs for 24 hours at 30 °C and analyzed via analytical SEC-HPLC. In Figure 6-5 the monomer retention times for all three proteins is depicted. The presence of the NDSBs did not decrease the retention times by stabilizing and therefore enlarging the hydration layer around the protein molecules. More importantly, the NDSBs did not partially denature the protein molecules wherefore the NDSBs used in this study were compatible with the multimeric protein structure in that they did not cleave the bonds between the subunits of the proteins.

In Figure 6-6 the retention times of Figure 6-5 were plotted as a function of the molecular weight of the proteins. The linear decrease of the retention times with increasing molecular weight was an indication that first, the separation by analytical size exclusion chromatography was purely size dependent. Secondly, there was no appreciable change of the NDSB treatment samples compared to the controls visible furthermore indicating the integrity of the overall three dimensional structure of the

proteins in the presence of the NDSBs. The chromatograms can be found in used for this

study can be found in Appendix B.4.2.
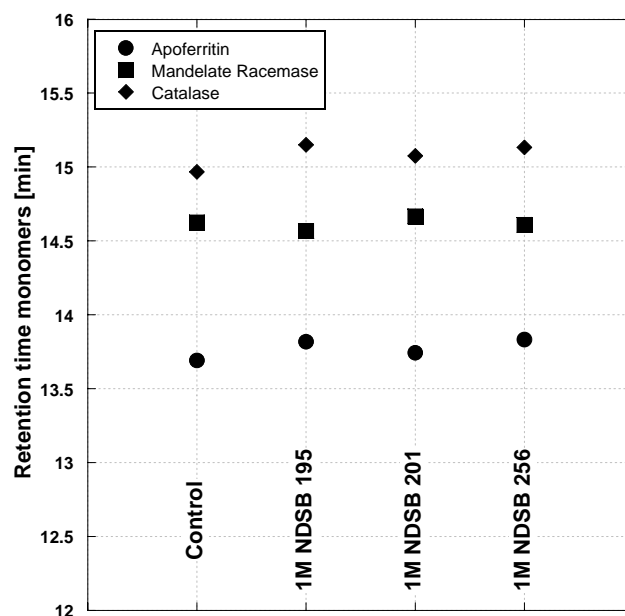


Figure 6-5. Multimeric protein stability in the presence of 1 M NDSBs
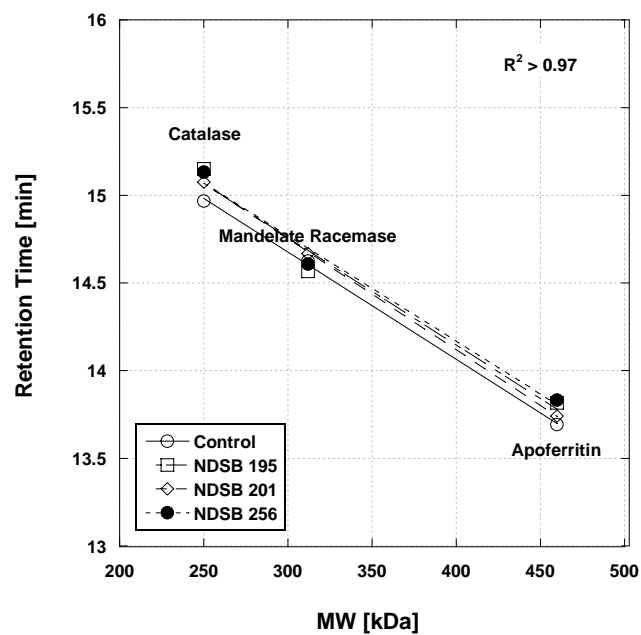


Figure 6-6. Protein separation via analytical SEC-HPLC by size

### 6.5.3 Static Light Scattering Experiments

The second virial coefficient determination of apoferritin solutions at pH 7.40 indicated a transformation of overall repulsive interactions to overall attractive interactions at the 12 mM and 13 mM $CaCl_2$ concentration interphase (Figure 6-7). The static light scattering measurements revealed that for the apoferritin dilution series used the plot according to Zimm was linear for all cadmium concentrations used. Hence the truncation of Equation (6.4) was valid and the second virial coefficient was dominant in this apoferritin concentration regime.
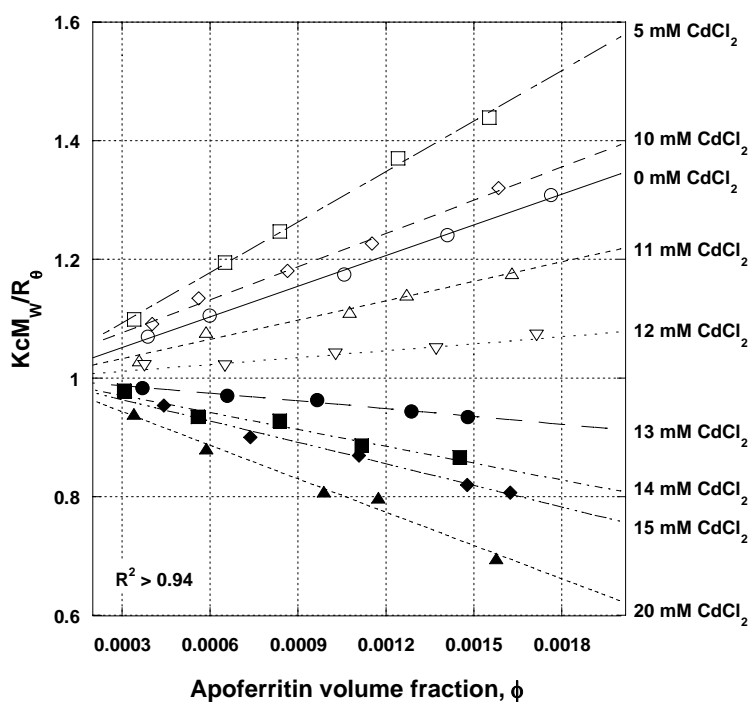


Figure 6-7: Static light scattering of horse spleen apoferritin at 0-20 mM $CdCl_2$ at 30 °C

The static light scattering results depicted in Figure 6-7 were in agreement with crystallization screening experiments where the transition from no crystal formation to crystal appearance was from 12 mM $CdCl_2$ to 13 mM $CdCl_2$ as well (see Figure 6-8). The graph in Figure 6-8 is a compilation of 3 different crystallization experiments where the first experiment covered the concentration range 0-11 mM $CdCl_2$, the second covered 10-20 mM $CdCl_2$ and the third experiment covered the concentration range of 15-24 mM $CdCl_2$. Hence there were overlaps of $CdCl_2$ concentrations were the crystallization outcome was identical in terms of crystal or no crystal appearance.
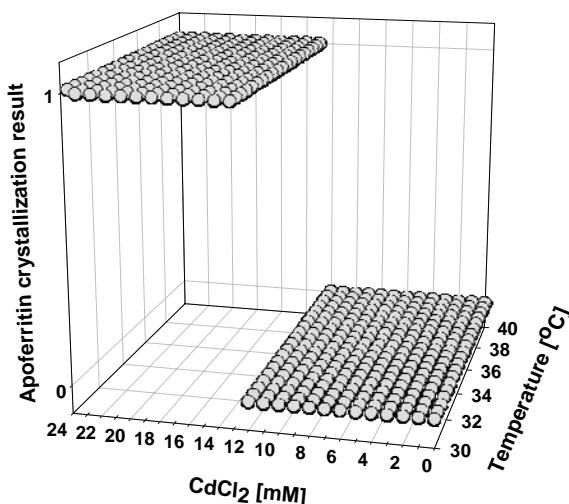


Figure 6-8: Apoferritin crystallization results with varying temperature and cadmium concentration at 8 mg/mL apoferritin (apoferritin crystallization result: 0 indicates no crystals, 1 indicates crystals)

In another apoferritin crystallization screening experiment the influence of varying apoferritin concentrations on the appearance of apoferritin crystals was tested. In the presence of 10 mM cadmium, i.e. under conditions where apoferritin crystallization

was not favored, the apoferritin concentration of 4, 8, 12 and 16 mg/mL did not lead to the formation of apoferritin crystals. However, in the presence of 15 and 20 mM cadmium all four apoferritin concentrations led to apoferritin crystallization. In all cases the phase transition occurred with respect to a change in cadmium concentration and not with respect to temperature (see Figure 6-9).
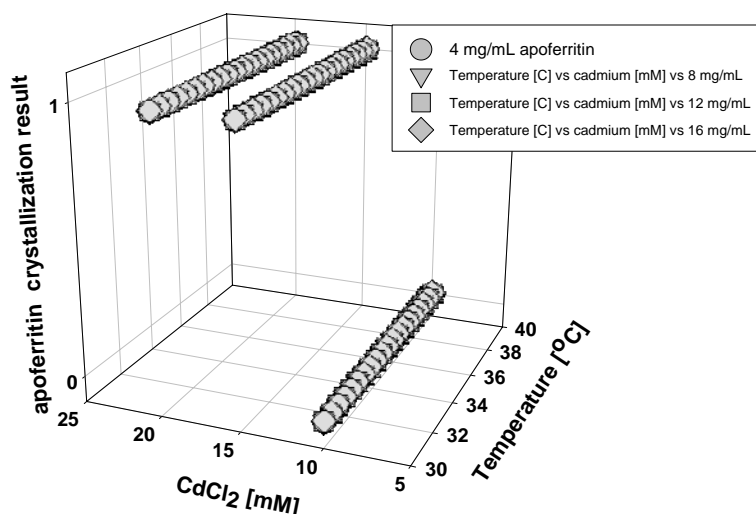


Figure 6-9: Apoferritin crystallization results with varying cadmium concentration (10, 15 and 20 mM), varying apoferritin concentration and temperature (apoferritin crystallization result: 0 indicates no crystals, 1 indicates crystals)

While temperature seemed not to have an impact on apoferritin phase transition at supersaturated conditions (supersaturated with respect to apoferritin concentration), temperature could have indeed influenced the protein-protein interactions in dilute solutions as the apoferritin crystal size increased with increasing temperature (see Chapter 5). To test this presumption the protein-protein interactions were measured by static light scattering at 30 °C and 40 °C, representing the two temperature extremes of

the crystallization experiments conducted earlier.   The second virial coefficient measurements in close proximity to the repulsive/attractive interaction interface indicated no significant differences in the protein-protein interactions for both temperatures (see Figure 6-10).
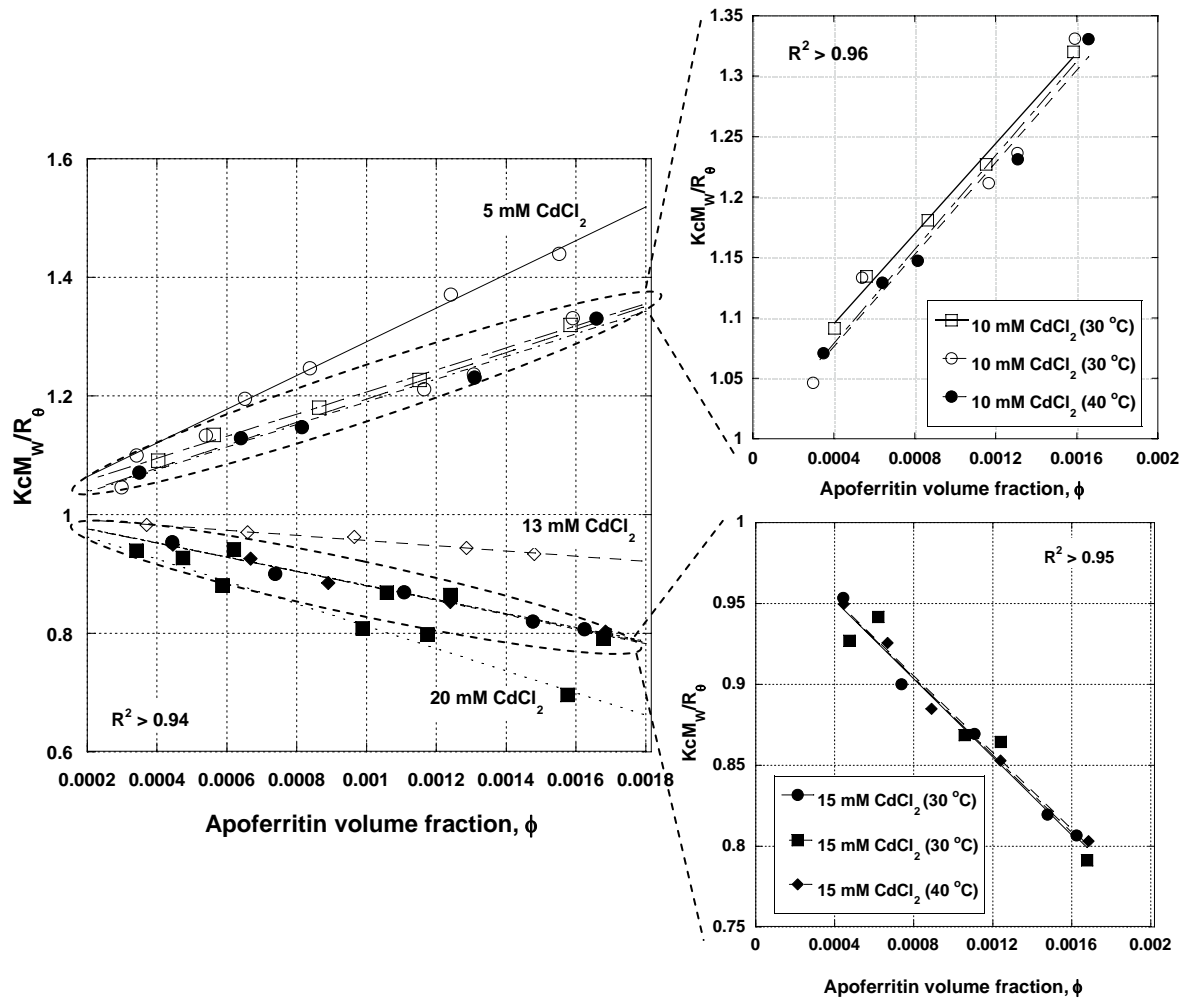


Figure 6-10:  Static light scattering of horse spleen apoferritin at 30 °C and 40 °C;  *Left*: combined results, *Right Top:* Results of 10 mM CdCl₂ experiments,  *Right Bottom*: experiments in the presence of 15 mM CdCl₂

The graph on the left hand side of Figure 6-10 also shows results for 5, 13 and 20 mM cadmium concentration taken from Figure 6-7 to indicate that although there

were some slight variations especially in the top insert of Figure 6-10, overall the variations were negligible. This was furthermore confirmed by the Analysis of Variance (ANOVA), which indicated that no significant differences were found between the repetitive static light scattering measurements of 10 and 15 mM $CdCl_2$ with a probability of $< 0.05$. Therefore all other static light scattering experiments were conducted at 30 °C to reduce any possible concentration effects due to solvent evaporation during data acquisition.

One interesting observation was that the second virial coefficient at 0 mM $CdCl_2$ had a repetitive lower positive slope and hence less repulsive intermolecular interactions compared to solutions containing 5 mM $CdCl_2$ (see Figure 6-7). Only at 10 mM $CdCl_2$ and beyond was the slope lower compared to 0 mM $CdCl_2$. To further investigate the unexpected result, solutions containing 0-5 mM $CdCl_2$ were measured via static light scattering. It was observed that indeed at very low cadmium concentrations (0-3 mM) apoferritin showed a salting-in effect and only beyond 4 mM $CdCl_2$ did the protein-protein interactions increase (Figure 6-11). In this graph repetitive measurements for 0, 5, 10 and 15 mM $CdCl_2$ were plotted as well. The close proximity of the repetitive measurements indicated good reproducibility of the second virial coefficient measurements. The Analysis of Variance (ANOVA) further revealed that significant differences were found between the repetitive measurements of 0, 5, 10 and 15 mM $CdCl_2$ with a probability of $< 0.05$.
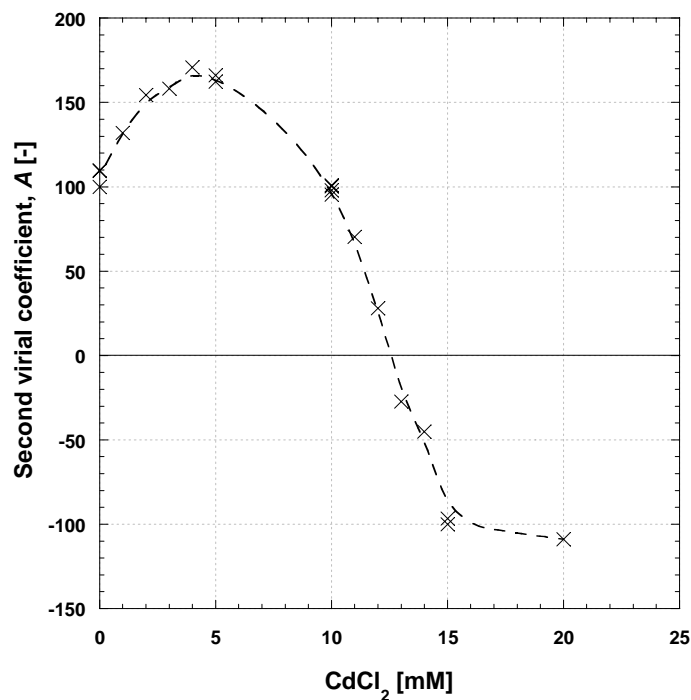
Figure 6-11: Horse spleen apoferritin intermolecular interactions as a function of $CdCl_2$ concentration at 30 °C; the broken line is a guide for the eye (multiple measurements at 0, 5, 10 and 15 mM $CdCl_2$ indicate stability of analysis)

While the presence of high divalent cation concentrations (100 mM of $Ba^{2+}$, $Sr^{2+}$, $Ca^{2+}$ or $Mg^{2+}$) did not induce apoferritin crystallization (data not shown), there was still the possibility of the elevated concentrations of these divalent cations to have an influence on the protein-protein interactions in dilute solutions. At more than three times the cadmium concentration, at which apoferritin crystallization occurred, the tested divalent cations actually increased the repulsive intermolecular forces between the apoferritin molecules in the dilute solution regime (Figure 6-12).
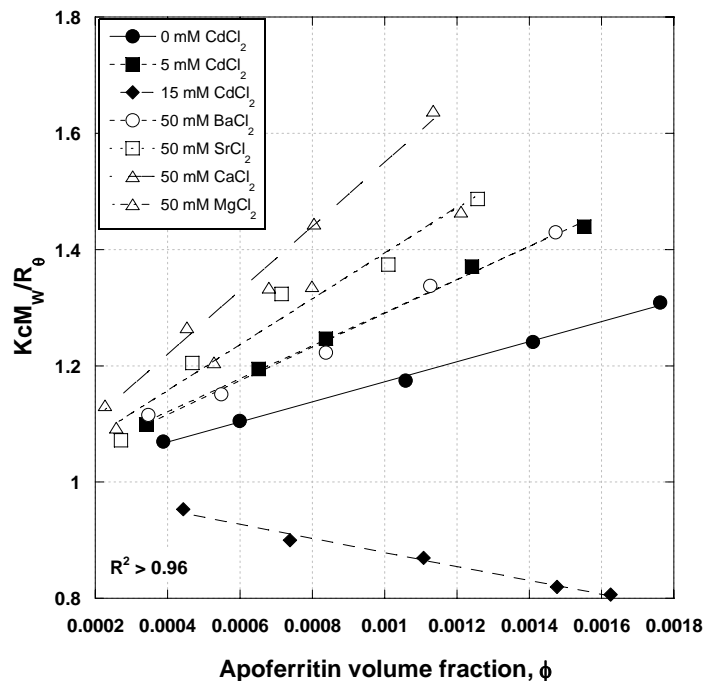
Figure 6-12. Influence of increased concentration (50 mM) of divalent cations on apoferritin intermolecular interactions (0, 5 and 15 mM CdCl$_2$ are depicted for reference)

In another experiment the influence of other divalent cations beside cadmium on the apoferritin intermolecular interactions were tested. In Figure 6-13 the results of the static light scattering experiments of horse spleen apoferritin are plotted. It was obvious that other divalent cations beside cadmium had no significant impact on protein-protein interactions. For 0, 5, 10 and 15 mM cation concentration the values for the second virial coefficients were similar to the values of 0 mM CdCl$_2$. In the same graph the results for 5 and 15 mM cadmium were included to indicate the overall scale of the variations of the light scattering results for the other divalent cations tested. The Analysis of Variance (ANOVA) further revealed that no significant differences were found between the groups containing 5 mM, 10 mM, 15 mM divalent cations and the repetitive measurements of

0 mM $CdCl_2$ with a probability of $< 0.05$. Hence, cadmium indeed seemed to be the only divalent cation that had an effect on protein-protein interaction between apoferritin molecules in solution.
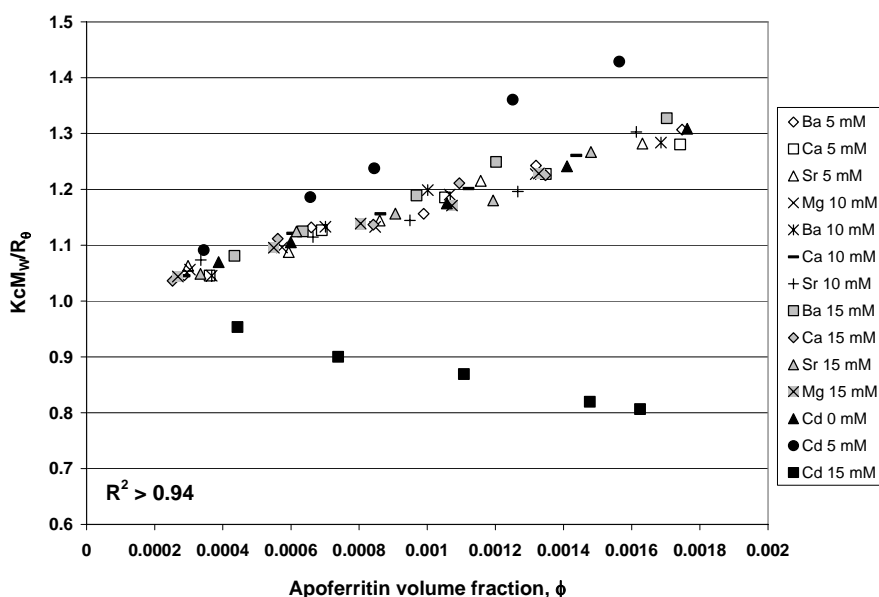


Figure 6-13: Horse spleen apoferritin protein-protein interaction in the presence of various divalent cations at 30 °C

After testing the influence of different divalent cations beside cadmium on the protein-protein interactions, potential additive effects of other divalent cations with cadmium were tested. Therefore the second virial coefficients of horse spleen apoferritin solutions in the presence of equal molar additions (10 and 15 mM) of cadmium and one extra divalent cation at a time were determined. In Figure 6-14 the results of the addition of 10 mM cadmium plus 10 mM of another divalent cation are depicted. Figure 6-15 shows the equivalent to Figure 6-14 but in the presence of 15 mM divalent cations. At

10 mM other divalent cations did not significantly alter the second virial coefficient of the apoferritin solutions, especially when compared to the results in the presence of 5 and 11 mM cadmium chloride alone. The Analysis of Variance (ANOVA) further revealed that no significant differences were found for the second virial coefficients of the repetitive measurements of 10 mM $CdCl_2$ (see Figure 6-11) and all the measurements including 10 mM CdCl2 and 10 mM of another divalent cation with a probability of $< 0.05$.
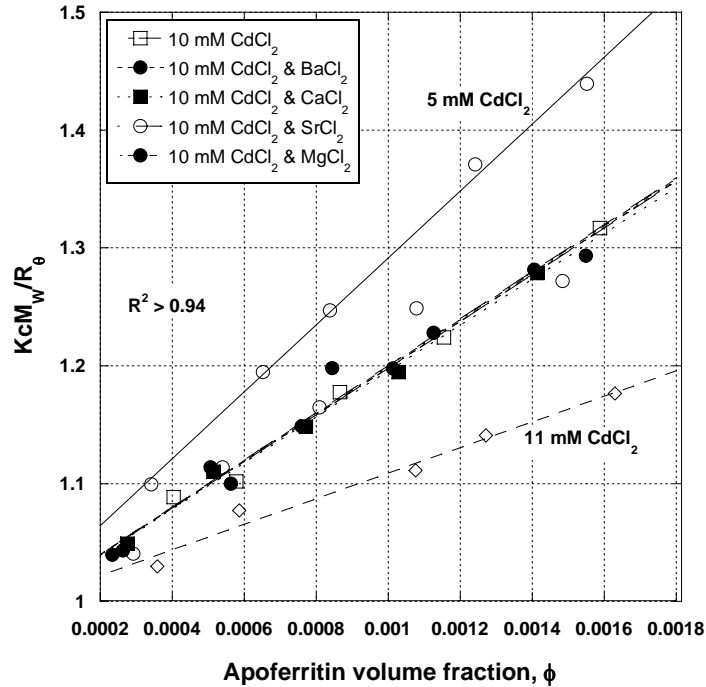


Figure 6-14: Influence of other divalent cations (10 mM) on horse spleen apoferritin protein-protein interaction in the presence of 10 mM $CdCl_2$

At 15 mM divalent cation concentration the results were similar to the results in Figure 6-14 in that other divalent cations had no significant effect on the outcome of the

second virial coefficient measurements compared to the results with 15 mM cadmium present alone. The only divergence was the presence of 15 mM calcium. In the presence of calcium the second virial coefficient seemed to be more negative indicating increased protein-protein interactions between apoferritin molecules in solution compared to the presence of only 15 mM cadmium. The Analysis of Variance (ANOVA) further revealed that no significant differences were found for the second virial coefficients of the repetitive measurements of 15 mM $CdCl_2$ (see Figure 6-11) and all the measurements including 15 mM CdCl2 and 15 mM of another divalent cation not including calcium with a probability of $< 0.05$.
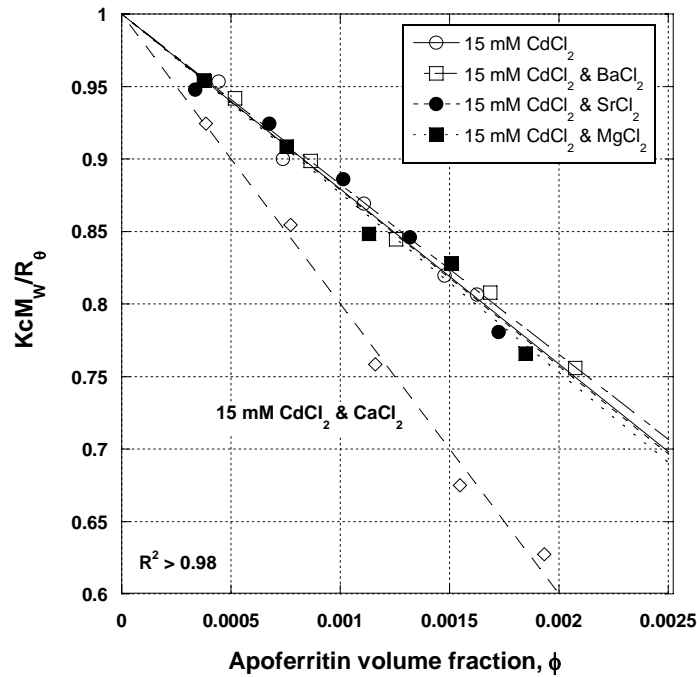


Figure 6-15: Influence of other divalent cations (15 mM) on horse spleen apoferritin protein-protein interaction in the presence of 15 mM $CdCl_2$

The results from the static light scattering experiments of the horse spleen apoferritin samples were compared to the second virial coefficient results indicating the existence of a crystallization slot (George and Wilson 1994; George et al. 1997). In Figure 6-16 the lower x-axis refers to the results in this study, whereas the upper x-axis belongs to the second virial coefficient measurements by George et al. The y-axis represents the three possible protein crystallization outcomes, namely precipitation, crystallization and no crystallization.
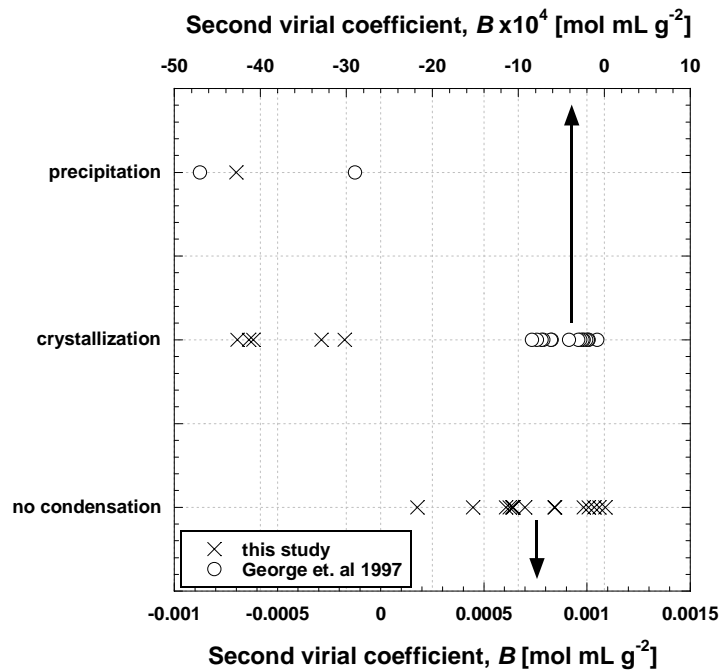


Figure 6-16. Dimensionless second virial coefficients for apoferritin (results from Figure 6-11) compared to the crystallization slot established by (George et al. 1997)

Next, ferritin molecules from two human tissue sources (human spleen and human liver apoferritin) that have been de-ironized were subjected to static light scattering and

compared to the horse spleen apoferritin sample. The human apoferritin molecules showed overall attractive interactions at lower cadmium levels (5 mM $CdCl_2$) compared to horse spleen apoferritin which displayed attractive interactions only above 13 mM $CdCl_2$ (Figure 6-17).
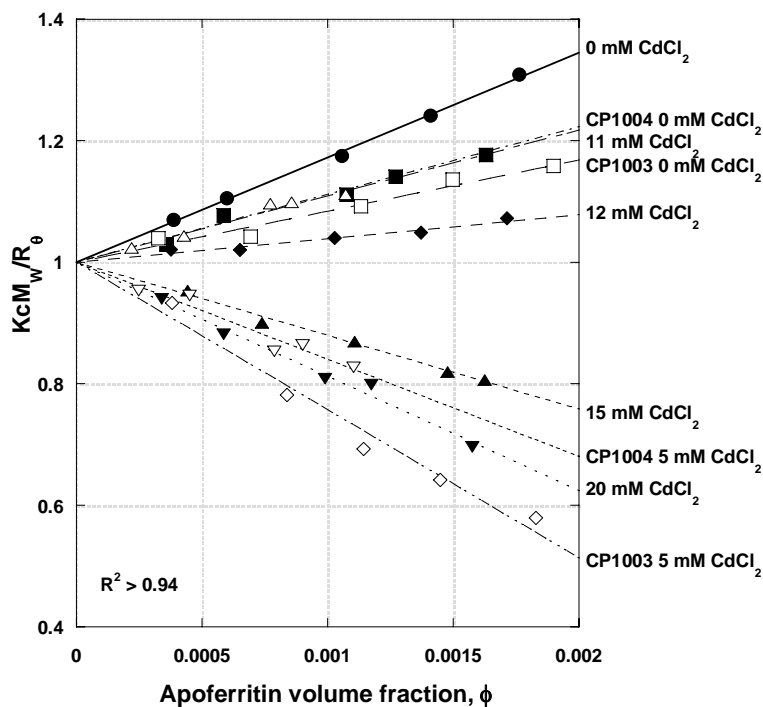


Figure 6-17: Static light scattering of purified human liver apoferritin (CP1003) and purified human spleen ferritin (CP1004) compared to horse spleen apoferritin

Furthermore in the absence of any divalent cations the human apoferritins displayed lower overall repulsive forces as can be seen from the smaller slopes of the lines in Figure 6-17 compared to the horse spleen apoferritin sample. Although (apo-) ferritins from different vertebrate sources have all essentially the same three dimensional structure, the primary structure (amino acid sequence) can bear large variations (Harrison

146

and Arosio 1996). Furthermore, as for apoferritin crystallization (Lawson et al. 1991) cadmium atoms are positioned at the interface between two neighboring protein molecules and coordinated by two carboxyl groups of glutamic or aspartic acid side chains each belonging to one of the two molecules (Trakhanov et al. 1998). Hence the variations in intermolecular interactions for apoferritin molecules from different sources in the absence and presence of cadmium ions could possibly be explained by disparities in the amino acid sequence of the protein molecules.

Since divalent cations other than cadmium seemed to have no apparent influence on the intermolecular interactions of horse spleen apoferritin under the conditions tested, the human apoferritins were subjected to light scattering experiments in the presence of other divalent cations, too. The concentration of the divalent cations was lower compared to the static light scattering experiments on horse spleen apoferritin (see Figure 6-13) to account for the overall higher intermolecular interactions of the human apoferritins compared to the horse spleen apoferritin even in the absence of divalent cations. In Figure 6-18 the results of the static light scattering experiments for human liver apoferritin (CP1003) are plotted in the presence of 5 mM and 20 mM divalent cations. Other earth alkali metals had no affect on the intermolecular interactions between apoferritin molecules, i.e. the effect was the same as in the absence of any divalent cations. Even at 20 mM divalent cation concentration the apoferritin interactions were not significantly different compared to the samples with 5 mM and no divalent cations present. The Analysis of Variance (ANOVA) indeed revealed that no significant differences were found between the groups containing 5 mM and 20 mM divalent cations and the repetitive measurements of 0 mM $CdCl_2$ with a probability of $< 0.05$.
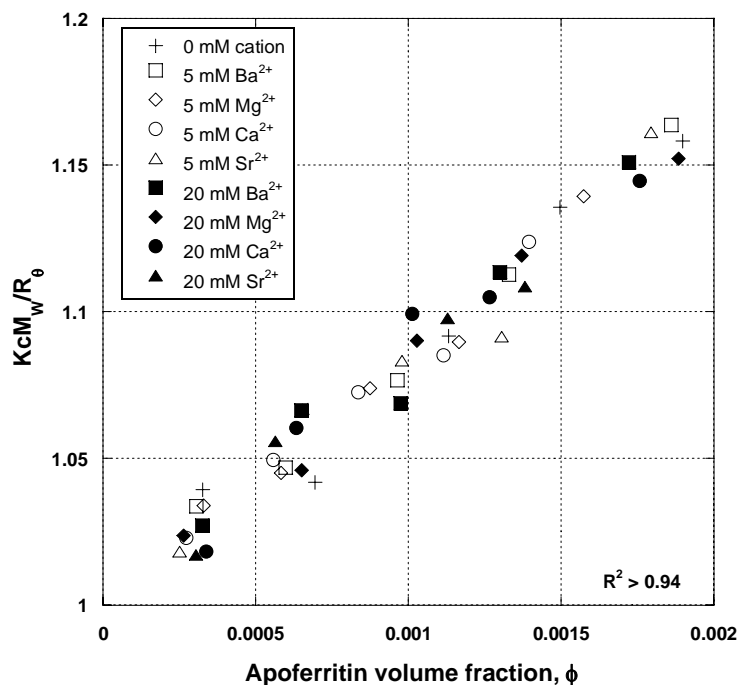
Figure 6-18:  Influence of other divalent cations besides cadmium on intermolecular interactions of human liver apoferritin (CP1003)

Comparable results for the static light scattering measurements were obtained for human spleen apoferritin (Figure 6-19).  The results for 0 mM and 5 mM $CdCl_2$ had a larger range along the x-axis since they were obtained with the higher concentrated apoferritin dilution series (0.1-0.5 mg/mL) compared to 0.05-0.25 mg/mL for the remaining solutions.  The Analysis of Variance (ANOVA) revealed that no significant differences were found between the groups containing 5 mM divalent cations and the repetitive measurements of 0 mM $CdCl_2$ with a probability of $< 0.05$.

Again, other divalent cations seemed not to have an impact on apoferritin intermolecular interactions and cadmium appeared to be the only universal cation that introduced overall attractive interactions in apoferritin from different sources.  Due to the

low amount of human spleen apoferritin available, no static light scattering experiments could be conducted in the presence of 20 mM divalent cations.
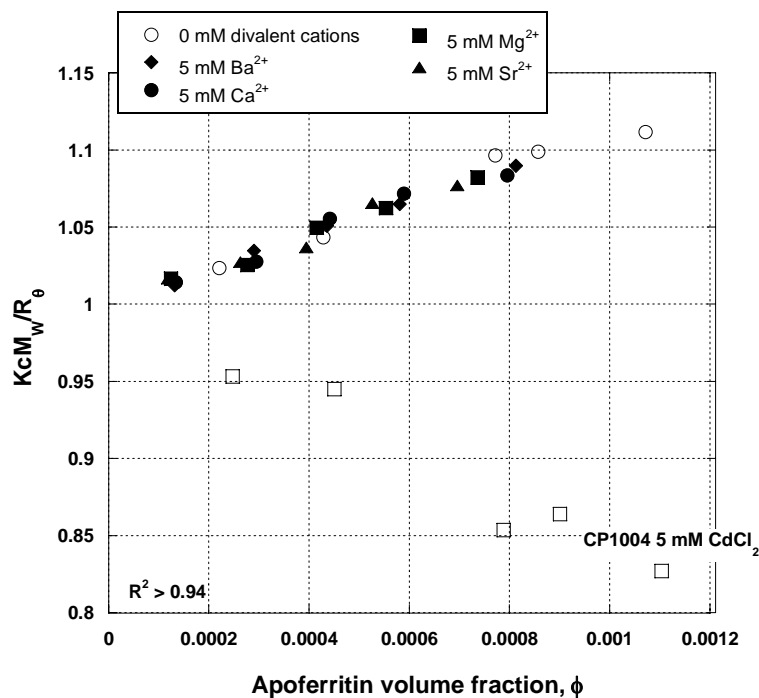


Figure 6-19: Influence of other divalent cations besides cadmium on the intermolecular interactions of human spleen apoferritin (CP1004)

The influence of certain protein solubility enhancing chemicals was tested both with crystallization experiments and static light scattering experiments. In Chapter 3 it was already established that the NDSBs to be used in the crystallization and static light scattering experiments did not compromise the structural conformation of the apoferritin molecules. From Figure 6-20 it can be seen that the overall outcome, i.e. positive or negative second virial coefficients depending on the cadmium concentration present, was not altered. Solutions with conditions that favored overall repulsive apoferritin

intermolecular interactions (10 mM cadmium) remained in the positive second virial coefficient regime. Solutions that displayed a negative second virial coefficient (15 mM cadmium) retained their overall attractive potential. The outcome was not too surprising since the addition of NDSBs did not increase the hydration layer around the apoferritin molecules (see Chapter 3.2) and therefore did not stabilize the protein molecules in solution to prevent their condensation.
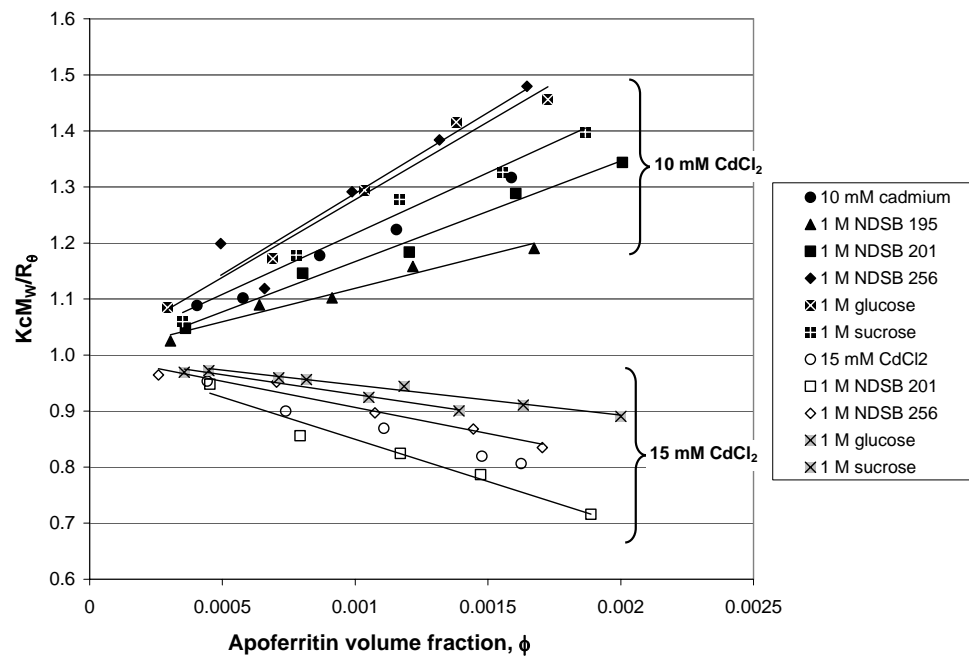


Figure 6-20: Protein-protein interactions of horse spleen apoferritin molecules in the presence of chemical additives

## 6.7 Discussion and Conclusions

To our knowledge for the first time the solution thermodynamics of apoferritin molecules from different species and different sources within one species were investigated and compared in the presence of various divalent cations that are of physiological significance.

The reason for investigating cations instead of anions was that at the physiological pH of 7.40 the apoferritin molecules exhibited an overall negative charge (see Figure 6-21) and therefore cations were the primary counter-ions to preferentially bind to the protein molecule. The cations investigated were all chloride salts to eliminate the possible impact of changing co-ions.
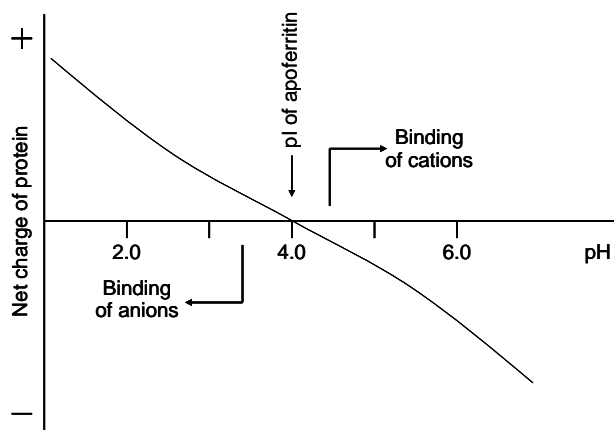


Figure 6-21: Schematic representation of the net charge of apoferritin as a function of pH (after (Bostroem et al. 2005), pI of apoferritin from (Petsev and Vekilov 2000)

The salting-in and salting-out effect has been reported earlier for apoferritin molecules in the presence of sodium chloride (Petsev et al. 2000). In the absence of cadmium ions apoferritin revealed a salting-out effect at increasing sodium concentration

until 150 mM sodium was reached above which the intermolecular interactions decreased. The inverse relationship was discovered in this study for increasing cadmium concentrations in the presence of 150 mM sodium ions. The replacement of the sodium ions by the cadmium ions might explain the decrease in intermolecular apoferritin interactions at low cadmium ion concentration: according to Figure 6-22 at 150 mM sodium ion concentration the apoferritin intermolecular attractions are maximized and therefore the replacement of sodium ions by cadmium ions would lead to a decrease in the intermolecular interactions, hence an increase in the second virial coefficient. Above 4 mM cadmium concentration the decrease in intermolecular interactions due to the replacement of sodium ions is compensated for by the induced attractive forces due to the binding of cadmium ions to the apoferritin molecules.

The values of the dimensionless second virial coefficients, $A$, in Figure 6-22 were overall lower compared to the values measured here. This can be explained by the higher pH used in this study (pH 7.4 vs. pH 5.0) and hence the apoferritin molecules displayed a larger net-positive charge and hence larger intermolecular repulsion (see Figure 6-21). On the other hand the dimensional second virial coefficient, $B$, was lower compared to the values depicted in Figure 6-16. This was due to the conversion from the dimensionless second virial coefficient, $A$, to the dimensional second virial coefficient, $B$, using Equation (3.12), where the square of the molecular weight made the $B$ values very small, especially with apoferritin being one of the larger proteins that have been crystallized to date (see Figure 6-23).
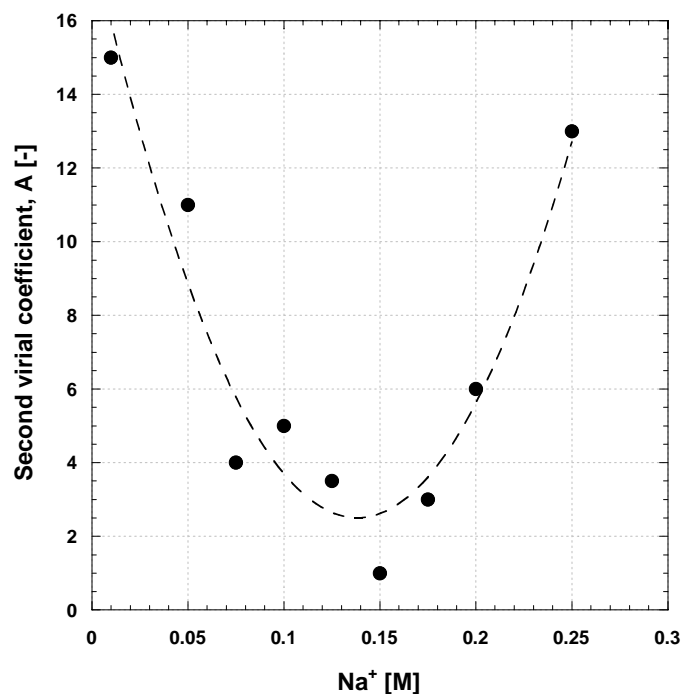
Figure 6-22: Dimensionless second virial coefficient $A$ for the apoferritin monomer as a function of the sodium cation concentration [$Na^+$]. (pH 5.0, no cadmium ions present) The broken line serves as a guide for the eye (Petsev et al. 2000)

The increase in intermolecular repulsive forces at elevated divalent cation concentrations (other than cadmium, see Figure 6-12) can also be explained with a cation exchange of the sodium ions with the metal ions, similar to the salting-in effect of cadmium at low concentrations mentioned above. Compared to cadmium ions the other divalent cations did not induce attractive interactions between the apoferritin molecules, even at very high concentrations. The lack of inducing attractive interactions was obvious from Figure 6-13 where the results of the static light scattering experiments in the presence of 5, 10 and 15 mM strontium, barium, calcium and magnesium ions, respectively, were similar to the results in the absence of divalent cations (0 mM

153

cadmium). The same was true for human liver apoferritin (CP1003) and human spleen apoferritin (CP1004) (see Figure 6-18 and Figure 6-19).
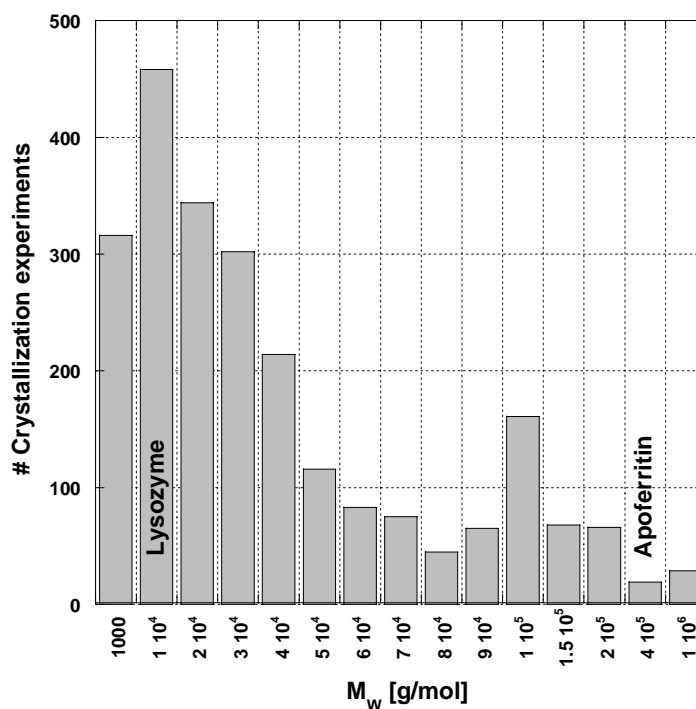


Figure 6-23. Histogram of the number of protein crystallization experiments as a function of the molecular weight of the proteins used; apoferritin and lysozyme are listed as examples for reference (data obtained from the BMCD database (Gilliland et al. 1994))

The testing of additive effects of other divalent cations in addition to cadmium on apoferritin intermolecular interactions revealed that only equimolar concentrations of calcium increased the attractive interactions in the presence of 15 mM cadmium but not in the presence of 10 mM cadmium. Thus, there is an indication of a threshold level of cadmium that is required above which other divalent cations might have additive effects on the apoferritin intermolecular interactions. Interestingly, calcium is also among the

divalent cations that are present at elevated levels in cataractous lenses compared to normal lenses (see Table 2-1).

The human apoferritin samples revealed an overall larger intermolecular attraction in the presence of cadmium ions compared to horse spleen apoferritin. Whereas human spleen apoferritin (CP1004) had similar second virial coefficients, the human liver apoferritin (CP1003) exhibited a lower slope on the Zimm plot and hence had slightly increased intermolecular attractions compared to the other apoferritin samples in the absence of cadmium (see Figure 6-17). The difference in 'background' levels of the intermolecular interactions can be explained by the different H/L chain ration (Arosio et al. 1978; Arosio et al. 1983; Harrison and Arosio 1996) and hence slightly different overall structural design.

The treatment of the apoferritin solutions with solubilizers did not change the overall outcome for the crystallization or the light scattering experiments. Although the presence of the solubilizers slightly changed the magnitude of the second virial coefficients of the protein solutions the overall attractive or repulsive interactions remained unchanged. Another possible treatment option for potential HHCS patients would be the reduction of the divalent cations by the addition of chelators. Unfortunately, the addition of ethylenediaminetetraacetic acid (EDTA) was not successful since chelators form chemical complexes with the metal ions of very low solubility and the complex therefore easily precipitates out of solution. Hence, the administration of chelators for the removal of cadmium ions would not be a viable treatment option for the prevention of HHCS, since any type of precipitate within the

ocular lens would compromise the tight packing of the lens fibers and therefore the undisturbed passage of light.

There are indications in the literature that the L-chain subunits and hence the L-rich apoferritins are more important in crystallization in the presence of cadmium compared to the H-rich apoferritins (Arosio et al. 1983). The tested L-rich apoferritins although from different species are all susceptible to cadmium induced condensation. Furthermore the crystallization outcome in terms of crystallization, precipitation or no condensation could be predicted by a single dilute solution thermodynamic parameter, namely the second virial coefficient.

Solubility is another important solution property affecting protein crystallization. Indeed, the solubility of proteins may be dependent on the second virial coefficient as can be seen in Figure 6-24 for lysozyme (Gripon et al. 1997; Guo B 1999; Haas C et al. 1999; Haas et al. 1999; Curtis et al. 2001). The solubility and the second virial coefficient both are determined by the protein–protein interactions. However, solubility depends on the short–range protein–protein interactions in the crystal phase with restricted orientations of the protein molecules, while the second virial coefficient provides a measure of the dilute protein–protein interactions that are Boltzmann–averaged over all distances and orientations in the liquid phase (Haas et al. 1999; Curtis et al. 2001).

The temperature independence of apoferritin solubility was reported in the literature (Petsev et al. 2001). The results from the static light scattering measurements at 30 °C and 40 °C indicated that there was no temperature effect on overall intermolecular interactions. Hence, the solubility of apoferritin can be assumed to be independent of temperature in the temperature range that was investigated. The significance of this

rather small temperature range becomes clear if one considers that the solubility of

lysozyme can change substantially over the same temperature range (Forsythe and Pusey

1996).
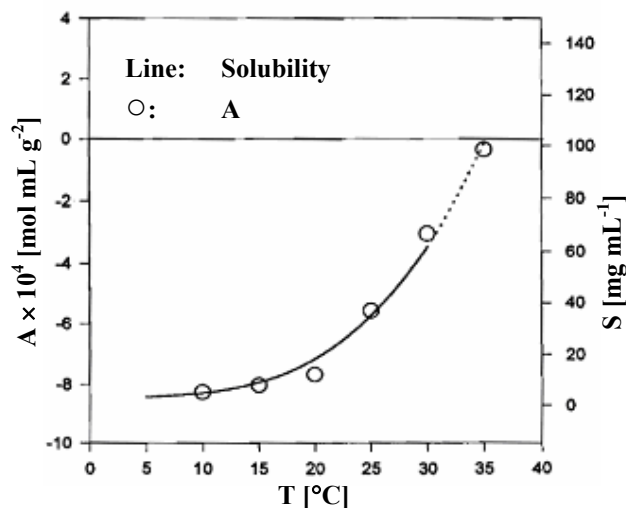


Figure 6-24:  Second virial coefficient and solubility as a function of temperature for lysozyme in 100 mM sodium acetate with 2.5% (w/v) NaCl at pH 4.2 (George et al. 1997)

In essence, the second virial coefficient is a highly predicative thermodynamic

parameter for apoferritin crystallization and static light scattering is an excellent method

for the system studied to measure that variable.  It was shown that cadmium is the leading

factor in apoferritin intermolecular interactions and in crystallization experiments over

temperature, apoferritin concentration and other divalent cations.  It is therefore essential

to find a means to prevent the binding of cadmium ions to the apoferritin molecules to

prevent potential cataract formation.  Unfortunately, the tested solubilizers were not able

to change the intermolecular interactions and were therefore unable to prevent apoferritin

crystal formation. Nevertheless, the search for a successful inhibitor of apoferritin crystallization has to be accelerated and intensified in future research to stop or at least prolong the onset of HHCS. The results obtained throughout the research can also give insight into naturally occurring biological crystallization events and into the pathophysiology of other protein condensation diseases.

## 6.8 Special Considerations about Cadmium

After various other divalent cations beside cadmium did not seem to induce attractive intermolecular apoferritin interactions, the physico-chemical properties of divalent cations in general and of cadmium in particular were considered to explain the observed phenomena.

In general, there exist direct and indirect effects of the addition of salt ions to protein solutions. The most important direct effect of additives on protein crystallization is the adsorption of ions onto protein charged groups to produce a net neutral species since only net neutral protein molecules crystallize, and the minimum solubility of a protein occurs at its isoelectric point. A protein at a pH above its isoelectric point has a net negative charge and must adsorb cations to produce a net neutral species; a protein at a pH below its isoelectric point has a net positive charge and must adsorb anions to produce a net neutral species (see Figure 6-21). The indirect effects are characterized by ions and organic solutes affecting protein crystallization via intervening water molecules through excluded volume, water activity and interfacial effects (Collins 2006).

As for the efficiency of monovalent salts to induce crystallization by generating attractive intermolecular interactions between protein molecules in solution it was found

that it likely to be limited to a few (preferentially low $M_W$) proteins, with lysozyme reflecting an extreme case (Tardieu et al. 2001). This notion is backed up by molecular simulations that showed that monovalent cations do not induce attractive intermolecular interactions, whereas for divalent cations the potential of mean force indeed is negative for some distance between the molecules and that at that distance the two like-charged proteins experience attraction (Prausnitz 2003). The minimum of the mean force corresponds to a separation distance sufficient to accommodate a monolayer of counterions between the two protein molecules (Tavares et al. 2004).

In general, cadmium atoms are positioned at the interface between two neighboring protein molecules and coordinated by two carboxyl groups of glutamic or aspartic acid side chains each belonging to one of the two molecules. This coordination is often supplemented by coordination bonds formed with carbonyl groups of the polypeptide backbone and/or with a water molecule. Similar cadmium coordinations at intermolecular contacts have been found in ferritin crystals. In native cubic horse spleen ferritin (Granier et al. 1997), two cadmium ions occupy special positions on a threefold axis and are coordinated by three glutamine or three aspartic acid residues, respectively. A third cadmium ion occupies a twofold axis and is coordinated by glutamic acid and aspartic acid residues from different molecules.

There exists strong evidence that the propensity of cadmium cations to form coordination bonds enables the development of cadmium bridges across the interfaces of protein molecules. Side groups of various amino acids, water molecules, and carbonyl groups of the protein backbone chain can serve as crystallization coordination partners. The unique pattern of the negative charge distribution on the surface of any given protein

molecule will necessitate the variation of the cadmium concentration to create the conditions essential for cadmium coordination and crystal formation (Trakhanov et al. 1998). Furthermore it was shown that the binding of divalent cations to protein molecules overcomes the salt exclusion due to the surface tension increase, leading to a decrease in the preferential hydration (Arakawa and Timasheff 1984).

The Hofmeister series was created by the evidence that neutral salts varied in their effect on the solubility of proteins. One group of salts could be ranked according to their efficiency at precipitating proteins, while a second group of salts could be ranked according to their efficiency at solubilizing proteins. Essentially this same total ordering of ions, with the same sign change between the two groups, can be generated by measuring their effect on protein stability or from many different physical measurements of aqueous salt solutions, such as the Jones-Dole viscosity $B$ coefficients (see Figure 6-25). The Jones-Dole viscosity $B$ coefficient is a direct measure of the strength of ion–water interactions normalized to the strength of water–water interactions in bulk solution: positive $B$ coefficients for strongly hydrated ions and negative $B$ coefficients for weakly hydrated ions. The point at which the Jones-Dole viscosity $B$ coefficient changes sign represents ideal behavior as defined by the strength of water–water interactions in bulk solution (no preferential interactions) (Collins 2004).

When comparing the values of the Jones-Dole viscosity $B$ coefficients in Figure 6-25 it becomes clear that with cadmium having a medium strong positive $B$ coefficient the extraordinary position of that divalent cation in the crystallization of apoferritin apparently does not follow the Hofmeister series for solubilizing or destabilizing salts.

Hence more research has to be devoted to better understand the extraordinary interaction between apoferritin and cadmium.
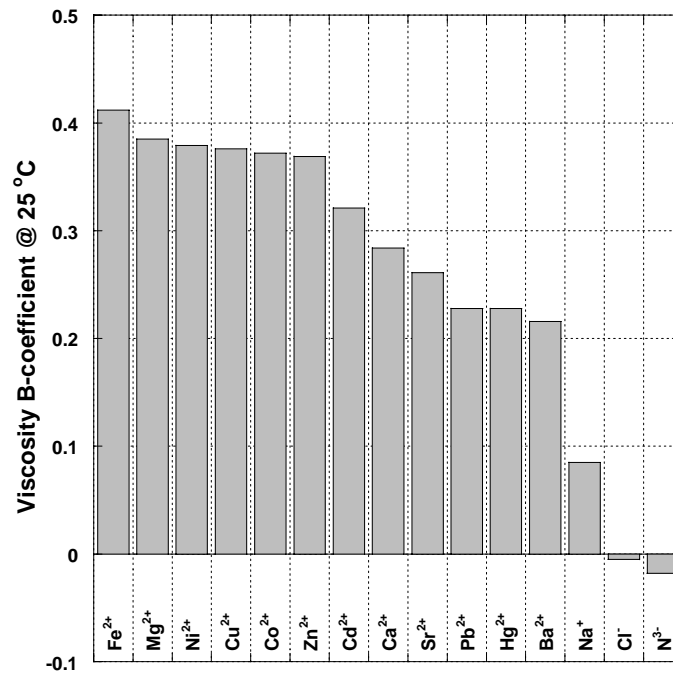


Figure 6-25.  Viscosity B-coefficients of ionic elements (Anon 2000)

# CHAPTER 7

# CONCLUSION AND RECOMMENDATIONS

## 7.1 Conclusions

The results of this research have an impact in terms of both advancing the fundamental science of macromolecular crystallization as well as proposing future clinical procedures for evaluating the tendency of patients to develop cataracts and in particular for preventing the occurrence of Hereditary Hyperferritinemia Cataract Syndrome (HHCS) through specific pharmacological interventions. Thus, this research may suggest innovative pharmacological approaches to prevent cataract and other protein condensation diseases.

To be able to conduct crystallization experiments on a small scale, a microbatch crystallization apparatus has been modeled, designed and improved that enables (1) multiple batch crystallization experiments at various temperatures and solution conditions in parallel and (2) quantitative monitoring of crystal growth without disturbing the progress of an experiment for observation. The multiwell microbatch crystallization device controlled the crystallization temperature and provided a thermal gradient with small temperature increments along the gradient. The setup allowed testing of a 2-dimensional matrix of crystallization conditions with temperature being one of them and to monitor crystal growth inline at defined time intervals.

The high-throughput crystallization apparatus has been constructed from readily available equipment, such as light microscopes with digital imaging capabilities. Despite

appreciable fluctuations in the ambient laboratory temperature the crystallization apparatus maintained constant temperatures in the wells over a period of days, with standard deviations of less than 0.03 °C per well. The design of the thermal gradient plate was kept very general so as to facilitate the use of any multiwell plate with a standard 96-well footprint, which can also be extended to vapor-diffusion crystallization experiments. Furthermore, the thermal insulation plate used can easily be altered to fit different automated microscope stages or other apparatuses. An initial set of crystallization experiments with the model protein lysozyme clearly demonstrated the effect of temperature on crystallization and showed the ability of the system to track crystal growth over long periods of time.

The primary application of the apparatus throughout the study was the crystallization of apoferritin under near physiological conditions. The crystallization experiments in the presence of divalent cations, mainly cadmium, required the quest for an appropriate buffer system. Tris-HCl was found to have a low temperature coefficient while at the same being compatible with cadmium.

The rationale for the conducted research was to evaluate the propensity of apoferritin to crystallize or precipitate out of physiologic fluids, thereby elucidating means to encourage the proteins to remain in solution. The means explored in this study was the use of solubilizers to stabilize the protein molecules in solution and therefore hinder solid-liquid phase separation. The commercially available solubilizers, different non-detergent sulphobetaines (NDSBs) and sugars, were therefore tested for their compatibility with the protein molecules. After circular dichroism did not work appropriately due to strong background absorbance of the solubilizers, analytical size-

exclusion chromatography was used successfully to elicit overall structural conformity of the protein molecules in the presence of solubilizers. The stability tests were extended to two other large multimeric proteins (Mandelate racemase and Catalase) to obtain a more general picture as to whether there exists the potential of the solubilizers to compromise the integrity of the quaternary structure of the proteins. In all cases, the solubilizers did not harm the protein structures and therefore were considered in the crystallization and static light scattering experiments.

The multiwell microbatch experiments of apoferritin demonstrated the dependence of apoferritin crystal growth kinetics and final crystal size on temperature and cadmium concentration. It was found that the phase change was solely a function of cadmium concentration and not a function of temperature for the temperature range studied. Nevertheless, the final crystal size was clearly affected by temperature and it was discovered that it increased as temperature increased. At elevated cadmium concentrations the impact of temperature in the final crystal size diminished. Only for the lowest cadmium concentration tested under which apoferritin crystallization occurred (15 mM $CdCl_2$) could the initial growth rates be determined, since at higher cadmium concentrations the apoferritin crystals had mostly reached their final crystal size by the time of the first image acquisition. The Arrhenius plot revealed an activation energy for apoferritin crystal growth of $\Delta E_G = 346$ kJ/mol, which was 10-fold greater compared to the activation energy for apoferritin nucleation reported previously. The larger activation energy of crystallization compared to the activation energy of nucleation offered an explanation for the formation of fewer and larger apoferritin crystals at higher temperatures. Hence, the results of this study showed that the crystal growth kinetics are

affected by temperature, profoundly under some conditions. Hence temperature control should be a prerequisite for apoferritin crystallizations, which is in contrast to published experiments, where that has not been consistently practiced.

Real therapeutical value for protein condensation diseases can be derived from the second virial coefficient measurement of protein solutions as this thermodynamic property might serve as a predictor for protein condensation irrespective of the path towards precipitation or crystallization, which may involve one or more of temperature, divalent cations and protein solubilizers. Indeed for conditions under which a dilute apoferritin solution revealed a positive second virial coefficient no apoferritin crystals were obtained even at concentrated protein solutions. On the other hand, dilute apoferritin solutions for which the second virial coefficient was determined to be negative always produced apoferritin crystals at elevated protein concentrations. This result can be invaluable for diagnostic purposes for families whose members are affected by the HHCS disease.

After the predictive character of the second virial coefficient was established for less expensive horse spleen apoferritin solutions under near physiological conditions, the static light scattering experiments were extended to apoferritin molecules from human sources. For all apoferritin samples used throughout the study cadmium seemed to be the only divalent cation that induced apoferritin crystallization. Compared to horse spleen apoferritins the intermolecular interactions of the human apoferritin samples were negative, i.e. overall attractive at much lower cadmium concentrations. Therefore the contamination with divalent cations is possibly much more crucial in humans and therefore in the cataract formation.

The possible treatment options for the particular protein condensation disease that was targeted in this study, the use of certain commercially available NDSBs and sugars, did not alter the overall attractive or repulsive protein interactions in solution which was predictable from the protein stability tests where the solubilizers did not form or stabilize a hydration layer around the protein molecule.

Finally, throughout this study it was determined that apoferritin crystallization only occurs in the presence of cadmium ions at a specific concentration and the second virial coefficient retains its predictive capacity irrespective of the means to generate the driving force for the protein to come out of solution.

## 7.2 Recommendations

The following recommendations are offered for future work:

(1) Although both the crystallization and static light scattering experiments were conducted under near physiological conditions (pH, temperature and salinity) the protein solution was still idealized in that purified homopolymeric protein solutions were used. Therefore, the research should be expanded to systems including apoferritin oligomers, mixtures of apoferritins with different H- to L-subunit rations and mixtures of proteins. The presence of apoferritin oligomers in solution was reported earlier (Thomas et al. 1998) to have led to higher nucleation rates and hence more but smaller crystals compared to the monomeric solution. To mimic the ocular lens environment more closely the intra- and intermolecular

interactions of apoferritins in the presence of crystallins (the majority of lens proteins belong to a single family of proteins called the crystallins) should be investigated.

(2) The solubilizers used in the study were basically three commercially available zwitterionic ammonium propane sulphonic derivatives. The search should be expanded to other NDSBs, some of which might have to be synthesized in the laboratory since the number of commercially available solubilizers is limited. In most protein stability and protein solubility research reported in the literature the NDSBs that were investigated were synthesized in the laboratory and the detailed recipes were made available (Vuillard et al. 1994; Vuillard et al. 1995).

(3) The apparent primacy of cadmium in apoferritin crystallization should be subject to further investigation. Calcium seemed to have an additive effect on the intermolecular apoferritin interactions but alone did not foster overall attractive forces between apoferritin molecules. Therefore the type of interactions between divalent cations and apoferritin molecules requires further examination.

(4) It is unclear whether the apoferritin crystals in HHCS originate in the inter- or intracellular lumen of the ocular lens (Brooks, personal communication). Naturally occurring crystallization events *in vivo* sometimes occur in membrane encapsulated vesicles (see Chapter 2.1) and hence the lipid double layer could also potentially function as a nucleation site. Lipid bilayers can easily be

integrated into the microbatch crystallization setup, since only the paraffin oil would need to be replaced with another type of oil that more closely mimics the naturally occurring lipid bilayers.

(5) The research should be extended to other protein condensation diseases where protein crystallization or even protein precipitation is the pathological cause of the disease. It was shown that static light scattering of dilute protein solutions that exhibit protein precipitation rather than crystallization can be evaluated as well.

# APPENDIX A

# THERMAL GRADIENT PLATE

## A.1 Designing the Thermal Gradient Plate

### A.1.1 First Generation Thermal Gradient Plate

The first generation thermal gradient plate was based on a device used for protein batch crystallization in glass pipettes (from now on called Luft device) (Luft et al. 1999). This included the overall dimensions and material used. The device was machined out of a sheet of aluminum since the material combines light weight to satisfy the load limitations of the automated microscope stage with an appreciable thermal conductivity to obtain a unidirectional and linear thermal gradient. Whereas the Luft device was designed to hold glass pipettes that have to be sealed off by melting the glass, the thermal gradient plate in Figure A-2 and A-3 was engineered to hold any regular multiwell plate with a standard 96-well plate footage.

One of the drawbacks of the Luft device is the exposure of the protein solution to elevated temperatures while sealing the glass pipettes by melting the glass. It has been shown that the thermal history of protein solutions has an effect on protein crystallization. Therefore heat treatment of any protein solution that is to be crystallized might compromise the crystallization outcome (Burke et al. 2001).
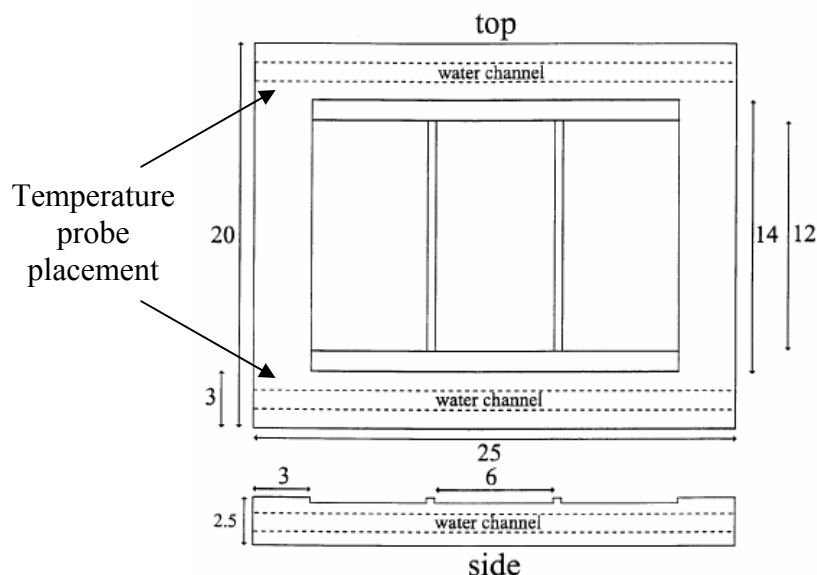
Figure A-1. Schematic drawing of the thermal gradient, machined out of an aluminum plate. There are three depressions, each capable of holding 50 micropipettes simultaneously. Dimensions are in cm. (Luft et al. 1999)

Furthermore the Luft device was not designed for online observation of the crystal growth progress and harvesting the crystals for x-ray diffraction studies is potentially problematic due to the enclosure in a solid glass pipette. The image acquisition problem has been included into the 1st generation thermal gradient plate by designing it to fit onto an automated stage of a light microscope (Figure A-3). The light microscope was fitted with a digital camera to allow for automated image acquisition (see Chapter 4.3 for details). The automated stage provides horizontal centering of the image field to a particular well at specified time intervals. The crystals can furthermore be harvested easily in a batch crystallization setup under oil for x-ray crystallography analysis. The crystallization solution does not have to be removed from its thermal environment for image analysis as in the case of the glass pipettes which could lead to further crystal growth or, even worse, to crystal dissolution.
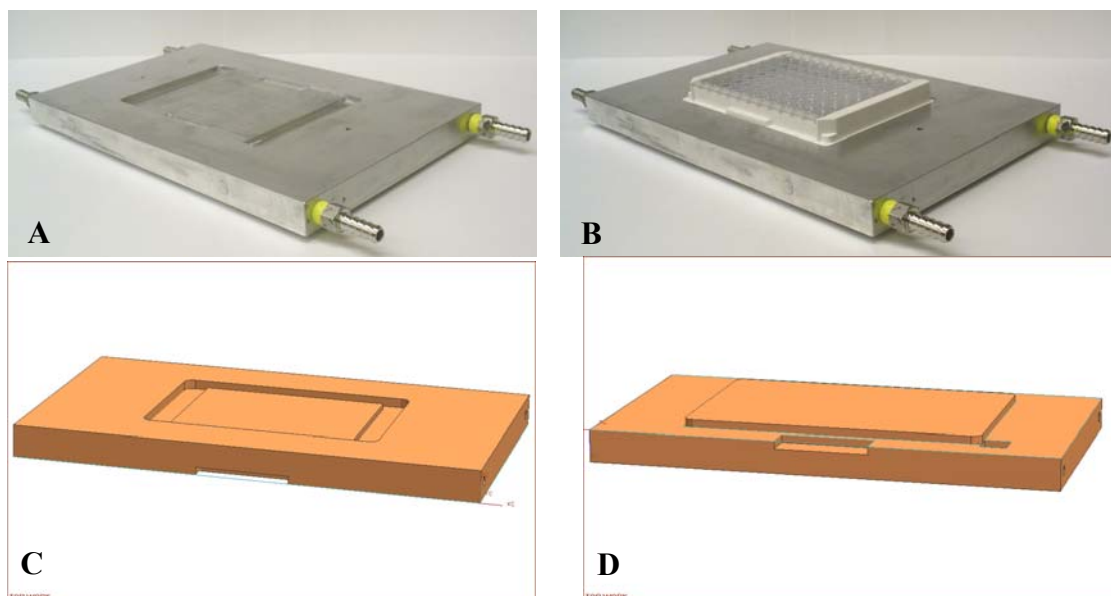
Figure A-2.  First generation thermal gradient plate; A. aluminum plate with Swagelok hose fittings connected to the water channels; B. aluminum plate with standard 96-well plate; C Schematic of 1st generation thermal gradient plate, top view; D Schematic of 1st generation thermal gradient plate, bottom view
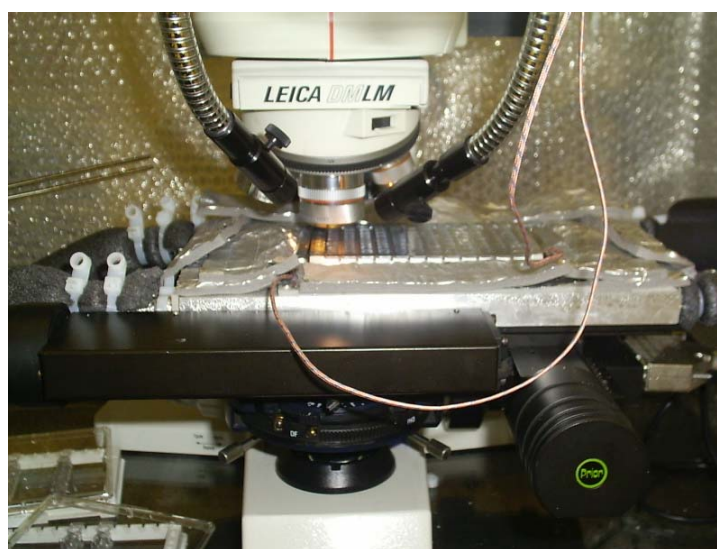


Figure A-3.  Thermal gradient plate mounted on top of the automated stage

The overall dimensions of the plate in Figure A-2 were dictated by the automated stage of the microscope that it was mounted onto. The bottom of the plate with its indentations (Figure A-2) was machined to fit tightly onto the automated stage without allowing any horizontal or vertical movement of the plate. The automated stage setup did not allow for a straight water channels from left to right across the plate as used in the second generation plate design (see Figure 4-3 and Chapter 4.3). It was therefore necessary to create a U-shape channel design (see Figure A-4) to accommodate the tubing connection to the water baths (see Figure A-2) that would otherwise interfere with the movement of the automated stage.
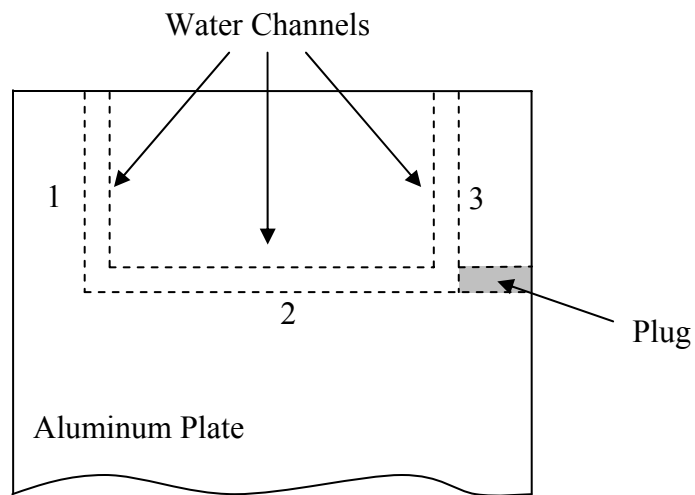


Figure A-4. Water Channel setup of 1$^{st}$ generation plate design (top view). The numbering refers to the order in which the channels have been drilled.

Two water channels were drilled according to Figure A-4 where channel number 2 was closed with an aluminum plug afterwards to create a u-shaped channel assembly. The ends of channels 1 and 3 where threaded to fit male ¼ inch inner diameter stainless

steel NPT-thread hose connectors (SS-4-HC-A-601, Swagelok).  The plate was heated and cooled through the water channels by connecting each of them to a circulating water bath (VWR 1157).  The detailed design with all dimensional information can be seen in Figure A-5 and Figure A-6.

**top**



Figure A-5. Technical drawing of the 1$^{st}$ generation thermal gradient plate – top view (dimensions in mm)

174

**bottom**

30.5
17 13.5
3

46 30
16
45

99

5 5

15

5

157 247

49

99

5 5

45

5

20 108 20

148

7.5 7.5

17

5

148
20 108 20
4
5
15
12
3 2 2
2

**side**

Figure A-6.  Technical drawing of the 1st generation thermal gradient plate – bottom view (dimensions in mm)

The temperature gradient was reported to be unidirectional and linear throughout the plate for the Luft device, determined by two thermocouples placed at the edge of the plate on opposite ends (Figure A-1). It was assumed that the temperatures within the glass pipettes were identical to the surface temperatures of the thermal gradient plate. No direct temperature measurements within the protein solutions were conducted because of the glass enclosure (Luft et al. 1999).

The surface temperature on the thermal gradient plate was measured with a surface temperature probe. A grid of measuring points was drawn onto the surface that houses the multiwell plate. The measuring points were equally spaced about 5 mm apart and parallel to the water channels.

The temperature gradient was not unidirectional but there was also a change in temperature parallel to the water channels. This observation worsened when the plate was actually placed onto the automated stage (data not shown). The automated stage, made of metal as well, functioned as a heat sink at the bottom of the thermal gradient plate. The plate design did not allow for additional insulation material to be added that would separate the thermal gradient plate from the automated stage.

## A.1.2 Technical Drawing of the Second Generation Thermal Gradient Plate
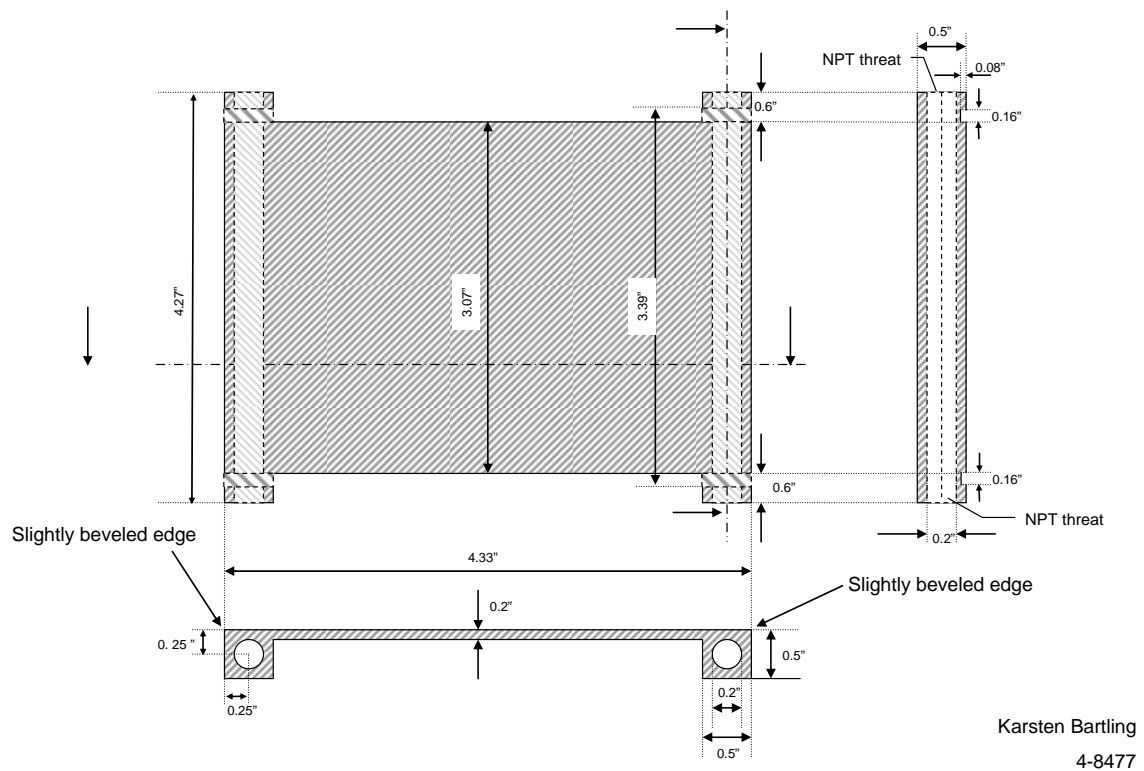


Figure A-7.  Technical drawing of modified thermal gradient plate (dimensions in inch)

**A.1.3 Technical Drawing of the Thermal Insulation Plate**
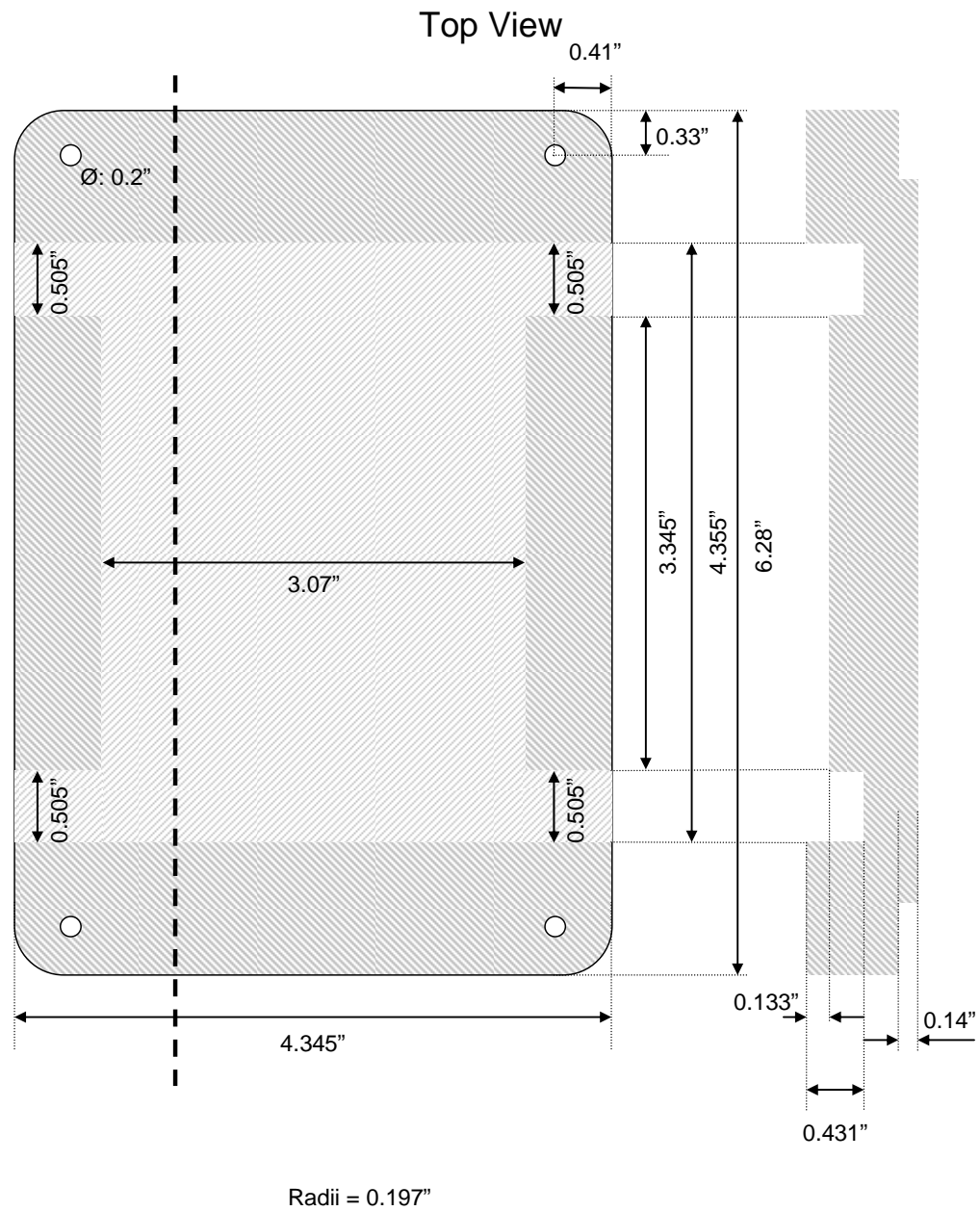
Top View



Figure A.8.  Technical drawing of the insulation plate – top view (dimensions in inch)
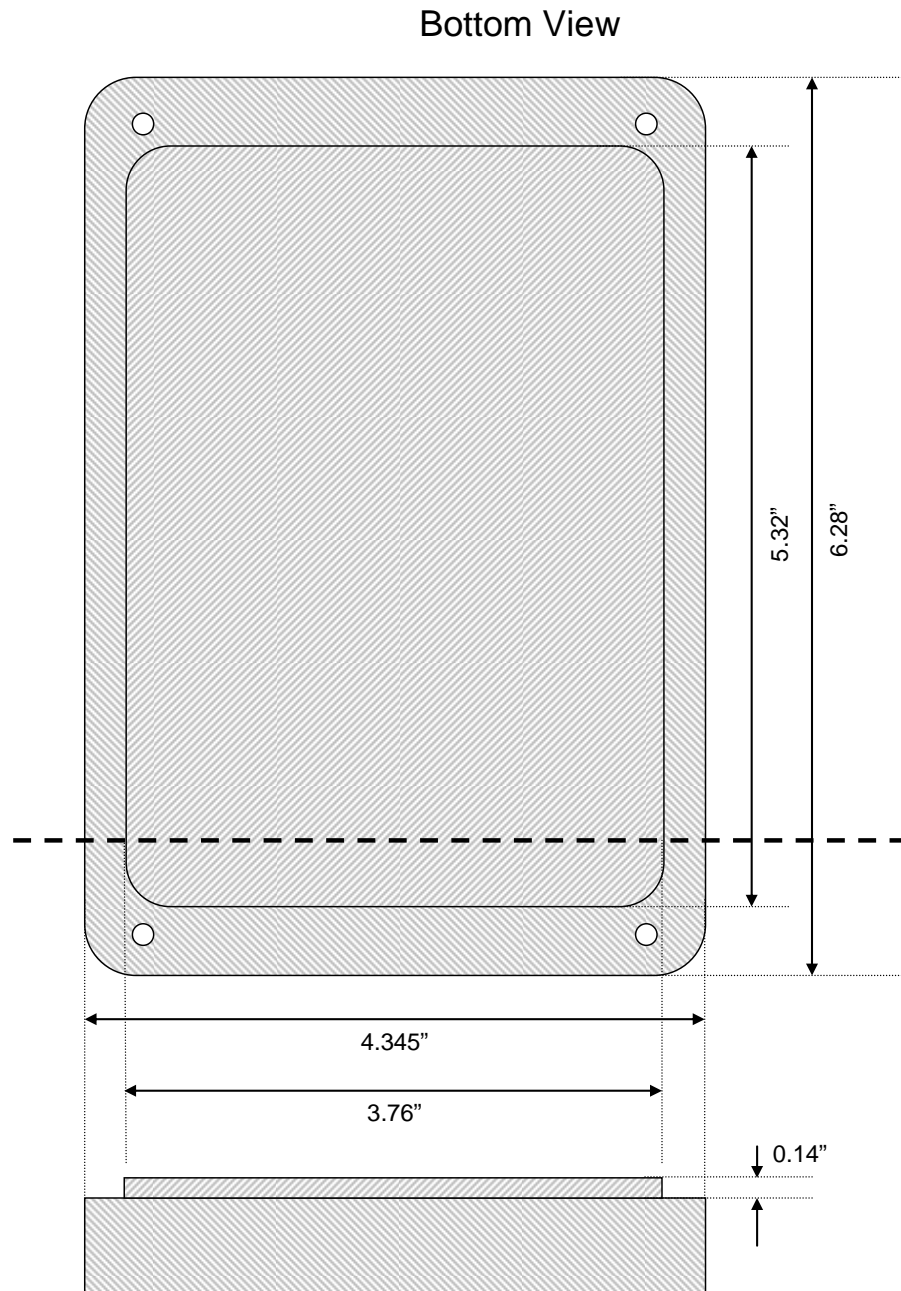
Bottom View



Figure A-9. Technical drawing of the insulation plate – bottom view (dimensions in inch)

## A.2 Image Pro Macros

Image-Pro Plus (version 4.9) allows for customized macro programming. Two macros have been created that allow for image acquisition of any multiwell plate configuration, including different well numbers, well patterns and well shapes (round, quadratic, etc.). Both macros have a built-in timer function that allows for timed image acquisitions. Furthermore, image filing is versatile in that the image file names can be altered to meet specific requirements. Throughout the macros comments have been placed to explain the function of certain program operations. The comments start with an apostrophe to distinguish them for the reader and for Image-Pro Plus from program commands. At times even program commands are made inactive by an apostrophe at the beginning of the line to indicate how the macros can be altered without having to delete program commands. The macros are kept highly versatile in that they use commands that will automatically implement the current settings within the Scope-Pro user interphase like the well pattern, well number and well location. In general, most settings that change from experiment to experiment will be automatically applied to the macros eliminating the need to change the macro itself.

The two macros are very similar and only differ in the ability to acquire multiple z-plane images versus single plane image acquisition. The first macro does not have any z-plane function and uses the initially set z-plane for image acquisition. The second macro is extended to allow for multiple image acquisitions in different z-planes per well. Although in theory both macros should have been able to be combined into one macro, selecting one as the number of z-planes in a single plane image acquisition led to an error message. After consulting with the technical staff from Media Cybernetics and Vashaw

Scientific, it was apparent that several command functions in the program manual actually did not work at all or were malfunctioning. Therefore two macros were generated to accommodate different z-plane image acquisitions.

The second macro for multiple z-plane image acquisitions worked well from a program standpoint. Unfortunately the automated stage hardware does not have any reference positioning tool were the movement in any direction is with respect to a fixed point in space. The movement in x and y-direction is accomplished by two separate motorized drives. The planar movement with respect to an initially set reference point is kept accurate over several image acquisition cycles. The movement in z-direction uses the focusing knob of the microscope to which a motorized drive is attached. This setup is not accurate with respect to vertical movement of the automated stage. As a result the focal plane shifts slightly with every image acquisition and therefore the multi z-plane image acquisition was not further used throughout the crystallization experiments.

## A.2.1 Single Plane Macro

```
Option Explicit
Declare Function GetTickCount Lib "kernel32" Alias "GetTickCount" () As Long
Global gList As Integer, gPoint As Integer

Sub Single_Plane_new ()

        Dim iDebug As Integer
        Dim NumGroups As Single
        Dim NumWells As Single
        Dim NumFields As Single
        Dim NumPlanes As Single
        Dim GroupLoopCtr As Integer
        Dim WellLoopCtr As Integer
        Dim FieldLoopCtr As Integer
        Dim PlaneLoopCtr As Integer
        Dim i As Integer
        Dim PathSpec As String * 255
        Dim FileSpec As String * 80
        Dim GroupSpec As String * 10
        Dim WellSpec As String * 10
        Dim FieldSpec As String * 10
        Dim PlaneSpec As String * 10
        Dim TimeSpec As String * 100
        Dim PicSpec As String *200
        Dim SamplePtn As String * 255
        Dim ScanPtn As String * 255
        Dim j As Integer
        Dim timestamp As Long
        Dim fTime As Long
        Dim tTime As Long
        Dim Pause As Long
        Dim fPause As Single
        Dim Iterations As Integer
        Dim LoopTime As Integer
        Dim CrystType As String * 20
        Dim MagType As String * 20
        Dim ProConc As String * 20
        Dim MyString As String * 60
        Dim ImageSpec As String * 10

' Change this to 1 to see debug comments

        iDebug = 1
```

'The next section allows for custom input that will be used later to "built" the file name and to specify the well type, tiled image analysis and image storage location. (Some of the commands are optional)

'ret = IpStGetString("What are you crystallizing (e.g. lysozyme)?", CrystType, 20)
'ret = IpStGetString("What magnification are you using (e.g. 5x)?", MagType, 20)
ret = IpStGetString("Enter the sample pattern (e.g. 'Nunc 384well plate' or 'Greiner 1536')", SamplePtn, 255)
ret = IpStGetString("Enter the scan area (e.g. 'Scan Area 384wells' or 'Scan Area 1536wells')", ScanPtn, 255)
ret = IpStGetString("Enter path into which to store images (e.g. D:\experiment\)", PathSpec, 255)
'ret = IpStGetString("What acquisition# is this (this is just for image naming purpose)", ImageSpec, 255)
'The following lines allow for timed image acquisition

ret = IpStGetFloat("Time Interval? (min)", fPause, 10, 0, 240, 0.5)
ret = IpStGetInt("How many Intervals (max 200)?", Iterations, 2, 1, 200)
Pause = Int(fPause * 60 * 1000)
LoopTime = Int(fPause * 60 * 10) \ 10


' Load a Sample Pattern.  This function will load the "outer" Sample Pattern.  NOTE! This pattern is one of the template well patterns and therefore will not have the origin set. This means that you will get an error to the IpStageWell Auto-Pro function.

ret = IpStageSamplePatternByName(SamplePtn)
If ret <> 0 Then
        MsgBox "Unable to load sample pattern '" & SamplePtn & "'"
        Debug.Print "Error IpStageSamplePatternByName('" & SamplePtn & "')"
        Debug.Print ret
        End
End If


' Load a Scan Area.

ret = IpStageScanPatternByName(ScanPtn)
If ret <> 0 Then
        MsgBox "Unable to load sample pattern '" & ScanPtn & "'"
        Debug.Print "Error IpStageScanPatternByName('" & ScanPtn & "')"
        Debug.Print ret
        End
End If

' Get number of groups.  This function will get the number of groups that are defined in the sample pattern.

```
        ret = IpStageGet(STG_NUM_GROUPS, 0, NumGroups)
        If ret <> 0 Then
                MsgBox "Unable to determine number of groups."
                Debug.Print "Error IpStageGet(STG_NUM_GROUPS, 0, NumGroups)"
                Debug.Print ret
                End
        Else
                If iDebug = 1 Then
                        Debug.Print "Number of groups: "; NumGroups
                End If
        End If
```

' If we're not set to use the current sample pattern, or if no groups have been defined the above function will return 0.  The default for 0 groups is to use all of the wells

```
        If NumGroups = 0 Then
                NumGroups = 1
        End If
```

'Show magnification tab

```
        ret = IpStageShowTab(STG_SHOW, STG_LENS)
```

' Start timer

```
        For j = 1 To Iterations
                fTime=GetTickCount()
                Do
                        ret=IpMacroWait(LoopTime)
                Loop While GetTickCount() - fTime <= Pause
```

' Start group loop

```
                        For GroupLoopCtr = 0 To NumGroups-1

                        ret = IpStageSampleGroupByNum(GroupLoopCtr)
                        If ret <> 0 Then
                                MsgBox "Unable to select group #" &
                                CStr(GroupLoopCtr)
                                Debug.Print "Error
                                IpStageSampleGroupByNum(GroupLoopCtr))"
                                Debug.Print ret
                                End
```

```
                Else
                        If iDebug = 1 Then
                                Debug.Print "Starting group: "; GroupLoopCtr
                        End If
                End If
```

' Get number of wells in this group

```
                ret = IpStageGet(STG_WELLS_IN_CURR_GROUP, 0,
                NumWells)
                If ret <> 0 Then
                        MsgBox "Unable to determine number of wells in group #"
                        & CStr(GroupLoopCtr)
                        Debug.Print "Error
                        IpStageGet(STG_WELLS_IN_CURR_GROUP, 0,
                        NumWells)"
                        Debug.Print ret
                        End
                Else
                        If iDebug = 1 Then
                                Debug.Print "Number of wells in this group: ";
                                NumWells
                        End If
                End If
```

' If we're not set to use the current sample pattern

```
                '       the above function will return 0.
                        If NumWells = 0 Then
                        NumWells = 1
                End If
```

' Start well loop
```
                For WellLoopCtr = 0 To NumWells-1
```

' Move the stage to the beginning position of the current well. This will also set the XY origin for the Scan Area

```
                ret = IpStageWell(WellLoopCtr)
                If ret <> 0 Then
```

' Note: An error at this point probably indicates that the origin is not set for the currently selected well pattern
```
                        MsgBox "Unable to go to well #" &
                        CStr(WellLoopCtr) & " in group #" &
```

```
                                        CStr(GroupLoopCtr) & Chr(13) & Chr(10) &
                                        "Make sure to set the pattern origin."
                                        Debug.Print "Error IpStageWell(WellLoopCtr)"
                                        Debug.Print ret
                                        End
                        Else
                                If iDebug = 1 Then
                                        Debug.Print "Current well: "; WellLoopCtr
                                End If
                        End If
```

' Get number of fields in this Scan Area.

```
                        ret = IpStageGet(STG_NUM_FIELDS, 0, NumFields)
                        If ret <> 0 Then
                                MsgBox "Unable to determine number of fields"
                                Debug.Print "Error
                                IpStageGet(STG_NUM_FIELDS, 0, NumFields)"
                                Debug.Print ret
                                End
                        Else
                                If iDebug = 1 Then
                                        Debug.Print "Number of fields in this Scan
                                        Area: "; NumFields
                                End If
                        End If
```

'Start field loop

```
                        For FieldLoopCtr = 0 To NumFields-1
```

' Move the stage into position for the current video frame

```
                                ret = IpStageField(FieldLoopCtr)
                                If ret <> 0 Then
                                        MsgBox "Unable to go to field #" &
                                        CStr(FieldLoopCtr) & " in well #" &
                                        CStr(WellLoopCtr) & " of group #" &
                                        CStr(GroupLoopCtr)
                                        Debug.Print "Error
                                        IpStageField(FieldLoopCtr)"
                                        Debug.Print ret
                                        End
                                Else
                                        If iDebug = 1 Then
```

```vbnet
                                        Debug.Print "Current field: ";
                                        FieldLoopCtr
                        End If
        End If
```

' Acquire a video frame and tag it with the Stage-Pro properties.

```vbnet
                        ret = IpStageAcqFrame(ACQ_NEW)
                        If ret < 0 Then
```

' Note: An error at this point probably indicates that the acquire is set to retain workspaces. This macro will create 4 x 96 images (384, assuming all of the default settings) and the current version of the application supports only 200. Since each image is saved to file by the macro, you should make sure that 'Preserve Workspaces' is not checked.

```vbnet
                                MsgBox "Unable to acquire image"
                                Debug.Print "Error
                                IpStageAcqFrame(ACQ_NEW)"
                                Debug.Print ret
                                End
                        End If
```

' Build a file name from the loop counters

' This will get the name of the well in which the current active image was captured

```vbnet
                        ret =
                        IpStageDocGetStr(STGINF_SAMPLENAM
                        E, DOCSEL_ACTIVE, MyString)
                        FileSpec = IpTrim(PathSpec) +
                        IpTrim(MyString) + " 0" + Str$(j) + ".tif"
                        If iDebug = 1 Then
                                Debug.Print FileSpec
                        End If
```

' Save the File

```vbnet
                        ret = IpWsSaveAs(FileSpec, "TIF")
                        If ret <> 0 Then
                                MsgBox "Unable to save image file
                                '" & FileSpec & "'"
                                Debug.Print "Error
                                IpWsSaveAs(FileSpec, TIF)
                                Debug.Print ret
                                End
                        End If
```

```
'Close all active image windows

                              ret = IpAppCloseAll()

                    Next FieldLoopCtr

               Next WellLoopCtr

          Next GroupLoopCtr

     Next j
     ret = IpStGetString("Acquisition Complete", PathSpec, 255)
End Sub
```

### A.2.2 Multiple z-Plane Macro

```
Option Explicit
Declare Function GetTickCount Lib "kernel32" Alias "GetTickCount" () As Long
Global gList As Integer, gPoint As Integer

Sub Multiwellpattern()

        Dim iDebug As Integer
        Dim NumGroups As Single
        Dim NumWells As Single
        Dim NumFields As Single
        Dim NumPlanes As Single
        Dim GroupLoopCtr As Integer
        Dim WellLoopCtr As Integer
        Dim FieldLoopCtr As Integer
        Dim PlaneLoopCtr As Integer
        Dim i As Integer
        Dim PathSpec As String * 255
        Dim FileSpec As String * 255
        Dim GroupSpec As String * 10
        Dim WellSpec As String * 10
        Dim FieldSpec As String * 10
        Dim PlaneSpec As String * 10
        Dim NumberSpec As String * 10
        Dim SamplePtn As String * 255
        Dim ScanPtn As String * 255
        Dim j As Integer
        Dim aTime As Long
        Dim fTime As Long
        Dim Pause As Long
        Dim fPause As Single
        Dim Iterations As Integer
        Dim LoopTime As Integer
        Dim TimeSpec As String * 10
        Dim CrystType As String * 255
        Dim MagType As String * 255
        Dim MyString As String * 60


' Change this to 1 to see debug comments

        iDebug = 1
```

'The next section allows for custom input that will be used later to "built" the file name and to specify the well type, tiled image analysis and image storage location. (Some of the commands are optional)

```
'ret = IpStGetString("What are you crystallizing (e.g. lysozyme)?", CrystType,
255)
'ret = IpStGetString("What magnification are you using (e.g. 5x)?", MagType,
255)
ret = IpStGetString("Enter the sample pattern (e.g. Nunc 384well plate)",
SamplePtn, 255)
ret = IpStGetString("Enter the scan area (e.g. Scan Area 384wells)", ScanPtn,
255)
ret = IpStGetString("Enter path into which to store images (e.g. D:\test\)?",
PathSpec, 255)
```

'The following lines allow for timed image acquisition

```
ret = IpStGetInt("How many time points?", Iterations, 2, 1, 200)
ret = IpStGetFloat("Time Interval? (min)", fPause, 10, 0, 240, 0.5)
Pause = Int(fPause * 60 * 1000)
LoopTime = Int(fPause * 60 * 10) \ 10
```

' Load a Sample Pattern.

```
ret = IpStageSamplePatternByName(SamplePtn)
If ret <> 0 Then
        MsgBox "Unable to load sample pattern '" & SamplePtn & "'"
        Debug.Print "Error IpStageSamplePatternByName('" & SamplePtn & "')"
        Debug.Print ret
        End
End If
```

' Load a Scan Area.

```
ret = IpStageScanPatternByName(ScanPtn)
If ret <> 0 Then
        MsgBox "Unable to load sample pattern '" & ScanPtn & "'"
        Debug.Print "Error IpStageScanPatternByName('" & ScanPtn & "')"
        Debug.Print ret
        End
End If
```

' Get number of groups.  This function will get the number of groups that are defined in the sample pattern.
```
ret = IpStageGet(STG_NUM_GROUPS, 0, NumGroups)
```

```
                If ret <> 0 Then
                        MsgBox "Unable to determine number of groups."
                        Debug.Print "Error IpStageGet(STG_NUM_GROUPS, 0, NumGroups)"
                        Debug.Print ret
                        End
                Else
                        If iDebug = 1 Then
                                Debug.Print "Number of groups: "; NumGroups
                        End If
                End If

' If we're not set to use the current sample pattern, or if no groups have been defined the
above function will return 0. The default for 0 groups is to use all of the wells

                If NumGroups = 0 Then
                        NumGroups = 1
                End If

' Get the path to the IMAGES directory

'        IpAppGetStr(GETAPPDIR, 0, PathSpec)
'        PathSpec = IpTrim(PathSpec) & "Images\"

                For j = 1 To Iterations
                        fTime=GetTickCount()
                        Do
                                ret=IpMacroWait(LoopTime)
                                Loop While GetTickCount() - fTime <= Pause

' Start group loop

                                For GroupLoopCtr = 0 To NumGroups-1

                                ret = IpStageSampleGroupByNum(GroupLoopCtr)
                                If ret <> 0 Then
                                        MsgBox "Unable to select group #" &
                                        CStr(GroupLoopCtr)
                                        Debug.Print "Error
                                        IpStageSampleGroupByNum(GroupLoopCtr))"
                                        Debug.Print ret
                                        End
                                Else
                                        If iDebug = 1 Then
                                                Debug.Print "Starting group: "; GroupLoopCtr
                                        End If
                                End If
```

```vba
' Get number of wells in this group

                    ret = IpStageGet(STG_WELLS_IN_CURR_GROUP, 0,
                    NumWells)
                    If ret <> 0 Then
                            MsgBox "Unable to determine number of wells in group #"
                            & CStr(GroupLoopCtr)
                            Debug.Print "Error
                            IpStageGet(STG_WELLS_IN_CURR_GROUP, 0,
                            NumWells)"
                            Debug.Print ret
                            End
                    Else
                            If iDebug = 1 Then
                                    Debug.Print "Number of wells in this group: ";
                                    NumWells
                            End If
                    End If

' If we're not set to use the current sample pattern the above function will return 0.
Pretend that there's one
                    If NumWells = 0 Then
                            NumWells = 1
                    End If

                    ' Start well loop
                    For WellLoopCtr = 0 To NumWells-1

' Move the stage to the beginning position for the of the current well. This will also set
the XY origin for the Scan Area

                            ret = IpStageWell(WellLoopCtr)
                            If ret <> 0 Then

' Note: An error at this point probably indicates that the origin is not set for the currently
selected well pattern
                                    MsgBox "Unable to go to well #" &
                                    CStr(WellLoopCtr) & " in group #" &
                                    CStr(GroupLoopCtr) & Chr(13) & Chr(10) &
                                    "Make sure to set the pattern origin."
                                    Debug.Print "Error IpStageWell(WellLoopCtr)"
                                    Debug.Print ret
                                    End
                            Else
                                    If iDebug = 1 Then
```

```vb
                    Debug.Print "Current well: "; WellLoopCtr
                End If
        End If
```

' Get number of fields in this Scan Area.
```vb
        ret = IpStageGet(STG_NUM_FIELDS, 0, NumFields)
        If ret <> 0 Then
                MsgBox "Unable to determine number of fields"
                Debug.Print "Error
                IpStageGet(STG_NUM_FIELDS, 0, NumFields)"
                Debug.Print ret
                End
        Else
                If iDebug = 1 Then
                        Debug.Print "Number of fields in this Scan
                        Area: "; NumFields
                End If
        End If

        'Start field loop
        For FieldLoopCtr = 0 To NumFields-1
```

' Move the stage into position for the current video frame

```vb
                ret = IpStageField(FieldLoopCtr)
                If ret <> 0 Then
                        MsgBox "Unable to go to field #" &
                        CStr(FieldLoopCtr) & " in well #" &
                        CStr(WellLoopCtr) & " of group #" &
                        CStr(GroupLoopCtr)
                        Debug.Print "Error
                        IpStageField(FieldLoopCtr)"
                        Debug.Print ret
                        End
                Else
                        If iDebug = 1 Then
                                Debug.Print "Current field: ";
                                FieldLoopCtr
                        End If
                End If
```

' Get number of planes in this field.  If planes in the Z axis have been defined find out how many.
```vb
                ret = IpStageGet(STG_NUM_PLANES, 0,
                NumPlanes)
                If ret <> 0 Then
```

```vb
                                        MsgBox "Unable to determine number of Z
                                        planes"
                                        Debug.Print "Error
                                        IpStageGet(STG_NUM_Planes, 0,
                                        NumPlanes)"
                                        Debug.Print ret
                                        End
                Else
                        If iDebug = 1 Then
                                Debug.Print "Number of planes in
                                this field: "; NumPlanes
                        End If
                End If

' If no planes have been defined or if Z is not installed then make the plane loop limit = 1,
That way we will still get into the Acquire code

                                        If NumPlanes = 0 Then
                                        NumPlanes = 1
                                        End If

' Start plane loop

                                        For PlaneLoopCtr = 0 To NumPlanes-1

                                        ret = IpStagePlane(PlaneLoopCtr)
                                                If ret <> 0 Then

' NOTE: No error here - If no planes defined then just ignore error and continue with
acquire!
                                                        Debug.Print "Error
                                                        IpStagePlane(PlaneLoopCtr)"
                                                        Debug.Print ret

' NOTE: No end here because no error.

                                                Else
                                                        If iDebug = 1 Then
                                                        Debug.Print "Current plane:
                                                        "; PlaneLoopCtr
                                                        End If
                                                End If

' Acquire a video frame and tag it with the Stage-Pro properties.

                                        ret = IpStageAcqFrame(ACQ_NEW)
```

194

If ret < 0 Then

```
                                        MsgBox "Unable to acquire image"
                                        Debug.Print "Error
                                        IpStageAcqFrame(ACQ_NEW)"
                                        Debug.Print ret
                                        End
                                End If
```

' This will get the name of the well in which the current active image was captured

```
                                        ret =
                                        IpStageDocGetStr(STGINF_SAMPLENAM
                                        E, DOCSEL_ACTIVE, MyString)
```

' Change to appropriate number of zeros if large scan area

```
                                        PlaneSpec = "P" + Format(PlaneLoopCtr,
                                        "0")
```

' Build a file name from the loop counters

```
                                        FileSpec = IpTrim(PathSpec) +
                                        IpTrim(MyString) + " 0" + Str$(j) +" " +
                                        IpTrim(PlaneSpec) + ".tif"

                                        If iDebug = 1 Then
                                                Debug.Print FileSpec
                                        End If
```

' Save the File

```
                                        ret = IpWsSaveAs(FileSpec, "TIF")
                                        If ret <> 0 Then
                                                MsgBox "Unable to save image file
                                                '" & FileSpec & "'"
                                                Debug.Print "Error
                                                IpWsSaveAs(FileSpec, TIF)
                                                Debug.Print ret
                                                End
                                        End If
```

```
              'Close all active image windows
                                              ret = IpAppCloseAll()

                                    Next PlaneLoopCtr

                            Next FieldLoopCtr

                        Next WellLoopCtr

                  Next GroupLoopCtr

        Next j
        ret = IpStGetString("Acquisition Complete", PathSpec, 255)
End Sub
```

# APPENDIX B

# APOFERRITIN PURIFICATION

## B.1 Ferritin De-Ironiaition

### B.1.1 Ferritin Pre-Deironization
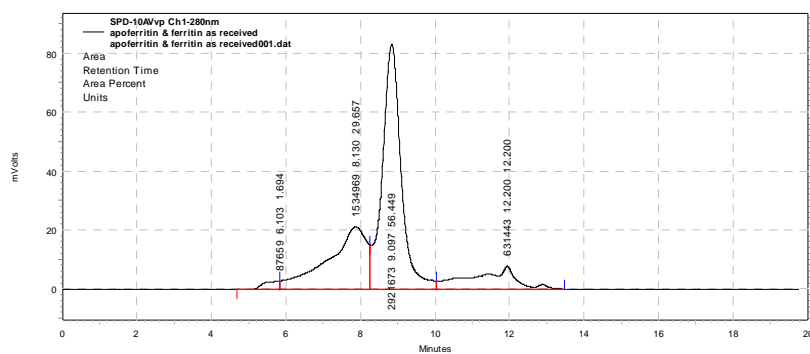


Figure B-1.  Equine Spleen Apoferritin (Sigma A-3641), as received, 5 mg/mL, 20μL injected
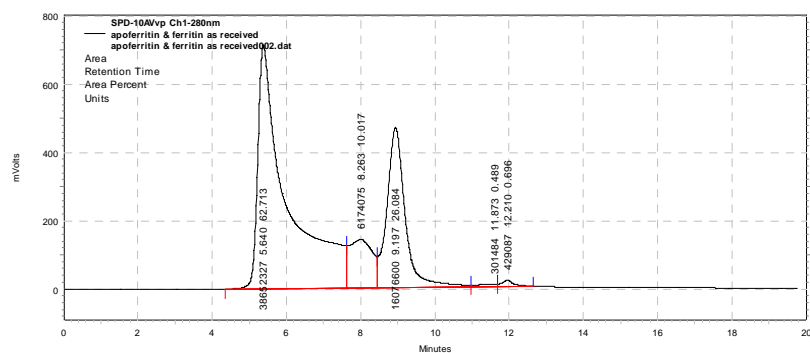


Figure B-2.  Equine Spleen Ferritin (Sigma F-4503), as received, 5 mg/mL, 20 μL injected
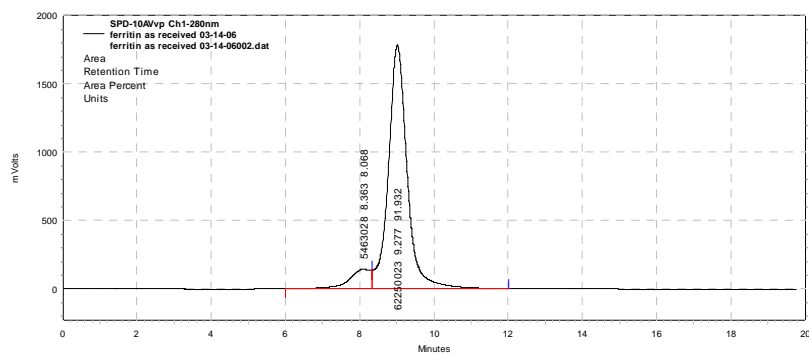
Figure B-3. Human Liver Ferritin, Pure (Cortex Biochem CP1003), as received, 3.5 mg/mL, 20μL injected
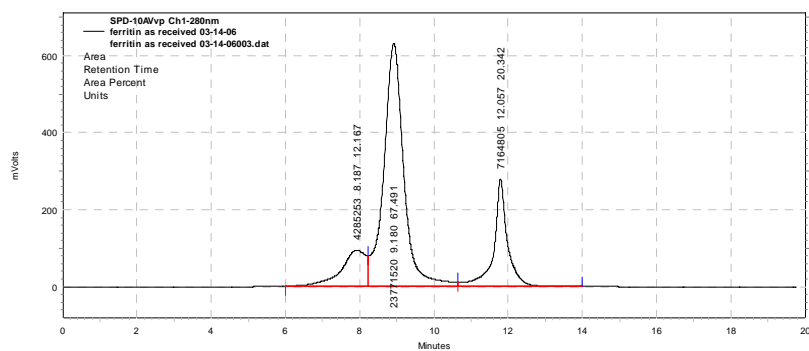


Figure B-4. Human Spleen Ferritin, Pure (Cortex Biochem CP1004), as received, 4.1 mg/mL, 20 μL injected

## B.1.2 Ferritin Post-Deironization
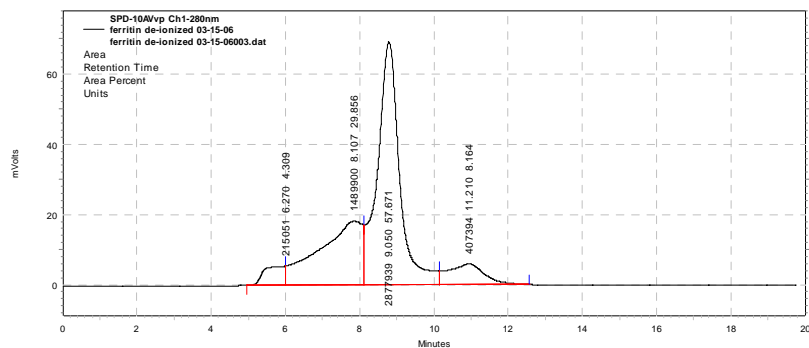


Figure B-5.  Equine Spleen (Apo-) Ferritin (Sigma F-4503), de-ironized, ~5 mg/mL, 20 µL injected
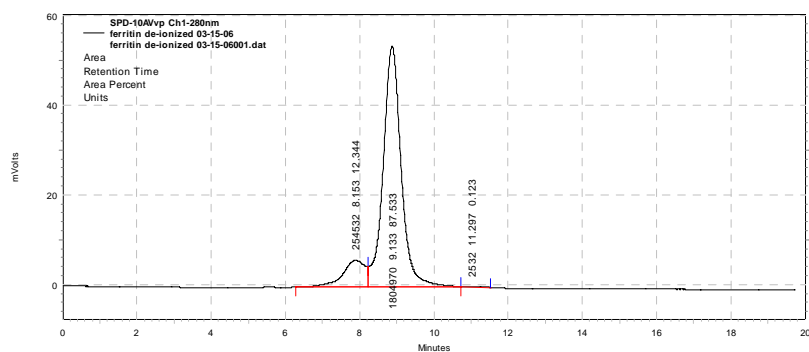


Figure B-6.  Human Liver Ferritin, Pure (Cortex Biochem CP1003), de-ironized, ~3.5 mg/mL, 20 µL injected
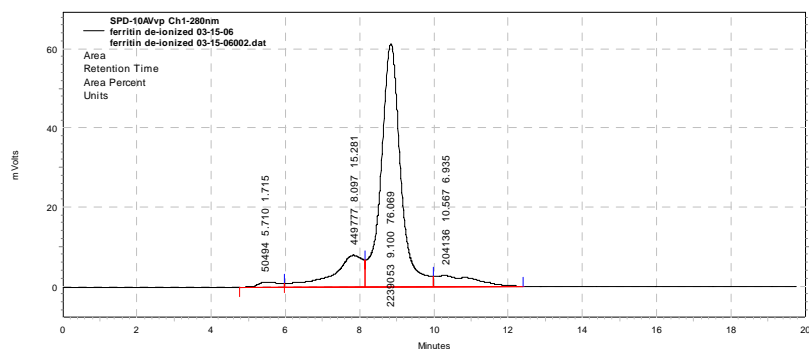


Figure B-7.  Human Spleen Ferritin, Pure (Cortex Biochem CP1004), de-ironized, ~4.1 mg/mL, 20 µL injected

## B.2 Preparative SEC-HPLC

If macromolecules other than proteins are to be purified, please be aware that the HiPrep 16/60 Sephacryl S-300 High Resolution column is designed for preparative purification of proteins and peptides only. The protocol can be altered in terms of flow rate, buffer composition, injection volume etc. Please consult with the column instruction manual for maximum flow rates, sample volume, pH stability, storage and handling.

All solutions are made with ultrapure water (Source: Labconco Waterpro P5) and are vacuum filtered (0.22 μm) prior to usage. The vacuum filtration removes particles that can clog the column and it degases the solution at the same time.

### B.2.1 Buffers

B.2.1.1 Running buffer

- 50 mM Tris-HCl, pH 7.40 @ 35 °C

  150 mM NaCl

  10 mM NaN$_3$ (preservative)

- Make 1000 mL of solution A:

  Trizma          6.057 g

  NaCl            8.766 g

  NaN$_3$          0.6501 g

- Make 1000 mL of solution B:

  HCl              50 mL of 1 N HCl

  NaCl           8.766 g

  NaN$_3$         0.6501 g

Mix A and B until desired pH is reached. To compensate for change in pH with temperature, use buffer calculator (http://researchlink.labvelocity.com/tools/buffer Calculator.jhtml) to calculate the pH at the current ambient temperature for it to be pH 7.40 at 35 °C.

B.2.1.2 Storage buffer

20% (v/v) Ethanol

B.2.1.3 Rinsing buffer

To make 1000ml:

NaN$_3$         0.6501 g

dH$_2$0        ad 1000ml

**B.2.2 Preparative SEC-HPLC Protocol**

This protocol was written for the purification of ≤ 2 mL of as-received protein solution. The column itself can handle a sample volume of up to 5 mL. However the current sample loop of the injector is 2 mL. Less than 2 mL sample volume is always possible with the current sample loop. Never let the column sit in any buffer other than

the rinsing or the storage buffer (salt in the buffer can precipitate out and clog the column). If purification is done on two consecutive days turn down the flow rate of the running buffer to about 0.05 – 0.1 mL/min overnight. The single most important operating restriction of any liquid chromatography column is to never let it run dry. The general steps involved in the preparative SEC-HPLC are depicted in Figure B-8.

```
        ┌─────────────┐
        │   20% EtOH  │
        └──────┬──────┘
               ↓
        ┌─────────────┐
        │Rinsing buffer│
        └──────┬──────┘
               ↓
        ┌─────────────┐
        │Running buffer│
        └──────┬──────┘
               ↓
        ┌─────────────┐
        │   Sample    │
        └──────┬──────┘
               ↓
        ┌─────────────┐
        │Rinsing buffer│
        └──────┬──────┘
               ↓
        ┌─────────────┐
        │   20% EtOH  │
        └─────────────┘
```
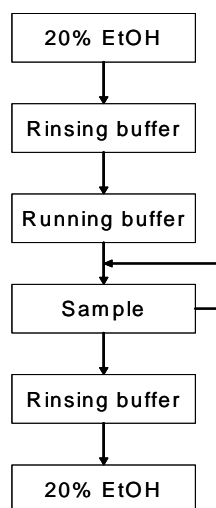
Figure B-8. Operation flow chart for preparative SEC-HPLC

Column specifications:

- Column volume: 120 mL
- Sample volume: up to 5 mL
- Recommended flow rate: 0.5 mL/min
- Maximum flow rate: 1 mL/min
- Maximum pressure: 21 PSI
- pH stability: 3-11

*Note*: Prepare sufficient amount of buffers. The column has to be equilibrated with at least 3-4 column volumes of buffer. Be aware that the column has to be washed again

with 3-4 column volumes of rinsing buffer after the purification step (see Figure B-8). Vacuum filter all the buffers with a 0.22 μm filter. This will filter and degas the buffers at the same time.

- Set pressure limits on LDC Analytical pump (CM4000) by pressing "Lim" on the keypad. The maximum pressure of the current column is 21 PSI, the lower limit should remain at 0 PSI. Confirm each entry by pressing enter, "Ent".

- Close the valve of the transport syringe (spring loaded) and disconnect from the column. While still disconnected from the column start the pump to purge the feeding tubes to the column. Connect the column: a) the top of the column to the outlet of the injection valve and b) the bottom of the column to the UV detector.

- The column is stored in 20% (v/v) ethanol if not used for more than 2 days. Start rinsing the column at low flow rate (0.3 mL/min). Always gradually increase flow rate to maximum flow rate, e.g. in 0.1 mL/min steps over ~ 5 minutes.

- Up to 3 different buffers can be connected to the pump at any time. Make sure that the pump draws from the correct line (buffer). Check by pressing the "%" button on the keypad of the pump. Set the time delay to 0.1 min (setting the delay time to a longer time period will cause the buffer change to be gradually rather than immediately). After switching the buffer the proportioning valves of the pump (Figure 2) will automatically switch to the corresponding buffer (A, B or C). The switch is accompanied by a loud clicking sound. It might take a few seconds until the click occurs, depending on the current flow rate. After the click occurred stop the flow immediately. Insert a syringe to the prime/purge valve at the pump, open the valve and drain ~ 10 mL. This will remove potential air trapped in the line to the buffer reservoir. Close the valve and restart the flow.
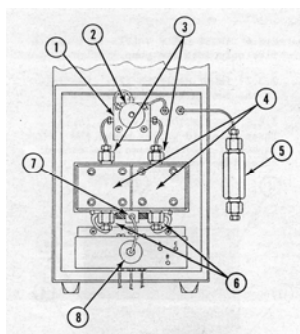
**LDC Analytical pump CM4000**
1. Pressure Transducer
2. Prime/Purge valve
3. Outlet check valves
4. Liquid ends
5. High pressure static mixer
6. Inlet check valves
7. Inlet manifold
8. proportioning valves

Figure B-9.  LDC Analytical Pump front panel

- After the column is equilibrated with the running buffer turn on the UV detector (minimize operating time to preserve lifetime of the lamp).

- Purge the reference loop (REF) of the UV detector by connecting the outlet of the column to the inlet of the reference loop.  Close the reference loop, set the UV detector to 280 nm and zero the detector.

- Make sure to rinse out the injection loop at the injection valve (Position B, see Figure 3) with the running buffer before loading the protein sample.  Otherwise the sample might get contaminated with residues from prior samples or other buffers that are still present in the sample loop.



**Position A**              **Position B**
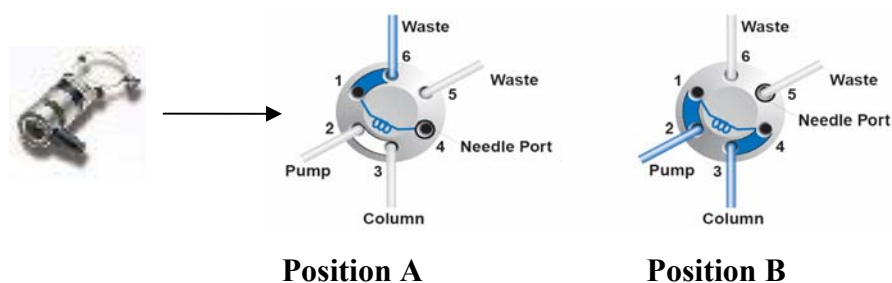
Figure B-10.  Rheodyne Injection Valve

- Switch injection valve to Position A (LOAD). Use a plastic syringe and a blunt-end needle to inject the sample. No prior treatment of the as-received apoferritin solution is required. Insert the needle all the way into the needle port and slowly inject the sample into the sample loop. *Note:* The liquid that drips out of a tube at the back of the injection valve is just running buffer that is being replaced by the sample. Remove the needle.

- Quickly switch the injection valve to Position B (INJECT) and start the timer.



Figure B-11. Schematic illustration HPLC column with storage syringe

- Apoferritin will elute from the column in the following order:
- Oligomers/Dimers > Monomers > Subunits
- At a flow rate of 0.5 mL/min the first peak will appear after ~1 hour, the monomers after ~1:27 hours and the subunits after ~3:00 hours. Go by the UV reading.

- Start collecting the monomer peak ~3 minutes after the UV reading increases again: place the tube of the column exit into a 50 mL centrifuge (Falcon) tube.

- Continue running the column with running buffer until the UV reading is almost zero again (baseline) after the subunit peak has passed.

- Change to rinsing buffer (see section 6) and rinse column with 3-4 column volumes.

- Decrease flow rate to 0.3 mL/min and change to 20% (v/v) EtOH and equilibrate with 3-4 column volumes.

- While still pumping attach the transport syringe to the exit of the column (see Figure 4), open the valve and let the syringe fill up. *Note:* Do not let the syringe fill up all the way, since the back pressure might be too high otherwise. Let it fill to about the 26-27 mL mark.

- Stop and turn off the pump, turn off the UV detector. Unplug the inlet tube to the column and insert a blind connector (do not close the valve at the transport syringe).

**B.2.3 Concentrating Eluted Protein Solution**

The purified apoferritin monomer solution that was collected is highly diluted. Therefore the sample has to be concentrated prior to crystallization experiments.

<u>B.2.3.1 Materials</u>

- Millipore Centricon YM-30 centrifugation filter (30 kD cut-off)

- Hermle Z 360 K centrifuge at 4 °C

- Hermle rotor 220.78

- UV spectrophotometer at 280 nm

- Costar Spin-X centrifugation filter (0.22 μm)

B.2.3.2 Centricon Maximum Centrifugal Force

Centricon filter devices with Ultracel YM-3 membranes:

without retentate vial:        6500 × g

with retentate vial:        7500 × g

during prerinsing:        5000 × g

Centricon filter devices with Ultracel YM-10, YM-30, and YM-50 membranes:

5000 × g

Centricon filter devices with Ultracel YM-100 membranes:

5000 × g for proteins;

2000 × g for nucleic acids (adjust the sample to 2 mL with TE or other

appropriate buffer prior to centrifugation)

B.2.3.3 Concentration steps

- Install Hermle rotor 220.78 and pre-cool the centrifuge to 4 °C
- Pre-rinse the Centricon centrifugation filters to remove trace amounts of glycerin (approx. 2 μL per device): add 2 mL of running buffer (see Figure B-12) and spin for about 20 minutes at 6500 rpm (5000 × g)
- Empty filtrate and retentate vial, inverse sample reservoir (see Figure B-13) and spin at 1000-3000 rpm (300-1000g) for 2 minutes
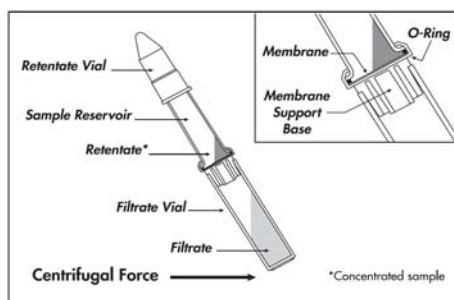
Figure B-12.  Sample loading into centrifugal filtration device

- Load diluted apoferritin solution (~1.7 mL) and spin at 6500 rpm (5000 × g) for about 20 minutes (make sure that the vials are equally full otherwise the centrifuge will be out of balance)
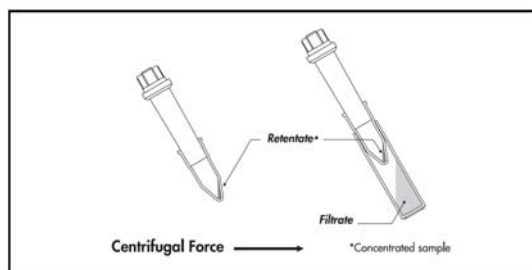


Figure B-13.  Product recovery from centrifugal filtration device

- Empty filtrate vial, load more apoferritin sample and spin; repeat until all apoferritin solution is concentrated.
- *Note:* there could be a greenish/brownish accumulation occurring at the membrane towards the end of the concentration runs.  This is an indication of concentration polarization due to the water flux through the membrane, causing a reduction in membrane performance.  To reduce this stir up the solution in the sample reservoir by aspirating a few times with the pipette (be careful not to touch the membrane)
- Pre-rinse Costar Spin-X centrifugation filters with running buffer (in Eppendorf centrifuge at room temperature for a few seconds) and filter the apoferritin solution to remove any potential dust particles
- Measure the apoferritin concentration via total protein assay (Chapter 4.2.1).

- Store purified apoferritin solution in 1.5 mL centrifuge tubes at 4 °C (refrigerator) until usage

B.2.3.4 Total Protein Assay calibration
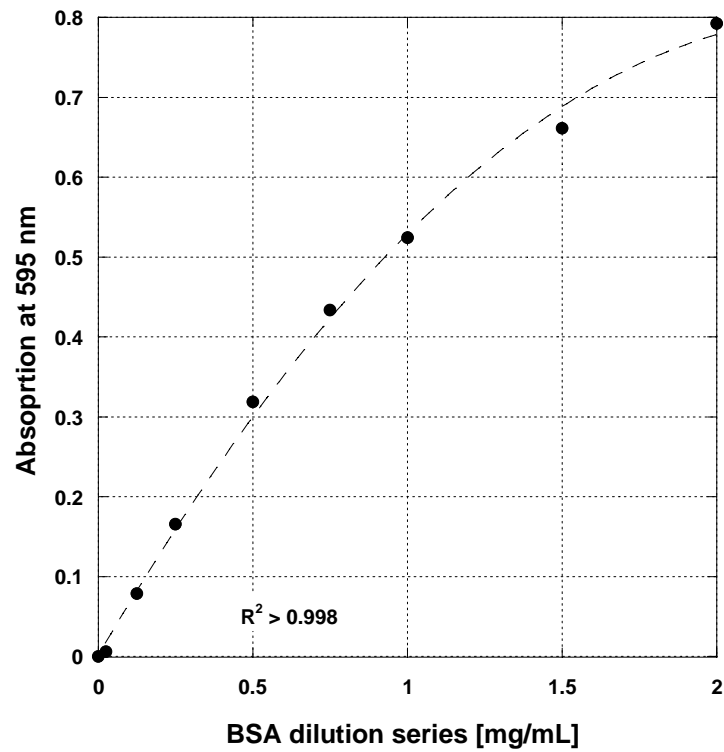


Figure B-14.  Calibration Total Protein Assay (example)

## B.2.4 Results of the Apoferritin Purification via SEC-HPLC
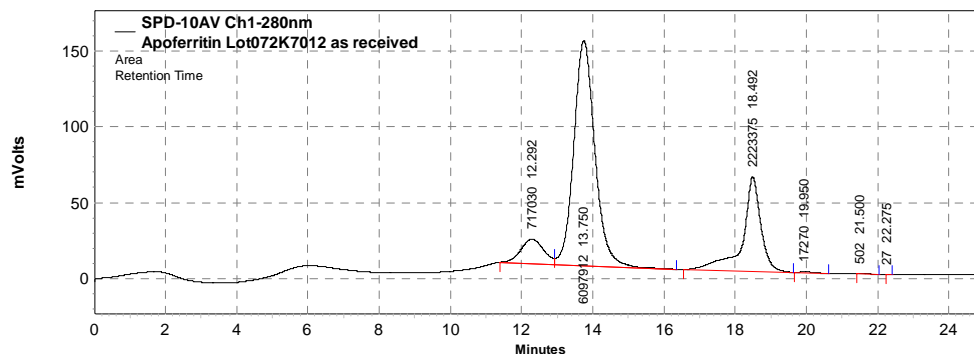


Figure B-15.  As-received apoferritin (55 mg/mL), 3 µL injected
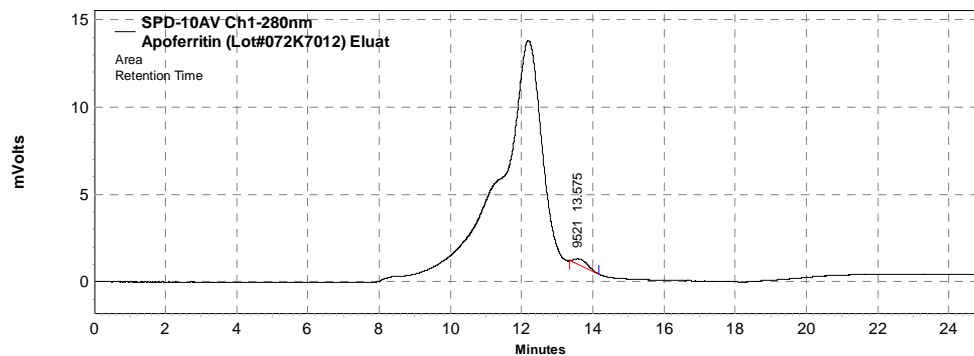


Figure B-16.  Apoferritin  (Sigma A3641, Lot# 072K7012), Peak 1, 20 µL injected, Oligomer fraction
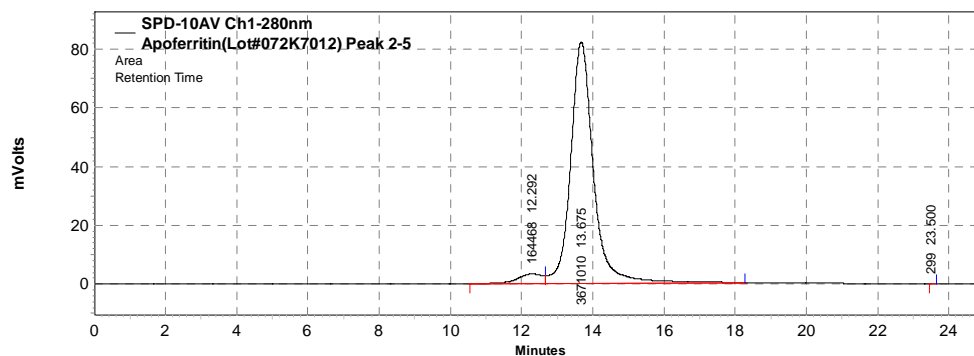


Figure B-17.  Apoferritin  (Sigma A3641, Lot# 072K7012), Peak 2, 20 µL injected, Monomer fraction
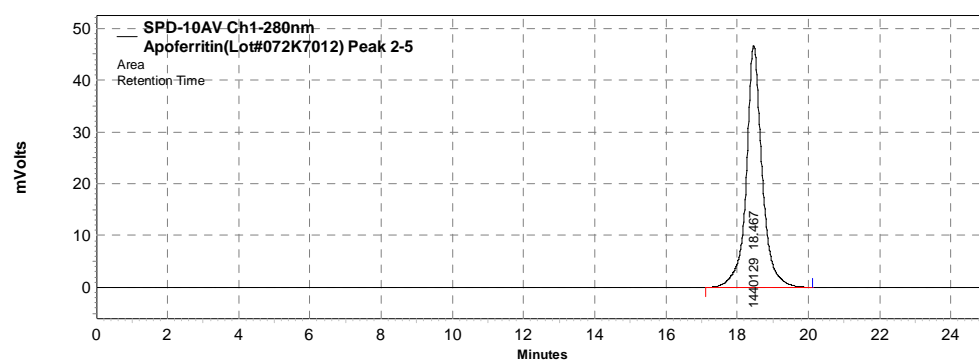
Figure B-18. Apoferritin (Sigma A3641, Lot# 072K7012), Peak 5, 20 μL injected, Subunit fraction

# B.3 Apoferritin Thermal Stability
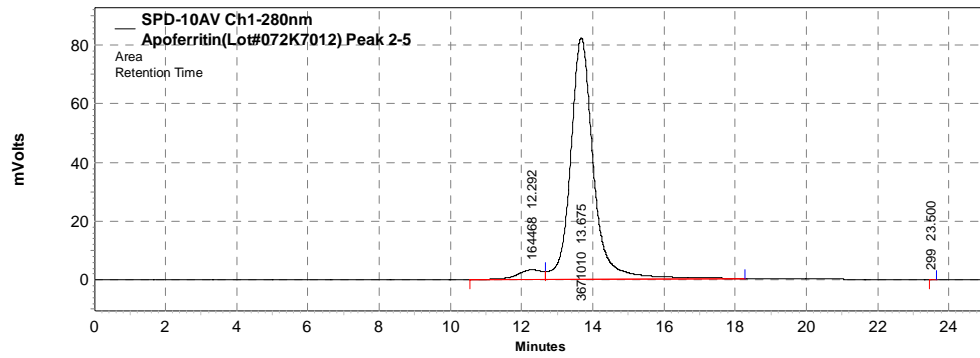


Figure B-19.  Purified apoferritin (8 mg/mL), 20 μL injected
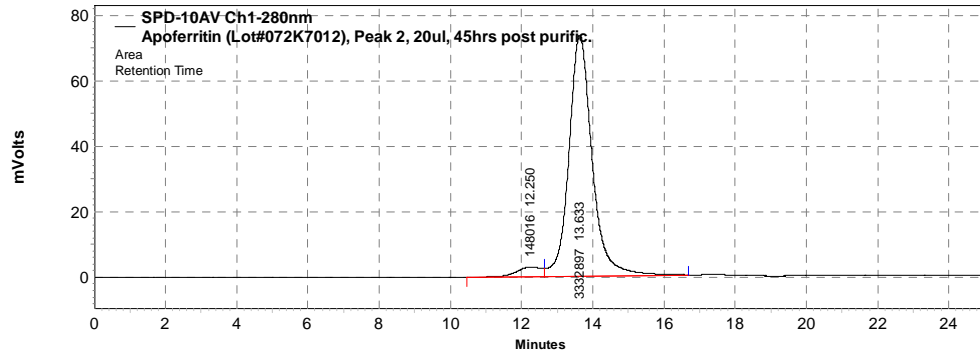


Figure B-20.  Purified apoferritin (8 mg/mL), stored at 37 °C for 72 hours, 20 μL injected
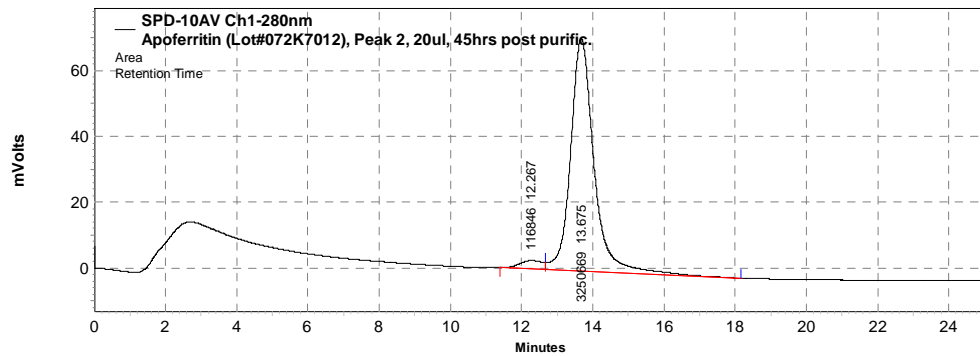


Figure B-21.  Purified apoferritin (8 mg/mL), stored at 4 °C for 72 hours, 20 μL injected

# B.4 Apoferritin Stability in the Presence of Solubilizers

## B.4.1 Control, 0 hours incubation
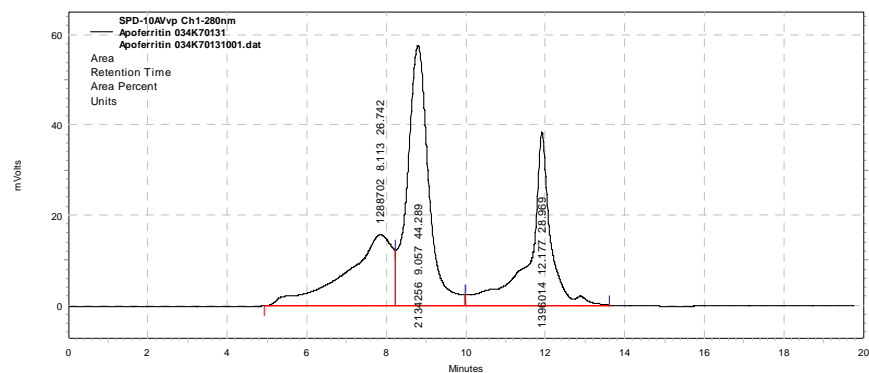


Figure B-22.  As-received apoferritin (8 mg/mL); sample set 1, control 1; 10 µL injected
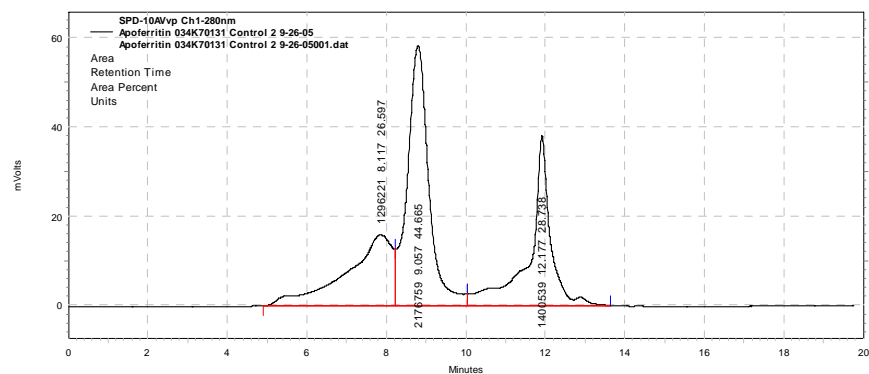


Figure B-23.  As-received apoferritin (8 mg/mL); sample set 1, control 2; 10 µL injected
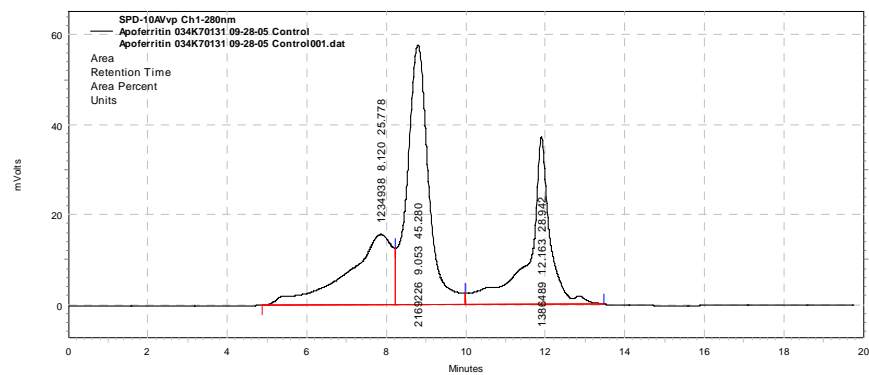
Figure B-24.  As-received apoferritin (8 mg/mL); sample set 2, control 1; 10 µL injected
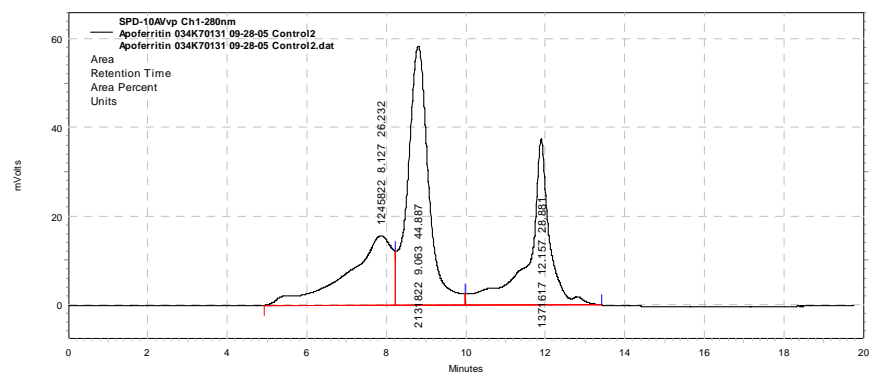


Figure B-25.  As-received apoferritin (8 mg/mL); sample set 2, control 2; 10 µL injected

## B.4.2 Sample set 1, 24 hour incubation at °C
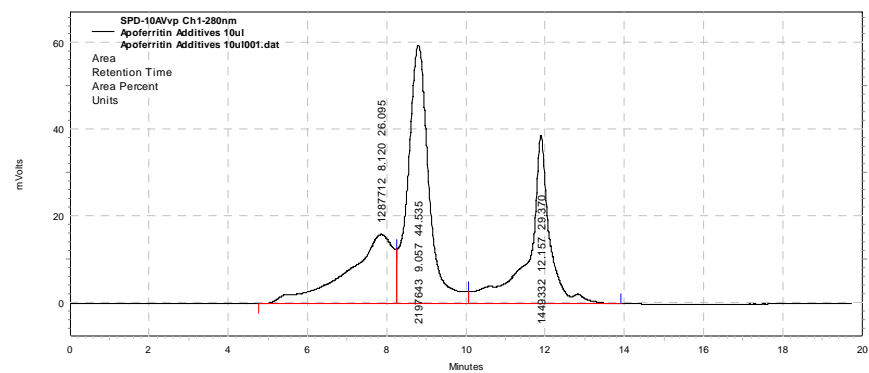


Figure B-26.  As-received apoferritin (8 mg/mL); control 1; 10 µL injected
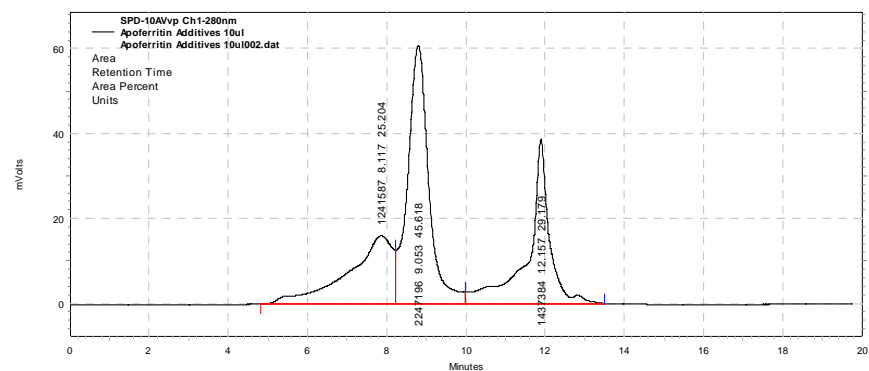
Figure B-27.  As-received apoferritin (8 mg/mL); control 2; 10 µL injected



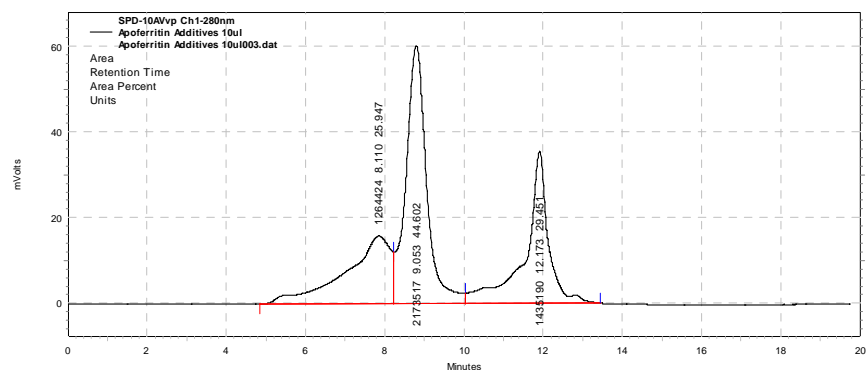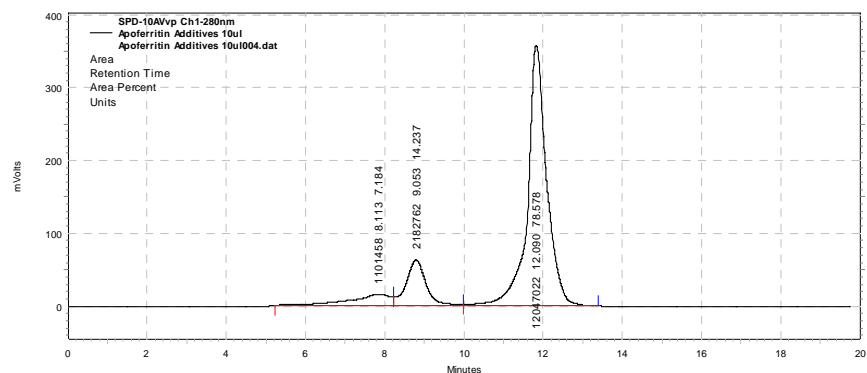Figure B-28.  As-received apoferritin (8 mg/mL); 1 M NDSB 195; 10 µL injected



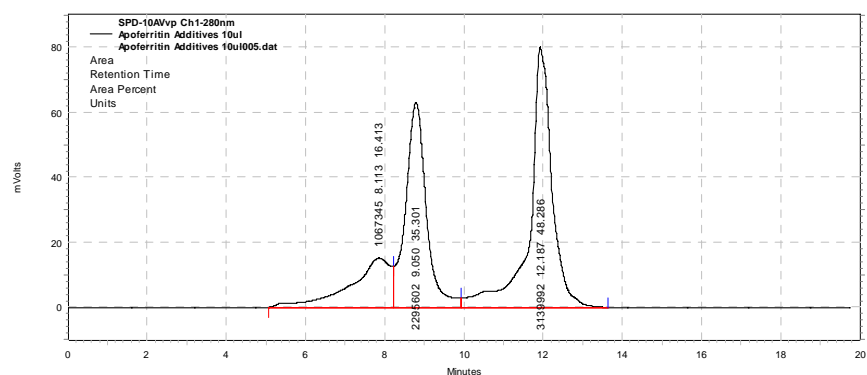Figure B-29.  As-received apoferritin (8 mg/mL); 1 M NDSB 201; 10 µL injected



Figure B-30.  As-received apoferritin (8 mg/mL); 1 M NDSB 256; 10 µL injected
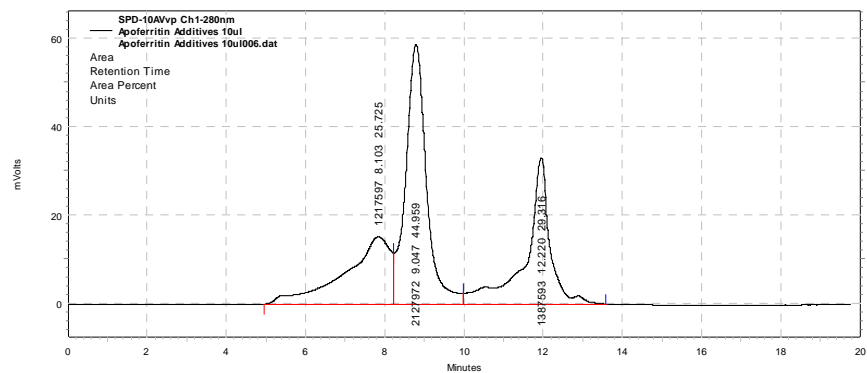
Figure B-31. As-received apoferritin (8 mg/mL); 1 M glucose; 10 µL injected
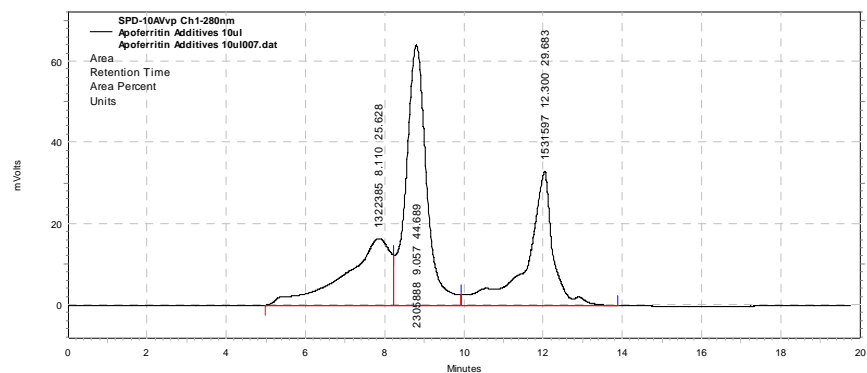


Figure B-32.  As-received apoferritin (8 mg/mL); 1 M sucrose; 10 µL injected
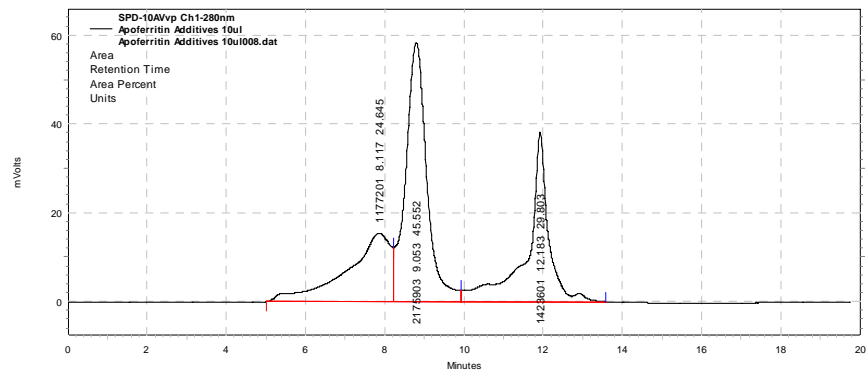
## B.4.3 Sample set 2, 24 hour incubation at 30 °C



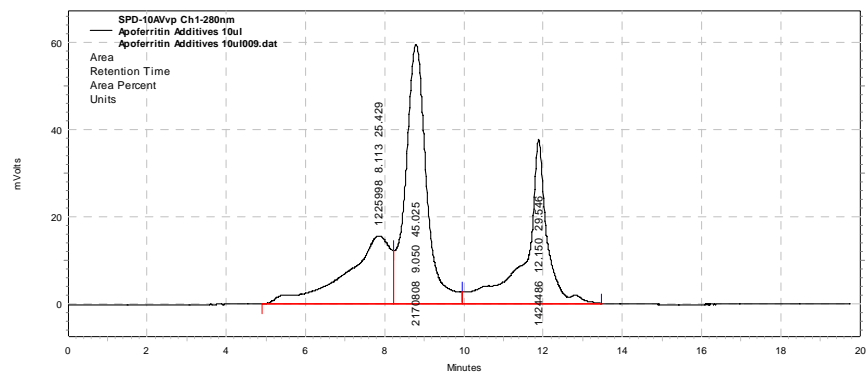Figure B-33.  As-received apoferritin (8 mg/mL); control 1; 10 µL injected

Figure B-34.  As-received apoferritin (8 mg/mL); control 2; 10 µL injected



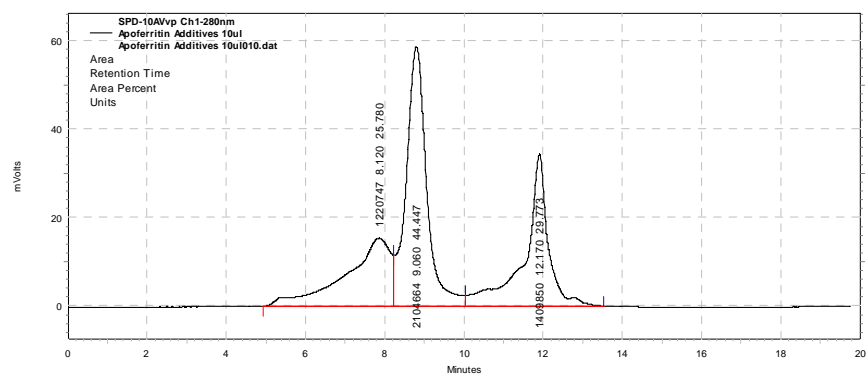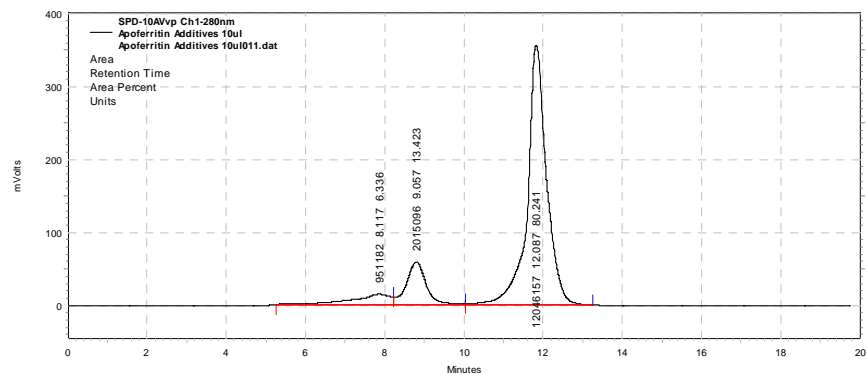Figure B-35.  As-received apoferritin (8 mg/mL); 1 M NDSB 195; 10 µL injected



Figure B-36.  As-received apoferritin (8 mg/mL); 1 M NDSB 201; 10 µL injected

Figure B-37.  As-received apoferritin (8 mg/mL); 1 M NDSB 256; 10 µL injected



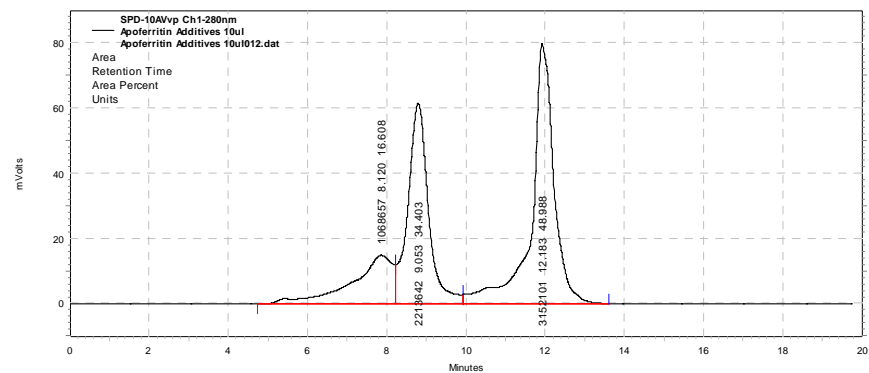Figure B-38.  As-received apoferritin (8 mg/mL); 1 M glucose; 10 µL injected
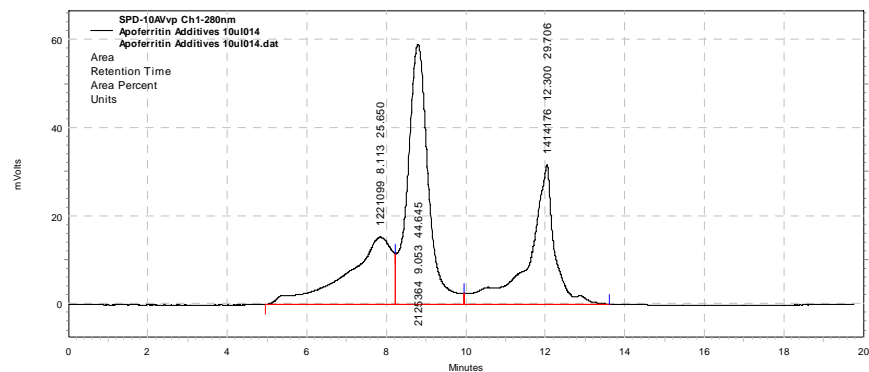


Figure B-39.  As-received apoferritin (8 mg/mL); 1 M sucrose; 10 µL injected

# B.5 Protein Stability in the Presence of Additives

## B.5.1 Apoferritin, 24 hour incubation
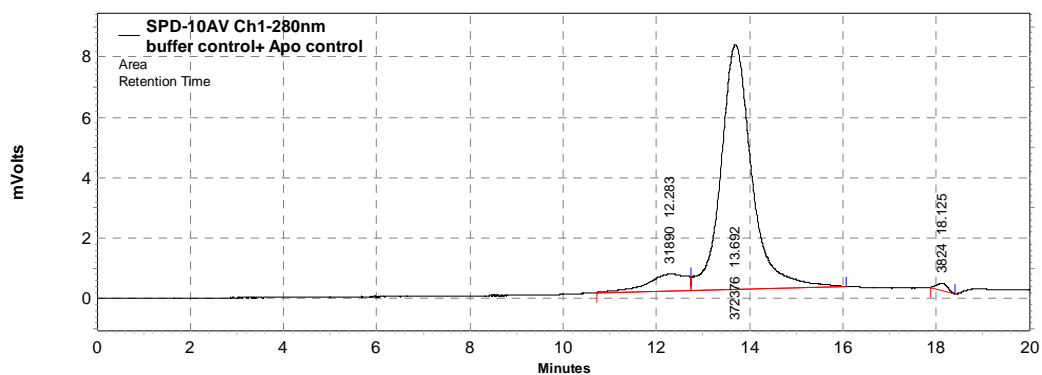


Figure B-40.  Purified apoferritin (8 mg/mL); control; 10 μL injected
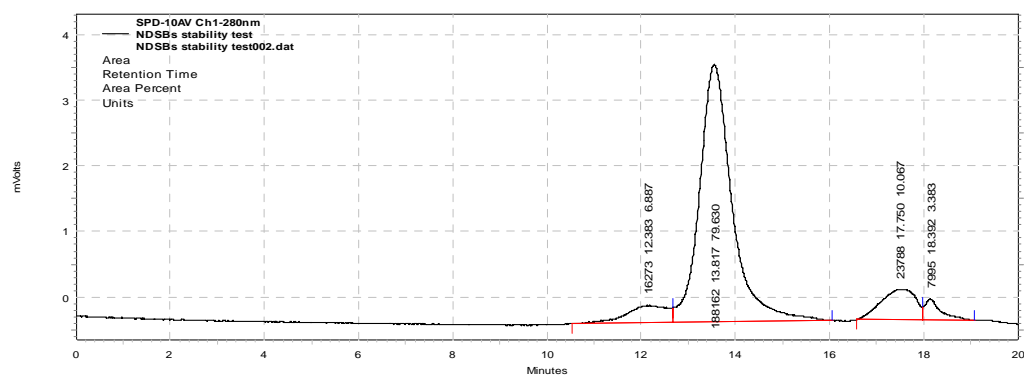


Figure B-41.  Purified apoferritin (8 mg/mL); 1 M NDSB 195; 10 μL injected
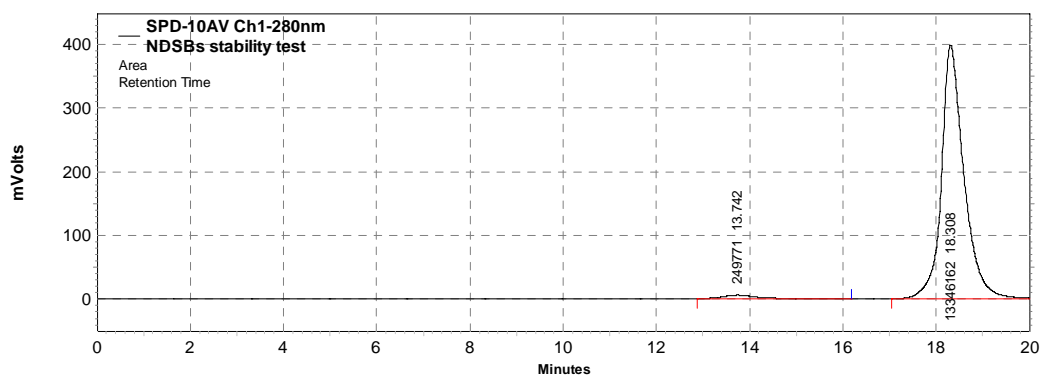
Figure B-42.  Purified apoferritin (8 mg/mL); 1 M NDSB 201; 10 µL injected
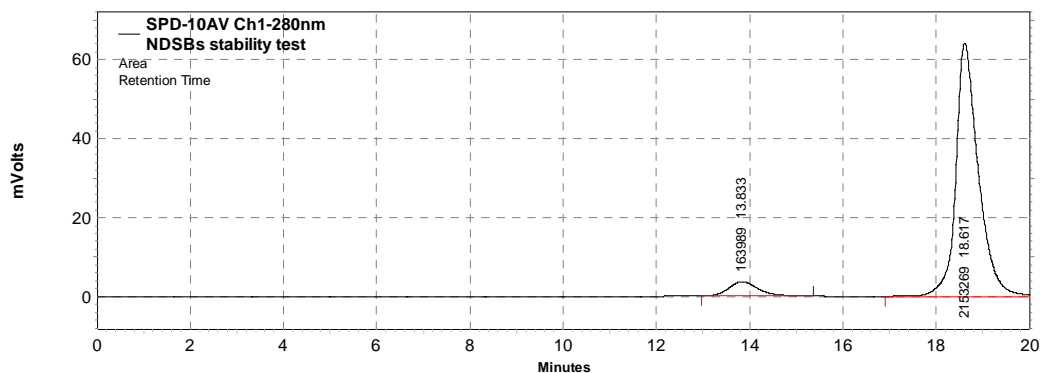


Figure B-43.  Purified apoferritin (8 mg/mL); 1 M NDSB 256; 10 µL injected

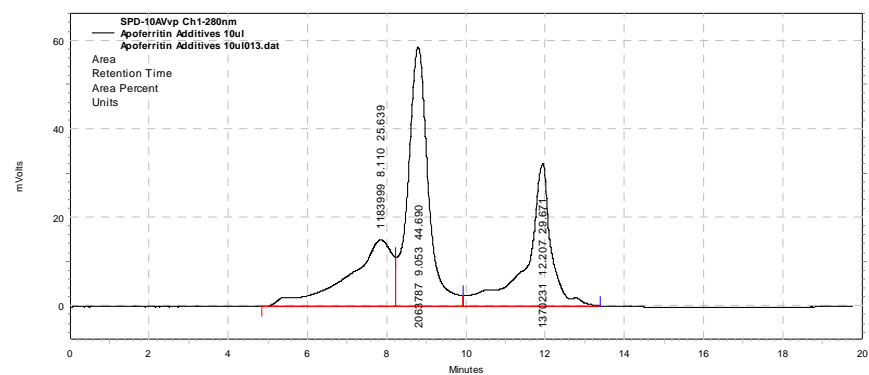## B.5.2 Mandelate Racemase, 24 hour incubation
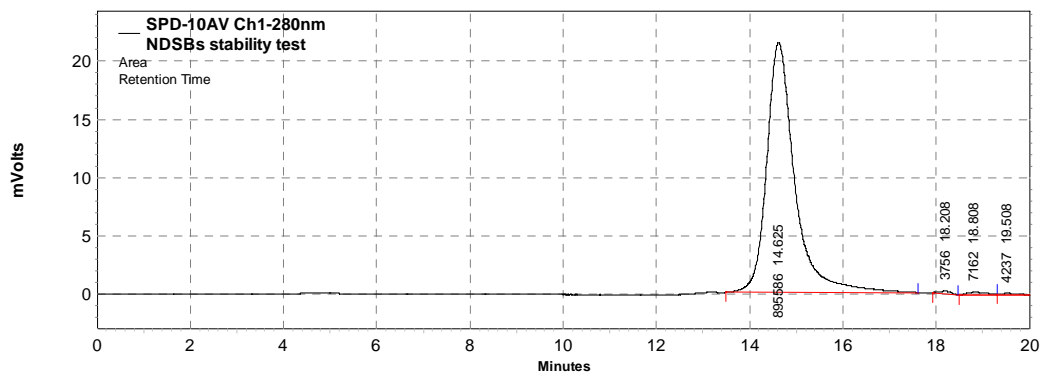


Figure B-44.  Mandelate racemase (8 mg/mL); control; 10 µL injected
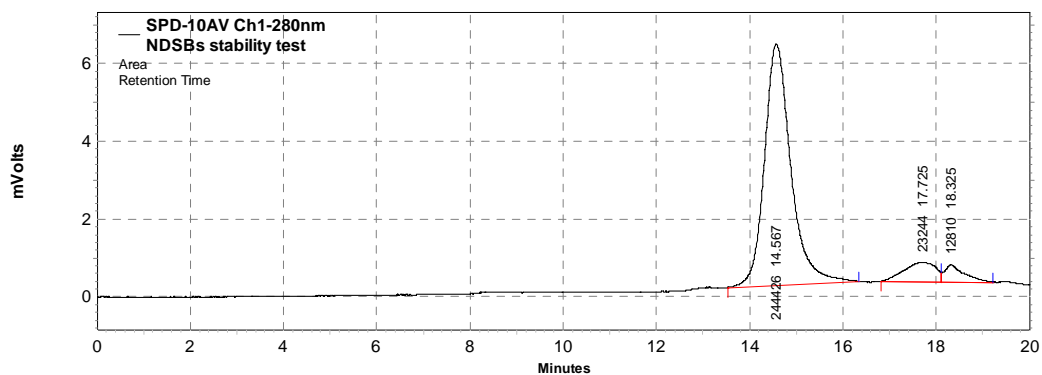
Figure B-45.  Mandelate racemase (8 mg/mL); 1 M NDSB 195; 10 µL injected
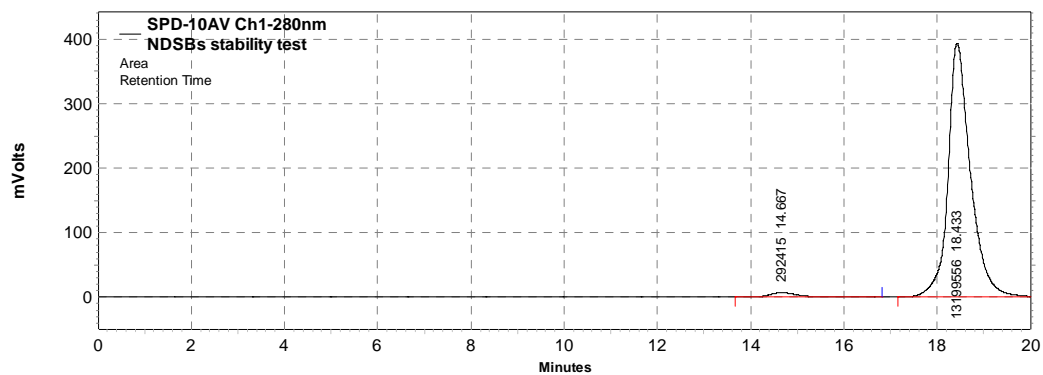


Figure B-46.  Mandelate racemase (8 mg/mL); 1 M NDSB 201; 10 µL injected
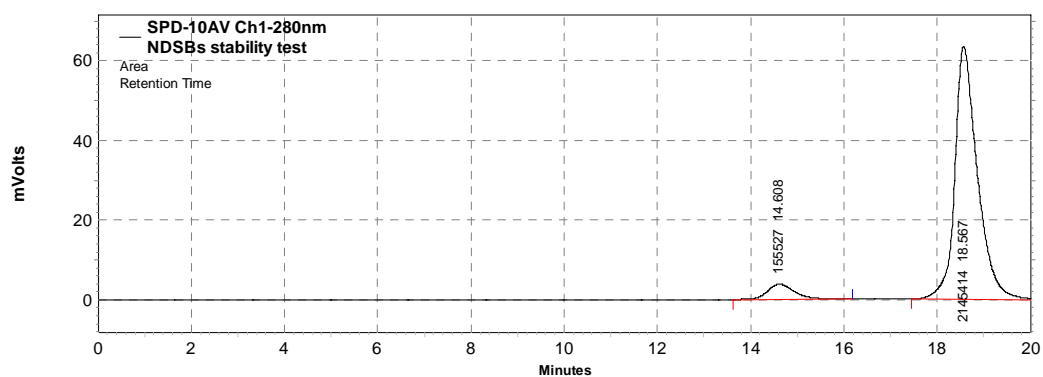


Figure B-47.  Mandelate racemase (8 mg/mL); 1 M NDSB 256; 10 µL injected

## B.5.3 Catalase, 24 hour incubation



Figure B-48.  Catalase (8 mg/mL); control; 10 µL injected
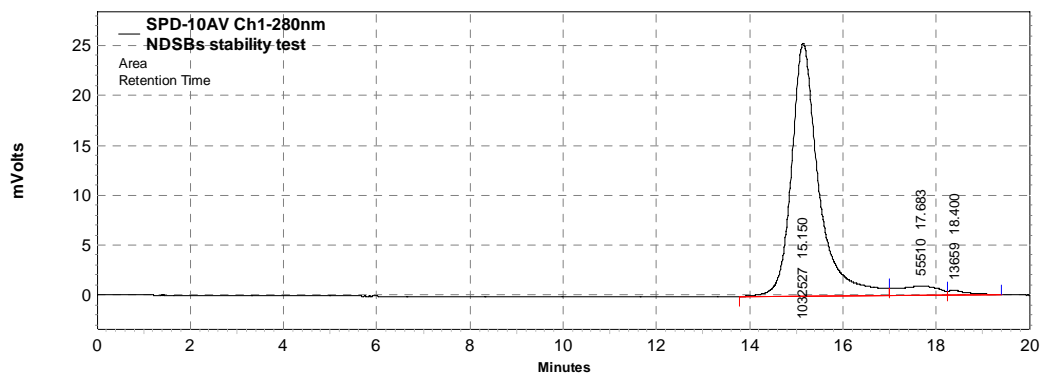


Figure B-49.  Catalase (8 mg/mL); 1 M NDSB 195; 10 µL injected
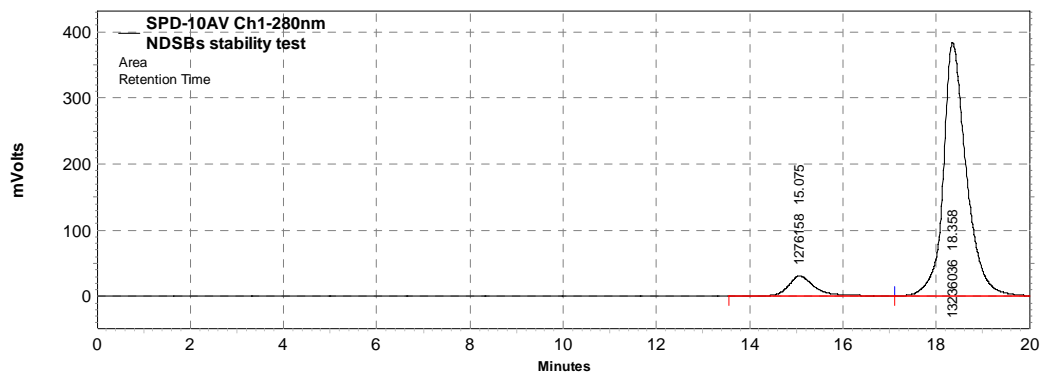


Figure B-50.  Catalase (8 mg/mL); 1 M NDSB 201; 10 µL injected

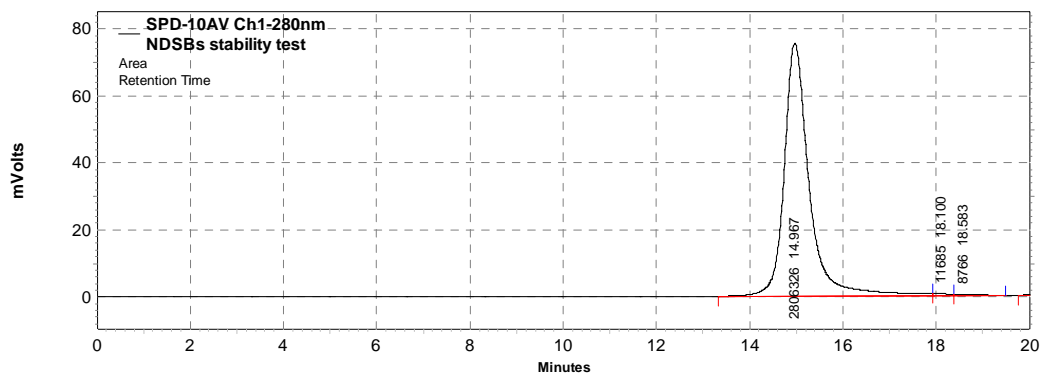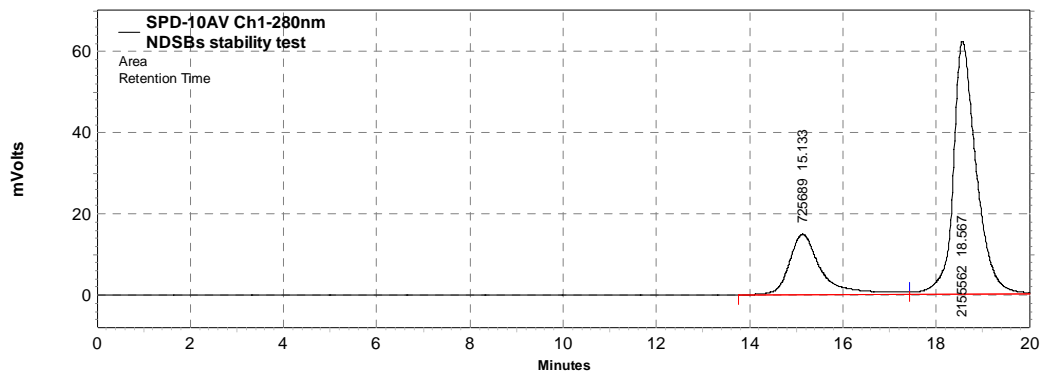Figure B-51.  Catalase (8 mg/mL); 1 M NDSB 256; 10 μL injected

## B.5.4 Buffers only
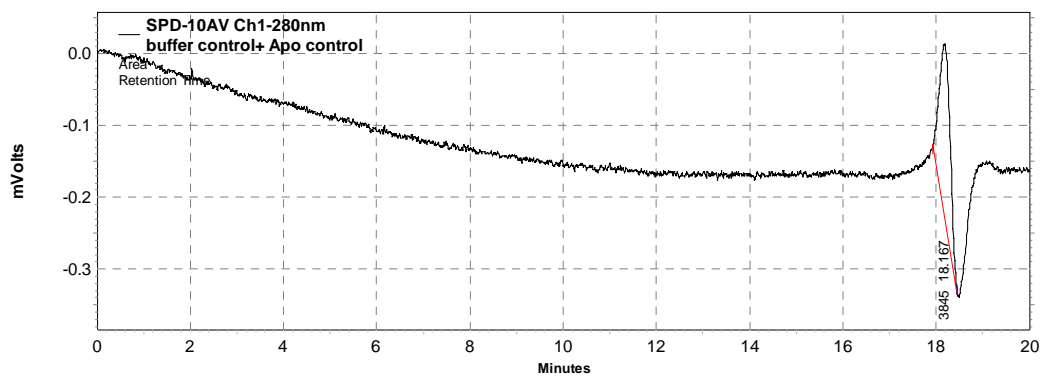


Figure B-52.  50 mM tris-HCL
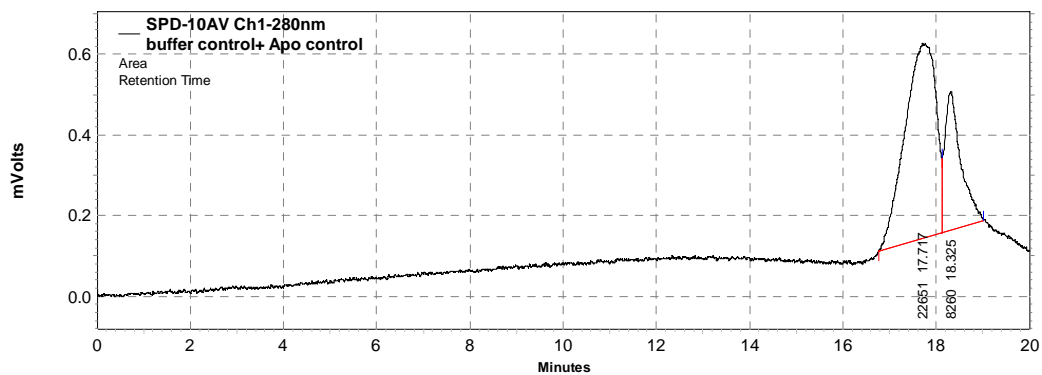


Figure B-53.  1 M NDSB 195
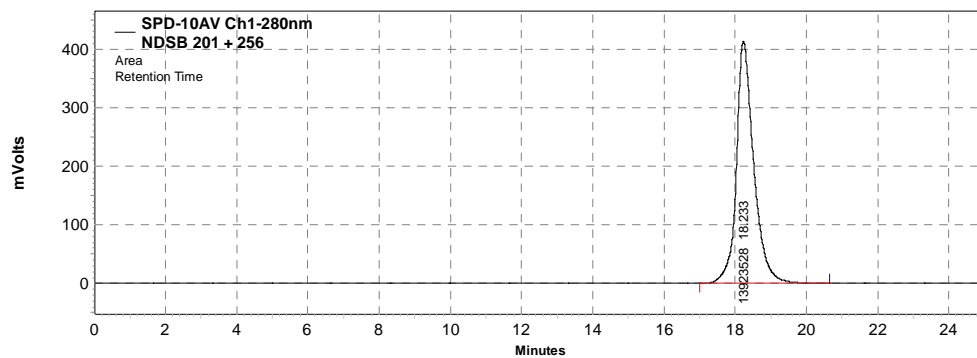
Figure B-54.  1 M NDSB 201
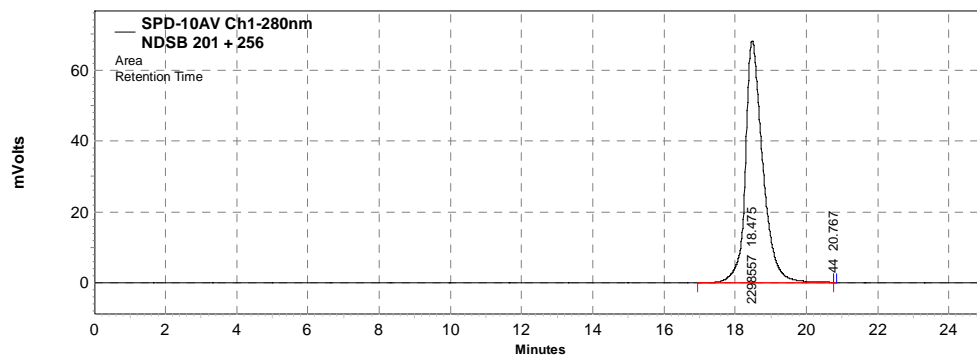


Figure B-55.  1 M NDSB 256

# REFERENCES

Abbott, A. (2000). "Structures by numbers." Nature 408(6809): 130-132.

Abel, J. J. (1926). "Crystalline Insulin." Proceedings of the National Academy of Sciences of the United States of America 12(2): 132-6.

Aisen, P., C. Enns, et al. (2001). "Chemistry and biology of eukaryotic iron metabolism." International Journal of Biochemistry & Cell Biology 33(10): 940-959.

Alghadyan, A. A. and E. Cotlier (1986). "Rise in Lens Temperature on Exposure to Sunlight or High Ambient-Temperature." British Journal of Ophthalmology 70(6): 421-426.

Alio, J. and M. Padron (1982). "Influence of Age on the Temperature of the Anterior Segment of the Eye - Measurements by Infrared Thermometry." Ophthalmic Research 14(3): 153-159.

Allerson, C. R., M. Cazzola, et al. (1999). "Clinical severity and thermodynamic effects of iron-responsive element mutations in hereditary hyperferritinemia-cataract syndrome." Journal of Biological Chemistry 274(37): 26439-26447.

Anon (2000). CRC Handbook of Chemistry and Physics. 81st Edition. Edited by David R. Lide (National Institute of Standards and Technology). CRC Press: Boca Raton, FL. 2000. 2556 pp. $129.95. ISBN 0-8493-0481-4.

Anon (2006). CRC Handbook of Chemistry and Physics, 86th Edition, edited by David R. Lide (National Institute of Standards and Technology). CRC Press (an imprint of Taylor and Francis Group): Boca Raton, FL. 2005. 2544 pp. $125.96. ISBN 0-8493-0486-5.

Arakawa, T. and S. N. Timasheff (1984). "Mechanism of Protein Salting in and Salting out by Divalent-Cation Salts - Balance between Hydration and Salt Binding." Biochemistry 23(25): 5912-5923.

Armstrong, R. A. (2000). "The genetics of cataract." Optometry Today: 33-35.

Arosio, P., T. G. Adelman, et al. (1978). "On Ferritin Heterogeneity." Journal of Biological Chemistry 253(12): 4451-4458.

Arosio, P., G. Gatti, et al. (1983). "Selective Crystallization of Horse Isoferritins." Biochimica Et Biophysica Acta 744(2): 230-232.

Arvan, P. (2004). "Secretory protein trafficking: Genetic and biochemical analysis." Cell Biochemistry and Biophysics(Suppl.): 169-177.

Avunduk, A. M., S. Yardimci, et al. (1999). "Cadmium and iron accumulation in rat lens after cigarette smoke exposure and the effect of vitamin E (alpha-tocopherol) treatment." Current Eye Research 18(6): 403-407.

Avunduk, A. M., S. Yardimci, et al. (1999). "Cataractous changes in rat lens following cigarette smoke exposure is prevented by parenteral deferoxamine therapy." Archives of Ophthalmology 117(10): 1368-1372.

Bartling, K., A. Sambanis, et al. (2005). "Multiwell microbatch crystallization on a thermal gradient." Crystal Growth & Design 5(4): 1559-1564.

Benedek, G. B. (1997). "Cataract as a protein condensation disease - The Proctor Lecture." Investigative Ophthalmology & Visual Science 38(10): 1911-1921.

Berg, M., M. Urban, et al. (2002). "Development and characterization of temperature-controlled microreactors for protein crystallization." Acta Crystallographica Section D-Biological Crystallography 58: 1643-1648.

Bergeron, L., L. F. Filobelo, et al. (2003). "Thermodynamics of the hydrophobicity in crystallization of insulin." Biophysical Journal 85(6): 3935-3942.

Berman, H. M., J. Westbrook, et al. (2000). "The Protein Data Bank." Nucleic Acids Research 28(1): 235-242.

Bjork, I. (1973). "Association-dissociation behavior and hydrodynamic properties of apoferritin monomer and dimer." European Journal of Biochemistry 36(1): 178-84.

Bonneau, D., I. Winterfuseau, et al. (1995). "Bilateral Cataract and High Serum Ferritin - a New Dominant Genetic Disorder." Journal of Medical Genetics 32(10): 778-779.

Bostroem, M., F. W. Tavares, et al. (2005). "Why forces between proteins follow different Hofmeister series for pH above and below pI." Biophysical Chemistry 117(3): 217-224.

Bron, A. J., G. F. J. M. Vrensen, et al. (2000). "The aging lens." Ophthalmologica 214(1): 86-104.

Brooks, D. G., K. Manova-Todorova, et al. (2002). "Ferritin crystal cataracts in hereditary hyperferritinemia cataract syndrome." Investigative Ophthalmology & Visual Science 43(4): 1121-1126.

Bryce, C. F. A. and R. R. Crichton (1973). "The Catalytic Activity of Horse Spleen Apoferritin - Preliminary kinetic studies and the effect of chemical modification." Biochemical Journal 133(2): 301-&.

Burke, M., R. Judge, et al. (2001). "The effect of solution thermal history on chicken egg white lysozyme nucleation." Journal of Crystal Growth 232(1-4): 301-307.

Cacioppo, E. and M. L. Pusey (1991). "The Solubility of the Tetragonal Form of Hen Egg-White Lysozyme from Ph 4.0 to 5.4." Journal of Crystal Growth 114(3): 286-292.

Cazzola, M. and R. C. Skoda (2000). "Translational pathophysiology: a novel molecular mechanism of human disease." Blood 95(11): 3280-3288.

Cekic, O. (1998). "Copper, lead, cadmium and calcium in cataractous lenses." Ophthalmic Research 30(1): 49-53.

Cekic, O. (1998). "Effect of cigarette smoking on copper, lead, and cadmium accumulation in human lens." British Journal of Ophthalmology 82(2): 186-188.

Chang-Godinich, A., S. Ades, et al. (2001). "Lens changes in hereditary hyperferritinemia-cataract syndrome." American Journal of Ophthalmology 132(5): 786-788.

Chayen, N. E. (1997). "The role of oil in macromolecular crystallization." Structure 5(10): 1269-1274.

Chayen, N. E. (1998). "Comparitive Studies of Protein Crystallization by Vapour-Diffusion and Microbatch Techniques." Acta Crystallographica Section D 54: 8-15.

Chayen, N. E. (1999). "Crystallization with oils: a new dimension in macromolecular crystal growth." Journal of Crystal Growth 196(2-4): 434-441.

Chayen, N. E. (2002). "Tackling the bottleneck of protein crystallization in the post-genomic era." Trends in Biotechnology 20(3): 98-98.

Chayen, N. E., P. D. S. Stewart, et al. (1992). "Microbatch Crystallization under Oil - a New Technique Allowing Many Small-Volume Crystallization Trials." Journal of Crystal Growth 122(1-4): 176-180.

Cicilano, M., G. Zecchina, et al. (1999). "Recurrent mutations in the iron regulatory element of L-ferritin in hereditary hyperferritinemia-cataract syndrome." Haematologica 84(6): 489-492.

Collins, K. D. (2004). "Ions from the Hofmeister series and osmolytes: effects on proteins in solution and in the crystallization process." Methods 34(3): 300-311.

Collins, K. D. (2006). "Ion hydration: Implications for cellular function, polyelectrolytes, and protein crystallization." Biophysical Chemistry 119(3): 271-281.

Conti, M., M. Galassi, et al. (1997). "Capillary isoelectric focusing: The problem of protein solubility." Journal of Chromatography A 757(1-2): 237-245.

Craig, J. E., J. B. Clark, et al. (2003). "Hereditary hyperferritinemia-cataract syndrome - Prevalence, lens morphology, spectrum of mutations, and clinical presentations." Archives of Ophthalmology 121(12): 1753-1761.

Crichton, R. R., S. Wilmet, et al. (2002). "Molecular and cellular mechanisms of iron homeostasis and toxicity in mammalian cells." Journal of Inorganic Biochemistry 91(1): 9-18.

Curtis, R. A., H. W. Blanch, et al. (2001). "Calculation of phase diagrams for aqueous protein solutions." Journal of Physical Chemistry B 105(12): 2445-2452.

DeMattei, R. C. and R. S. Feigelson (1992). "Controlling Nucleation in Protein Solutions." Journal of Crystal Growth 122(1-4): 21-30.

DeMattei, R. C. and R. S. Feigelson (1993). "Thermal Methods for Crystallizing Biological Macromolecules." Journal of Crystal Growth 128(1-4): 1225-1231.

Doye, J. P. K., A. A. Louis, et al. (2004). "Inhibition of protein crystallization by evolutionary negative design." Physical Biology 1(1): P9-P13.

Doye, J. P. K. and W. C. K. Poon (2006). "Protein crystallization in vivo." Current Opinion in Colloid & Interface Science 11(1): 40-46.

Erie, J. C., J. A. Butz, et al. (2005). "Heavy Metal Concentrations in Human Eyes." American Journal of Ophthalmology 139(5): 888-893.

Expert-Bezancon, N., T. Rabilloud, et al. (2003). "Physical-chemical features of non-detergent sulfobetaines active as protein-folding helpers." Biophysical Chemistry 100(1-3): 469-479.

Feeling-Taylor, A. R., S. T. Yau, et al. (2004). "Crystallization mechanisms of hemoglobin C in the R state." Biophysical Journal 87(4): 2621-2629.

Forsythe, E. L. and M. L. Pusey (1996). "The effects of acetate buffer concentration on lysozyme solubility." Journal of Crystal Growth 168(1-4): 112-117.

Fowlis, W. W., L. J. Delucas, et al. (1988). "Experimental and Theoretical-Analysis of the Rate of Solvent Equilibration in the Hanging Drop Method of Protein Crystal-Growth." Journal of Crystal Growth 90(1-3): 117-129.

Francis, P. J., V. Berry, et al. (1999). "Lens biology - development and human cataractogenesis." Trends in Genetics 15(5): 191-196.

Freeman, R. D. and I. Fatt (1973). "Environmental Influences on Ocular Temperature." Investigative Ophthalmology 12(8): 596-602.

Funk, F., J. P. Lenders, et al. (1985). "Reductive mobilization of ferritin iron." Europen Journal of Biochemistry 152(1): 167-172.

Galkin, O. and P. G. Vekilov (2001). "Nucleation of protein crystals: critical nuclei, phase behavior, and control pathways." Journal of Crystal Growth 232(1-4): 63-76.

Galkin, O. and P. G. Vekilov (2004). "Mechanisms of homogeneous nucleation of polymers of sickle cell anemia hemoglobin in deoxy state." Journal of Molecular Biology 336(1): 43-59.

Garcia-Ruiz, J. (2003). "Nucleation of protein crystals." Journal of Structural Biology 142(1): 22-31.

Georgalis, Y. and W. Saenger (1993). "Time-resolved light scattering studies on protein precrystallization fractal clusters." Advances in Colloid and Interface Science 46: 165-83.

George, A., Y. Chiang, et al. (1997). "Second virial coefficient as predictor in protein crystal growth." Methods in Enzymology 276(Macromolecular Crystallography, Part A): 100-110.

George, A. and W. W. Wilson (1994). "Predicting Protein Crystallization from a Dilute-Solution Property." Acta Crystallographica Section D-Biological Crystallography 50: 361-365.

Gilliland, G. L., M. Tung, et al. (1994). "Biological Macromolecule Crystallization Database, Version-3.0 - New Features, Data and the Nasa Archive for Protein Crystal-Growth Data." Acta Crystallographica Section D-Biological Crystallography 50: 408-413.

Gilliland, G. L., M. Tung, et al. (2002). "The biological macromolecule crystallization database: crystallization procedures and strategies." Acta Crystallographica Section D - Biological Crystallography 58: 916-920.

Girelli, D., R. Corrocher, et al. (1997). "Hereditary hyperferritinemia-cataract syndrome caused by a 29-base pair deletion in the iron responsive element of ferritin L-subunit gene." Blood 90(5): 2084-2088.

Good, N. E., G. D. Winget, et al. (1966). "Hydrogen ion buffers for biological research." Biochemistry 5(2): 467-77.

Goralska, M., B. L. Holley, et al. (2003). "Identification of a mechanism by which lens epithelial cells limit accumulation of overexpressed ferritin H-chain." Journal of Biological Chemistry 278(44): 42920-42926.

Granier, T., B. Gallois, et al. (1997). "Comparison of the structures of the cubic and tetragonal forms of horse-spleen apoferritin." Acta Crystallographica Section D-Biological Crystallography 53: 580-587.

Gripon, C., L. Legrand, et al. (1997). "Lysozyme-lysozyme interactions in under- and super-saturated solutions: a simple relation between the second virial coefficients in H2O and D2O." Journal of Crystal Growth 178(4): 575-584.

Guex, N. and M. C. Peitsch (1997). "SWISS-MODEL and the Swiss-PdbViewer: An environment for comparative protein modeling." Electrophoresis 18(15): 2714-2723.

Guo B, K. S., McDonald H, Asanov A, Combs LL, Wilson WW (1999). "Correlation of second virial coefficients and solubilities useful in protein crystal growth." Journal of Crystal Growth 196(2-4).

Guo, L., R. S. Johnson, et al. (2000). "Biochemical characterization of endogenously formed eosinophilic crystals in the lungs of mice." Journal of Biological Chemistry 275(11): 8032-8037.

Haas C, J. Drenth, et al. (1999). "Relation between the solubility of proteins in aqueous solutions and the second virial coefficient of the solution." Journal of Physical Chemistry B 103(14): 2808-2811.

Haas, C., J. Drenth, et al. (1999). "Relation between the solubility of proteins in aqueous solutions and the second virial coefficient of the solution." Journal of Physical Chemistry B 103(14): 2808-2811.

Hanlon, D. P., D. S. Watt, et al. (1966). "The Interaction of Divalent Metal Ions with Tris Buffer in Dilute Solution." Analytical Biochemistry 16(2): 225-&.

Harding, J. J. (1995). "Cigarettes and Cataract - Cadmium or a Lack of Vitamin-C." British Journal of Ophthalmology 79(3): 199-200.

Harrison, P. M. and P. Arosio (1996). "The ferritins: Molecular properties, iron storage function and cellular regulation." Biochimica Et Biophysica Acta-Bioenergetics 1275(3): 161-203.

Havel, H. A. (1995). Spectroscopic methods for determining protein structure in solution. New York, VCH.

He, W. and S. Li (2000). "Congenital cataracts: gene mapping." Human Genetics 106(1): 1-13.

Heiler, D. J. and S. F. Groemminger (1998). Treatment of contact lenses with an aqueous solution including sulfobetaine compounds. US: 8.

Howard, S. B., P. J. Twigg, et al. (1988). "The Solubility of Hen Egg-White Lysozyme." Journal of Crystal Growth 90(1-3): 94-104.

Huang, H. Q., Q. M. Lin, et al. (2000). "Construction of a ferritin reactor: An efficient means for trapping various heavy metal ions in flowing seawater." Journal of Protein Chemistry 19(6): 441-447.

Incropera, F. P. and D. P. Dewitt (2000). Fundamentals of Heat and Mass Transfer, 4th Update Edition.

Islam, P., R. Hill, et al. (2003). "Activation energy for crystal growth in stoichiometric CaAl2Si2O8 and Ca2Al2Si2O9 glasses." Journal of Materials Science Letters 22(18): 1287-1289.

Jolles, P. and J. Berthou (1972). "High-Temperature Crystallization of Lysozyme - Example of Phase Transition." FEBS Letters 23(1): 21-&.

Jones, W. F., J. M. Wiencek, et al. (2001). "Improvements in lysozyme crystal quality via temperature-controlled growth at low ionic strength." Journal of Crystal Growth 232(1-4): 221-228.

Juarez-Martinez, G., C. Garza, et al. (2001). "A dynamic light scattering investigation of the nucleation and growth of thaumatin crystals." Journal of Crystal Growth 232(1-4): 119-131.

Juarez-Martinez, G., P. Steinmann, et al. (2002). "High-throughput screens for postgenomics: Studies of protein crystallization using microsystems technology." Analytical Chemistry 74(14): 3505-3510.

Judge, R. A., E. L. Forsythe, et al. (1998). "The effect of protein impurities on lysozyme crystal growth." Biotechnology and Bioengineering 59(6): 776-785.

Judge, R. A., R. S. Jacobs, et al. (1999). "The effect of temperature and solution pH on the nucleation of tetragonal lysozyme crystals." Biophysical Journal 77(3): 1585-1593.

Kempen, A. T. W., F. Sommer, et al. (2002). "Determination and interpretation of isothermal and non-isothermal transformation kinetics; the effective activation energies in terms of nucleation and growth." Journal of Materials Science 37(7): 1321-1332.

Kmoch, S., J. Brynda, et al. (2000). "Link between a novel human gamma D-crystallin allele and a unique cataract phenotype explained by protein crystallography." Human Molecular Genetics 9(12): 1779-1786.

Kuhn, P., K. Wilson, et al. (2002). "The genesis of high-throughput structure-based drug discovery using protein crystallography." Current Opinion in Chemical Biology 6(5): 704-710.

Lauring, L. and F. Wergelan (1970). "Ocular Toxicity of Newer Industrial Metals." Military Medicine 135(12): 1171-&.

Lawson, D. M., P. J. Artymiuk, et al. (1991). "Solving the structure of human H ferritin by genetically engineering intermolecular crystal contacts." Nature (London, United Kingdom) 349(6309): 541-4.

Lens, A. (1999). Ocular anatomy and physiology. Thorofare, NJ, SLACK Inc.

Lilie, H., E. Schwarz, et al. (1998). "Advances in refolding of proteins produced in E-coli." Current Opinion in Biotechnology 9(5): 497-501.

Liu, F., F. Sommer, et al. (2004). "Determination of nucleation and growth mechanisms of the crystallization of amorphous alloys; application to calorimetric data." Acta Materialia 52(11): 3207-3216.

Lorber, B. and R. Giege (1992). "A versatile reactor for temperature controlled crystallization of biological macromolecules." Journal of Crystal Growth 122(1-4): 168-175.

Luft, J., D. Rak, et al. (1999). "Microbatch macromolecular crystallization on a thermal gradient." Journal of Crystal Growth 196: 447-449.

Malkin, A. J. and A. McPherson (1993). "Light-Scattering Investigations of Protein and Virus Crystal-Growth - Ferritin, Apoferritin and Satellite Tobacco Mosaic-Virus." Journal of Crystal Growth 128(1-4): 1232-1235.

Malkin, A. J. and A. McPherson (1994). "Light-Scattering of Nucleation Processes and Kinetics of Crystallization in Macromolecular Systems." Acta Crystallographica Section D 50: 385-395.

Mapstone, R. (1968). "Determinants of Corneal Temperature." British Journal of Ophthalmology 52: 729-741.

Margolin, A. L. (1996). "Novel crystalline catalysts." Trends in Biotechnology 14(7): 223-230.

McPherson, A. (1985). "Crystallization of macromolecules: General Principles [5], Use of polyethylene glycol in the crystallization of macromolecules [6], Crystallization of proteins by variation of pH and temperature [7]." Methods in Enzymology 114: 112-127.

McPherson, A. (1999). Crystallization of biological macromolecules. New York, Cold Spring Harbor Laboratory Press.

Merlini, G. and V. Bellotti (2003). "Molecular mechanisms of amyloidosis." New England Journal of Medicine 349(6): 583-596.

Michaelis, L. (1947). "Ferritin and Apoferritin." Advances in protein chemistry 3: 53-66.

Mumford, A. D., I. A. Cree, et al. (2000). "The lens in hereditary hyperferritinaemia cataract syndrome contains crystalline deposits of L-ferritin." British Journal of Ophthalmology 84(7): 697-700.

Nordberg, M. (1984). "General aspects of cadmium: transport, uptake and metabolism by the kidney." <u>Environmental Health Perspectives</u> 54: 13-20.

Nugent, J. and J. Whelan (1984). <u>Human cataract formation</u>. London; Newark, NJ, Pitman; Distributed in North America by CIBA Pharmaceutical Co. (Medical Education Division).

Pead, S., E. Durrant, et al. (1995). "Metal Ion Binding to Apo, Holo, and Reconstituted Horse Spleen Ferritin." <u>Journal of Inorganic Biochemistry</u> 59(1): 15-27.

Petsev, D. N., B. R. Thomas, et al. (2001). "Temperature-independent solubility and interactions between apoferritin monomers and dimers in solution." <u>Journal of Crystal Growth</u> 232(1-4): 21-29.

Petsev, D. N., B. R. Thomas, et al. (2000). "Interactions and aggregation of apoferritin molecules in solution: Effects of added electrolytes." <u>Biophysical Journal</u> 78(4): 2060-2069.

Petsev, D. N. and P. G. Vekilov (2000). "Evidence for non-DLVO hydration interactions in solutions of the protein apoferritin." <u>Physical Review Letters</u> 84(6): 1339-1342.

Post, C., B. Johansson, et al. (1984). "Organ distribution and protein binding of cadmium in autopsy material from heavy smokers." <u>Environmental Research</u> 34(1): 29-37.

Prausnitz, J. M. (2003). "Molecular thermodynamics for some applications in biotechnology." <u>Journal of Chemical Thermodynamics</u> 35(1): 22-+.

Price, D. J. and J. G. Joshi (1983). "Ferritin - Binding of Beryllium and other divalent metal ions." <u>Journal of Biological Chemistry</u> 258(18): 10873-10880.

Racz, P. and A. Erdohelyi (1988). "Cadmium, lead and copper concentrations in normal and senile cataractous human lenses." <u>Ophthalmic Research</u> 20(1): 10-13.

Rayment, I. (2002). "Small-scale batch crystallization of proteins revisited: an underutilized way to grow large protein crystals." <u>Structure</u> 10: 147-151.

Roetto, A., S. Bosio, et al. (2002). "Pathogenesis of hyperferritinemia cataract syndrome." <u>Blood Cells Molecules and Diseases</u> 29(3): 532-535.

Rosenberger, F. and E. J. Meehan (1988). "Control of Nucleation and Growth in Protein Crystal-Growth." <u>Journal of Crystal Growth</u> 90(1-3): 74-78.

Rosenbluth, R. F. and I. Fatt (1977). "Temperature-Measurements in Eye." Experimental Eye Research 25(4): 325-341.

Sankar, M. and R. G. Bates (1978). "Buffers for the physiological pH range: thermodynamic constants of 3-(N-morpholino)propanesulfonic acid from 5 to 50 DegC." Analytical Chemistry 50(13): 1922-4.

Schwartz, B. (1965). "Environmental Temperature and the Ocular Temperature Gradient." Laboratory Sciences 74: 237-243.

Smith, J. M., H. C. Van Ness, et al. (1995). Chemical Engineering Thermodynamics, The McGraw-Hill Companies, Inc.

Stefanini, S., S. Cavallo, et al. (1996). "Thermal stability of horse spleen apoferritin and human recombinant H apoferritin." Archives of Biochemistry and Biophysics 325(1): 58-64.

Stevens, R. C. (2000). "High-throughput protein crystallization." Current Opinion in Structural Biology 10(5): 558-563.

Sulochana, K. N., S. Ramakrishnan, et al. (1998). "Cadmium and superoxide dismutase in tobacco chewers with cataract." Indian Journal of Pharmacology 30(6): 413.

Sulter, G. J., L. Looyenga, et al. (1990). "Occurrence of peroxisomal membrane proteins in methylotrophic yeasts grown under different conditions." Yeast 6(1): 35-43.

Tanford, C. (1961). Physical Chemistry of Macromolecules, John Wiley & Sons, Inc.

Tardieu, A., S. Finet, et al. (2001). "Structure of the macromolecular solutions that generate crystals." Journal of Crystal Growth 232(1-4): 1-9.

Tavares, F. W., D. Bratko, et al. (2004). "The role of salt-macroion van der Waals interactions in the colloid-colloid potential of mean force." Current Opinion in Colloid & Interface Science 9(1-2): 81-86.

Taylor, V. L., K. J. AlGhoul, et al. (1996). "Morphology of the normal human lens." Investigative Ophthalmology & Visual Science 37(7): 1396-1410.

Thomas, B. R., D. Carter, et al. (1998). "Effect of microheterogeneity on horse spleen apoferritin crystallization." Journal of Crystal Growth 187(3-4): 499-510.

Trakhanov, S., D. I. Kreimer, et al. (1998). "Cadmium-induced crystallization of proteins: II. Crystallization of the Salmonella typhimurium histidine-binding protein in complex with L-histidine, L-arginine, or L-lysine." Protein Science 7(3): 600-604.

Trakhanov, S. and F. A. Quiocho (1995). "Influence of Divalent-Cations in Protein Crystallization." Protein Science 4(9): 1914-1919.

Tsekova, D., S. Popova, et al. (2002). "Nucleation rate determination by a concentration pulse technique: application on ferritin crystals to show the effect of surface treatment of a substrate." Acta Crystallographica Section D-Biological Crystallography 58: 1588-1592.

Ueno, T., M. Suzuki, et al. (2004). "Size-selective olefin hydrogenation by a Pd nanocluster provided in an apo-ferritin cage." Angewandte Chemie-International Edition 43(19): 2527-2530.

Vallee, B. L. and D. D. Ulmer (1972). "Biochemical effects of mercury, cadmium, and lead." Annual Review of Biochemistry 41: 91-128.

Vekilov, P. G. (2002). "Self-assembly of apoferritin molecules into crystals: thermodynamics and kinetics of molecular level processes." Progress in Crystal Growth and Characterization of Materials 45(3): 175-193.

Vekilov, P. G. and A. A. Chernov (2002). The physics of protein crystallization. Solid State Physics: Advances in Research and Applications, Vol 57. S. F. Ehrenreich H. San Diego, Academic Press. 57: 1-147.

Vekilov, P. G., A. R. Feeling-Taylor, et al. (2002). "Solvent entropy contribution to the free energy of protein crystallization." Acta Crystallographica Section D-Biological Crystallography 58: 1611-1616.

Velev, O. D., E. W. Kaler, et al. (1998). "Protein interactions in solution characterized by light and neutron scattering: comparison of lysozyme and chymotrypsinogen." Biophysical Journal 75(6): 2682-2697.

Vuillard, L., B. Baalbaki, et al. (1996). "Protein crystallography with non-detergent sulfobetaines." Journal of Crystal Growth 168(1-4): 150-154.

Vuillard, L., C. Braun-Breton, et al. (1995). "Non-detergent sulfobetaines: a new class of mild solubilization agents for protein purification." Biochemical Journal 305(1): 337-43.

Vuillard, L., D. Madern, et al. (1995). "Halophilic Protein Stabilization by the Mild Solubilizing Agents Nondetergent Sulfobetaines." <u>Analytical Biochemistry</u> 230(2): 290-294.

Vuillard, L., N. Marret, et al. (1995). "Enhancing Protein Solubilization with Nondetergent Sulfobetaines." <u>Electrophoresis</u> 16(3): 295-297.

Vuillard, L., T. Rabilloud, et al. (1994). "A New Additive for Protein Crystallization." <u>FEBS Letters</u> 353(3): 294-296.

Waku, K. (1984). "The chemical form of cadmium in subcellular fractions following cadmium exposure." <u>Environmental Health Perspectives</u> 54: 37-44.

Weber, P. C. (1997). "Overview of protein crystallization methods." <u>Macromolecular Crystallography, Part A</u> 276: 13-22.

Wong, K. K. W., T. Douglas, et al. (1998). "Biomimetic Synthesis and Characterization of Magnetic Proteins (Magnetoferritin)." <u>Chemistry of Materials</u> 10(1): 279-285.

World Health Organization (2004). Vision 2020: The Right to Sight, the Global Initiative for the Elimination of Avoidable Blindness, World Health Organization. Fact Sheet No. 282: 1-4.

Wu, J. Z., D. Bratko, et al. (1998). "Interaction between like-charged colloidal spheres in electrolyte solutions." <u>Proceedings of the National Academy of Sciences of the United States of America</u> 95(26): 15169-15172.

Yau, S. T., D. N. Petsev, et al. (2000). "Molecular-level thermodynamic and kinetic parameters for the self-assembly of apoferritin molecules into crystals." <u>Journal of Molecular Biology</u> 303(5): 667-678.

Zimm, B. H. (1948). "Apparatus and Methods for Measurement and Interpretation of the Angular Variation of Light Scattering; Preliminary Results on Polystyrene Solutions." <u>Journal of Chemical Physics</u> 16(12): 1099-1116.

Zimm, B. H. (1948). "The Scattering of light and the Radial Distribution Function of High Polymer Solutions." <u>Journal of Chemical Physics</u> 16(12): 1093-1099.

# VITA

Karsten Bartling

Karsten Bartling was born in Kassel, Germany. He attended public schools in Kaufungen and Kassel, Germany, and received a B.A. in Biotechnology from The University of Applied Science, Giessen-Friedberg, Germany in 2000. He took an engineering position in the biotechnology department (R&D) at Fresenius-Kabi in Germany before coming to Georgia Tech to pursue a doctorate in Chemical & Biomolecular Engineering. When he is not working on his research, Mr. Bartling enjoys outdoor activities with his wife.